NASA CR-114305
Fairchild Hiller Report No. FHR-4000

DETAILED INVESTIGATION OF FLOWFIELDS WITHIN LARGE-SCALE HYPERSONIC INLET MODELS

By
William R. Seebaugh, Robert W. Doran, and Joseph P. DeCarlo

April 1971

FINAL REPORT
Prepared Under Contract No. NAS2-5719 by
FAIRCHILD HILLER
Farmingdale, Long Island, N.Y.
for Ames Research Center
NATIONAL AERONAUTICS AND SPACE ADMINISTRATION

TABLE OF CONTENTS

FOREWORD

This final report was prepared by the Republic Aviation Division of Fairchild Hiller Corporation, Farmingdale, New York, for NASA-Ames Research Center, Moffett Field, California, under Contract NAS2-5719.

The research reported herein was conducted under the technical cognizance of Mr. Earl C. Watson and Mr. A. Vernon Gnos of the Airbreathing Propulsion Branch, NASA-Ames Research Center.

The contract effort was conducted at Republic Aviation Division of Fairchild Hiller under the overall supervision of Dr. Robert J. Sanator and the technical management of Dr. William R. Seebaugh. Mr. Robert W. Doran and Mr. Joseph P. DeCarlo aided in the preparation of this report and made significant contributions to the engineering effort. Mr. Erich Muller and Mr. Laurence P. Weinberger also participated in a major way in the investigation. Mr. Robert J. Cavalleri served as technical consultant in the areas of inviscid and viscous flowfield analysis.

The major portion of the research discussed in this report was conducted as Phase II of the investigation of hypersonic inlets under contract NAS2-5719. Pertinent information generated during Phase I of the investigation under contract NAS2-5052 is included in this report in the interest of clarity and completeness. The entire Phase I program is discussed in detail in the report "Investigation of Hypersonic Flows in Large-Scale Model Internal Passages," Fairchild Hiller Report No. 3834, Nov. 30, 1969, by J. P. DeCarlo, D. Shamshins, W. R. Seebaugh, and R. Doran. Results from the following test programs, conducted at the NASA-Ames 3.5-Foot Hypersonic Wind Tunnel, are presented in this final report:

Phase I	Instrument Calibration	9-13 September 1968
	Inlet Forebody Flowfields	2-13 February 1969
	Inlet Throat Flowfields	14 February - 17 March 1969
Phase II	Instrument Calibration	26 January - 6 February 1970
	Detailed Inlet Internal Flowfields	27 April - 19 May 1970
		15 July - 4 August 1970

The participation of the personnel named above in the analytical and test phases of this research program is gratefully acknowledged. Further acknowledgement is

extended to the members of the Preliminary Design and Engineering Support departments of Republic Aviation Division of Fairchild Hiller and to the staff of the NASA-Ames 3.5-Foot Hypersonic Wind Tunnel.

LIST OF TABLES

LIST OF ILLUSTRATIONS

SUMMARY

Analytical and experimental investigations were conducted to determine the characteristics of the internal flows in model passages representative of hypersonic inlets and also sufficiently large for meaningful data to be obtained. The goal of the program was to improve the current methodology for the design of the internal contours of hypersonic inlets. The experimental results were used in the evaluation and improvement of analytical techniques for computing the flowfields in internal passages.

Three large-scale inlet models, each having a different compression ratio, were designed to provide high performance and approximately uniform static-pressure distributions at the throat stations. A wedge forebody was used to simulate the flowfield conditions at the entrance of the internal passages, thus removing the actual vehicle forebody from consideration in the design of the wind-tunnel models. Tests were conducted in the NASA-Ames 3.5-Foot Hypersonic Wind Tunnel at a nominal test Mach number of 7.4 and freestream unit Reynolds number of 2.7×10^6 per foot. From flowfield survey data at the inlet entrance, the entering inviscid and viscous flow conditions were determined prior to the analysis of the data obtained in the internal passages. Detailed flowfield survey data were obtained near the centerlines of the internal passages to define the boundary-layer development on the internal surfaces and the internal shock-wave configuration. Finally, flowfield data were measured across the throats of the inlet models to evaluate the internal performance of the internal passages. These data and additional results from surface instrumentation and flow visualization studies were utilized to determine the internal flowfield patterns and the inlet performance.

The experimental results revealed that a high level of total pressure recovery, approximately 0.85 (relative to the entrance conditions) for the core flow of the internal passages, was achieved for each inlet design. Within the accuracy of the measurements, the recovery was in agreement with the predicted level and was independent of the internal compression ratio over the range tested. The desired uniform static-pressure distributions at the throat stations were not obtained experimentally. The techniques employed to analyze the boundary-layer development gave generally good results for integral properties; however, further improvement is required in the analysis of the effects of boundary-layer transition on the subsequent boundary-layer development, in the analysis of the boundary-layer development downstream of blunt leading edges,

and in the prediction of the detailed characteristics of shock wave-boundary layer interactions. The lack of agreement between analysis and experiment observed for the internal flowfields did not adversely affect the ability to design inlet passages with high internal performance.

INTRODUCTION

The aerodynamic performance of the air-induction system is an important factor in establishing the viability of a hypersonic vehicle design. The inlet performance is primarily a function of the internal contour design. The basis for the development and assessment of analytical techniques for internal contour design most often is a wind tunnel test of scale models of representative hypersonic inlets. Previous experimental investigations (ref. 1, for example) have been performed with scale models of entire vehicle configurations. This procedure results in very small internal flow passages, and measurements of the internal flowfield development are very difficult to obtain. Consequently, the ability to improve the methods of designing and analyzing hypersonic air-induction systems depends, in a large part, upon the development of techniques of testing large-scale inlet models in relatively small test facilities.

The overall objective of the present investigation was to improve the current methodology for the design of the internal contours of hypersonic inlets. This objective was accomplished in the following manner:

(1) A method of testing large internal passages was devised.

(2) Current analytical and design techniques were applied in the design of several inlet configurations with different amounts of internal compression.

(3) Calibrations of instrumentation for flowfield surveys were obtained.

(4) Detailed measurements were obtained in internal passages with different amounts of internal compression. The heights of the internal passages were of the order of inches.

(5) The analytical and design techniques were evaluated by comparison of predictions and test results.

A typical hypersonic vehicle configuration (fig. 1) employs a conical compression surface that forms the vehicle forebody and delivers air to engine modules that are located circumferentially about the fuselage at the end of the compression surface. Because the diameter of the hypersonic vehicle is large, the flow at the inlet entrance and within the internal passages is basically two-dimensional in nature. A wedge forebody may then be used to simulate the flowfield conditions at the entrance of the inlet, effectively removing the actual vehicle forebody from consideration in the sizing of a wind tunnel model. This procedure was followed in the current investigation, and resulted in a one-third scale model of an internal passage with an overall model size

compatible with the NASA-Ames 3.5-Foot Hypersonic Wind Tunnel. Consequently, reliable and detailed flowfield data were obtained within the internal passages with relative ease, thus permitting the determination of the effects of compression ratio on inlet performance, a meaningful comparison of predicted and measured performance, and a critical evaluation of the analytical techniques employed in the design of the internal contours.

SYMBOLS

Symbol		Unit
L_i	length of region of shock wave-boundary layer interaction	in.
$\dot{m}$	mass flow	slug/sec-ft
M	Mach number	
P	pressure	psia
$\dot{q}$	heat-transfer rate	BTU/sec-ft^2
R	recovery factor, $(T_{t_{measured}}-T_{true})/(T_{t_{true}}-T_{true})$	
Re	Reynolds number	
T	temperature	°R
U	streamwise velocity component	ft/sec
X, Y, Z	spatial coordinates	in.
α	angle of attack	deg
δ	boundary-layer thickness	in.
δ^*	displacement thickness	in.
ϵ	flow-deflection angle	deg
θ	momentum thickness, surface angle	in.
λ	cowl turning angle	deg
ρ	density	slug/ft^3
τ	shearing stress	lb/ft^2
$\bar{\chi}$	viscous-interaction parameter	

Subscripts

1, 2	stations specified in figure 10
corr	corrected for flowfield-property effects
e	boundary-layer edge
i	defines the location of a member of an array of data
o	station at which laminar boundary-layer calculations are initiated
p	pitot

Subscripts

s	pertaining to a geometric surface
t	stagnation condition, station at which transition from laminar to turbulent boundary-layer flow is complete
w	wall
∞	tunnel freestream

Superscript

$'$	coordinate measured relative to a geometric surface

AERODYNAMIC DESIGN OF INTERNAL PASSAGES

In the design of the internal passages, it was desirable to simulate a typical vehicle configuration while simultaneously satisfying the requirements for testing in the NASA-Ames 3.5-Foot Hypersonic Wind Tunnel. Figure 1 shows a Mach 10 to 12 high-wing hypersonic cruise vehicle and the relationship of the inlet to the fuselage and the aerodynamic surfaces of the vehicle. The vehicle design is discussed in detail in reference 1. The internal passages are located in retractable propulsion modules at the aft end of the vehicle forebody. For a cruise aircraft with Mach 10 to 12 capability, a limitation imposed by vehicle requirements is that the cowl length is less than 20% of the forebody length. This relative size is as shown in figure 1. Because of the large vehicle diameter, the modules have nearly rectangular cross sections and the flow approaching the inlet openings is approximately two-dimensional. A typical module can then be represented by a two-dimensional internal passage with a two-dimensional wedge forebody that provides the proper flow conditions at the inlet-entrance station, and the flowfields within the internal passages can be treated by methods of analysis for two-dimensional flows.

Several additional design factors discussed in reference 1 are pertinent to the present investigation. Consideration of the combined effects of cone shock-wave strength, internal volumetric efficiency, and surface temperature requires that the cruise vehicle fuselage have an initial half-angle of seven degrees. The conical forebody is followed by an isentropic compression surface with a final angle of 19 degrees (12 degrees of isentropic compression). The inlet-entrance Mach number depends upon the flight Mach number, the vehicle angle of attack, and the circumferential location of the engine module. A representative inlet-entrance Mach number of six was selected for the present study. This condition can be simulated in the Mach 7.4 nozzle of the NASA-Ames 3.5-Foot Hypersonic Wind Tunnel with a seven-degree wedge forebody. The aerodynamic heating conditions encountered by a full-scale cruise vehicle dictate the use of some degree of bluntness for the cowl leading edge. This requirement must be observed in any representative inlet-model design. The cowl length imposes a limitation on the rate of compression of the internal flow because of the necessity of maintaining attached boundary layers on the compression surfaces. Finally, the compression surfaces at the throat station are nearly parallel to the vehicle axis.

A wide range of inlet compression ratio is desired when different applications are considered. The definition of compression ratio used in this report is the ratio of the static pressure at the inlet throat to the static pressure at the inlet entrance (throat pressure/entrance pressure). Internal-passage compression ratios of two, eight, and twelve were selected for the present study. With a representative forebody compression ratio (entrance pressure/freestream pressure) of 30 for the range of flight conditions and engine locations considered, the inlet pressure-ratio range of 2-12 yields overall compression ratios (throat pressure/freestream pressure) of 60 to 360.

The aforementioned design considerations and the characteristics of the NASA-Ames 3.5-Foot Hypersonic Wind Tunnel were the primary factors in the selection of the wind-tunnel model size and the test conditions. Preliminary studies indicated that an overall length of approximately 50 inches would maximize the internal passage height while ensuring wind-tunnel starting. Simulation of the vehicle-forebody flowfield required that a turbulent boundary layer be established on the wedge forebody at the entrance to the internal passage. Natural transition to a turbulent boundary layer on a seven-degree wedge at a freestream Mach number M_∞ of 7.4 occurs in a relatively short length (ref. 2) with a stagnation pressure P_{t_∞} of 600 psia and a stagnation temperature T_{t_∞} of 1460 degree R (Reynolds number equal to 2.7×10^6 per foot). The internal passages were designed for this test condition. Finally, the wedge-forebody length (to the inlet-entrance station) and the height of the cowl lip above the forebody surface were fixed at 32.0 and 3.5 inches, respectively, giving an internal passage size of approximately one-third of full scale.

Upon comparison of the surface angle of the vehicle forebody at the inlet-entrance station (19 degrees relative to the vehicle axis) and the corresponding flow direction at the inlet-entrance station of the wind-tunnel model (7 degrees relative to the tunnel axis), it is observed that the wind-tunnel model is rotated through an angle of 12 degrees relative to the vehicle axis. All surface angles and flow-directions for the wind-tunnel model, particularly the internal cowl-surface angle and the flow direction at the throat station, may be visualized in the vehicle reference frame by adding an increment of 12 degrees to the surface angle or flow direction of interest.

Wedge Forebody

The requirement for a seven-degree wedge forebody was established, as indicated above, by vehicle and wind-tunnel considerations. When translating this requirement

into hardware, the seven degrees becomes the effective wedge angle to the freestream flow. The effective surface slope at any point is then the sum of the geometric surface slope of the model itself and the incremental slope induced by the boundary-layer displacement thickness. As discussed in reference 3, the geometric contour of the wedge forebody was obtained by subtracting the computed displacement thickness from the coordinates of the seven-degree effective wedge. The displacement thickness was calculated using the method of reference 4 and the assumption that a turbulent boundary layer exists over the entire wedge forebody at the nominal test conditions ($M_\infty = 7.4$, $P_{t_\infty} = 600$ psia, and $T_{t_\infty} = 1460°R$). The effective and geometric coordinates from the leading edge (inlet station X = 0) to the inlet entrance (inlet station X = 32.0 in.) are given in figure 2 and also in table 1. The surface slopes are given in table 1.

Cowl Leading Edge

The minimum practical leading-edge diameter for a Mach 12 cruise vehicle using regenerative cooling is approximately 0.125 in. (ref. 5). Since the model was approximately one-third scale, a leading-edge diameter of 0.045 in. was selected for the present investigation. Early in the study (ref. 3) it became evident that comparisons of the experimentally measured performance of the three inlets (compression ratios of two, eight, and twelve) would be most meaningful if all inlets were designed for the same theoretical total-pressure recovery. This design requirement was satisfied by employing the same contour in the immediate region of the cowl leading edge and maintaining the same point of impingement of the cowl shock wave on the forebody surface for all internal passages. Within these limitations, a cowl leading-edge design resulting in a high level of the average total-pressure recovery downstream of the shock wave was established. As shown in reference 3, for a fixed degree of bluntness the only variable in the region of the cowl leading edge is the internal surface angle λ. Variations in this angle change the total pressure recovery and the surface static-pressure distribution downstream of the shoulder of the blunt leading edge. The results of a cowl-lip efficiency study are shown in figures 3 and 4. A value of λ relative to the model axis of +1.0 degree (13 degrees relative to the vehicle axis) was selected on the basis of near-maximum total-pressure recovery with a relatively high cowl-surface static pressure. The latter result is important since a high initial surface pressure reduces the gradients that must be imposed downstream in order to reach the desired throat pressure, thus reducing the tendency toward boundary-layer separation on the cowl surface.

Inviscid Internal Flow

For the mixed-compression inlet considered in the present study, the shock wave originating at the leading edge of the wedge forebody passes outside of the cowl leading edge. The shock wave generated at the blunt-cowl leading edge immediately enters the internal passage and must be reduced in strength if the goal of maximum total-pressure recovery at the inlet throat is to be realized. Figure 3 shows that the shock-wave strength is nearly constant downstream of station X = 34.0 in. for a constant (effective*) value of λ equal to +1.0 degree. The resulting shock wave intersects the effective wedge-forebody contour (seven-degree wedge) at station X = 44.25 in. (fig. 5). The effective cowl contour is straight (λ = +1.0 degree) to station X = 34.25 in. for all inlets. A Mach wave from this station passes through station X = 44.25 in. on the centerbody; therefore, any cowl-surface turning downstream of station X = 34.25 in. does not influence the cowl shock wave. Figure 5 delineates the wave pattern. The region upstream of the Mach wave crossing the inlet from cowl station X = 34.25 in. to centerbody station X = 44.25 in. was the same for all internal passages.

An additional factor that has an important influence on the integration of the inlet with the remainder of the propulsion system is the degree of uniformity of the flow at the inlet throat. Any attempt at designing for uniform throat flow is compromised by the presence of shock waves within the flowfield. The goal of maximum pressure recovery and the desirable characteristic of uniform throat flow are satisfied simultaneously if the cowl shock wave is cancelled at its first point of impingement upon the wedge forebody. The remaining flow to the throat is then shock-free and the contours may be designed to give constant static pressure at the throat station. The contours of the internal passages were designed to effect cancellation of the cowl shock wave at the centerbody surface and to provide nearly uniform static-pressure distributions at the throat stations.

After defining the flow along the cowl shock wave to the cancellation station, as discussed above, additional contour sections were designed for isentropic compression to pressure ratios of eight and twelve for the high-compression

* As for the wedge forebody, the term "effective" refers to the surface formed by adding the displacement thickness of the boundary layer to the "geometric" surface.

inlets, and for a slight expansion to a compression ratio of two for the low-compression design. Any cowl turning was introduced downstream of station X = 34.25 in., which was the origin of the Mach wave from the cowl surface to the intersection of the cowl shock wave and the effective centerbody surface.

With the definition of the aforementioned characteristics of the inlets, the aerodynamic design of the contours of the internal passages was initiated. The contours were defined regionally, as shown in figure 5, and as follows:

(1) The effective centerbody contour in region I is a seven-degree wedge. The seven-degree wedge flowfield in region I and the cowl contour in region II upstream of station X = 34.25 in. determine the cowl shock-wave location.

(2) The flowfield in region II, bounded by the cowl shock wave and a Mach wave originating at the shock-wave impingement location, station X = 44.25 in., is determined by the flow properties downstream of the shock wave and the effective cowl contour in region II.

(3) The flowfield in region III is determined by the flow properties at the boundary between regions II and III and the effective centerbody contour in region III.

(4) The flowfield in region IV is determined by the flow properties at the boundary of regions III and IV and the effective cowl contour in region IV.

The inlets that were designed by the above procedure were designated P2, P8, and P12, respectively, for the compression ratios of two, eight, and twelve. The highest compression-ratio inlet, P12, presented the greatest design challenge and the procedure followed for this inlet is discussed in detail in the following paragraphs. The P8 inlet was essentially a derivative of the P12 design. A different procedure was utilized to design the P2 inlet since the internal passage is an expansion field. After a discussion of the P12 inlet contour design, the approaches applicable to the P8 and P2 inlets are briefly reviewed.

Region II Cowl Contour and Wave-Cancellation Surface, P12 Inlet. - The effective cowl surface upstream of station 34.25 in. was selected as a result of a cowl lip

efficiency study (ref. 3). The effective centerbody contour upstream of the shock-wave impingement point, station X = 44.25 in., is simply a seven-degree wedge. Since the flow behind the Mach wave connecting the aforementioned points is known, the specification of the cowl surface contour in region II permits a complete solution of the flow in this region by the method of characteristics (ref. 6). Preliminary studies reported in reference 3 defined the approximate length of the region of cowl-surface turning (to station X = 48.0 in.) and the approximate turning angle (15 degrees, resulting in an exit flow angle toward the vehicle axis of 2 degrees), that could be attained without separating a laminar boundary layer. The criterion of maintaining an attached laminar boundary layer on the cowl was adopted because sufficient correlations for transition length were not available and a conservative approach was appropriate. A design that would not exceed incipient-separation limits for a laminar boundary layer certainly would not cause turbulent boundary-layer separation in the event of early transition.

At this point, continued definition of the flowfield in region II required specification of the cowl shock-wave cancellation surface. The computer program of reference 6, which defines regions by shock-wave boundaries, was used without modification by allowing a reflected wave of vanishing strength to exist downstream of the impingement station. In order to completely cancel the cowl shock wave it would be necessary to turn the centerbody parallel to the flow direction behind the shock wave at the impingement station. This requirement was approximated by permitting an infinitesimally-weak reflected shock wave (Mach wave) to exist, thus allowing the flowfield solution of reference 6 to proceed in the normal fashion.

After satisfying the computer-program requirement of an infinitesimally-weak reflected shock wave for the downstream boundary of region II, the final cowl contour in this region was defined. The major problem was the prevention of secondary shock-wave formation by compression-wave coalescence in the vicinity of the shock-wave impingement station. The iterative procedure used to define the final effective cowl contour in region II is discussed in reference 3.

Region III Centerbody Contour, P12 Inlet. - The results of the flowfield calculations for region II and the effective centerbody contour in region III are required to define the entire flowfield in the latter region. In order to maintain an infinitesimally-weak reflected wave (Mach wave) and also produce a relatively uniform flowfield at the throat station, the concept of Mach wave cancellation was employed in

the development of the centerbody contour in region III. Since each incoming Mach wave was a compression wave, this concept was implemented by turning the surface in the direction of the flow downstream of the impinging wave, thereby cancelling the wave. The stepwise procedure used for this region is presented in reference 3. The centerbody-surface static pressure reached the design level ($P/P_\infty = 37.5$, where $P/P_\infty = 3.135$ at the inlet-entrance station) at approximately station X = 49.60 in., and the upstream wave defining the boundary of region III intersected the cowl surface at approximately station X = 48.0 in.

Region IV Cowl Contour, P12 Inlet. - The concept of Mach wave cancellation was also applied in the design of the cowl contour immediately downstream of station X = 48.0 in. The turning of the cowl surface was terminated at station X = 48.18 in.

Design Pressure Distributions, P12 Inlet. - The predicted surface static-pressure distributions are shown in figures 6 and 7 for the centerbody and cowl, respectively, of the P12 inlet. As shown on figure 6, the cowl shock wave impinges upon the centerbody surface at approximately station X = 44.25 in. After the shock wave is cancelled, the centerbody static pressure increases monotonically to the design compression ratio of 37.5 at station X = 49.6 in. The discontinuous N-shaped distribution at station X = 50.0 in. is a result of the impingement and cancellation of the weak compression wave used to define the boundaries between regions I, II, and III. Although this weak wave affects the surface static-pressure distribution, its presence is not significant since the surface pressure downstream returns to the design level. The surface static-pressure distribution on the P12 inlet cowl (fig. 7) also exhibits the effects of this weak wave at station X = 48.0 in. The surface pressure returns to nearly the design value immediately downstream, although a reduction in pressure of about ten percent occurs downstream of station X = 50.0 in.

Design Procedure for P8 Inlet. - Observation of the surface static-pressure distributions (figs. 6 and 7) shows that the design pressure ratio for the P8 inlet ($P/P_\infty = 25.0$) is reached at station X = 48.5 in. on the P12 inlet centerbody and at station X = 45.3 in. on the P12 inlet cowl. The contours for the P8 inlet were derived from the P12 inlet contours by using the existing contours up to the aforementioned stations and eliminating any further turning of the surfaces. The resulting surface static-pressure distributions are shown on figures 6 and 7; the distributions

for the P8 inlet are identical to those for the P12 inlet to $P/P_\infty = 25.0$ and that ratio is maintained to the P8 inlet throat.

Design Procedure for P2 Inlet. - The design pressure ratio for the P2 inlet ($P/P_\infty = 6.25$) is lower than the minimum surface static-pressure ratio achieved by the P8 and P12 inlets (fig. 7); therefore, the internal passage for the P2 inlet must provide an expanding flowfield. The contours of the P2 inlet were obtained by using the previously designed contour in region I, cancelling the shock wave at the centerbody (station X = 44.25 in.), and then expanding the flow slightly to the throat station X = 47.0 in. The resulting pressure distributions are shown in figures 6 and 7.

Summary of Effective Inlet Contours. - The preceding discussion was concerned with the development of the effective inlet contours, that is, the inviscid contours before the application of boundary-layer corrections. When used as input data for the inviscid flow computer program (ref. 6), these contours define the pressure distributions shown in figures 6 and 7. The mode of operation of the computer program was unconventional in the sense that the axial coordinates and surface angles (X and ϵ) were input instead of the axial and normal coordinates (X and Y). The former technique was used to simplify the procedure of obtaining smooth surfaces by integrating to obtain the normal coordinates rather than differentiating to obtain the surface angles. The values of X and ϵ used to obtain the pressure distributions of figures 6 and 7 are given in table 2 for the three inlet designs, together with the normal coordinates computed from the equation

$$Y_i = Y_{i-1} + \tfrac{1}{2}\left[\left(\frac{dY}{dX}\right)_i + \left(\frac{dY}{dX}\right)_{i-1}\right]\left[X_i - X_{i-1}\right] \qquad (1)$$

Boundary Layer

The pressure distributions discussed in the previous section and the corresponding velocity distributions were used as edge conditions to compute the boundary-layer development for the test conditions $P_{t_\infty} = 600$ psia, $T_{t_\infty} = 1460°R$, and $T_w = 545°R$.

Centerbody Turbulent Boundary Layer. - The calculations for the centerbody were obtained using the modified Reshotko-Tucker procedure (ref. 4) and represent extensions of the wedge-forebody solutions. The boundary-layer thickness distributions for the three inlets, shown in figure 8, are identical upstream of the shock-

wave impingement location, station X = 44.25 in. Large reductions in the thickness parameters occur across the shock-wave cancellation region, which was represented by a rapid but continuous pressure increase. The distribution downstream of station X = 40.0 in. are shown in an expanded scale in figure 8b. Both δ and δ^* decrease with distance downstream of the shock-wave impingement location for the P8 and P12 inlets. The boundary-layer thicknesses at the throat decrease with increasing compression ratio.

Cowl Laminar Boundary Layer. - The method of Clutter and Smith (ref. 7) was used to compute the boundary-layer development on each cowl surface, under the assumption that the boundary layer remains laminar over the entire cowl length. The results of the calculations, which resulted in positive values of wall shear (no separation) for all inlets, are shown in figure 9 in terms of the boundary-layer thickness and displacement thickness. The distributions show a successive decrease in boundary-layer thickness with increasing compression ratio, and, for the P8 and P12 inlet cowls, the thickness parameters decrease within the regions of high adverse pressure gradient.

Geometric Internal Contours

The general procedure described below for obtaining the geometric inlet contours involved the correction of an effective inviscid contour by subtracting the boundary-layer displacement thicknesses predicted by the methods of references 4 and 7. A special procedure was developed for the shock-wave cancellation region to account for the boundary-layer development across a shock-induced pressure rise.

Wedge Forebody Contour. - As discussed previously, the geometric contour for the wedge forebody was obtained by subtracting the displacement thickness from the coordinates of a seven-degree wedge. The effective and geometric coordinates of the wedge forebody are given in figure 2 and also in table 1.

Centerbody Contours. - The centerbody contours from the inlet-entrance station (X = 32.0 in.) to approximately station X = 43.4 in. are extensions of the wedge-forebody contour and are identical for the three inlets. The geometric contours in this region were obtained by subtracting the displacement thickness from the seven-degree effective-wedge contour.

The centerbody contours downstream of station X = 43.4 in. were determined by a procedure developed during the present investigation to design contours through shock-wave cancellation regions. Simple subtraction of the computed displacement thickness (fig. 8) from the effective contours yields geometric contours with forward-facing steps at the shock-wave impingement stations (X = 44.25 in.). Since a contour of this nature was unacceptable a new approach to the step-by-step development of the contours in the interaction regions was required. This approach is presented in detail in reference 3, and outlined in the following paragraphs.

The discontinuous contour obtained by subtracting the displacement thickness δ^* from the effective contour is shown in figure 10a. This discontinuous contour is designated the basic contour line (BCL). Also shown in figure 10a are the region upstream of the incident shock wave (region A), the region immediately downstream of this shock wave (region B), and the boundary-layer edge δ. The station at which the incident shock wave intersects the boundary-layer edge, X = 43.397 in., is denoted by station 1, and is the same for the three inlets (the position of the boundary-layer edge is determined by adding the quantity $\delta - \delta^*$ to the effective contour). The inviscid flow properties in regions A and B, calculated using the method of characteristics (ref. 6), are the same for the P2, P8, and P12 inlets. The flowfield and boundary-layer properties at station 1 for all inlets are

Mach number	$M_1 = 6.03$
Flow direction	$\epsilon_1 = 7.00°$
Boundary-layer thickness	$\delta_1 = 0.502$ in.
Displacement thickness	$\delta_1^* = 0.283$ in.

The inviscid-flow calculation also yields the conditions at station 2 (where the axial location of station 2 is to be determined):

Mach number	$M_2 = 5.22$
Flow direction	$\epsilon_2 = 1.34°$

The pressure ratio P_2/P_1 across the impinging shock wave is 2.284. Application of the control-volume approach of Kutschenreuter, et al, (ref. 8) across the region of interaction for the above conditions gives the following ratios of boundary-layer properties:

$$\delta_2/\delta_1 = 0.575, \quad \delta_2 = 0.289 \text{ in.}$$

$$\delta_2^*/\delta_1^* = 0.575, \quad \delta_2^* = 0.163 \text{ in.}$$

The interaction-region length was estimated to be equal to that given by the correlations of Pinckney (ref. 9) for the flow conditions of interest:

$$\text{Interaction-region length } L_i \approx 2\delta_1 \approx 1.0 \text{ in.}$$

The properties given above were used to establish the geometric inlet contours in the regions of interaction. Since the inviscid flowfields in region III (fig. 5) are different for the three inlet designs, the geometric inlet contours throughout the interaction regions are no longer identical, even though the same effective contours upstream of station X = 44.25 in. and the same boundary-layer properties at station 2 are used for all inlets. For each inlet, a line is constructed parallel to the direction of the inviscid streamline downstream of the incident shock wave (at angle $\epsilon_2 = 1.34°$). This line originates at the axial station where the incident shock wave intersects the effective contour. Station 2 is now defined as the axial station at which the distance between the line constructed at $\epsilon_2 = 1.34°$ and the effective contour equals 0.163 in., which is the value of δ_2^* computed above (see fig. 10b). The interaction length is incorporated into the design by extending the line at angle $\epsilon_2 = 1.34°$ upstream an amount equal to L_i (1.0 in.), defining station 3 as shown in figure 10b. The final geometric contour for each inlet is obtained by fitting a smooth curve between stations 1 and 3, retaining the straight segment between stations 3 and 2, and fairing a curve from station 2 tangent to the basic contour line in the minimum distance (fig. 10c). The above procedure applies directly for the P8 and P12 inlets, but was modified for application to the P2 inlet contour since station 2 (fig. 10b) was downstream of the throat. For the latter case, the axial location of station 3 was set equal to that obtained for the P12 inlet contour, and the straight segment (at angle $\epsilon_2 = 1.34°$) was extended to the throat.

The geometric centerbody coordinates defined by the procedures presented above are given in table 3 for the P2, P8, and P12 inlets. The effective and geometric centerbody contours are compared in figure 11 for the three inlets.

Cowl Contours. - The geometric contours of the cowl surfaces were obtained by subtracting the displacement thicknesses given in figure 9 from the respective effective contours. The final geometric contours are given in table 3 and compared to the effective contours in figure 11.

TEST APPARATUS AND MODELS

Wind Tunnel Facility

The experimental programs of the present investigation were conducted in the NASA-Ames 3.5-Foot Hypersonic Wind Tunnel. The facility, shown schematically in figure 12, is a blow-down tunnel with a run time of from one to four minutes at the nominal test conditions used in the investigation. Those conditions were

Mach number	M_∞	= 7.4
Total pressure	P_{t_∞}	= 600 psia
Total temperature	T_{t_∞}	= 1460°R
Reynolds number	Re_∞	= $2.7 \times 10^6 ft^{-1}$

for most tests. Several tests were conducted at lower total pressures to investigate the effects of Reynolds number on the internal flow development within the inlet models. Total pressures as low as 200 psia were used in this study. Total pressures from 75 to 1350 psia were used during a series of instrument calibration tests to simulate inlet internal conditions. Acquisition of test data was accomplished through a 108-channel Beckman analog-to-digital system. The data were recorded on magnetic tape and processed by an IBM 7094 digital computer.

Test Models

Two different sets of models were utilized during the wind-tunnel investigations. Flat-plate models with sharp leading edges were used to generate a series of flow conditions approximating the predicted internal-passage conditions in order to test and calibrate surface and flowfield survey instrumentation. These calibration models were mounted on a model-injection mechanism and were, therefore, suitable for heat-transfer as well as pressure measurements. Three internal-passage models were constructed as interchangeable installations for the inlet model tests. The same wedge forebody was used to generate the inlet-entrance flow for all internal passage models. The entire wedge-forebody and inlet assembly was attached to the model support strut by a rigid undercarriage and sting support.

Calibration-Plate Models. - A photograph of a typical calibration plate installed on the injection mechanism of the 3.5-Foot Hypersonic Wind Tunnel is shown in

figure 13. This plate was 46.55 in. long and 17.25 in. wide and was equipped with a water-cooled sharp leading edge. The plate was instrumented with surface static-pressure orifices and surface thermocouples in addition to the instrumentation actually undergoing calibration. The plate was constructed of solid stainless steel to provide nearly constant wall temperatures during calibration runs and also to prevent bending due to uneven temperature distributions through the model. The angle of the plate relative to the freestream flow was varied from approximately two to fifteen degrees, providing a test Mach number range from 4.5 to 7.0. This plate was employed in the calibration of thermocouple probes and a flow-direction-sensitive static pressure probe, and was also used to test the structural integrity of a series of flow-field rakes.

A second flat plate, 24.0 in. long and 12.0 in. wide, was used to obtain calibrations of thermocouple probes, to test the structural integrity of thermocouple wires, to determine the response time of heat-transfer gages and the applicability of the transient technique for heat-transfer measurements, and to determine the response times of static pressure orifices. Because of its small size, this plate could be tested at angles of attack as high as 20 degrees and at tunnel total pressures from approximately 75 to 1350 psia. This range of test conditions permitted simulation of the entire range of flow conditions predicted for the P2, P8, and P12 inlets. A discussion of the calibration instrumentation and results is presented following the description of the inlet models.

Inlet Models. - The important design features of the inlet models are (fig. 14):

(1) Wedge forebody, undercarriage, and sting support common to all internal passages.

(2) Interchangeable internal passages.

(3) Remotely controlled rotation scheme for internal passages.

(4) Glass inserts in sidewalls to permit schlieren observation of internal passage flowfields.

The basic wedge-forebody model, shown in figure 15, was a sharp leading-edge wedge 36.4 in. long and 18.0 in. wide that was installed in the wind tunnel at a nominal leading-edge inclination of 6.5 degrees. This angle of attack was compatible

with the boundary-layer corrections given above for an effective wedge angle of seven degrees. The wedge surface was constructed of solid aluminum of approximately one-inch thickness and was fitted with a water-cooled sharp leading edge constructed of stainless steel. The mass of the aluminum plate and the cooling provided at the leading edge, when coupled with relatively short test runs, resulted in nearly isothermal wall conditions during operation.

Each internal passage was comprised of a centerbody block, a cowl block, and two sidewalls. The centerbody and cowl blocks and sidewalls were constructed of aluminum and the sidewalls were equipped with sharp stainless-steel leading edges. The cowl leading edges and the forward portion of the cowl blocks were water cooled; the combination of water cooling and the large masses of aluminum provided nearly isothermal wall conditions during the relatively short tunnel runs. The dimensions that were common to the internal passages for the P2, P8, and P12 inlets were the inlet-entrance height above the wedge surface (3.5 in.), the width of the internal passage (14.0 in.), and the diameter of the cowl leading edge (0.045 in.). These dimensions are indicated on figure 14, together with the nominal axial location of the inlet throat and the throat height for each internal passage.

The remote-control rotation scheme for the internal passages served several important functions. First, the contraction ratio of the inlet could be varied by rotating the inlet, thus ensuring starting of the internal passage. Second, rotation of the entire internal passage (centerbody, cowl, and both sidewalls) permitted construction of a well-sealed internal passage with a mechanically fixed alignment of the centerbody and cowl surfaces. Third, the rotation scheme allowed the inlet cowl to close upon the wedge so that the airflow was almost entirely diverted from the internal passage before and during the wind-tunnel starting process. Shielding of the internal passage from the tunnel flow was desirable in maintaining uniform and low surface temperature within the internal passage and preventing instrumentation damage during the tunnel starting process. Finally, when the P8 and P12 internal passages were in the closed position, model blockage to the wind tunnel was minimized during the critical phase of tunnel starting. After stabilization of the tunnel flow, these internal passages were opened for data acquisition. For some tests, the P2 inlet model proved to present excessive wind-tunnel blockage when closed, thus prohibiting starting of the tunnel. In these instances, the tunnel was started with the internal

passage in the open position. After data acquisition, the internal passages were rotated to the closed position prior to tunnel shutdown to prevent instrumentation damage.

Representative photographs of the inlet models mounted in the wind tunnel are given in figures 16 and 17. The extended structures attached to the upper surfaces of the models are protective shields for flow-survey instrumentation. The glass inserts in the inlet model sidewalls used for flow visualization are also shown in the photographs.

Instrumentation and Data Analysis

Tunnel Parameters. - The freestream total pressure was sensed by a probe located within the settling chamber and measured by one of a series of transducers that comprised part of the permanent tunnel installation. The maximum error in the tunnel total pressure was estimated to be about 0.3% of the measured pressure. The total temperature was measured with a triply shielded thermocouple probe (Rosemount Engineering Model 103H) located within the region of undisturbed flow under the leading edge of the model. Temperatures were also measured in the heater section of the wind tunnel. The shielded probe attached to the model was considered to be a more accurate sensor of the total temperature within the test section, and the freestream total temperature for each data point was taken as the temperature measured by the shielded probe at the same time during the run. The estimated maximum error in the freestream total-temperature measurement was about 0.7% of the absolute temperature. The freestream pitot pressure was measured by a pitot tube located at the leading-edge station adjacent to the freestream total-temperature probe. The Mach number was computed from the ratio of freestream pitot pressure to freestream total pressure, and also from the wind tunnel calibrations using the freestream total pressure and the heater temperature. The test section Mach number computed using the former procedure varied between 7.35 and 7.45, whereas the tunnel calibrations yielded a value of 7.40 ± 0.01 at the wedge-forebody tip location (station $X = 0$).

An attempt was made to maintain the nominal test conditions during each run and also between runs that used the same conditions. Test condition variations during individual runs were within acceptable tolerances for the majority of tests; however, relatively large variations in the average total temperature occurred within

some groups of runs where constant conditions were highly desirable. The significance of the variations in test section conditions will be discussed upon presentation of the experimental results.

Surface Pressure and Temperature. - Surface pressures on the calibration plates and on the wedge forebody and within the internal passages of the inlet models were sensed by 0.0625-in. diameter orifices. The locations of the orifices for the inlet models, which were drilled normal to the surfaces (fig. 18a), are given in table 4. The orifices were connected to Statham absolute strain-gage pressure transducers with appropriate ranges by lengths of stainless steel and plastic tubing. The transducers were calibrated periodically, and the maximum error for the static pressures was estimated to be about 3% of the measured pressure. The maximum response time for a static-pressure measurement was determined during the calibration tests to be about five seconds.

Surface temperatures were measured using thermocouple junctions imbedded in the plate surfaces as shown in figure 18b. Thirty-gage chromel-alumel thermocouple wire was used; a junction was formed by passing the wires through a 0.040 in. diameter hole in the surface and forcing a conical pin, constructed of the plate material and flattened on one side, into the hole until electrical continuity between the thermocouple wires was established. The excess pin material was then removed, the surface polished, and the wires cemented to the under-surface of the plate. The locations of the surface thermocouples are given in table 4. The estimated maximum error of the surface thermocouples was about 5% of the measured temperature.

Surface Heat-Transfer Rate. - Heat-transfer gages of the design shown in figure 18c were installed on the calibration plates and within the internal passages of the inlet models (table 4). The gage design utilized an electrolytic-free copper disc as a calorimetric mass and a thermocouple as a temperature sensor. The disc, with a diameter of 0.125 in., was inserted in a 0.375-in. diameter ceramic insulator. Chromel-alumel thermocouple wires were resistance welded to the copper disc and the entire assembly was press-fitted into the model surface. Additional ceramic-paste insulation was added on the underside of the surface to ensure bonding of the gage to the model.

The heat transfer gages of the aforementioned design performed well during the calibration tests, however, no useful results were obtained for the inlet models. The problems appeared to lie with the procedure used to adapt the transient heat-transfer technique to a model that was present in the wind tunnel during the starting process. It was observed that the internal passages were not completely sealed from the airflow when in the closed position, thus modifying the temperature histories of the heat transfer gages. To obtain heat transfer data within the P2 and P8 inlet models, commercially available constant-condition heat transfer gages were installed at one cowl station in each internal passage. The gages used were Hy-Cal models C-1170-A-05-060 (range 0-5 BTU/ft^2-sec) and C-1301-A-15-072 (range 0-15 BTU/ft^2-sec). Calibration curves supplied by the manufacturer were used to obtain heat-transfer rates from the output voltages.

Surface Shearing Stress. - Wall shearing stress measurements were made at the inlet-entrance station on the wedge forebody (X = 32.0 in.) using both a Stanton tube and a commercial skin-friction gage, Kistler model 322M102. The Stanton tube was comprised of a segment of razor blade cemented to the surface with its leading edge directly above the upstream edge of a circular pressure orifice (fig. 18d). The correlation of reference 10 was used to compute the wall shear from the measured pressure. The skin friction gage was also used at one cowl station each in the P2 and P8 inlet models. The gage was calibrated before and after each series of runs, and the resulting calibrations were used in the data-reduction procedure to obtain wall shearing stress.

Flowfield Surveys. - Surveys of pitot pressure, static pressure, and total temperature were made across the inlet-entrance station, along the internal passages near the centerlines for the P2 and P8 inlet models, and across the throat stations for all internal passages. Individual probes and rakes comprised of several probes were used as required. The probe types included round and flattened pitot tubes, singly shielded and unshielded total-temperature probes, and direct-reading and conical static-pressure probes. Each type was tested and calibrated, when necessary, during the instrument calibration tests utilizing the flat plate models.

Pitot pressure probes: Pitot pressure measurements were obtained using 0.040-in. diameter stainless steel tubes with either round tips (for inviscid-flow measurements) or tips flattened to 0.020-in. height (for boundary-layer surveys).

Calibration tests showed that the time lag for pitot pressures was essentially zero and that the readings were unaffected by flow inclination through a range of angles of attack of at least 12 degrees. Readings were obtained using Statham absolute strain-gage pressure gages and the maximum error was about 2% of the measured pressure.

Singly shielded total-temperature probes: The design for a total temperature probe with a single shield and two vent holes is shown in figure 19. This particular design combined the total temperature probe with a pitot pressure probe. The sensing element was comprised of a chromel-alumel thermocouple with magnesium-oxide insulation. The shield was formed of gold-plated stainless steel tubing. Calibration data for the singly shielded probe are presented in figure 20 in terms of the probe recovery-factor variation with the parameter $P_p/(T_t)^{7/4}$. The latter parameter was derived by Winkler (ref. 11) and relates the local heat-transfer coefficient at the probe tip and the thermal resistance of the wire. As shown in figure 20, this type of probe required rather large corrections for a portion of the range of the parameter $P_p/(T_t)^{7/4}$ obtained during the inlet model tests. This undesirable characteristic, together with the requirement for an individual calibration of each probe, provided the impetus for the development of a more versatile total-temperature probe.

Exposed-thermocouple total-temperature probe: The basic requirements for a total temperature probe are: simple construction, minimum calibration, simple repair, fast response, and reproducibility of measurements. An early design of an exposed thermocouple probe used in the present investigation is shown in figure 21. Support for the exposed thermocouple element was provided by the forked arrangement of two 0.040-in. diameter stainless-steel tubes, supported in turn by larger tubes that were brazed to a vertical wedge-shaped strut. The chromel-alumel thermocouple junction was formed by passing one wire through each tube, removing the insulation from the ends of the wires, inserting a ceramic insulator over each wire, and finally spot-welding the junction at the mid-point between the tips of the support tubes. Thermocouple wires with diameters from 0.003 to 0.010 in. were used on a series of test probes. The results of calibration tests showed that the exposed thermocouple probes responded rapidly to temperature changes, had sufficient strength to withstand the high pressures within the internal passages (with the exception of the 0.003 in. diameter wires), and could be assembled and repaired with relative ease. As shown in figure 22, the recovery factors obtained outside of the

plate boundary layer for a series of probes were essentially constant over a range of the variable $P_p/(T_t)^{7/4}$. These characteristics indicated that this type of probe would be acceptable for inlet testing. When the probes shown in figure 21 were used to survey boundary layers, however, considerable flow interference occurred and the flow in the region of the thermal element was disturbed by the wire supports. For this reason, further development of the basic probe design was undertaken.

The flow disturbances observed with the early design for the exposed thermocouple probe were attributed to the flow blockage between the probe and the surface when the probe was well submerged in a boundary layer. To prevent these disturbances the forked support design shown in figure 21 was replaced by a plate support with sharp leading edges (fig. 23). Extensive testing of the probes of the revised design revealed no flow disturbances when wedge support struts were used, and the measured recovery factors were within the range 0.95 ±0.01. When the wedge-shaped vertical strut was replaced by a round shaft (fig. 24), flow disturbances were again introduced and a round-shaft probe was therefore considered unsatisfactory. The design for the exposed thermocouple probe shown in figure 23 was adapted for inlet model testing by adding a pitot tube and, in some cases, by combining two sets of thermocouple and pitot probes into a four-element probe (fig. 24) with variable inter-probe spacing.

Static pressure probes: Two types of static pressure probes were used for flowfield surveys. A small-diameter (0.020 in.), direct-reading probe with measuring orifices located on the probe shaft is shown in figure 25a. This probe senses the stream pressure directly and requires a single pressure transducer for the output reading since all orifices are interconnected. Calibration tests revealed a maximum stabilization time of approximately 10 seconds. The second static-pressure probe design, figure 25b, was comprised of a 0.0937 in. diameter shaft with a 30°-conical tip (included angle). Two pressures are sensed with this probe, allowing measurements of stream angle as well as static pressure when the appropriate calibrations are employed. The techniques presented in reference 12 were used during probe calibration tests and for reduction of measured data during inlet model tests. The response time of this probe was about five seconds.

Inlet-entrance flowfield surveys: Flowfield data were obtained at nine lateral stations at the inlet-entrance station, X = 32.0 in. The lateral coordinates of the

survey stations are shown in figure 26. To acquire data at these stations, the model was installed in the wind tunnel with no internal passage, as shown in figure 15. The rakes of pitot pressure probes, total temperature probes, and static pressure probes shown in figure 27 were installed using sliding supports that were manually set and locked into position between runs. Singly shielded total temperature probes were used in this part of the experimental investigation since interference-free exposed-thermocouple probes were not developed until after the inlet-entrance flowfield tests. The small diameter, direct-reading probes were employed for static pressure measurements. Data for the inlet-entrance flowfield surveys were recorded once each second for a total of twenty data points.

All measurements were initially adjusted to the nominal test conditions by multiplying the measurement by the ratio of the nominal test condition (total pressure or total temperature) to the actual test condition at the time of the measurement. Pitot pressure measurements are presented in this report in the form of ratios of adjusted pitot pressure to the nominal tunnel total pressure. A nominal test-section static pressure was computed for the nominal test conditions using the ideal-gas equations and real-gas corrections of reference 13. The static pressure measurements presented herein are given in the form of ratios of measured static pressure to nominal (real gas) tunnel static pressure. Mach numbers were calculated using the ideal-gas equations of reference 13 from the ratio of pitot pressure to surface static pressure and from the ratio of pitot pressure to probe-measured static pressure for points corresponding to the heights of the pitot pressure probes. Interpolated values of probe-measured static pressure were used when static pressure measurements were not available for the exact heights of the pitot pressure probes. The real-gas corrections for Mach number (ref. 13) were small and were not applied to the data presented in this report. The total pressure recovery profiles were computed from the Mach numbers and the measured static pressures using the ideal-gas equations and were then corrected for real-gas effects using the methods and charts given in reference 13. Recovery results are presented as ratios of total pressure (real gas) to tunnel total pressure. Further corrections to the total temperature readings for flowfield-property effects were made using the calibration of figure 20 and the Mach numbers computed by the aforementioned procedures. Velocities, static temperatures, and densities were then calculated from the Mach numbers and corrected total temperatures using the ideal-gas equations without real-gas corrections. The boundary-layer thickness δ for each profile was determined and the

various boundary-layer parameters, including displacement thickness, momentum thickness, and mass flow, were computed from the profile data. The criteria used for establishing the boundary-layer edge from the profile data are discussed in later sections.

Real-gas corrections were also considered upon presentation of analytical results for comparison to experimental data. The corrections for real-gas effects (ref. 13) were small for the ratios of static pressure to freestream static pressure, Mach number, total-pressure recovery, and velocity, and no corrections were applied for these parameters. The predicted pitot-pressure distributions were corrected for real-gas effects using the charts of reference 13.

Internal-passage flowfield surveys: The objective of the internal-passage flowfield surveys was to determine the boundary-layer development, shock-wave locations, and flowfield properties near the centerlines of the passages and in particular throughout regions of shock wave-boundary layer interaction. The probe assembly was located at the desired survey station by placing one of a series of contoured inserts with an opening for the probe into a long slot in the cowl block. The insert was contoured so that the internal contour of the cowl block was restored when the insert was in place. The slot and insert were wider than the probe head, so that a probe assembly of the type shown in figure 23 could be installed from outside the inlet without removing the cowl block. Internal flowfield surveys were obtained for the P2 and P8 inlet models. A multi-rake probe comprised of two rakes with variable inter-rake spacing (manually adjustable, fixed during tunnel run) with an exposed thermocouple probe and one flattened pitot tube on each rake (fig. 24) was used for the P2 inlet, whereas a single-rake probe with one exposed thermocouple and one flattened pitot tube was employed in the P8 inlet model tests. Static pressures were also measured at several stations using the flow-direction-sensitive conical probe. An automatic probe-drive mechanism with 25 preset stops for data sampling was used to advance the flowfield probes. Six data points were taken at each vertical survey position, and from 6 to 13 positions were sampled during a single tunnel run. The axial distance between survey stations was from 0.5 to 2.0 in., and from three to nine tunnel runs were required for a complete survey from the centerbody surface to the cowl surface of an internal passage. The wedge-shaped cover mounted above the inlet model in figure 16 was used to protect the

probe-drive mechanism and also to contain the pressure transducers used in conjunction with the flowfield survey probes.

For the internal flowfield surveys, Mach numbers were computed using the ideal-gas equations from the ratio of pitot pressure to surface static pressure for all stations and from the ratio of pitot pressure to probe-measured static pressure, employing interpolated pitot pressures, for stations with conical static-pressure probe data. When using surface static pressures, the cowl value was used for survey points between the cowl shock wave and the cowl surface, and the centerbody value was used for profile segments between the cowl shock wave and the centerbody surface. The remaining flowfield and boundary-layer properties were computed as described above for the inlet-entrance station. For boundary-layer calculations, the total temperature readings were corrected using a constant recovery factor of 0.95 (fig. 22).

Inlet throat flowfield surveys: At the throat station, manually-adjustable double pitot-pressure and shielded total temperature probes (fig. 27) and direct-reading static pressure probes, shown mounted in the inlet throat in figure 28, were used to obtain flowfield data at five of the nine lateral stations given in figure 26. The structure shown above the cowl in figure 17 was used to protect the probes from the tunnel flow. Throat flowfield surveys were obtained for the P2, P8 and P12 inlet models. Throat-station profile data were also obtained using traversing exposed thermocouple probes for the P2 and P8 inlet models and using the traversing conical static-pressure probe for the P2 inlet model; thus, comparisons of results determined with different types of instrumentation are available for these cases. The data-reduction procedures presented above for the inlet-entrance station and the internal flowfield surveys were used to obtain throat flowfield results from the measured data. Interpolated values of probe-measured static pressure were used when direct-reading static pressures were not available at the exact heights of the pitot pressure probes for the off-centerline lateral stations of the P8 inlet model and for all lateral stations of the P12 inlet model. No interpolated static pressures were employed for the P2 inlet model or for the centerline station of the P8 inlet model.

RESULTS AND DISCUSSION

Experimental results and analytical predictions are presented and compared in the following sections for the inlet-entrance station, the internal passages of the P2, P8, and P12 inlet models, and the inlet performance as delineated by the flowfield properties measured at the throat stations of the inlet models. The original distributions and profiles computed while designing the effective inlet contours are compared to experimental data for the design angle of attack of the model, 6.5 degrees. These analytical results are collectively referred to as the design analysis. In addition, the results of further analytical solutions that reflect pertinent experimental measurements not accounted for in the design analysis are included for the wedge forebody and the upstream portions of the internal passages for the three inlet models. The methods of analysis for the following flow components were modified for the final calculations:

(1) The freestream flowfield approaching the inlet model was altered to include the effects of the non-uniformity of the flow in the test section of the NASA-Ames 3.5-Foot Hypersonic Wind Tunnel.

(2) The calculation procedure for the boundary layers on the wedge forebody and the centerbody contours upstream of regions of shock wave-boundary layer interaction was modified to include laminar, transitional, and turbulent boundary-layer development.

(3) The calculation procedure for the boundary layers on the cowl surfaces between the cowl leading edges and the interactions with the wave system reflected from the centerbody (when a reflected wave was present) was modified to include the influence of the bluntness-induced entropy layer and also to include laminar, transitional, and turbulent boundary-layer development (when boundary-layer transition was observed).

The specific procedures employed for the final analysis of the aforementioned flow components are discussed as the results are presented and also in the appendices. No revised predictions were made for off-design test conditions.

Inlet-Entrance Flowfield

The design flowfield at the inlet-entrance station was that produced by a seven-degree wedge at a Mach number M_∞ of 7.4. The predicted flowfield properties for this condition were: Mach number M = 6.032, static-pressure ratio $P/P_\infty = 3.135$, and total pressure recovery $P_t/P_{t_\infty} = 0.863$. The geometric contour was obtained by subtracting the displacement thickness of the boundary layer, computed by the method of reference 4, from the coordinates of the seven-degree wedge. The predicted boundary-layer thickness and displacement thickness at the inlet-entrance station, X = 32.0 in., were 0.386 and 0.218 in., respectively.

The axial and radial variations in the wind tunnel characteristics were defined before beginning the final analytical calculations. The freestream Mach number was determined from the ratio of tunnel total pressure and pitot pressures measured at two locations with the inlet model located in the test section, utilizing the tables and real-gas corrections of reference 13. The average Mach numbers were 7.40 at the tip of the wedge forebody, station X = 0, and 7.58 at the inlet entrance station, X = 32.0 in. Mach numbers were also known at several intermediate stations from the wind-tunnel calibrations. The tunnel Mach-number distribution defines an expanding flowfield which is also characterized by flow divergence about the tunnel centerline. The flow-angle calibrations were rather erratic; therefore, a map of flow angularity was constructed using Prandtl-Meyer theory (ref. 13) with zero angularity at the tunnel centerline.

The final predictions of the flowfield over the wedge forebody used the geometric coordinates given in table 1. The properties of the laminar boundary layer in the region of the sharp leading edge were computed using the weak viscous-interaction model reported by Hayes and Probstein (ref. 14) for a 6.45-degree wedge at the test conditions $M_\infty = 7.4$, $P_{t_\infty} = 600$ psia, $T_{t_\infty} = 1460°R$, and the wall temperature $T_w = 545°R$. These conditions gave a value of 2.94 for the interaction parameter $\bar{\chi}$ at station X = 0.1 in., which represents a moderate-strength viscous interaction. The displacement-thickness distribution was computed for the above conditions by the method of reference 14 and the results added to the geometric body coordinates to give a new effective surface. The inviscid flow was then computed by the method of characteristics (ref. 6) using the new effective surface and the non-uniform tunnel characteristics. The displacement-thickness distribution was verified by again computing the

boundary-layer characteristics, using the inviscid pressure distribution, by the method of Lubard and Schetz (ref. 15). The results of the two calculations were nearly identical (see Appendix A for further discussion).

The inviscid-flow and laminar boundary-layer properties computed as described above were retained to the transition station, X = 14.0 in. This station was near the end of transition, as determined by fluorine-sublimation studies conducted during the experimental phase of the investigation. This result is in good agreement with previous transition data (ref. 2), as shown in figure 29. The boundary-layer solutions for the wedge forebody and centerbody between transition and station X = 43.4 in. were obtained using the method of Sasman and Cresci (ref. 16). Preliminary calculations with a discontinuous transition process at station X = 14.0 in. yielded excessively rapid growth of the boundary layer, compared with experimental results. In order to match the experimental displacement thickness at station X = 32.0 in., the turbulent boundary-layer solution was started at station X = 18.0 in. A smooth increase in displacement thickness was assumed between stations X = 14.0 and 18.0 in. An iterative procedure between the inviscid solution and the boundary-layer displacement thickness was used to obtain a self-consistent solution for the entire flowfield upstream of the inlet-entrance station. The calculation procedure for the final analysis and the resulting displacement-thickness distribution are discussed further in Appendix A.

Surface Measurements and Probe Surveys. - The predicted and measured surface static-pressure distributions at the centerline of the wedge forebody for the design angle of attack of 6.45 degrees may be compared in figure 30a. The original analytical solution (solid line), yields a constant ratio of 3.135. The final distribution (dashed line) begins at an initially high value in the region of leading-edge interaction, decreases with distance to the transition location, increases in the region of initially rapid growth of the turbulent boundary layer, and finally decreases again to slightly less than the seven-degree wedge value at station X = 35.0 in. The occurrence of a moderately-strong viscous interaction was evidenced experimentally by the initially high surface pressure (fig. 30a) and the shock-wave curvature near the leading edge observed in schlieren photographs of a calibration plate at α = 6.4 degrees. The reduction in pressure to the value for a seven-degree wedge near station X = 6.0 in. is a result of the less rapid growth of the initially laminar boundary layer as compared to the turbulent boundary layer assumed during the design phase. The experimental

pressure distribution exhibits an increase downstream of the transition location, and the final analytical distribution is in good agreement with experiment to station X = 25.0 in. Downstream of this station, the experimental pressure ratio falls below the seven-degree wedge value. The divergence between experiment and analysis in this region is attributed primarily to the three-dimensional effects present in the experimental results. The lateral variation in surface static pressure at the inlet-entrance (fig. 30b) exhibits a decrease of about seven percent of the centerline value at about 5.5 in. from the centerline. Surface oil flows were obtained with the large calibration plate (0.75 in. narrower than the forebody wedge of the inlet model); a photograph of the surface streamline pattern for $\alpha = 6.4$ degrees is shown in figure 31. The lateral pressure distributions and the oil flow results indicate the presence of symmetrical outflow from the centerline toward the edges of the plate. The inlet-entrance station, X = 32.0 in., and the station at which the swept sidewalls intersect the centerbody surface are shown on the oil-flow pattern. The flow angles at the surface determined from the oil flow photograph vary from zero to approximately 7 degrees at the lateral positions of the inlet-model sidewalls, Z = ±7.0 in., at the inlet-entrance station and to about 6 degrees where the flow at the centerbody surface enters the internal passage. It is believed that the outflow indicated by the lateral pressure decrease and the oil-flow results is responsible for the decrease in static pressure below the final analytical prediction. The influence of the outflow upon the flowfields within the internal passages will be discussed in a later section.

The surface temperature data obtained along the centerline of the wedge forebody to the inlet-entrance station are shown in figure 32 for a typical test run. The leading edge and the plate to about station X = 10.0 in. were water cooled, and the influence of the cooling is shown in the longitudinal distribution. The experimental distribution reaches the design level ($T_w = 545°R$) near the inlet-entrance station, X = 32.0 in. The surface temperature at station X = 32.0 in. did not vary with lateral distance. The temperature rise over the entire wedge forebody during a data sequence of 11 seconds duration was negligible.

Pitot pressure, total temperature, and static pressure measurements were obtained at nine lateral stations at the inlet-entrance station, X = 32.0 in., using the instrumentation shown in figure 27. The pitot pressure profiles were obtained using two rakes of nine probes each for a total of 13 tunnel runs, and then reorganized into

profiles extending from $Y' = 0.05$ to 4.20 in. The centerline profile is shown in figure 33, and the analytical predictions (computed using the real-gas corrections of ref. 13) are compared to the experimental data. The analytical predictions are shown only for the inviscid-flow regions and are terminated at the experimental boundary-layer height. The measured pitot pressures increase with normal distance within the boundary layer and to about $Y' = 2.5$ in., decrease gradually between this height and the wedge-forebody shock wave, and then decrease discontinuously to the freestream value above the shock wave. Comparison of the data and the original predictions shows that the flow is not uniform between about $Y' = 2.5$ in. and the shock wave, but rather exhibits the characteristics of a flow expanding in the direction normal to the surface. The final analytical results exhibit the same trends as the experimental data, indicating that the inclusion of the effects of the leading-edge viscous interaction and the non-uniform flowfield of the wind-tunnel test section provides qualitative agreement between the final analysis and the experimental results. The lack of precise agreement between the predicted and measured pitot pressures in the region between the boundary-layer edge and about $Y' = 2.5$ in. may be interpreted relative to the effects of the leading-edge viscous interaction on the downstream flowfield (Appendix A). It appears that a strong viscous interaction in the immediate vicinity of the leading edge would perturb the leading-edge shock wave sufficiently to lower the computed pitot pressures in this region; however, no additional evidence is available to support the use of a strong-interaction analysis. Therefore, the weak interaction theory was retained for the final analytical solution.

The probe-measured static pressures and the corresponding analytical predictions for the centerline of the wedge forebody are shown in figure 34. Flowfield static pressures were obtained only between the edge of the boundary layer and the shock wave; 10 tunnel runs were required to obtain the data shown in figure 34 and at the remaining lateral stations. The measured values are higher than the surface value and the design predictions over the entire flowfield. The distribution of measured static pressure defines an expanding flowfield over the region between $Y' = 2.5$ in. and the shock wave, as does the final prediction (fig. 34). The shape of the measured static-pressure distribution is in qualitative agreement with the final analysis, but the level appears to be too high. The high levels may have been caused by viscous-interaction and boundary-layer effects on the 0.020-in. diameter probes.

The centerline Mach-number distribution was computed from the ratio of pitot pressure to surface static pressure and from the ratio of pitot pressure to probe-measured static pressure (interpolated as required). The results are compared to analytical predictions in figure 35. The original prediction for flow over a seven-degree wedge gives a Mach number of 6.032 over the entire flowfield, whereas the final analysis predicts a variation in Mach number from 5.95 at the edge of the boundary layer to 6.11 at $Y' = 3.5$ in.(cowl leading-edge height). The Mach numbers derived from the measured data fall below both predictions when either surface static or probe-measured pressures are employed.

Distributions of total-pressure recovery corresponding to the Mach number distributions discussed above are shown in figure 36. The real-gas corrections of reference 13 were used for the analytical predictions and in obtaining the experimental results from the measured quantities. The final analytical distribution exhibits a substantial recovery loss just outside of the edge of the boundary layer and a slight decrease over the entire flowfield relative to the design level for a seven-degree wedge. The experimental recovery levels fall below both predictions.

The lack of agreement between the predicted Mach numbers and recoveries and the experimental data (figs. 35 and 36) is attributed primarily to the high static-pressure levels used in the data reduction. As shown in figure 34, the distribution of probe-measured static pressure has the same general shape as that for the final analysis, and it may be concluded that a significant static-pressure decrease occurs between the edge of the boundary layer and the wedge-forebody shock wave. The probe-measured static pressures were corrected by reducing the measured values so that the corrected distribution was equal to the surface value between $Y' = 0$ and 0.45 in. (approximate boundary-layer edge) and was approximately parallel to the final predicted distribution between $Y' = 0.45$ and 1.16 in. This method yielded a correction factor of 0.92. The resulting static-pressure distribution is shown in figure 37, together with the distributions of Mach number and total pressure recovery computed using the measured pitot pressures (fig. 33) and the corrected static-pressure distribution. The trend of the recovery data is indicated by the solid line, and the final analytical distributions are shown by the dashed lines. The final predictions are in good agreement with the experimental static-pressure and Mach-number distributions; however, the predicted recovery is again higher than the experimental level.

Estimates of the experimental error associated with each property, computed using the error limits given in a preceding section for the measured quantities, are shown in figure 37. The results of the final analytical calculations generally fall within these error bands for all centerline data at the inlet-entrance station. Also shown in figure 37 are the properties at $Y' = 3.6$ in. computed from the ratio of pitot pressure to tunnel total pressure, assuming uniform flow along the streamline between the shock wave and the probe, and accounting for the non-uniformity of the wind-tunnel flow and the losses through the oblique shock wave. This procedure yields a lower static-pressure ratio and higher values of Mach number and total pressure recovery than were obtained from the pitot pressures and corrected static pressures. As a final comparison between experiment and analysis, the computed and experimentally observed locations of the leading-edge shock wave are shown in figure 38. As the comparison indicates, the difference between the final analytical shock-wave height and the experimental result at the inlet-entrance station, $X = 32.0$ in., is small.

Total temperature measurements were obtained at the inlet-entrance station between the wedge-forebody surface and $Y' = 0.8$ in. during the same tunnel runs as the probe-measured static pressures. These measurements were made to aid in the selection of the edge of the boundary layer and for use in calculating boundary-layer properties. The total temperature distribution near the model centerline, corrected using the calibration curve of figure 20, is shown in figure 39. The large scatter is a result of combining data from many tunnel runs and the results are not adequate for the determination of the edge of boundary layer. The corrected total-temperature distributions were used in computing the boundary-layer velocity profiles and integral properties.

The profile data presented above were obtained at or near the centerline of the model at the inlet-entrance station. The envelopes of the measured flowfield properties for all lateral stations are shown in figure 40. The centerline distributions are given by the solid lines. The dashed lines bracket both the scatter and the trends of the data between $Z = -3.2$ and $+2.5$ in. Further variations for stations outboard of the central region are also indicated in figure 40. The pitot pressure variation for the central region is small (fig. 40a) with the largest changes occurring near the edge of the boundary layer. The trend of decreasing pitot pressure with increasing lateral distance from the centerline is symmetric about $Z = 0$. The variation in the lateral

static-pressure distributions (fig. 40a) was obtained by correcting the probe-measured values in the manner described in the preceding paragraphs. The corresponding envelopes of Mach number and total pressure recovery are shown in figure 40b. The results indicate that the flow properties determined from pressure measurements lie within the error bands for the centerline data for Z between -3.2 and +2.5 in. (fig. 37). The scatter in the results outboard of the central region covers the entire range shown in figures 40a and b. The corrected total-temperature distributions across the entire inlet-entrance station, shown in figure 40c, fall between the dashed lines, indicating that the total temperature distribution is not a strong function of the distance from the centerline of the model.

The flowfield at the inlet-entrance station provides the basis for evaluation of the performance of the internal passages. Consideration of the experimental results shown in figures 37 and 40, the relatively large error limits associated with the experimental total-pressure recovery, and the results of the final analysis leads to the following estimates regarding the recovery at the inlet-entrance station:

(1) The recovery at the edge of the boundary layer across the inlet-entrance station equals the final analytical value of 0.75.

(2) The centerline recovery just downstream of the oblique shock wave equals the final analytical value of 0.85.

(3) For evaluation of internal passage performance, the recovery at the inlet-entrance station is estimated to equal 0.8. This value is approximately equal to the average of the final predicted recovery and the experimental recovery at the model centerline.

Boundary-Layer Transition. - As discussed above, transition from laminar to turbulent boundary-layer flow occurred on the wedge-forebody at about station X = 14.0 in. This result was obtained using the fluorine-sublimation technique. The turbulent nature of the boundary-layer at the inlet-entrance station, X = 32.0 in., was verified by the shearing-stress data obtained using a skin-friction gage. The measured shear stress at this location was $\tau_w = 1.33$ lb/ft^2. The value computed using the method of Sasman and Cresci (ref. 16) was 20% lower than the experimental result. The result obtained with the Stanton tube, (fig. 18d) was only 0.75 lb/ft^2, and it was concluded that the measurement made with the device used was unacceptable. As shown in the following section, the velocity profiles at the inlet-entrance station also indicated a fully-developed turbulent boundary layer.

Boundary-Layer Properties. - The velocity distributions through the boundary layer for the nine lateral positions at the inlet-entrance station were computed from the pitot pressure distributions, the surface static pressures, and the total temperature distributions (corrected using calibration curve of fig. 20). The boundary-layer thickness δ for each lateral station was obtained from the pitot pressure measurements by the following procedure:

(1) a straight line was drawn through the pitot-pressure distribution near the outer edge of the boundary layer (region of variable P_p/P_{t_∞}).

(2) a second straight line was drawn through the distribution in the inviscid flowfield (region of constant P_p/P_{t_∞}), and

(3) the point of intersection of the two lines was defined as the boundary-layer edge.

The velocity distribution near the model centerline, normalized by the thickness determined as above and the corresponding velocity U_e, is shown in figure 41. Also shown are the envelope of the experimental distributions at the nine lateral stations, the design velocity profile predicted assuming a turbulent boundary layer over the entire wedge forebody (ref. 4), and the final analytical distribution computed by the method of Sasman and Cresci (ref. 16). As discussed previously, the final boundary-layer results were obtained by beginning the turbulent boundary-layer calculation at station X = 18.0 in. The experimental profile is appreciably fuller than the original prediction, and the shape of the experimental profile is relatively unaffected by the lateral distance from the model centerline. Considerably better agreement with experiment was obtained by the final analytical procedure.

The lateral variations in the boundary-layer integral properties at the inlet entrance, shown in figure 42, are qualitatively consistent with the other indications of spanwise outflow from the centerline discussed previously. The final analytical predictions are in good agreement with the centerline values of boundary-layer thickness and displacement thickness (Appendix A). The agreement is not as good for momentum thickness. This lack of agreement appears to be a result of both experimental inaccuracies in computing momentum thickness from relatively few profile points and the use of the turbulent skin-friction relations of references 4 and 16 coupled with the discontinuous flow model for boundary-layer transition.

Internal Passage Flowfields

The design predictions for the internal flowfields of the P2, P8, and P12 inlet models were identical upstream of a Mach wave that traverses each internal passage from cowl station X = 34.25 in. to centerbody station X=44.25 in. Following cancellation of the cowl shock wave, the design flowfield within each internal passage was determined by the amount of expansion or compression and the shape of the surface contours required to achieve the desired compression ratio at the throat station.

The final predictions of the flowfields within the internal passages used the final inlet-entrance predictions discussed in the preceding section and the geometric coordinates given in table 3. The iterative procedure for the final wedge-forebody flowfield (Appendix A) was continued to the centerbody station at which the cowl shock wave intersected the edge of the centerbody boundary layer. Simultaneously, a similar iterative procedure was employed to obtain a coupled inviscid-viscous solution for the region between the cowl shock wave and the cowl surface (see Appendix B for details). In this region, the inviscid-flow computer program (ref. 6) was modified to permit a prescribed streamwise entropy variation at the inviscid-viscous interface. The procedure extended the normal displacement-thickness correction by matching the mass flow of the boundary layer, computed by the method of Lubard and Schetz (ref. 15), to the mass flow along the cowl shock wave from the stagnation streamline. The entropy at the inviscid-viscous interface was then determined from the distributions of entropy and mass flow normally computed along the cowl shock wave by the method of reference 6. The coupled inviscid-viscous solution for the cowl surface was continued to the experimentally-determined transition location. After an assumed discontinuous transition process to a turbulent boundary layer, the coupled solution was continued using the method of Sasman and Cresci (ref. 16) to compute the boundary-layer development downstream of transition. A detailed description of the coupled inviscid-viscous solution for the cowl surfaces is presented in Appendix B.

Experimental results for the internal passages are presented in the form of surface static pressures and temperatures; pitot-pressure, static-pressure, and total temperature surveys; flowfield patterns determined from the analysis of pressure data and schlieren photographs; and Mach number, total pressure recovery, and velocity distributions computed from the measured data. Methods of detecting the

location of boundary-layer transition are discussed, and distributions of boundary-layer thickness and integral properties are presented. Survey data were obtained only at the throat station for the P12 inlet model.

Surface Measurements and Probe Surveys. - No survey data were obtained in the region of the cowl leading edge; however, the cowl shock-wave location was determined by schlieren observations, figure 43. The experimental shock wave is closer to the leading edge than indicated by the design location. The shock-wave shape predicted by the final analysis is in somewhat better agreement with experiment. This comparison indicates that the Mach number at the cowl leading edge may be higher than that indicated by the experimental results at the inlet-entrance station (fig. 37). The results shown in figure 43 apply to all inlet models.

P2 inlet model: The predicted and measured distributions of surface static pressure and the internal shock-wave pattern for the P2 inlet model at the design angle of attack of 6.45 degrees are shown in figure 44. The schlieren photograph shows that the impinging shock wave was about 0.5 in. downstream of the design location and that a reflected shock wave was obtained rather than a complete cancellation of the impinging shock wave. The impinging shock wave is well defined and penetrates far into the boundary layer with only slight curvature. A single reflected shock wave emerges from the boundary layer immediately upstream of the throat station. As shown on the photograph, the location of the impinging shock wave is accurately predicted by the techniques used during the final analysis.

The measured surface-static pressures for the centerbody are compared to the predictions in the lower graph of figure 44. The measured rise begins at about station X = 44.5 in. The faired portion of the shock-wave cancellation surface, which generates an expanding flowfield, is well upstream of the pressure rise caused by the shock-wave reflection. This results in a decrease in surface pressure between stations X=43.4 and 44.5 in. After shock-wave impingement, the centerbody surface pressure increases to nearly the design level at the throat station, X = 47.0 in. The final prediction for the centerbody surface pressure, shown by the dashed line in figure 44, is terminated at the intersection of the predicted impinging shock wave and the edge of the boundary layer.

The combined effects of the non-uniform flow at the inlet-entrance station and the coupling of the inviscid and boundary-layer solutions for the cowl surface result

in the differences in the design and final predictions for the cowl surface pressure (upper graph of fig. 44). Both results are generally in good agreement with the measured static-pressure distribution.

The lateral distributions of surface static pressure at the throat station of the P2 inlet model, station X = 47.0 in., are shown in figure 45. Both distributions are nearly constant in the regions critical to the internal flowfield surveys, between Z = -3.0 and +3.0 in.; however, there is some evidence of corner effects, particularly for the centerbody surface. The lateral position of the flowfield surveys, Z = -2.095 in., is within the region of essentially constant static pressure. Oil-flow patterns obtained on the centerbody surface confirmed that the corner effects were confined to small regions near the sidewalls.

Typical surface temperature distributions for the internal passage of the P2 inlet model are shown in figure 46. The unflagged symbols indicate the distribution at the beginning of a data sequence, and the flagged symbols give the final temperatures after a run time of 20 sec. Comparison of the distributions shows that the water cooling maintains constant wall conditions over the entire cowl surface. The temperature level was somewhat higher for the centerbody surface, and a small temperature increase occurred during the run. The entire range of surface temperatures shown in figure 46 is not sufficiently large to affect calculations based on a constant surface temperature of 545°R. The lateral variations in surface temperature for the P2 inlet model were negligible.

Pitot pressure and total temperature measurements were obtained within the internal passage of the P2 inlet model at ten stations (fig. 47): X = 39.0, 40.0, 42.0, 43.0, 44.0, 44.5, 45.0, 45.5, 46.0, and 47.0 in. A two-rake probe assembly of the design shown in figure 24 with one exposed thermocouple and one flattened pitot tube on each rake was used to obtain data along the station lines of figure 47, where the length of the bar indicates the extent of each survey. Data were obtained through the centerbody boundary layer at four stations upstream of the interaction region on the centerbody, at five stations within the interaction region (between the stations at which the impinging shock wave enters the upstream boundary layer and the reflected shock wave emerges from the downstream boundary layer), and at the throat station. Cowl boundary-layer profiles were measured at ten stations. The pitot pressures were not corrected for flow inclination since the maximum angle of attack of the probe relative

to the local flow direction was less than 10 degrees. Data were recorded at height intervals of about 0.025 in., after allowing sufficient time for stabilization of the pressure and temperature readings. Since each complete survey was comprised of a number of tunnel runs (from three to five for the P2 inlet model), two overlapping points were recorded at the junctions of profile segments.

The pitot pressure and total temperature distributions, adjusted to the nominal tunnel conditions P_{t_∞} = 600 psia and T_{t_∞} = 1460°R, are shown in figure 48, parts (a) - (j). The total temperature distributions shown in figure 48 were not corrected for flowfield-property effects. Additional total temperature profiles, corrected using the calibration data of figure 22, are discussed upon presentation of the boundary-layer results. The surface pressures for the centerbody and cowl (flagged symbols) are averages of individual surface static pressures for each profile segment. Cowl and centerbody pressures for each profile segment were recorded when the probe was at its maximum distance from the respective surface. The final pressures at each station are the numerical averages over all profile segments. The surface temperatures (flagged symbols) were obtained in a similar manner; however, the individual readings were obtained with the probe at its minimum distance from the surface. This procedure minimizes the effects of probe interference on surface pressure readings while simultaneously affording the best possible matching of surface and probe-measured temperature data. The pitot pressure profiles at stations X = 40.0 and 42.0 in. (figs. 48b and c) show the apparent edges of the boundary layers on both inlet surfaces and the cowl shock-wave locations, which appear as near-discontinuities about 0.05 in. thick. The pitot pressure increases rapidly as the probe moves above the shock wave into the region of lower Mach number. The shock wave is also defined at stations X = 43.0 and 44.0 in. (figs. 48d, e) as it enters the centerbody boundary layer. The shock wave does not again appear on a profile until station X = 47.0 in. (fig. 48j) where the rapid decrease in pitot pressure in the Y′ - direction near Y′ = 0.4 in. defines the reflected shock wave observed in the schlieren photograph of figure 44. Several sets of pitot pressure results are shown in figure 48j for the throat station, X = 47.0 in. The circular symbols denote data obtained with the traversing probe at lateral station Z = -2.095 in. The scatter near Y′ = 0.4 in. delineates an apparent change in the reflected shock-wave location between tunnel runs. The region of low pitot pressure between about Y′ = 0.5 and 1.0 in. defines an expansion region that propagates across the flowfield upstream of the reflected shock wave. The two sets of pitot pressures between Y′ = 1.2 and 2.2 in. illustrate the poorest agreement obtained between profile

segments for any detailed survey. Additional data obtained at the centerline station are shown by the triangular symbols. The centerline results are in good agreement with the detailed surveys between the centerbody surface and $Y' = 1.2$ in., and with the higher values obtained with the traversing probe between $Y' = 1.2$ and 2.2 in. This result indicates that the lower pitot pressures in the latter region may be in error. This severe non-repeatability, which only occurred at this station, may have resulted from variations in tunnel conditions between tunnel runs or from undetected leaks in the pressure measuring apparatus. Special precautions were taken during subsequent tests (the survey at station $X = 47.0$ was the initial survey of the test program) to maintain constant tunnel conditions between runs and to eliminate leakage in the pressure instrumentation. The pitot pressure distributions near the cowl surface delineate a rather thick region of variable flow properties for all stations, and conclusions regarding the cowl boundary-layer development cannot be made without consideration of total temperature data. Interpretation of the results near the cowl surface is also made difficult by the lack of agreement in measured pitot pressures at the junctions of the segments comprising several of the profiles.

The total temperature distributions shown in figure 48 are in good agreement at profile segment junctions when adjusted to the nominal test-section total temperature of 1460°R. An immediate observation upon comparison of the shapes of the pitot pressure and total temperature distributions is that both profiles indicate approximately the same boundary-layer thickness on the centerbody surface; whereas the total temperature distributions indicate a much thinner viscous region on the cowl surface in comparison with the apparent boundary-layer thickness indicated by the pitot pressure profiles.

The analytical predictions are compared to experimental data for representative stations in figure 48, parts (b), (i), and (j), corresponding to $X = 40.0$, 46.0, and 47.0 in., respectively. As for the inlet-entrance station, the analytical results were computed using the real-gas corrections of reference 13 and are terminated at the experimental boundary-layer thickness for each surface. Downstream of station $X = 40.0$ in., the final analytical results are terminated at the experimental boundary-layer edge for the cowl surface and at the boundary of the theoretical expansion associated with the curvature downstream of station $X = 43.4$ in. for the centerbody surface. At the station upstream of the interaction region, figure 48b, the measured pitot pressures are lower than the design predictions over nearly the entire height of the internal

passage and the experimental shock wave is closer to the cowl. After accounting for the effects of the non-uniform flow at the inlet-entrance station and the coupling between the bluntness induced flowfield and the boundary layer on the cowl surface, somewhat better agreement between analysis and experiment is obtained. The design pitot-pressure distribution at station X = 46.0 in., figure 48i, is nearly uniform over the lower half of the internal passage, but the predicted pitot pressure exceeds the measured level. The final prediction is in qualitative agreement with experiment over the upper half of the passage; however, the predicted pitot-pressure level near $Y' = 1.0$ in. remains somewhat higher than that obtained experimentally. Similar results were obtained at the throat station, X = 47.0 in. (fig. 48j). The design analysis predicts a nearly uniform flowfield with no reflected wave, whereas an expansion and a reflected shock wave are delineated by the experimental distribution. The pitot pressure level predicted by the design analysis is again considerably higher than the measured level across the central region at the throat station. The final prediction is generally in better agreement with experiment.

The pitot pressure distributions are shown superimposed upon the internal passage contours of the P2 inlet model in figure 49. The cowl shock wave crosses the internal passage and enters the centerbody boundary layer between stations X = 42.0 and 43.0 in. (The actual shock-wave locations are determined by projecting the discontinuities in pressure to the respective vertical axes.) Neither the shock wave nor the edge of the boundary layer is clearly defined within the interaction region as the boundary-layer flow merges continuously with the inviscid flow. The reflected shock wave is clearly shown only at the throat station. The length of the interaction region, determined experimentally as the distance between the upstream intersection of the impinging shock wave with the edge of the boundary layer and the downstream intersection of the reflected shock wave with the edge of the boundary layer, is approximately 4.0 in. for the P2 inlet model, considerably in excess of the design interaction-region length of 1.0 in. The apparent discontinuity in pitot pressure in the center of the passage for station X = 40.0 in. is a result of poor agreement at the junctions of profile segments.

Composite total-temperature distributions are given in figure 50 for the P2 inlet model. The viscous region as defined by the regions of variable total temperature is thinner for the cowl surface and the regions of variable total temperature on the cowl surface are characterized by much higher gradients. A small hump is also present

near the edge of the high-gradient region near the cowl for many of the profiles. The total temperature distributions across the central portion of the internal passage are quite uniform. The readings were not affected by the presence of shock waves.

Static pressures were measured within the flowfield of the P2 inlet model using the flow-direction-sensitive conical probe (fig. 25b). Data were obtained with this probe at stations X = 44.5, 45.5, 46.0, and 47.0 in. (lateral station Z=-2.095 in.), and reduced by the procedure outlined in reference 12. The reduced static pressures and flow angles (relative to a reference line in the axial direction) are delineated by the circular and square symbols, respectively, in figure 51, parts (a)-(d). Additional static-pressure measurements were made at the inlet centerline at the throat station (X = 47.0 in.) using the direct-reading probes shown in figures 25a and 28. The direct-probe results that were obtained at the heights of the pitot pressures at the inlet centerline (fig. 48j) are shown by the triangular symbols in figure 51d.

The probe-measured static pressures at station X = 44.5 in. (fig. 51a) indicate that the flowfield static pressure increases throughout the region traversed by the probe and exceeds the predicted levels in the central portion of the passage. The experimental pressure would, of course, decrease to the indicated value at the cowl surface. Relatively few experimental points were obtained at station X = 45.5 in. (fig. 51b). The distribution at station X = 46.0 in., figure 51c, again exceeds the predicted levels in the central portion of the passage. Only two data points were obtained at the throat station, X = 47.0 in., using the conical probe (fig. 51d). The additional measurements obtained at the inlet centerline with the direct-reading probes define a nearly uniform distribution across the upper half of the passage. No valid measurements were obtained through the expansion and reflected shock wave delineated by the pitot pressure distribution (fig. 48j). The difference in level of the two sets of experimental data near $Y' = 0.4$ in. at the throat station (fig. 51d) is attributed to the close proximity of the reflected shock wave and also to observed lateral variations in the flowfield properties. No significant improvements in agreement between analysis and experiment were realized with the final analysis. The lateral distributions at the throat station for the P2 inlet model are discussed following the presentation of the boundary-layer properties.

Reduced flow-angularity data are also presented in figure 51, parts (a)-(c). At station X = 44.5 in. (fig. 51a), the results show the effect of the turning of the center-

body surface. The resulting expansion propagates across the passage, as shown by the distributions at stations X = 45.5 and 46.0 in. (figs. 51b and c, respectively). No flow-angle data were obtained outside of the centerbody boundary layer as the throat station, X = 47.0 in. The final analytical predictions for the flow angularity are within 1.5 degrees of the measured values over the region between the expansion originating at the centerbody surface and the cowl surface. This limited agreement, and that for the static pressure distributions, indicates that the conical probe detects the presence and direction of gradients in static pressure and flow angularity. The pressure levels obtained with the device, however, are somewhat questionable.

Mach numbers were computed from the ratio of pitot pressure to surface static pressure for all stations, and from the ratio of pitot pressure to probe-measured static pressure (at the same lateral station) for points outside of the boundary layer at stations where flowfield static-pressure data were obtained. The design and final analytical predictions are compared to representative experimental Mach number distributions in figure 52 for stations X = 40.0, 46.0, and 47.0 in. Only one experimental distribution, computed using the surface static pressure, is shown in figure 52a since no flowfield static pressures were obtained at this station. The experimental and predicted Mach number distributions are nearly uniform in the inviscid flow regions above and below the shock wave, and the agreement between both predictions and experiment is good. Similar results were obtained for the inviscid-flow region above $Y' = 0.8$ in. at station X = 46.0 in., figure 52b. The experimental results using the surface static pressure (circular symbols) between the edge of the centerbody boundary layer and $Y' = 0.8$ in. are in error since the static pressure is known to vary in this region (fig. 51c). The conical-probe results (square symbols) indicate the correct trend. The presence of an expansion wave and a reflected shock wave outside of the centerbody boundary layer is not shown by the available data at the throat station, X = 47.0 in. The predicted and experimental results at the throat station are in good agreement between $Y' = 1.0$ in. and the edge of the cowl boundary layer.

Distributions of total pressure recovery corresponding to the Mach number distributions discussed above are presented in figure 53. The real-gas corrections of reference 13 were used for the analytical predictions and in obtaining the reduced experimental data. The experimental levels obtained using the surface static pressure exhibit the predicted trends at station X = 40.0 in. (fig. 53a), and, with the exception of the region between the shock wave and the edge of the centerbody boundary layer, the

agreement with data is fair for both analytical predictions. The difference between analysis and experiment near the centerbody at this station is similar in magnitude to that observed at the inlet-entrance station (fig. 37). Considerable scatter in the two experimental distributions is evident at station X = 46.0 in. (fig. 53b), especially for the conical probe results (square symbols). This result appears to be associated with the extreme sensitivity of the total pressure recovery to errors in the experimentally determined static pressure level. The distribution obtained using the surface static pressure (circular symbols)is consistent with the results obtained at other stations between approximately $Y' = 1.4$ in. and the edge of the cowl boundary layer, and the agreement between analysis and experiment is fair in this region. The corresponding distribution within the expansion region between the edge of the centerbody boundary layer and about $Y' = 0.8$ in. was not valid since the cowl static pressure was used in the data reduction procedure. Three distributions of total pressure recovery are shown for the throat station, X = 47.0 in. (fig. 53c). The levels obtained at the inlet centerline using the direct-reading probe data and the corresponding pitot pressures (triangular symbols) are believed to best represent the total-pressure recovery of the portion of the internal passage between $Y' = 1.0$ in. and the edge of the cowl boundary layer. These results are also in good agreement with the higher levels obtained from the traversing probes using the surface static pressure and with the predicted distributions. No reduced data using surface static pressure are shown for the region between the edge of the centerbody boundary layer and $Y' = 1.0$ in. since the static pressure was known to vary in this region. Distributions of total pressure recovery at several lateral stations at the throat of the P2 inlet model are presented following a discussion of boundary-layer results. A complete tabulation of the traversing probe results, including pitot pressure and total temperature (adjusted to $P_{t_\infty} = 600$ psia and $T_{t_\infty} = 1460°R$), static pressure (adjusted to $P_{t_\infty} = 600$ psia), Mach number, corrected total temperature, and velocity, is given in reference 17 for the P2 inlet model.

As shown in figures 44-53, the limited results obtained by the final analytical procedure are generally in good agreement with experimental data for the P2 inlet model. The location of the cowl shock wave is accurately predicted. The predicted surface pressure distributions are in good agreement with the measured results, with somewhat better agreement obtained for the centerbody surface. The static pressure and flow-angle distributions across the internal passage are predicted with fair accuracy. The pitot pressure and total pressure recovery levels are over-predicted

in the central region of the flowfield at all stations by about the same degree as for the inlet-entrance station. The Mach number distributions are predicted with good accuracy throughout nearly all of the internal passage flowfield.

P8 inlet model: Predicted and experimental results for the P8 inlet model are presented in the following paragraphs in the same manner as above for the P2 inlet model. The major differences between the two sets of data follow from the differences in the characteristics of the internal passages: the P2 inlet flowfield is an expansion, whereas the P8 design exhibits an overall compression from the inlet entrance to the throat station.

Surface static-pressure distributions and the internal flowfield pattern are shown in figure 54 for the P8 inlet model at the design conditions. The cowl shock wave enters the centerbody boundary layer at the upstream edge of the schlieren window and a complex reflected wave system emerges further downstream. Because of the additional compression and the added length of the internal passage, the reflected wave system interacts with the cowl boundary layer and again enters the inviscid flowfield near the throat station, X = 49.5 in. The results of surface oil-flow studies and observations of a number of black-and-white and color schlieren photographs reveal the following characteristics of the reflected wave system:

(1) Weak shock waves propagate from the corners formed by the intersections of the swept sidewalls and the centerbody surface toward the centerline of the internal passage.

(2) The cowl shock wave curves upstream in the regions between the corner shock waves and sidewalls, generating the first light band of the reflected wave system (Wave A). This wave exists only near the sidewalls.

(3) The cowl shock wave is straight over the central portion of the passage, and the reflection from the centerbody occurs farthest downstream in this central region. The reflected shock wave is slightly curved (in the lateral direction) between the central region and the areas swept by the corner shock waves. This curvature causes the apparent multiple-wave appearance of the main reflected shock wave (Wave B, fig. 54).

(4) The reflected shock wave impinges upon the cowl surface at approximately station X = 49.0 in. and the wave reflected from the cowl surface propagates toward the center of the passage (Wave C).

(5) No evidence of boundary-layer separation was observed in the regions of high adverse pressure gradient.

The measured surface-static pressures on the centerbody, shown in the lower graph of figure 54, are quite unlike the design predictions. A slight decrease in pressure occurs in the region of surface curvature between station X = 43.4 in., which is the beginning of the faired portion of the shock-wave cancellation surface, and the steep pressure rise caused by the shock-wave reflection process. The centerbody static pressure surpasses the design prediction at station X = 45.25 in., undergoes a series of oscillations, and finally reaches a plateau at about 90% of the design level at the throat station, X = 49.5 in. The final prediction for the centerbody surface pressure to station X=42.9 in. is identical to that shown on figure 44 for the P2 inlet model.

Comparison of the centerbody surface static-pressure distributions for the P2 and P8 inlet models, figures 44 and 54, respectively, shows that the initial pressure rise associated with the cowl shock-wave impingement is further upstream for the latter case. The P8 inlet model was designed for a higher overall pressure ratio, and the additional compression resulting from the cowl curvature for the P8 inlet model increases the effective strength of the incident-reflecting shock-wave system. Since a stronger interaction has a larger upstream influence, the surface pressure rise for the P8 inlet model begins upstream of that for the P2 inlet model. The aforementioned effects of the additional compression are similar to those observed by Seebaugh and Childs (ref. 18) for conical impinging shock waves, and the resulting effects on the upstream influence are qualitatively similar for both cases.

The experimental cowl pressures fall below the design analytical prediction upstream of approximately station X = 48.5 in. The reflected shock wave impinges upon the cowl surface at about station X = 49.0 in., and the experimental pressure level exceeds the design prediction downstream of this station. The use of the final analytical techniques for the cowl surface (Appendix B) does not improve the agreement between analysis and experiment. The final prediction is terminated at station X=47.5 in., the approximate location at which the theoretical expansion associated with the centerbody curvature downstream of station X=43.4 in. impinges upon the cowl surface.

The lateral surface-pressure distributions at the P8 inlet model throat, centerbody station X = 49.5 in. and cowl station X = 49.66 in., are presented in figure 55. Both distributions exhibit relatively strong corner effects in the regions farthest from the passage centerline. The lateral position of the flowfield surveys, Z = -2.095 in., is near the outer extremity of the central region of nearly constant surface pressures. The surface static pressure readings used in conjunction with the pitot pressures obtained using the traversing probes were selected after examination of the lateral pressure distributions and generally were taken from the constant pressure regions. Observation of the oil-flow patterns on both the centerbody and cowl surfaces indicated that the internal flow was essentially parallel to the model centerline inboard of lateral stations Z = ±3.0 in. from axial station X = 41.0 in. to the throat station for the P8 inlet model.

Surface temperatures measured in the internal passage of the P8 inlet model are given in figure 56. As with the P2 inlet model, the water cooling limits the cowl surface temperature rise during the 20 sec. data sequence. At the throat station, however, the cowl temperature increases by about 10 percent. The increases in centerbody temperature are also significant within and downstream of the region of shock-wave reflection. In order to minimize the effects of the surface-temperature increase on the measurements within the boundary layers, data near the surfaces were obtained at the beginning of each tunnel run. As for the P2 inlet model, the lateral variations in surface temperature were negligible.

Pitot pressures and total temperatures were measured at 13 stations within the P8 internal passage (fig. 57): X = 41.0, 42.0, 43.0, 44.0, 44.5, 45.0, 45.5, 46.0, 47.0, 48.0, 48.5, 49.0, and 49.5. Data were obtained at three centerbody stations upstream of the interaction region, at five stations within the interaction region (between the stations at which the impinging shock wave enters the upstream boundary layer and the reflected shock wave emerges from the downstream boundary layer), and at four stations between the interaction region and the throat station. Cowl boundary-layer surveys were obtained at seven stations upstream of the cowl interaction region and at four stations between the beginning of the interaction region and the throat station. As shown by the lengths of the bars of figure 57, only centerbody profile data were obtained at stations X = 44.5 and 45.5 in., and only cowl profile data were measured at station X = 48.5 in.

Survey results, adjusted to the nominal tunnel conditions P_{t_∞} = 600 psia and T_{t_∞} = 1460°R, are presented in figure 58, parts (a) - (m), for the P8 inlet model. The total temperature distributions shown in figure 58 were not corrected for flow-field-property effects. These profiles were obtained with a series of six single-rake probes with one exposed thermocouple and one flattened pitot tube on each rake. Only one rake was used during each tunnel run. In order to minimize run times and thereby limit the surface temperature increases, only one overlapping point was taken at each profile-segment junction. The pitot pressure profiles at stations X = 41.0 and 42.0 (figs. 58a, b) show the apparent edge of the boundary layer on both inlet surfaces and the location of the cowl shock wave. The pitot pressure increases rapidly as the probe moves above the shock wave and then continues to increase in the compression region between the shock wave and the edge of the cowl boundary layer. The incident shock wave is also defined at station X = 43.0 (fig. 58c) as it enters the centerbody boundary layer. A shock wave is again discernible at station X = 45.5 in. (fig. 58g) where the rapid decrease in pitot pressure at about Y′ = 0.30 in. defines a reflected shock wave. As for the P2 inlet model (station X = 46.0 in., fig. 48i), the region of lower pitot pressure above the shock wave appears to define an expansion wave. Since an up-running expansion is indistinguishable from a down-running compression on the pitot pressure distribution, examination of the cowl surface static-pressure distribution (fig. 54) was necessary to verify the presence of an expansion upstream of the reflected shock wave. In contrast to that for the P2 inlet model, the reflected shock wave for the P8 inlet model is well outside of the boundary layer at station X = 47.0 in. (fig. 58i). Downstream of this station, the shock wave propagates across the internal passage and is imbedded in the cowl boundary layer at station X = 48.5 in. (fig. 58k). Finally, the shock wave is reflected from the cowl surface and again enters the central flowfield at the throat station, X = 49.5 in. (fig. 58m). The pitot pressure data represented by the circular symbols on figure 58m, as for all profiles in figure 58, parts (a) - (l), were obtained with the traversing probe at lateral station Z = -2.095 in., whereas the triangular symbols delineate centerline results. The difference in level exhibited by the two sets of data for station X = 49.5 in. (fig. 58m) between about Y′ = 3.0 and 0.6 in. may be attributed to the effects of variations in wind tunnel conditions and also to observed lateral variations in flowfield properties at the throat station.

As observed for the P2 inlet model, the pitot pressure and adjusted total temperature distributions shown in figure 58 indicate approximately the same boundary-layer thickness on the centerbody for the P8 inlet model. The total temperature distributions delineate a thinner viscous region on the cowl surface in comparison to the apparent boundary-layer edge indicated by the peaks in the pitot-pressure profiles.

Analytical results, computed using the real-gas corrections of reference 13, are compared to experimental data in figures 58, parts (a), (h), (i), (l), and (m), for stations X = 41.0, 46.0, 47.0, 49.0, and 49.5 in., respectively. The predictions are terminated at the experimental boundary-layer thickness for each surface at the upstream station, and the final analytical profiles are shown only for the region between the edge of the cowl boundary layer and the boundary of the theoretical expansion associated with the centerbody curvature downstream of station X = 43.4 in. No final predictions are given at station X = 47.0 in. and further downstream since the aforementioned expansion wave reaches the edge of the cowl boundary layer near that station. As for the P2 inlet model, the experimentally measured pitot pressures are lower than the design predictions over nearly the entire passage height and the experimental shock wave is closer to the cowl surface at the station upstream of the interaction region (fig. 58a). The results of the final analysis, which account for the non-uniform flow at the inlet-entrance station and the inviscid-viscous coupling on the cowl surface, are in somewhat better agreement with the measured pitot pressures at station X = 41.0 in. The shock-wave height is predicted accurately by the final analytical procedure. The design pitot-pressure level at station X = 46.0 in. (fig. 58h) exceeds the measured result over nearly the entire passage. The final prediction, shown only for the upper portion of the internal passage, exceeds the experimental level at $Y' = 0.7$ in., and decreases to the measured level at the edge of the cowl boundary layer. At station X = 47.0 in. (fig. 58i), the design prediction does not include the expansion region and the reflected shock wave delineated by the experimental distribution. Further downstream, at stations X = 49.0 and 49.5 (figs. 58l and m, respectively) the design analytical distributions do not resemble the measured profiles.

Composite pitot-pressure and total-temperature distributions are shown superimposed upon the P8 internal passage contours in figures 59 and 60, respectively. The cowl shock wave enters the centerbody boundary layer (fig. 59) between stations X = 42.0 and 43.0 in., re-enters the central flowfield between stations X = 46.0 and 47.0 in., and enters the cowl boundary layer just upstream of station X = 48.5 in.

The shock wave again enters the central flowfield at the throat station, X = 49.5 in. The centerbody boundary layer downstream of the interaction region is well defined at the three downstream stations, permitting an assessment of the changes in boundary-layer properties across the interaction region. The length of the interaction region, determined experimentally as the distance between the upstream intersection of the impinging shock wave with the edge of the boundary layer and the downstream intersection of the reflected shock wave with the edge of the boundary layer, is approximately 3.5 in. for the P8 inlet model. This length is somewhat less than that for the P2 inlet model (about 4.0 in.), but remains considerably larger than the design interaction-region length of 1.0 in. In contrast to the results obtained with the P2 inlet model (fig. 49), the pitot pressures near the cowl surface do not increase continuously with distance from the surface. This is a result of the compression between the cowl shock wave and the cowl surface. Poor overlapping of profile segments occurred only at station X = 47.0 in. As observed for the P2 inlet model (fig. 50), the total temperature distributions across the central portion of the internal passage (fig. 60) are quite uniform and are not affected by the presence of shock waves.

Measured static pressures and flow angles are presented in figure 61 for the P8 inlet model. The data were obtained at stations 45.0 and 46.0 in. (lateral station Z = -2.095 in.) using the conical static-pressure probe (fig. 25b). Additional static-pressure measurements were obtained at the throat station centerline (X = 49.5 in.) using the direct-reading probes shown in figures 25a and 28. The direct-probe results that were obtained at the heights of the pitot pressures at the inlet centerline (fig. 58m) are shown in figure 61c.

The probe-measured static pressures at station X = 45.0 in. (fig. 61a) are in good agreement with the design prediction for Y′ greater than about 0.6 in., and indicate that the flowfield undergoes a compression between this height and the cowl surface. This compression was also noted in the pitot pressure measurements (fig. 58f). The final analytical distribution exceeds the design and experimental levels in the aforementioned region. A similar compression was observed at station X = 46.0 in., figure 61b. The measurements at the throat station, X = 49.5 in., (fig. 61c), obtained using the direct-reading probes, define a nearly uniform distribution between the centerbody and about Y′ = 0.6 in. The presence of the reflected shock wave causes the pressure increase between Y′ = 0.6 in. and the cowl surface. The observed com-

pression region near the cowl surface is not present in the design prediction since there was no reflected shock wave in the original design.

Reduced flow-angularity results are also presented in figure 61. At stations X = 45.0 and 46.0 in. (figs. 61a and b, respectively), the experimental results exhibit the influence of the turning of the centerbody downstream of station X = 43.4 in. The magnitude of the flow angularity between Y′ = 0.6 and 0.8 in. at station X = 45.0 is predicted within one degree by both analyses; however, the predicted distributions do not indicate the experimentally observed trends near the edge of the boundary layer. Both experimental distributions shown in figures 61a and b were obtained in relatively close proximity to a region of shock wave-boundary layer interaction and extremely rapid changes in pressure and flow angularity would tend to be smoothed because of the relatively large size of the static pressure probe (fig. 25b). Flow angles were not determined at the throat station, figure 61c.

As for the P2 inlet model, Mach number distributions were computed using both surface and probe-measured static pressures. The predictions are compared to the experimental results in figure 62 for stations X = 41.0, 46.0, 47.0, 49.0, and 49.5 in. Only one experimental distribution is shown for stations X = 41.0, 47.0, and 49.0 in. since no flowfield static pressures were obtained at those stations. At station X = 41.0 in. (fig. 62a) the Mach number distribution between the edge of the centerbody boundary layer and the cowl shock wave is nearly uniform and the agreement between both predictions and experiment is good. No experimental results are shown for the region between the cowl surface and Y′ = 2.0 in. since the static pressure is known to vary in this region and no flowfield static pressures were measured at this station. Results that include the measured static-pressure variation are shown in figure 62b for station X = 46.0 in. (square symbols). Mach numbers computed using surface static pressures are also shown between the edge of the centerbody boundary layer and Y′ = 0.6 in. to illustrate the error introduced by assuming constant static pressure over this region. The probe-measured static pressure was nearly equal to the cowl surface value at Y′ = 0.6 in. (fig. 61b) and the assumption of constant static pressure between Y′ = 0.6 in. and the cowl surface appears to be valid for the determination of Mach number. The Mach number predictions agree with the measured results near the edge of the cowl boundary layer; however, the design analytical distribution is not in good agreement with experiment between Y′ = 0.3 and 0.7 in. at station X = 46.0 in. Similar results

were obtained at station X = 47.0 in. (fig. 62c). The experimental distribution at this station was computed using the surface static pressures and appears to be in error between $Y' = 0.4$ and 0.7 in. The good agreement between the predicted and experimental Mach number distributions from the edge of the centerbody boundary layer to $Y' = 0.45$ in. at station X = 49.0 in. (fig. 62d) may be fortuitous since the experimental pitot pressure shown in figure 581 is not predicted by the design analysis. The experimental data within the cowl boundary layer at station X = 49.0 in. were obtained in a region of large axial and normal pressure gradients and the Mach numbers obtained near the edge of the cowl boundary layer using the surface static pressure appear to be too low. Two sets of data are shown for the throat station, X = 49.5 in. (fig. 62e). The results at lateral station Z= -2.095 in. (circular symbols) were obtained using surface pressures, whereas the centerline data (triangular symbols) were obtained from the ratio of pitot pressure to probe-measured static pressure. The differences between the experimental distributions and between analysis and experiment appear to be associated with the differences in pitot pressure levels shown in figure 58m.

Distributions of total pressure recovery corresponding to the Mach number distributions discussed above are given in figure 63. The real-gas corrections of reference 13 were used for the analytical predictions and in obtaining the reduced experimental results. The experimental recovery results obtained at station X=41.0 in. using surface pressures are shown in figure 63a. The predicted and experimental levels are in good agreement at the edge of the cowl boundary layer. No experimental results are shown for the variable pressure region between the cowl shock wave and $Y' = 2.0$ in. The difference between analysis and experiment between the edge of the centerbody boundary layer and the cowl shock wave is greater than that observed for the P2 inlet model (fig. 53a), but is nearly within the experimental uncertainty level given in figure 37 for the inlet-entrance station. Rather poor agreement between analysis and experiment was obtained for station X = 46.0 in. (fig. 63b). The experimental levels between the edge of the centerbody boundary layer and about $Y' = 0.8$ in. are believed to be in error since higher recovery levels were consistently obtained at the stations further downstream. The low recovery levels obtained at station X=46.0 in. again appear to be caused by the sensitivity of experimental pressure recovery to errors in static pressure. As observed for the Mach number distribution, the experimental results for station X = 47.0 in. (fig. 63c) obtained using the surface static pressure appear to be in error between $Y' = 0.4$ and 0.7 in. A similar observation also applies

to the data presented for Y' greater than 0.7 in. at station X = 49.0 in. (fig. 63d). The two experimental distributions at the throat station (X = 49.5 in., fig. 63e) are in good agreement within the boundary layers and near the edge of the cowl boundary layer, whereas the levels obtained with the probe-measured static pressures and the corresponding pitot pressures at the inlet centerline (triangular symbols) are higher over the central region of the passage. This difference in level appears to be mainly associated with the higher pitot-pressure levels at the centerline (fig. 58m) since the static pressure was nearly constant between the centerbody surface and Y' = 0.6 in. The design analysis over-predicts the recovery level across the entire throat station at the inlet centerline and at lateral station Z = -2.095 in. Distributions of total pressure recovery at several additional lateral stations at the throat of the P8 inlet model are presented following a discussion of the boundary-layer results. A complete tabulation of the traversing probe results is given in reference 17 for the P8 inlet model.

As evidenced by the results shown in figures 54-63 for the P8 inlet model, the limited results obtained during the final analysis are not generally in good agreement with experiment. As for the P2 inlet model, the location of the cowl shock wave was accurately predicted. The agreement between analysis and experiment for the surface pressure is good for the centerbody surface to station X = 42.9 in., but only fair for the cowl surface to station X = 47.5 in. The pitot pressure and total-pressure recovery levels are generally over-predicted in the region between the center of the internal passage and the centerbody boundary layer. The predicted total-pressure recovery and Mach number distributions are in good agreement with experiment only near the edge of the cowl boundary layer upstream of station X = 46.0 in.

P12 inlet model: The results obtained for the P12 inlet model (fig. 64) continue the progressive changes in surface static-pressure distributions and flowfield patterns observed upon comparison of the results for the P2 and P8 inlet models (figs. 44 and 54, respectively). Since the centerbody contours of the P8 and P12 inlet models are nearly identical upstream of station X = 48.0 in. (deviations are within ±0.002 in.), the previous discussion concerning the characteristics of the impinging and reflected shock waves for the P8 inlet model applies directly to the P12 inlet model. The cowl shock wave enters the centerbody boundary layer at the upstream edge of the schlieren window in the P12 inlet model (fig. 64) and the reflected wave system emerges downstream of the interaction region. Because of the additional compressive turning of the cowl surface of the P12 inlet model downstream of station X = 45.0 in., the second

reflection occurs further upstream on the cowl surface than for the P8 inlet model and the down-running shock wave enters the centerbody boundary layer immediately upstream of the throat station, X = 49.9 in.

The measured centerbody surface static-pressure distribution, given in the lower graph of figure 64, is similar to the distribution for the P8 inlet model (fig. 54) upstream of approximately station X = 48.0 in. Downstream of this station the centerbody static pressure closely follows the design prediction until the pressure level reaches about 85% of the design value. This level is maintained to the throat station, X = 49.9 in.

The cowl surface contours for the P8 and P12 inlet models are identical upstream of station X = 45.0 in., and the experimental results are similar in this region (figs. 54 and 64, respectively). The cowl pressure continues to increase downstream of this station for the P12 inlet model (fig. 64), but again fails to reach the design level until the reflected shock wave impinges upon the cowl surface. The cowl pressure exceeds the design level at station X = 49.0 in., and returns to the design level at the throat station, X = 50.08 in.

The lateral distributions in surface pressure at the P12 inlet model throat are shown in figure 65. The cowl distribution is quite uniform and exhibits little corner influence. This result is attributed to the relatively large distance between the secondary reflected shock wave and the cowl surface in the throat region. The corresponding lateral distribution for the centerbody indicates extreme corner effects. The centerbody pressures at the throat station also fluctuated over the range shown in figure 65 for a series of runs, indicating that the flow in this region varied somewhat from one run to another. The circular symbols denote the average distribution, which is symmetric about the model centerline.

The characteristics of the surface temperature distributions for the P12 inlet model (figure 66) are similar to those for the P8 inlet model (fig. 56).

Because of the small height of the internal passage of the P12 inlet model and the difficulty experienced in obtaining repeatable surface pressures at the throat station, no longitudinal survey data were obtained for this internal passage. Throat flowfield properties were measured and results are presented following a discussion of boundary-layer data for the P2 and P8 inlet models.

An attempt was made during the development of the final predictions to improve the design analysis for the shock wave-boundary layer interaction by accounting for certain differences in the flowfields of the three inlet models. As shown in reference 18 for conical impinging shock waves, the presence of a strong compression following an impinging shock wave resulted in changes in boundary-layer properties at the downstream station of the interaction region. Since such a compression was present for the P8 and P12 inlet models, this factor was believed to contribute to the lack of success in cancelling the reflected shock waves for these cases. The presence or absence of a reflected wave was, therefore, not assumed a priori in the application of the control-volume analysis of reference 18, but was determined during the solution procedure. The method also considered the influence of the surface turning within the interaction region introduced in the original design to effect cancellation of the reflected shock wave. Solutions for the flowfields of the three inlet models were attempted by employing an iterative procedure that coupled the interaction-region model for the boundary layer properties and the method-of-characteristics for the external flowfield. Unfortunately, a completely self-consistent solution for the entire flowfield could not be obtained. The interaction-region length and the properties of the boundary layer immediately downstream of the interaction region were adquately predicted; however, the resulting surface pressure distributions were physically unrealizable. The difficulties in obtaining valid solutions appeared to be associated with the inability to properly include the effects of the surface turning within the interaction region in the control-volume model. It appears doubtful that an analysis of the type described above is capable of providing the detailed results needed in the analysis of such a complex flow situation.

Boundary-Layer Transition. - Commercially available gages were installed at one cowl station in each internal passage to obtain heat-transfer and skin-friction data within the P2 and P8 inlet models. These measurements, upon comparison to predicted levels, permitted an assessment of the state of the boundary layer at the cowl station of interest. Additional data, including surface pitot pressures, schlieren photographs, fluorine-sublimation patterns, and boundary-layer velocity profiles were used to determine the approximate location of transition from laminar to turbulent boundary-layer flow for the P8 inlet model.

Results of heat-transfer and skin-friction measurements obtained at cowl stations X = 47.0 and 47.25 in. for the P2 and P8 inlet models, respectively, are compared

to analytical predictions in table 5. The results shown were selected from tunnel runs with near-nominal freestream conditions, and the predicted values were computed using the nominal test conditions. For the P2 inlet model, both laminar and turbulent solutions were started at the cowl leading edge. The method of Lubard and Schetz (ref. 15) was used for the laminar calculations, whereas the turbulent results were obtained using the analysis of Sasman and Cresci (ref. 16). A comparison of the calculated heat-transfer rates and shearing stresses for the laminar and turbulent boundary layers (table 5) indicates that the turbulent values are approximately an order of magnitude greater than the laminar values at cowl station X = 47.0 in. for the P2 inlet model. The measured values are of somewhat greater magnitude than the analytical results for laminar flow, but are substantially smaller than the predicted values for turbulent flow. It is concluded that the boundary layer is laminar or possibly transitional at cowl station X = 47.0 in. for the P2 inlet model. Observations of schlieren photographs and fluorine-sublimation patterns did not provide any consistent evidence regarding transition for the cowl of the P2 inlet model, and surface pitot-pressure data were inconclusive because of difficulties encountered with the surface pitot probe.

The measured surface pitot-pressure distribution for the cowl surface of the P8 inlet model, shown in figure 67, indicates that transition occurred between stations X = 41.0 and 44.0 in. The velocity-profile development, shown in a later section, also supports this conclusion. Additional surface pitot-pressure measurements with variable freestream total pressure (fig. 68) show that transition apparently was completed at station X = 47.25 in. for $P_{t\infty}$ equal to 300 psia, and that the nondimensional surface pitot pressure is essentially independent of the freestream conditions for $P_{t\infty}$ greater than 300 psia. The measured values of shearing stress and heat transfer rate at station X = 47.25 in. lie between the values predicted by the laminar and turbulent boundary-layer analyses (table 5). The analytical estimates for laminar flow were obtained using the Lubard-Schetz analysis (ref. 15). The turbulent estimates were obtained by starting the turbulent boundary-layer solution at station X = 42.0 in. (between the estimated start and end of transition) and computing the boundary-layer development using the method of reference 16. The resulting estimates are greater than the experimentally measured values, indicating that the boundary-layer analysis, which incorporates a discontinuous flow model for boundary-layer transition and a skin-friction correlation for fully-developed turbulent boundary layers (ref. 16), may over-estimate the heat-transfer rate and shearing stress. The experimental boundary layer may also not be fully turbulent at station

X = 47.25 in.; however, the observed boundary-layer profile development (discussed in detail in the following section) indicates that transition from laminar to turbulent boundary-layer flow is complete at cowl station X = 44.0 in. for the P8 inlet model.

Boundary-Layer Properties. - Typical total temperature and velocity profiles and longitudinal variations in boundary-layer properties along the centerbody and cowl surfaces are discussed in the following paragraphs for the P2 and P8 inlet models. The corrected total-temperature distributions through the boundary-layers were obtained from the measured profiles using a constant recovery factor equal to 0.95 (fig. 22). The velocity distributions were computed from the pitot-pressure distributions, the surface static pressures, and the corrected total-temperature distributions using the ideal-gas relationships of reference 13. No real-gas corrections were applied to the velocities. Two criteria were used in the determination of the boundary-layer thickness:

(1) The boundary-layer thickness was set equal to the height at the peak or immediately outside of the hump (when a hump was present) of the corrected total-temperature distribution for all centerbody and cowl stations except those centerbody stations with well-defined shock waves within the boundary layer.

(2) For those cases with a well-defined shock wave within the boundary layer as determine by criterion (1), the boundary-layer thickness was equated to the shock-wave height. Only three centerbody-surface profiles were subject to this criterion.

The criteria described above were applied to the internal-passage flowfield data for the P2 inlet model as follows:

Station	Centerbody	Cowl
39.0	(1)	(1)
40.0	(1)	(1)
42.0	(1)	(1)
43.0	(1)	(1)
44.0	(2)	(1)
44.5	(1)	(1)
45.0	(1)	(1)
45.5	(1)	(1)
46.0	(1)	(1)
47.0	(1)	(1)

Similarly, for the P8 inlet model:

Station	Centerbody	Cowl
41.0	(1)	(1)
42.0	(1)	(1)
43.0	(1)	(1)
44.0	(1)	(1)
44.5	(1)	-
45.0	(1)	(1)
45.5	(2)	-
46.0	(2)	(1)
47.0	(1)	(1)
48.0	(1)	(1)
48.5	-	(1)
49.0	(1)	(1)
49.5	(1)	(1)

Typical corrected total-temperature distributions through the boundary layer on the centerbody of the P2 inlet model are shown in figure 69. The profile at station X = 42.0 in. (fig. 69a) is representative of the profiles at all stations upstream of the interaction region (stations X = 39.0 to 42.0 in.). With the exception of a reduction in boundary-layer thickness as determined by criterion (1) above, there is no observable change in the corrected total-temperature distributions throughout the region of shock wave-boundary layer interaction (figs. 69c-e). The boundary-layer thickness at station X = 44.0 in. (fig. 69b) was determined using criterion (2).

Boundary-layer velocity profiles corresponding to the corrected total-temperature distributions discussed above for the centerbody of the P2 inlet model are also shown in figure 69. The profile at station X = 42.0 in. (fig. 69a) is representative of the velocity profiles at all stations upstream of the interaction region. The experimental profiles at stations 44.0 and 46.0 in., figures 69b and d, respectively, exhibit distorted shapes near the edge of the boundary layer due to the presence of the impinging and reflected shock waves at these stations. The profile at station X = 44.0 in. was terminated by the impinging shock wave. The changes in nondimensional velocity-profile shape through the interaction region for the P2 inlet-model centerbody are shown in figure 70. The disturbance caused by the shock wave appears at station 44.0 in., approaches the surface ($Y' = 0$) upstream of station X = 45.0, and then propagates toward the edge of the boundary layer. The velocity-profile shape changes from that for a well-developed turbulent boundary

layer at station X = 42.0 in. to a somewhat less full but still turbulent profile at the throat station, X = 47.0 in. All velocity profiles shown in figures 69 and 70 were computed using constant static pressure (surface value) through the boundary layer.

The total temperature and velocity distributions computed during the final analysis using the method of reference 16 are compared to the experimental results in figure 69a for station X = 42.0 in. The corresponding non-dimensional velocity profile is also shown in figure 70. The latter figure shows that the velocity profile computed during the final analysis, which is a power-law distribution in the transformed plane (ref. 16), is considerably fuller than the experimental distribution. The predicted velocity profile intersects the experimental distribution when compared on a dimensional basis (fig. 69a) because of the disparity between the predicted and experimental boundary-layer thicknesses. The relative relationship between the experimental velocity and corrected total-temperature distributions, with the total-temperature ratio greater than the velocity ratio at any height within the boundary layer, is predicted by the final analysis.

The streamwise variations in measured boundary-layer properties are shown in figure 71 for the centerbody surface of the P2 inlet model. The boundary-layer thickness at station X = 44.0 in. (flagged symbol, fig. 71a), which was determined using criterion (2), does not follow the trend of the thicknesses determined using criterion (1). The computed results for stations X = 44.0 through 46.0 in. (figs. 71b to e) are flagged to indicate that the assumption of constant static pressure through the boundary layer may give incorrect results for these stations, which are within the region of shock wave-boundary layer interaction. The boundary-layer properties upstream of the interaction region (stations X = 39.0 through 43.0 in.) and downstream of the interaction region (station X = 47.0 in.) appear quite reasonable: increasing thickness parameters upstream of the interaction region, decreasing to the final values at the throat station; nearly constant Mach number upstream of the interaction region with a reduction across the interaction region; and an increasing trend of boundary-layer mass flow upstream of the interaction region, with a negligible increase across the interaction region.

As for the inlet-entrance station, X = 32.0 in. (fig. 42), the design analysis under-predicts the boundary-layer thickness while over-predicting the displacement thickness upstream of the interaction region (figs. 71a, b). The design prediction for

the thickness downstream of the interaction is in good agreement with experiment, whereas the predicted displacement thickness exceeds the measured value by about 15% at the throat station, X = 47.0 in. The final analytical prediction for the displacement thickness upstream of the interaction region is in better agreement with experiment (fig. 71b); however, the predicted boundary-layer thickness is considerably greater than that observed experimentally (fig. 71a). The boundary-layer thicknesses for both predictions were obtained by inverting the compressibility transformation used in the analyses (refs. 4 and 16), with the velocity profiles represented by power laws in the transformed plane. Since the predicted profile for the final analysis is fuller than that obtained experimentally (fig. 70), the ratio δ/δ^* for the predicted profile is greater than the experimental value. The experimental profile was fuller than that obtained by the design analysis; therefore, the opposite relationship was obtained for the ratio δ/δ^*. This ratio is extremely sensitive to the shape of the velocity profile, and a large discrepancy in boundary-layer thickness such as illustrated by the final prediction in figure 71a may be obtained simultaneously with relatively good agreement for displacement thickness. Since the boundary-layer mass flow is proportional to the quantity $(\delta-\delta^*)$, an error in thickness yields a comparable error in mass flow (fig. 71e). The momentum thickness upstream of the interaction region, figure 71c, was predicted with fair accuracy by the final analytical method. The Mach number at the edge of the boundary layer was accurately predicted by the final analysis (fig. 71d).

Corrected total-temperature distributions are presented in figure 72 for the cowl surface of the P2 inlet model. The boundary-layer thickness for each station was equated to the distance from the cowl surface to the peak or to the outer edge of the hump (when a hump was present) in the corrected total-temperature distribution. Since the humps were not well-defined for some profiles (stations X = 44.0 and 45.5 in., for example) and relatively few data points were obtained near the cowl surface for all profiles, the application of criterion (1) leads to an uncertainty of approximately ± 0.015 in. for the cowl-surface boundary-layer thickness. As shown in figure 72, the segments of the total-temperature distributions below about $Y' = 0.1$ in. do not change appreciably with distance over the extent of the profile surveys, although some irregularity is observed for the profile at the throat station (fig. 72e). The effect of the hump near the boundary-layer edge is evident in the profile at station X = 40.0 in. (fig. 72b).

Typical velocity profiles corresponding to the total-temperature distributions discussed above are shown in figures 72 and 73. The non-dimensional velocity profiles for the P2 inlet-model cowl (fig. 73) do not exhibit any trends with distance between stations X = 39.0 and 47.0 in; however, some departure from the typical profile shape is observed at station X = 39.0 in. In contrast to the centerbody results, the velocity varies continuously throughout the region from the cowl surface to well beyond the edge of the boundary layer as determined by criterion (1). This is a result of the influence of the entropy layer associated with the blunt cowl leading edge, and persists throughout the region of the cowl flowfield surveys.

The final predictions for the total-temperature and velocity profiles, obtained using the method of Lubard and Schetz (ref. 15) assuming a laminar boundary layer over the entire cowl surface, are given at stations X = 39.0 and 47.0 in. (figs. 72a and e, respectively). The non-dimensional velocity profile is also given in figure 73 for station X = 39.0 in. This profile is representative of all non-dimensional analytical velocity distributions for the P2 inlet model cowl, and is in good agreement with experiment between stations X = 40.0 and 47.0 in. The experimental velocity profile at station X = 39.0 in. departs somewhat from the analytical distribution, as indicated by the comparisons in figure 73. The predicted total-temperature distributions merge with the corresponding velocity distributions within the boundary layer (fig. 72). This result is not in agreement with experiment. The comparison of the predicted and measured profiles and the general lack of changes in the measured profiles with distance support the previous conclusion that the cowl boundary layer is laminar at the upstream stations for which boundary-layer surveys were obtained and possibly becomes transitional near the throat station.

The boundary-layer properties for the cowl surface of the P2 inlet model are presented in figure 74. All parameters exhibit a nearly constant and then increasing trend with distance, with some fluctuations about the trend lines. The scatter in displacement thickness and boundary-layer mass flow (figs. 74b and d, respectively) is attributed primarily to the aforementioned uncertainty in the application of criterion (1) for the selection of the cowl boundary-layer thickness. The design analysis did not predict the observed boundary-layer development. Accounting for the inviscid-viscous coupling at the edge of the boundary layer in the final analysis results in good agreement

between analysis and experiment for the region between stations X = 42.0 and 45.0 in. The apparent thickening of the boundary layer downstream of station X = 45.0 in. may indicate the beginning of boundary-layer transition.

Corrected total-temperature distributions are presented in figure 75 for the centerbody surface of the P8 inlet model. As for the P2 inlet model (fig. 69), the major change in the total-temperature distribution results from the reduction in boundary-layer thickness through the interaction region. The distributions downstream of the interaction region remain similar between stations X = 47.0 and 49.0 in. The surface temperature is highest at the throat station, X = 49.5 in., and the measurements at that station indicate somewhat higher temperatures throughout the boundary layer than at the upstream stations. The boundary-layer thickness at station X = 46.0 in. (fig. 75d) was determined using criteria (2).

A number of velocity profiles for the P8 inlet-model centerbody are shown in figure 75. Little variation in profile shape was noted upstream of the interaction region, and the profile at station X = 42.0 in. (fig. 75a) is a typical profile. As shown in figure 58, parts (a) - (c), the impinging shock wave enters the boundary layer at about station X = 43.0 in. and is near the surface at about station X = 45.0 in. (fig. 75c). The reflected shock wave emerges from the boundary layer between stations X = 46.0 and 47.0 in. (figs. 75d and e, respectively). The centerbody boundary layer downstream of station X = 47.0 in. is free of strong disturbances (figs. 75f, g, and h). The continuous change in the shape of the non-dimensional velocity profiles through the centerbody interaction region between stations X = 42.0 and 45.0 in. are illustrated in figure 76a. The shape of the profile at station X = 46.0 in. is influenced by the shock wave at the edge of the boundary layer. Downstream of station X = 46.0 in. the profile begins to recover the typical turbulent shape. The redevelopment of the centerbody boundary layer is further emphasized upon comparison of the downstream profiles to the distribution obtained at centerbody station X = 42.0 in. (solid line) in figure 76b. The thickness change in this region is small, and the profiles appear to have reached a similar shape at stations X = 49.0 and 49.5 in.

The predicted total-temperature and velocity distributions, which are identical to those presented in figure 69a for the P2 inlet model, are compared to the experimental results in figure 75a for station X = 42.0 in. The corresponding non-dimensional velocity profile is also shown in figure 76a. As for the P2 inlet-model centerbody, the

predicted profile is fuller than the experimental distribution (fig. 76a). The predicted profile again intersects the experimental distribution when compared on a dimensional basis because of the differences in the analytical and experimental boundary-layer thicknesses (fig. 75a).

The boundary-layer properties computed from the centerbody profile data for the P8 inlet model are shown in figure 77. The boundary-layer thickness at station X = 46.0 in. is flagged to indicate that the relatively low value results from the presence of a shock wave within the profile. The computed properties for stations X = 44.0 to 46.0 in. (flagged symbols) are questionable since the variation in static pressure through the boundary layer is known to be large, whereas constant static pressure was assumed in the calculations. The distributions of properties upstream of the interaction region are similar to those shown in figure 71 for the P2 inlet model and the predictions are identical for the two cases. The redevelopment of the turbulent boundary layer downstream of the interaction region is characterized by a slight increase in thickness, a slight decrease in displacement thickness, and a moderate increase in momentum thickness. The Mach number at the boundary-layer edge decreases slightly between the end of the interaction region and the throat station, X = 49.5 in. The increase in boundary-layer mass flow across the interaction region is difficult to assess because of the scatter in the data near station X = 46.0 in. This increase may be as great as 40% of the value at station X = 43.0 in.

The development of the boundary layer on the cowl surface of the P8 inlet model differs markedly from that observed for the P2 inlet model in the regions of the flowfield surveys. The initial corrected total-temperature distribution at station X = 41.0 in. (fig. 78a) is similar to the distribution at station X = 40.0 in. for the P2 inlet model (fig. 72b). Downstream of this station, the total-temperature profiles for the P8 inlet model become considerably fuller (figs. 78c and d). The boundary-layer thickness also increases with distance between stations X = 42.0 and 48.0 in. The wave system reflected from the centerbody impinges upon the cowl boundary layer downstream of the latter station, and the boundary-layer thickness decreases across the region of shock wave-boundary layer interaction. As for the P2 inlet model cowl, relatively few data points were obtained within the cowl boundary layer for the P8 inlet model and the uncertainty in boundary-layer thickness determined by criterion (1) is approximately ±0.015 in.

The boundary-layer profiles for the P8 inlet-model cowl are shown in figures 78 and 79. The initial profile shape at station X = 41.0 in. (fig. 78a) is similar to the corresponding profile for the P2 inlet model. The shape of the profile changes rapidly between stations X = 41.0 and 43.0 in. (fig. 78c) and the profile appears to be turbulent at station X = 44.0 in. (fig. 78d). This result is consistent with the aforementioned conclusions regarding boundary-layer transition on the P8 inlet model cowl. The profile shape does not change appreciably downstream of station X = 44.0 in. The changes in profile shape through the transition region and the lack of changes further downstream are more clearly delineated in figures 79a and b. The turbulent profile at centerbody station X = 42.0 in. is shown by the solid lines. As shown in figure 79a, the distributions change from laminar to turbulent profiles between stations X = 41.0 and 44.0 in., and then maintain the turbulent shape to the throat station, X = 49.5 in. (fig. 79b). As for the P2 inlet model, the velocity continues to increase beyond the edge of the boundary layer as determined by criterion (1); however, the observable effects of the cowl leading-edge bluntness are smaller for the P8 inlet model.

The final predictions for the total-temperature and velocity distributions at station X = 41.0 in. (fig. 78a) were obtained using the laminar boundary-layer analysis of reference 15, whereas the distributions at station X = 44.0 and 47.0 in. (figs. 78d and g, respectively) were predicted by the analysis of reference 16. The non-dimensional laminar boundary-layer profile is also given in figure 79a for station X = 41.0 in. The latter profile is in good agreement with the measured profiles at stations X = 41.0 and 42.0 in., indicating that the boundary layer is laminar at the upstream stations. The disagreement between the predicted and measured distributions evident in figure 78a for this station is a result of the under-prediction of the boundary-layer thickness during the final analysis. As for the centerbody boundary layer, the predicted total-temperature ratio is higher than the predicted velocity ratio at any point within the turbulent boundary layer (stations X = 44.0 in. and 47.0 in., figs. 78d and g, respectively). This relative relationship is in agreement with the experimentally observed results. At station X = 44.0 in. (fig. 78d), the predicted velocity profile is fuller than the experimental distribution. Somewhat better agreement between the predicted and measured velocity distributions was obtained at station X = 47.0 in. (fig. 78g).

The streamwise variations in boundary-layer properties for the cowl surface of the P8 inlet model are given in figure 80. The computed data at stations X = 48.5 and 49.0 in. (flagged symbols) are results for regions of high normal pressure gradient and are questionable since the surface static pressure was used in the data reduction procedure. The boundary-layer thickness generally increases with increasing axial distance upstream of the region of interaction with the reflected shock wave. The displacement and momentum thicknesses decrease in the region of high adverse pressure gradient upstream of station X = 46.0 in., and then increase in the region of more rapid growth of the turbulent boundary layer between station X = 46.0 in. and the region of shock wave-boundary layer interaction. The boundary-layer mass flow increases throughout the region of the flowfield surveys, with a large increase across the interaction region. As for the P2 inlet model, the design analysis does not predict the observed boundary-layer growth. The thickness parameters are under-predicted by the final analysis in the laminar region. The predictions for the turbulent-boundary layer development downstream of station X = 42.0, obtained by the method of Sasman and Cresci (ref. 16), appear to be in good agreement with experimental data between stations X = 44.0 and 47.5 in.; however, this agreement may be fortuitous since the predicted boundary-layer growth rate is greater than that obtained experimentally. The final predictions were terminated at the point of impingement of the theoretical expansion associated with the centerbody turning downstream of station X = 43.4 in. upon the edge of the cowl boundary layer.

Boundary-layer velocity profiles at several centerbody stations for the P2 and P8 inlet models are compared in figure 81a. The profiles at station X = 42.0 in. are nearly coincident, indicating the high degree of repeatability of the measurements and flow conditions. At station X = 44.0 in., which is near the beginning of the interaction region for both inlet models, the impinging shock wave results in disturbances in both profiles. The profiles at the station immediately downstream of the interaction region (X = 47.0 in.) show that the boundary layer is thinner for the P8 inlet model, a consequency of the higher overall pressure rise for the higher compression inlet. The velocity profiles for the P2 and P8 inlet-model cowls are shown in figure 81b. At the upstream station, the velocity distributions have similar shapes. At the downstream stations, differences in the profile shapes are observed as the boundary layer undergoes transition for the P8 inlet model (station X = 44.0 in.) and develops under the influence of an adverse pressure gradient (station X = 46.0 in.).

No results for the internal boundary-layer development are available for the P12 inlet model since internal flowfield surveys were not obtained for that inlet. Since the P8 and P12 inlet models were of similar design to centerbody station X = 48.0 in. and cowl station X = 45.0 in., it is believed that the boundary-layer development for the two inlets differs mainly in the region downstream of these stations. Several profile points were measured within the centerbody boundary layer at the throat station for the P12 inlet model and approximate values of the boundary-layer thickness parameters were extracted. These results are compared to the design predictions in the following table:

Parameter	δ, in.	δ^*, in.	θ, in.
Experiment	0.160	0.084	0.010
Design Prediction	0.170	0.068	-

A complete tabulation of the boundary-layer profile properties is given in references 17 for the P2 and P8 inlet models.

The use of the techniques described in the appendices for the final analysis generally resulted in better predictions for the boundary-layer thickness and the displacement thickness than were obtained by the design analysis (figs. 71, 74, 77, and 80). An exception to this analytical improvement is evident in figures 71 and 77, where the comparisons indicate that the centerbody boundary-layer thickness was poorly predicted by the final analysis.

Inlet Performance

Results of throat flowfield surveys are presented in the following paragraphs for the P2, P8, and P12 inlet models. The experimental results are presented in the form of distributions of pitot pressure, static pressure, Mach number, and total pressure recovery. The predicted results were presented in the previous section for the P2 and P8 inlet models. Additional predictions are presented in this section for the P12 inlet model.

Flowfield measurements in the form of pitot pressure, static pressure, and total temperature were obtained at lateral throat stations five through nine (fig. 26) for the P2, P8, and P12 inlet models. Distributions of Mach number and total pressure recovery were computed from the measured data. Results are presented in this section only for lateral stations at which complete pitot and static pressure measurements were obtained; therefore, the survey results outside of the boundary layers at lateral station Z = -2.095 in. for the P2 and P8 inlet models are not included. Total temperature distributions across the inlet throat stations are not presented since relatively few points were obtained within the boundary layers and the data obtained are well-represented by the distributions shown in figures 48 and 58.

P2 inlet model: The pitot-pressure distribution obtained at the throat-station centerline of the P2 inlet model is compared to the analytical distributions in figure 48j. This profile is reproduced by the solid curve in figure 82a. Also shown in this figure are the envelopes of the pitot pressure distributions at the lateral throat stations for the P2 inlet model. The pitot pressure ratios fall within a range of 0.035 ± 0.0015 for the region inboard of approximately Z = -2.1 in. and between $Y' = 1.0$ and 2.0 in. (dashed lines). The pitot pressure level is generally lower in the region outboard of Z = -2.1 in., expecially within the centerbody boundary layer.

The distribution of probe-measured static pressure at the model centerline, previously shown in figure 51d, is given by the solid line in figure 82b. No valid static-pressure measurements were obtained through the expansion and reflected shock wave delineated by the pitot pressure distribution ($Y' = 0.38$ to 1.00 in.). The values at the centerline and at the lateral stations near the centerline fall between about 5.0 and 6.0 and, relative to an inlet-entrance pressure ratio P/P_∞ of 3.135, represent internal-passage compression ratios from about 1.7 to 2.0. The pressure level near the sidewall is somewhat higher, especially near the centerbody surface. A representative overall average compression ratio for the P2 inlet model is approximately 1.9.

Mach numbers were computed from the ratio of pitot pressure to probe-measured static pressure. No results are given for the region for which no static pressures were obtained ($Y' = 0.38$ to 1.00 in.). The envelopes of the Mach number distributions are shown in figure 82c; the centerline profile is compared to the analytical distributions in figure 52c. As shown in figure 82c, the scatter in the

Mach number profiles is small in the central region inboard of Z = -2.1 in. for Y′ between 1.0 and 2.1 in. and increases within the boundary layers. The Mach numbers outboard of Z = -2.1 in. are generally lower than the values at stations closer to the centerline.

Total-pressure recovery distributions corresponding to the Mach number distributions discussed above are shown in figure 82d in terms of the centerline distribution and the envelopes of the lateral distributions. The indicated recoveries, based on the tunnel freestream total pressure, fall between 0.61 and 0.79 for Y′ between 1.0 and 2.0 in. The total pressure recovery of the inlet-entrance flow was also determined relative to the tunnel freestream flow. The flow outside of the centerbody boundary layer for the P2 inlet model traverses only one shock wave between the inlet-entrance and throat stations. The maximum predicted recovery across this shock wave is about 0.96, thus recovery levels in the inviscid core flow for the internal passage (relative to the inlet-entrance flow) of approximately that level may be anticipated. Division of the pressure recoveries given in figure 82d by the inlet-entrance recovery, taken here as a representative value of 0.8, yields experimental recovery levels from 0.76 to 0.99 for the internal passage of the P2 inlet model. A representative recovery level for inviscid core flow of the P2 inlet model, relative to the inlet-entrance station, is about 0.85, with an experimental scatter of approximately ± 0.15.

P8 inlet model: Results for the centerline of the P8 inlet model were presented previously in figures 58, 61, 62, and 63. The centerline profiles are shown by solid lines in the envelopes of lateral distributions of flowfield properties shown in figure 83. The range of variation of pitot pressure ratio is shown in figure 83a. The variations from the centerline distribution are larger than observed for the P2 inlet model.

The static pressure levels at the throat of the P8 inlet model are lower than the design level within the inviscid flowfield and increase to a level near the cowl surface that is higher than the design level (fig. 61). The lateral variations in static pressure, shown in figure 83b, are relatively small within the central region and increase at the lateral stations outboard of Z = -3.2 in. The open band between Y′ = 0.68 and 0.74 in. indicates a region in which the static pressure readings were affected by the presence of a shock wave in the vicinity of the tips of the probes.

The compression ratio of the P8 inlet model, measured relative to the inlet-entrance pressure ratio of 3.135, decreases across the passage from about 7.2 at the centerbody surface to a minimum of about 7.0 near $Y' = 0.5$ in. and then increases to about 13.0 at the cowl surface. An overall compression ratio for this inlet model appears to be approximately 8.0; however, the excursions from this level are rather large.

As shown in figure 62, the experimentally determined Mach numbers at the throat station of P8 inlet model are nearly equal to the design value. The variations from this distribution are small in the region not influenced by the sidewall (fig. 83c), and the deviations increase near the sidewall. No Mach numbers are shown for the region of interference between the shock wave and the static pressure probes.

The lateral variations in total pressure recovery (fig. 83d) are small between about $Y' = 0.45$ and 0.68 in. for the P8 inlet model; however, large variations are observed between the centerbody surface and about $Y' = 0.45$ in. The range of the measured recoveries, based upon the tunnel freestream total pressure, is from about 0.60 to 0.77 for Y' between 0.40 and 0.68 in. With a representative inlet-entrance recovery of 0.8, the aforementioned results yield internal-passage recovery levels from 0.75 to 0.96 for the core flow of the P8 inlet model. A representative recovery level for the P8 inlet model is then about 0.85 with an experimental scatter of approximately $\pm$ 0.10. In selecting these representative levels the extremely low recovery results indicated by the dashed lines between $Y' = 0.2$ and 0.4 in. (fig. 83d) were not considered. Only six data points were obtained within this region at lateral stations $Z = -3.19$ and -4.65 in., whereas many more higher levels were measured at the stations inboard of $Z = -3.19$ in. The flow traversing the central core of the throat region for the P8 inlet model crosses two internal shock waves. Evidently, the recovery losses resulting from the additional shock wave, relative to the P2 inlet model with one internal shock wave, are within the scatter of the data.

P12 inlet model: Since flowfield predictions were not shown previously for the P12 inlet model, the design analytical predictions are compared to experimental results in this section.

The measured pitot-pressure distribution at the centerline of the P12 inlet model throat is compared to the design prediction in figure 84a. No reflected shock wave is present for the design analysis. The experimental reflected shock wave is

in the vicinity of the edge of the centerbody boundary layer at this station. The pitot-pressure distribution is not adequately predicted by the design analytical procedure. The lateral variations in pitot pressure are large for the P12 inlet model. This is in agreement with the observed fluctuations in the surface static-pressure distribution across the throat station (fig. 65).

The measured static pressure distribution at the throat station centerline for the P12 inlet model is shown in figure 84b, together with the envelope of the lateral distributions. The experimental distribution is near the design level above the reflected shock wave, but the scatter is quite large. The compression ratio for the P12 inlet model, relative to the inlet-entrance compression ratio of 3.135, varies between about 10.0 and 15.0, with an overall level of approximately 12.0.

The variations in Mach number at the throat station centerline for the P12 inlet model are large and the experimental level is not in good agreement with the predicted distribution (fig. 84c). The Mach number decreases markedly in the region of influence of the sidewall.

The experimental distribution of total pressure recovery for the P12 inlet model (fig. 84d) is near the design level between the reflected shock wave and the cowl surface. The sidewall effect is again clearly exhibited by the lateral variations in total pressure recovery. The range of recovery levels relative to the tunnel freestream flow is about 0.55 to 0.80, yielding internal passage recoveries from 0.69 to 1.00 (based on the approximate inlet-entrance level of 0.8) for Y' between 0.30 and 0.56 in. Only three values in excess of 0.95 were obtained, and these results were computed using probe-measured static pressures (or interpolated values) that exceeded the surrounding levels. The static pressure probes used in this region were subjected to severe dynamic loadings and high flow angles, and, as a result, the highest recovery levels are somewhat suspect. A representative recovery level for the internal passage of the P12 inlet model is again about 0.85, with a scatter of approximately ± 0.15. The flow outside of the centerbody boundary layer for the P12 inlet model passes through three shock waves. The presence of the additional shock waves apparently does not result in additional losses relative to those incurred within the internal passages of the P2 and P8 inlet models.

The results for the three internal passages indicate that recovery levels of approximately 0.85 (relative to the inlet-entrance flow) were obtained at the throat stations for all inlet models, even with one or two additional shock waves within internal passages that were designed for shock-wave cancellation. During the process of the data reduction, it became apparent that the calculation of recovery from experimental data was extremely sensitive to the static pressure measurements. Since measurement of flowfield static pressure is difficult and the accuracy of the measurement is questionable, an error limit of about ± 0.15 is associated with the resulting pressure recovery data. The differences in recovery levels between the three inlets are within the experimental accuracy of the results, and no trends with compression ratio can be identified. The results are believed to indicate reliably a high level of recovery for all internal passages.

Off-Design Operation

Data were obtained at off-design conditions for the P2 and P8 inlet models by changing the angle of attack of the entire model. An overspeed condition was achieved by decreasing the geometric wedge angle to 4.5 degrees, and underspeed operation was obtained α = 8.5 degrees. The inlet-entrance Mach numbers at the overspeed and underspeed conditions were approximately 6.3 and 5.7, respectively. Only surface static-pressure distributions are shown for off-design test conditions.

Centerbody and cowl surface pressure distributions for the P2 inlet model at the off-design conditions are compared to the results at the design condition (α= 6.5 degrees) in figure 85. Schlieren observations at α = 4.5 degrees (overspeed condition) revealed that the experimental cowl shock wave was closer to the cowl surface for the lower angle of attack. This result is supported by examining the centerbody static-pressure distribution, lower graph of figure 85, which indicates that the pressure rise begins about 0.5 in. downstream of that for α= 6.5 degrees. The throat pressure level is also lower for the overspeed case; however, the internal compression ratios (throat pressure/entrance pressure) for the two cases are approximately equal. The opposite trends were observed for the underspeed condition (α = 8.5 degrees). The cowl shock wave moves closer to the centerbody surface and impinges upon that surface upstream of the location for the design angle of attack. The internal compression ratio is again relatively unaffected by increasing the angle of attack of the model. The cowl static-pressure distributions exhibit an increase in level

accompanied by an increase in the magnitude of the pressure drop between stations X = 38.9 and 47.0 in. with increasing angle of attack. The ratio of cowl throat pressure to inlet-entrance pressure does not change significantly over the range of angle of attack shown in figure 85.

Similar results are presented in figure 86 for the P8 inlet model. For the underspeed case (α = 8.5 degrees) the reflected wave system, as observed on schlieren photographs, was much narrower and more sharply defined than for the design or overspeed cases. As for the P2 inlet model, the point of shock-wave impingement on the centerbody surface (lower graph of fig. 86 for P8 inlet model) moves upstream with increasing angle of attack. The point of impingement of the reflected shock wave upon the cowl surface (upper graph of fig. 86) also moves upstream as the angle of attack is increased. Considerable variation in the internal compression ratio (throat pressure/entrance pressure) was observed for the P8 inlet model.

The inlet-entrance pressure increases with increasing angle of attack and, in general, the throat pressure ratios exhibit the same trends for both inlet models at the off-design conditions. More significant than the increase in throat pressure with increasing angle of attack is the behavior of the pressure differential across the throat station (fig. 87). The differential considered in figure 87 is the difference between the cowl and centerbody pressure ratios, that is, $(P/P_\infty)_{cowl} - (P/P_\infty)_{centerbody}$. The differential for the P2 inlet model is small compared to that for the P8 inlet model. In addition, the differential for the P2 inlet model changes from positive to negative over the range of angle of attack tested, whereas the pressure differential for the P8 inlet model increases with increasing angle of attack.

CONCLUDING REMARKS

Analytical and experimental investigations were conducted to determine the characteristics of the internal flows in model passages representative of hypersonic inlets. Current analytical and design techniques were applied in the design of several inlet configurations with different amounts of internal compression. Effective inlet-surface contours that provided high performance and approximately uniform theoretical static-pressure distributions at the throat stations were initially designed by the methods of analysis for inviscid flow. The effects of the boundary-layer development were included in the inlet design by correcting the effective contours for the boundary-layer displacement thickness. The resulting geometric contours were incorporated into the design of a series of wind tunnel models.

A successful simulation technique was devised for testing large-scale inlet models in the Mach 7.4 nozzle of the NASA-Ames 3.5-Foot Hypersonic Wind Tunnel. This technique, which effectively removed the vehicle forebody as a factor to be considered in the sizing of the wind-tunnel model, used a two-dimensional wedge forebody to provide a Mach number at the entrance to the internal passages corresonding to that for a vehicle operating at flight Mach numbers between 10 and 12. Also, by this technique, one-third scale models of internal flow passages that provided throat heights on the order of one inch could be tested in the wind tunnel.

The experimental results and the comparisons with the analytical predictions presented in this report show that:

(1) A high level of total pressure recovery, approximately 0.85 for the core flow of the internal passage, was achieved for each inlet design. Within the accuracy of the measurements, estimated at ±0.15, the recovery was in agreement with the predicted level and was independent of the internal compression ratio over the range from two to twelve.

(2) The desired uniform static-pressure distributions at the throat stations, which were predicted by the design analysis, were not obtained experimentally because of the presence of unpredicted reflected shock waves.

(3) The agreement between the predicted and experimental results for the boundary-layer integral properties was generally good outside of regions of shock wave-boundary layer interaction. Improvement of the analytical techniques described in this report is required to account for the effects of boundary-layer transition on the development of the boundary layer through and downstream of transition regions,to predict the profile shapes for turbulent boundary layers, to predict the boundary-layer development downstream of blunt leading edges, and to predict the detailed characteristics of shock wave-boundary layer interactions and the boundary-layer development downstream of interaction regions.

The displacement-thickness correction scheme used in the design of the internal contours did not adequately describe the coupling between the boundary layers and the inviscid flowfields, particularly through regions of shock wave-boundary layer interaction. As a result, the predicted characteristics of the internal flowfields did not agree with those obtained experimentally. In spite of the shortcomings of the analytical methods, they were successfully employed to design inlet passages that provided high internal performance.

APPENDIX A

WEDGE-FOREBODY FLOWFIELD ANALYSIS

The calculation procedures for the final flowfield predictions for the wedge forebody are presented in this appendix. The final predictions were made using the geometric wedge-forebody coordinates given in table 1. The design requirement for the wedge forebody was the simulation of an inlet-entrance Mach number of approximately six in a freestream flowfield with a Mach number of approximately 7.4. Assuming a uniform freestream flowfield, oblique shock-wave theory yields an effective wedge angle of seven degrees for the aforementioned conditions. The geometric contour of the wedge-forebody was obtained by subtracting the computed boundary-layer displacement thickness from the coordinates of the seven-degree effective wedge. The boundary-layer properties were obtained assuming a fully-developed turbulent boundary layer along the entire length of the wedge forebody. Further, the leading edge of the actual wedge forebody, to station X = 2.5 in., was constructed as a straight wedge with an angle ϵ_s of 6.45 degrees.

The boundary-layer transition data of reference 2 (fig. 29) indicate that a substantial region in which the boundary layer is not turbulent exists at the test conditions of the present investigation. The transition location determined during the present study using the fluorine-sublimation technique, also shown in figure 29, is in agreement with the data of reference 2. It can, therefore, be expected that the actual boundary-layer growth over the plate is somewhat different than that predicted during the design phase of the study. This is particularly true in the vicinity of the sharp leading edge, and considerable attention is given in this appendix to the mutual interaction of the laminar boundary layer and the inviscid flowfield near the leading edge of the plate.

During the design of the wedge forebody and the internal passages, it was assumed that the flow within the wind-tunnel test section was uniform at a Mach number of 7.4. With the model installed in the test section, the Mach number upstream of the wedge-forebody shock wave varied from 7.4 at station X = 0.0 in. (leading edge) to 7.58 at station X = 32.0 in. (inlet entrance). The Mach numbers at several intermediate stations were known from the wind-tunnel calibrations. Associated with the Mach number distribution was a variation in freestream flow

direction. The flow-angle distribution determined from the wind-tunnel calibrations was erratic; therefore, a map of flow direction was constructed using Prandtl-Meyer theory (ref. 13) with zero angularity at the wind-tunnel centerline. The flow angle varied from -0.40 degree at the leading edge of the wedge forebody (below wind-tunnel centerline) to +0.44 degree just above the wedge-forebody shock wave at the inlet-entrance station (above wind-tunnel centerline). The aforementioned variations in freestream flow properties are of sufficient magnitude to affect the flowfield over the wedge forebody and at the inlet-entrance station.

For the final analysis, the overall approach to the wedge-forebody flowfield was expanded relative to the design analysis to include the following:

(1) Viscous interaction at the leading edge.

(2) Boundary-layer development including laminar, transitional, and turbulent regions.

(3) Prescribed variation of freestream flowfield.

The viscous interaction analysis of reference 14 permits prediction of the laminar displacement-thickness growth along the wedge forebody in terms of the inviscid flowfield properties that would exist without the presence of a boundary layer. The freestream conditions upstream of the wedge-forebody leading edge, the initial angle of the wedge, the surface temperature, and a length scale determine the value of the interaction parameter $\bar{\chi}$. The length scale must be determined before $\bar{\chi}$ can be properly evaluated. As the length scale becomes progressively smaller, the geometry of the tip becomes increasingly important. Eventually, a blunt leading-edge situation with a detached shock wave is reached, and the interaction is considered to be strong. No experimental evidence was available to support the use of strong interaction theory for the present investigation; therefore, the weak interaction theory was applied in the final analysis.

For the present analysis, the length scale was selected as 0.1 in., approximately 40 times the actual diameter of the "sharp" leading edge of the wedge forebody. At this distance from the leading edge, the value of the interaction parameter $\bar{\chi}$ is 2.94, near the upper limit of the second-order weak-interaction theory of reference 14. The displacement-thickness distribution between station X_o = 0.1 in. and the approximate transition location, station X_t = 14.0 in., was computed using the aforementioned

weak-interaction analysis for the conditions $M_\infty = 7.4$, $P_{t_\infty} = 600$ psia, $T_{t_\infty} = 1460°R$, $T_w = 545°R$, and $\epsilon_s = 6.45$ degrees. The result is shown in figure 88a. An effective inviscid contour was obtained by adding the displacement-thickness distribution to the geometric wedge-forebody coordinates between stations X_o and X_t. The coordinate of the effective surface at station X_o was used to define an equivalent upstream wedge, as shown in the sketch. The initial deflection angle ϵ_o of the effective wedge was 9.81 degrees.

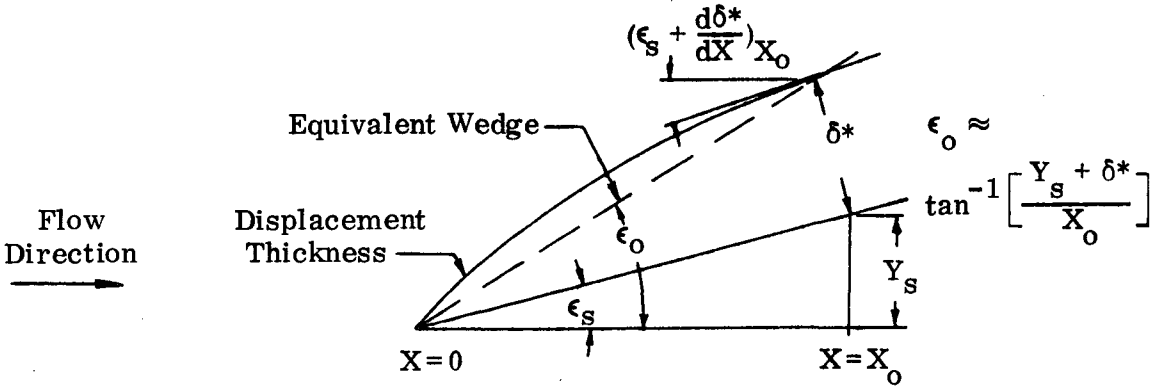

With the effective inviscid contour defined between stations X = 0.0 and 14.0 in., the method-of-characteristics solution of reference 6 was employed to determine the characteristics of the inviscid flowfield. The variation of freestream flow properties given above was employed. At X_o (0.1 in.) the disparity between ϵ_o and $(\epsilon_s + \frac{d\delta^*}{dX})$ results in a centered expansion at this point and a smooth effective surface downstream. The results of the inviscid calculation were then used as edge conditions for the laminar boundary-layer solutions of Clutter and Smith (ref. 7) and Lubard and Schetz (ref. 15). The initial conditions were prescribed by the boundary-layer displacement thickness given by the interaction analysis, the profile shape from the similar solutions of reference 19, and the boundary-layer thickness derived from the displacement thickness and the velocity profile. The computed displacement-thickness distributions were in close agreement with that predicted by the interaction analysis. Figure 88a summarizes these results. The distribution obtained by the Lubard-Schetz method (ref. 15) was used as the final analytical prediction.

The initial displacement thickness of the turbulent boundary layer at station X = 14.0 in. was taken as the laminar value and the downstream boundary-layer growth was computed using the method of Sasman and Cresci (ref. 16). The resulting displacement thickness at station X = 32.0 in. was considerably in excess of the experimentally measured value at that station. This disagreement was attributed to the inability of the discontinuous transition model to yield the proper boundary-layer growth through the transition region. The discontinuous model assumes that the boundary layer downstream of station X_t grows as a fully-developed turbulent boundary layer, whereas the actual boundary layer does not undergo a discontinuous change in growth rate. In order to match the experimental displacement thickness at station X = 32.0 in., the turbulent boundary-layer solution was started at station X = 18.0 in. The resulting turbulent displacement-thickness distribution was then graphically faired to the laminar distribution between stations X = 14.0 and 18.0 in. The entire displacement-thickness distribution was added to the geometric forebody coordinates to define an overall effective surface contour. The method-of-characteristics program, with varying freestream properties, was employed to arrive at a new set of turbulent boundary-layer edge conditions. An iterative procedure between the inviscid solution and the boundary-layer displacement thickness was used to obtain a self-consistent solution for the entire flowfield upstream of the inlet-entrance station. Several iterations were required for this purpose. The resulting displacement-thickness distribution is shown in figure 88b. The final effective contour is shown and compared to the design contour in figure 89, and is also given in table 6.

The final analysis, including the approximate effects of the leading-edge viscous interaction, indicates a measurable degree of shock-wave curvature in the vicinity of the leading edge. This curvature is a highly localized phenomena, and the shock wave angle rapidly approaches that predicted for a seven-degree wedge. The result is a small outward displacement of the shock wave from the original design position. A schlieren photograph of the actual shock-wave position is shown on figure 38. The superimposed analytical shock locations indicate excellent agreement between the final analysis and data, and further that both lie outside the design shock-wave position.

The variation in the shock-wave angle near the wedge-forebody leading edge is nearly equal to the change in the effective surface slope, approximately 2.5 degrees. That even larger variations are realizable, in fact probable, is evidenced by schlieren

photographs of shock-wave patterns near the leading edges of other flat-plate models tested in the NASA-Ames 3.5-Foot Hypersonic Wind Tunnel. Larger initial shock-wave angles would be obtained from the final interaction analysis if the coordinate $X_o = 0.1$ in. were decreased to more closely approach the limit of the weak-interaction theory of reference 14. The use of strong-interaction theory would effect a similar result.

The experimental axial surface-pressure distribution, figure 30a, indicates a region of high pressure near the leading edge. This pressure level rapidly decreases below the design value, later rises above that value, and finally drops off and becomes nearly constant. The average pressure over the entire length of the forebody very closely approximates the design ratio of 3.135. The pressure level and streamwise variation predicted by the final analysis, also shown on figure 30a, shows a high degree of similarity to the experimental data. These predictions display a slight lag with respect to the data that appears to be a result of the approximations used in defining the process of boundary-layer transition. The first data point suggests that a stronger leading-edge interaction yielding a higher surface pressure in the immediate region of the leading edge could have been assumed in the interaction analysis.

The distribution of pitot pressures at the inlet-entrance station is shown and compared to analytical predictions on figure 33. Again the design analysis predicts a uniform distribution in the inviscid stream. The final analysis predicts an increase in pitot pressure up to approximately $Y' = 1.25$ in., and a monotonic decrease thereafter. The data exhibit the same trendwise variation. The effect of the leading-edge interaction is to reduce the pitot pressure in the lower portion of the profile, whereas the variation of freestream properties tends to decrease the pitot pressure in the upper region of the profile.

APPENDIX B

BLUNT LEADING-EDGE FLOWFIELD ANALYSIS

The methods used to obtain the final analytical predictions for the regions near the cowl leading edge, including the boundary-layer development over the cowl surfaces upstream of the stations where the effects of the turning of the centerbody are felt on the cowl surfaces, are discussed in this appendix. The final analysis was conducted using the geometric cowl surface coordinates given in table 3, parts (d) - (f), and the final inlet-entrance predictions presented in Appendix A. The design analysis for the flowfield in the region of the 0.045 in. diameter blunt-cowl leading edge is discussed in reference 3. The inviscid blunt-body solution of Lomax and Inouye (ref. 20) was employed to predict the flowfield in the region of the stagnation point for the design approach Mach number of 6.032. A profile of flow properties across the shock layer from the cowl surface to the cowl shock wave in the supersonic region was used as an input line to start the method-of-characteristics program (ref. 6). The maximum Mach number at any point of this profile was 1.3. The results of a cowl-lip efficiency study, performed using the method of reference 6 (figs. 3 and 4), were used to select an effective internal angle of +1.0 degree for the cowl surface from the point of tangency with the circular leading edge to cowl station X = 34.25 in. for all inlets. The boundary-layer displacement thickness was computed using the method of reference 7 and the geometric contour for each cowl surface was obtained by subtracting the computed displacement thickness from the effective inviscid contour.

The approach used for the design analysis assumed inviscid flow in the stagnation region upstream of the starting line for the method-of-characteristics solution, and separated the flowfield downstream of the starting line into a viscous boundary layer and an inviscid region between the boundary-layer displacement thickness and the cowl shock wave. When the effective inviscid contour (inviscid-viscous interface at a distance from the geometric contour equal to the computed boundary layer-displacement thickness) is used as the boundary for the method-of-characteristics solution, the entropy at the effective surface normally does not vary with axial distance. For a surface with a blunt leading edge, the high-entropy flow (entropy layer) that passes through the cowl shock wave in the region of the stagnation point enters

the boundary layer as the boundary-layer mass flow increases with distance from the stagnation point. The result is that the entropy at the viscous-inviscid interface decreases with axial distance until the mass flow in the boundary layer equals the mass that traverses the cowl shock wave upstream of the station at which the entropy increase across the cowl shock wave becomes constant. This phenomenon was approximated in the design analysis by equating the entropy at each effective surface point to the lower entropy at the nearest upstream flowfield point, thus allowing the entropy to decrease with axial distance along the inviscid-viscous interface.

The coupling procedure described above for the design analysis was not controllable in the sense that the entropy variation along the inviscid-viscous interface was not related to the rate of absorption of the entropy layer into the boundary layer. This inconsistency was eliminated in the final analytical solution by the following procedure:

(1) The blunt-body solution, including the variation of entropy with mass flow downstream of the cowl shock wave, was obtained using the method of reference 20 for the final upstream Mach number of 6.11.

(2) The inviscid flowfield and the variation of entropy with mass flow downstream of the cowl shock wave were computed for the remainder of the flowfield over the design effective surface using the method of characteristics (ref. 6). The approximate entropy calculation discussed above for the design analysis was used in this step.

(3) The laminar boundary-layer development from the input line to the tangent point of the circular cylinder and the straight portion of the effective cowl contour (at $\lambda = +1.0$ degree) was computed for the edge conditions determined in steps (1) and (2) using the method of Clutter and Smith (ref. 7). The computed velocity profile at the tangent point was used as the initial profile for subsequent boundary-layer calculations.

(4) The laminar boundary-layer development over the remainder of the cowl surface for the P2 inlet model or to the experimental transition location for the P8 and P12 inlet models, including the mass-flow variation with axial distance, was computed using the analysis of Lubard and Schetz (ref. 15) for the edge conditions of steps (1) and (2).

(5) The entropy at the inviscid-viscous interface was determined by matching the distributions of entropy and mass flow along the cowl shock wave, from steps (1) and (2), and the boundary-layer mass flow from step (4).

(6) A new effective contour was formed by adding the displacement thickness of step (4) to the geometric cowl coordinates. The cowl shock-wave location and the flowfield properties downstream of the shock wave were again computed by the method of characteristics.

An iterative procedure between the inviscid solution and the boundary-layer displacement thickness was effected by repeating steps (4) to (6) until successive iterations yielded unchanging solutions for both the inviscid flowfield and the boundary-layer. This coupled solution was used for the final analytical predictions for the entire cowl surface of the P2 inlet model and to station X = 42.0 in. (approximate transition location) for the P8 and P12 inlet models. After an assumed discontinuous transition process to a turbulent boundary layer, the coupled solution for the P8 and P12 inlet models was continued using the method of Sasman and Cresci (ref. 16) to compute the turbulent boundary-layer development.

During the development of the technique discussed above, it became evident that the smoothness of the computed cowl static-pressure distribution was highly dependent upon the entropy distribution at the inviscid-viscous interface. The approximate scheme used for the entropy variation in the design analysis always yielded a smooth pressure distribution. When the entropy along the cowl surface was held constant at the stagnation point value, the pressure distribution became very irregular. When an attempt was made to match the entropy by the aforementioned procedure between the input line from the blunt-body solution and the tangent point of the circular cylinder with the straight portion of the cowl contour, a smooth pressure distribution

in this region could not be obtained and discontinuities developed within the flowfield. The occurrence of this problem was attributed to the inability to match the entropy to sufficient accuracy (6-8 significant figures). Consequently, the approximate procedure employed in step (2) was retained for this short segment of the cowl contour. The difference in the entropy at the tangent point obtained by the two procedures was negligible.

The design and final surface-pressure predictions for the upstream portions of the cowl surfaces of the three inlet models are presented and compared to experimental data in figure 90. For the P2 inlet model (fig. 90a) the pressure level for the design analysis approaches the final value monotonically, whereas the distribution for the final analysis exhibits several inflection points. The experimental data for the P2 inlet model, which were obtained at two lateral stations (Z = - 1.0 and -3.19 in.) show that a difference in level of about 5% of the measured value occurred between these lateral stations over the entire length of the cowl surface. Both predicted distributions fall between the experimental levels upstream of about station X = 42.0 in., and exceed the experimental levels downstream of this station. The predicted pressure level for the final analysis depends upon the rate of absorption of the entropy layer, which determines the total pressure at the edge of the boundary layer, and the rate of growth of the boundary-layer displacement thickness. The displacement thickness is always greater for the final analysis as compared to the design predictions (fig. 74), thus the resulting lower static pressure level for the final analysis is attributed to the lower rate of decrease of entropy at the inviscid-viscous interface, which in turn results in a lower total-pressure level at the edge of the boundary layer (fig. 53). The predictions become essentially equivalent at about station X = 45.0 in.

Similar comparisons may be made for the P8 and P12 inlet models, figure 90b and c, respectively. The predicted pressure levels obtained using the final analytical procedure are lower than the design predictions upstream of station X = 39.5 in., exceed the design levels between stations X = 39.5 and 44.5 in., and again fall below the design levels downstream of station X = 44.5 in. (figs. 54 and 64). The agreement between the design analysis and experiment is good upstream of about station X = 40.0 in. for the P8 inlet model (fig. 90b), and good agreement is maintained for a greater distance for the P12 inlet model (fig. 90c). Relatively poorer agreement between the final analysis and experiment was realized over the entire region shown in figures 90b and c. Improvement in the simulation of the boundary-layer growth in the regions

influenced by the cowl leading edge and also subjected to the effects of adverse pressure gradients and boundary-layer transition is evidently required in order to effect better agreement between analysis and experiment. The effective cowl-surface coordinates resulting from the final analysis are given in table 6, parts (b), (c), and (d), respectively, for the P2, P8, and P12 inlet models.

REFERENCES

1. Sanator, R. J., DeCarlo, J. P., Boccio, J. L., and Shannon, J. A., "Development and Evaluation of an Inlet for Scramjet-Powered Hypersonic Cruise Vehicles," AFFDL-TR-68-48, Volumes I, II, and III, April 1968.

2. Polek, T., NASA-Ames Research Center, Private Communication, April 1970.

3. DeCarlo, J. P., Shamshins, D., Seebaugh, W. R., and Doran, R., "Investigation of Hypersonic Flows in Large-Scale Model Internal Passages," Final Report, Contract NAS2-5052, Fairchild Hiller Report No. FHR 3834, November 1969.

4. Torrillo, D. T. and Savage, S. B., "A Brief Review of Compressible Laminar and Turbulent Boundary-Layer Separation," Republic Aviation Report No. 2324, April 1964.

5. Sanator, R. J., Boccio, J. L., and Shamshins, D., "Effect of Bluntness on Hypersonic Two-Dimensional Inlet Type Flows," NASA CR-1145, October 1968.

6. Cavalleri, R., "Description and Instructions for a Method of Characteristics Computer Program for Design and Analysis of Supersonic Inlets," Fairchild Hiller Report No. FHR 3963, June 1970.

7. Clutter, D. and Smith, A. M. O., "Solution of the General Boundary Layer Equations for Compressible Laminar Flow, Including Transverse Curvature," Douglas Aircraft Report LB 31009, February 1963.

8. Kutschenreuter, P. H. Jr., Brown, D. L., Hoelmer, W., et al, "Investigation of Hypersonic Inlet Shock-Wave Boundary-Layer Interaction," AFFDL-TR-65-49, Part II, April 1966.

9. Pinckney, S. Z., "Semiempirical Method for Predicting Effects of Incident - Reflecting Shocks on the Turbulent Boundary Layer," NASA TND-3029, October 1965.

10. Smith, K. G., Gaudet, L., and Winter, U. G., "The Use of Surface Pitot Tubes as Skin-Friction Meters at Supersonic Speeds," GBARC R&M 3351, 1964.

11. Winkler, E. M., "Stagnation Temperature Probes for Use at High Supersonic Speeds and Elevated Temperatures," NAVORD Report 3834, October 1954.

12. Vahl, W. A. and Weirich, R. L., "Calibration of a 30° Included-Angle Cone for Determining Local Flow Conditions in Mach Number Range of 1.51 to 3.51," NASA Report TND-4679, August 1968.

13. Ames Research Staff, "Equations, Tables, and Charts for Compressible Flow," NACA Report 1135, 1953.

14. Hayes, W.D. and Probstein, R.F., Hypersonic Flow Theory, Academic Press, New York, 1959, pp. 333-353.

15. Lubard, S. and Schetz, J.A., "The Numerical Solution of Boundary Layer Problems," Proceedings 1968 Heat Transfer and Fluid Mechanics Institute, Stanford Univ. Press, June 1968, pp. 137-150.

16. Sasman, P.K. and Cresci, R.J., "Compressible Turbulent Boundary Layer with Pressure Gradient and Heat Transfer," AIAA Journal, Vol. 4, No. 1, January 1966, pp. 19-25.

17. Seebaugh, W.R., "Summary of Profile Data Obtained Within Large-Scale Hypersonic Inlet Models," Fairchild Hiller Report No. FHR 4000-1, April 1971.

18. Seebaugh, W.R., and Childs, M.E. "Influence of Suction on Shock Wave-Turbulent Boundary Layer Interactions for Two-Dimensional and Axially Symmetric Flows," NASA CR-1639, September 1970.

19. VanDriest, E.R., "Investigation of Laminar Boundary Layer in Compressible Fluids using the Crocco Method," NACA TN 2597, January 1952.

20. Lomax, H. and Inouye, M., "Numerical Analysis of Flow Properties about Blunt Bodies Moving at Supersonic Speeds in an Equilibrium Gas," NASA TR R-204, July 1964.

Table 1. Effective and Geometric Coordinates for Wedge Forebody.

X, In.	Y_{eff}, In.	Y_{geom}, In.	$(dY/dX)_{eff}$	$(dY/dX)_{geom}$
0	0	0	0.12278	0.11305
.5	.06139	.05653		
1.0	.12278	.11305		
1.5	.18417	.16957		
2.0	.24556	.22609		
2.56	.3143	.2894		
4.2	.5157	.4748		0.11367
8.4	1.0314	.9590		0.11563
12.6	1.5470	1.446		0.11614
16.8	2.0627	1.9347		0.11650
21.0	2.5784	2.4246		0.11675
25.2	3.0941	2.9154		0.11694
29.4	3.6097	3.4069		0.11712
32.0	3.9290	3.7117		0.11725
33.6	4.1254	3.8991		0.11733
37.8	4.6411	4.3918		0.11738
42.0	5.1568	4.8849		0.11742

Table 2. Effective Coordinates for Internal Passages, Design Analysis

(a) P2 Inlet Centerbody

X, In.	ϵ, Deg.	Y, In.
28.0	7.0	3.43784
44.1	7.0	5.41467
44.2	1.3855	5.42202
44.25	1.3375	5.42321
44.31	1.3375	5.42461
44.3187	1.2	5.42480
44.35	1.1	5.42543
46.4181	0.76	5.45900
60.0	2.5	5.84559

Table 2. Continued.

(b) P8 Inlet Centerbody

X, In.	ϵ, Deg.	Y, In.
28.0	7.0	3.43784
44.1	7.0	5.41467
44.2	1.3855	5.42202
44.25	1.3375	5.42321
44.31	1.25	5.42456
44.3187	0.15	5.42467
44.35	-0.1	5.42468
44.375	-0.3	5.42460
44.4	-0.48	5.42443
44.425	-0.6	5.42419
44.45	-0.72	5.42390
44.475	-0.86	5.42356
44.5	-0.95	5.42316
44.55	-1.175	5.42224
44.6	-1.35	5.42113
44.65	-1.53	5.41988
44.7	-1.71	5.41846
44.75	-1.87	5.41690
44.8	-2.03	5.41520
44.85	-2.20	5.41335
44.9	-2.35	5.41136
44.95	-2.5	5.40925
45.0	-2.66	5.40699
45.05	-2.8	5.40461
45.1	-2.95	5.40210
45.2	-3.2	5.39673
45.3	-3.47	5.39090
45.4	-3.7	5.38463
45.5	-3.92	5.37797
45.6	-4.15	5.37092
45.7	-4.34	5.36350
45.8	-4.56	5.35572
45.9	-4.77	5.34755
46.0	-4.97	5.33903
46.1	-5.2	5.33014
46.2	-5.35	5.32090
46.3	-5.59	5.31133
46.4	-5.80	5.30135
46.5	-6.0	5.29102
46.6	-6.2	5.28033
46.8	-6.61	5.25788
47.0	-7.09	5.23386
47.2	-7.5	5.20825
47.4	-7.97	5.18109
47.6	-8.4	5.15232
47.8	-8.9	5.12189
48.0	-9.36	5.08975
48.25	-10.0	5.04711
49.5	-10.0	4.82670
52.0	-10.0	4.38588

Table 2. Continued.

(c) P12 Inlet Centerbody

X, In.	ϵ, Deg.	Y, In.
28.0	7.0	3.43784
44.1	7.0	5.41467
44.2	1.3855	5.42202
44.25	1.3375	5.42321
44.31	1.25	5.42456
44.3188	0.15	5.42467
44.35	-0.1	5.42468
44.375	-0.3	5.42460
44.4	-0.48	5.42443
44.425	-0.6	5.42419
44.45	-0.72	5.42390
44.475	-0.86	5.42356
44.5	-0.95	5.42316
44.55	-1.175	5.42224
44.6	-1.35	5.42113
44.65	-1.53	5.41988
44.7	-1.71	5.41846
44.75	-1.87	5.41690
44.8	-2.03	5.41520
44.85	-2.2	5.41335
44.9	-2.35	5.41136
44.95	-2.5	5.40925
45.0	-2.66	5.40699
45.05	-2.8	5.40461
45.1	-2.95	5.40210
45.2	-3.2	5.39673
45.3	-3.47	5.39090
45.4	-3.7	5.38463
45.5	-3.92	5.37798
45.6	-4.15	5.37092
45.7	-4.34	5.36350
45.8	-4.56	5.35572
45.9	-4.77	5.34756
46.0	-4.97	5.33904
46.1	-5.2	5.33014
46.2	-5.35	5.32090
46.3	-5.59	5.31133
46.4	-5.8	5.30136
46.5	-6.0	5.29102
46.6	-6.2	5.28033
46.8	-6.61	5.25788
47.0	-7.09	5.23386
47.2	-7.5	5.20825
47.4	-7.97	5.18109
47.6	-8.4	5.15232
47.8	-8.9	5.12189
48.0	-9.36	5.08975
48.75	-11.4	4.95233
49.5	-14.0	4.78322
52.0	-14.0	4.15990

Table 2. Continued.

(d) P2 Inlet Cowl

X, In.	ϵ, Deg.	Y, In.
32.0111	-29.9943	7.19718
32.0120	-27.9458	7.19669
32.0126	-26.0636	7.19636
32.0132	-24.3351	7.19607
32.0138	-22.6535	7.19581
32.0146	-20.4380	7.19549
32.0157	-17.6693	7.19513
32.0171	-13.9548	7.19473
32.0188	-9.40777	7.19437
32.0212	-3.38732	7.19411
32.0246	1.0	7.19404
34.25	1.0	7.23288
42.1	2.035	7.44086
60.0	2.035	8.07688

Table 2. Continued.

(e) P8 Inlet Cowl

X, In.	ϵ, Deg.	Y, In.
32.0111	-29.9943	7.19718
32.0120	-27.9458	7.19669
32.0126	-26.6036	7.19636
32.0132	-24.3351	7.19607
32.0138	-22.6535	7.19581
32.0146	-20.4380	7.19549
32.0157	-17.6693	7.19513
32.0171	-13.9548	7.19473
32.0188	-9.40777	7.19437
32.0212	-3.38732	7.19411
32.0246	1.0	7.19404
34.25	1.0	7.23288
34.5	0.7	7.23659
41.8521	-6.095	6.88897
42.0	-6.25	6.87298
42.5	-6.8	6.81579
43.0	-7.3	6.75395
43.5	-7.86	6.68741
44.0	-8.41	6.61594
44.5	-9.02	6.53929
44.75	-9.32	6.49893
45.0	-9.64	6.45719
45.25	-10.0	6.41391
52.0	-10.0	5.22371

Table 2. Concluded.

(f) P12 Inlet Cowl

X, In.	ϵ, Deg.	Y, In.
32.0111	-29.9943	7.19718
32.0120	-27.9458	7.19669
32.0126	-26.0636	7.19636
32.0132	-24.3351	7.19607
32.0138	-22.6535	7.19581
32.0146	-20.4380	7.19549
32.0157	-17.6693	7.19513
32.0171	-13.9548	7.19473
32.0188	-9.40777	7.19437
32.0212	-3.38732	7.19411
32.0246	1.0	7.19404
34.25	1.0	7.23288
34.5	0.7	7.23659
41.8521	-6.095	6.88897
42.0	-6.25	6.87298
42.5	-6.8	6.81579
43.0	-7.3	6.75395
43.5	-7.86	6.68741
44.0	-8.41	6.61594
44.5	-9.02	6.53929
44.75	-9.32	6.49893
45.0	-9.64	6.45719
45.25	-10.0	6.41391
45.5	-10.34	6.36907
45.75	-10.7	6.32264
46.0	-11.09	6.27452
46.25	-11.48	6.22463
46.5	-11.92	6.17286
46.75	-12.4	6.11899
47.0	-12.9	6.06288
47.25	-13.5	6.00424
47.5	-14.0	5.94306
47.75	-14.0	5.88073
48.0	-14.0	5.81840
48.01	-14.0	5.81591
48.0125	-13.8	5.81529
48.013	-14.0	5.81516
48.07	-14.0	5.80095
48.1	-14.15	5.79343
48.15	-14.2	5.70808
48.17	-14.0	5.77578
48.18	-13.8	5.77330
49.7	-13.8	5.39996
52.0	-14.0	4.83076

Table 3. Geometric Coordinates for Internal Passages.

(a) P2 Inlet Centerbody

X, In.	Y_{geom}, In.	dY/dX
36.34375	4.22130	-
43.3975	5.04911	0.11742
44.7725	5.1613	0.023392
47.9300	5.24130	0.023392
48.4800	5.2513	-
48.9550	5.2513	-
49.4600	5.2433	-
49.965	5.2163	-
50.4600	5.1830	-
51.000	5.12130	-

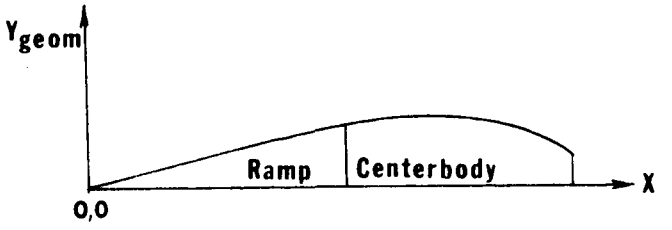

Table 3. Continued.

(b) P8 Inlet Centerbody

X, In.	Y_{geom}, In.	dY/dX
36.34375	4.2213	-
43.3975	5.0491	0.11742
44.7475	5.1588	0.023392
45.7475	5.18219	0.023392
47.5236	5.07359	-
48.1469	4.97879	-
48.5174	4.91474	-
49.0190	4.82517	-
49.5211	4.73518	-
50.0233	4.6454	-
50.5000	4.5567	-
51.000	4.4577	-
51.5000	4.3513	-
52.0000	4.2366	-
52.500	4.1126	-
53.000	3.9788	-
53.624	3.7983	-

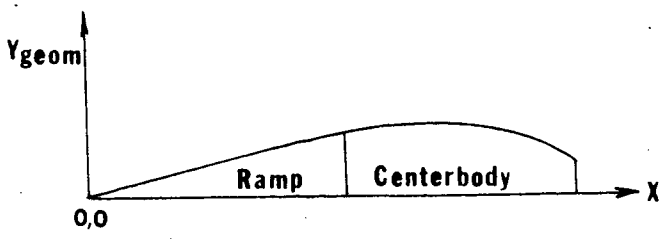

Table 3. Continued.

(c) P12 Inlet Centerbody

X, In.	Y_{geom}, In.	dY/dX
36.34375	4.22130	-
43.3975	5.04911	0.11742
44.7775	5.16130	0.023392
45.7775	5.1847	0.023392
47.5241	5.07302	-
48.1494	4.97819	-
49.0210	4.81320	-
49.2763	4.76118	-
49.50610	4.71192	-
49.6448	4.68019	-
49.8535	4.62771	-
50.0628	4.57546	-
50.6000	4.44067	-
51.0000	4.33754	-
51.5000	4.20369	-
52.0000	4.02650	-
52.5000	3.91204	-
53.000	3.74750	-
53.6240	3.52130	-

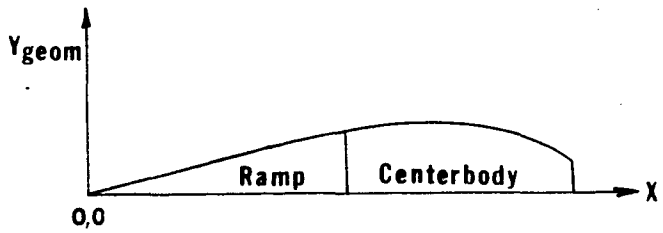

Table 3. Continued.

(d) P2 Inlet Cowl

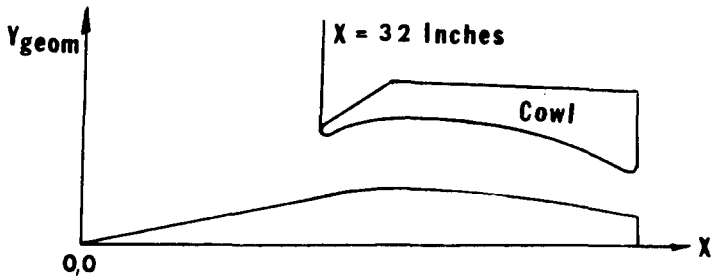

X, In.	Y_{geom}, In.	X, In.	Y_{geom}, In.
32.	7.21656	40.08001	7.39675
32.011	7.19727	41.08993	7.43144
32.01262	7.19647	42.28459	7.47412
32.01386	7.19592	43.19172	7.50772
32.01569	7.19528	44.19371	7.54481
32.01884	7.19458	45.04622	7.57609
32.02458	7.19440	46.10587	7.61436
32.06260	7.19524	46.43918	7.62523
32.07511	7.19565	46.90328	7.64214
32.10012	7.19644	47.36739	7.65886
32.12650	7.19723	51.0	7.910
32.15498	7.19804		
32.18417	7.19883		
32.21677	7.19968		
32.26414	7.20088		
32.32265	7.20239		
32.33634	7.20275		
32.47899	7.20605		
32.76177	7.21261		
32.79807	7.21348		
33.1989	7.22214		
33.63747	7.23120		
34.07282	7.24016		
35.34376	7.26696		
36.10955	7.28481		
37.04974	7.30825		
38.22742	7.34011		
39.03457	7.36281		

Table 3. Continued.

(e) P8 Inlet Cowl

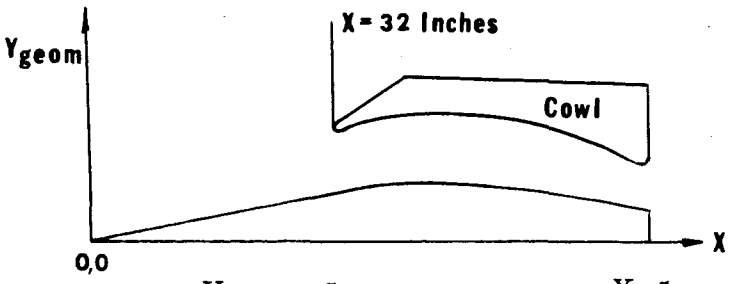

X, In.	Y_{geom}, In.	X, In.	Y_{geom}, In.
32.	7.21656	39.20993	7.12987
32.011	7.19727	40.08112	7.06796
32.01262	7.19647	41.12656	6.97741
32.01386	7.19592	42.15666	6.87073
32.01569	7.19528	43.04127	6.76367
32.01884	7.19458	44.16081	6.60679
32.02458	7.19440	45.16441	6.44276
32.06260	7.19524	45.70070	6.34822
32.07511	7.19565	46.21000	6.25852
32.10012	7.19644	46.67177	6.17722
32.1265	7.19723	47.1002	6.10165
32.15498	7.19804	47.48014	6.03456
32.18417	7.19883	48.24162	5.90086
32.21677	7.19968	48.52829	5.85091
32.26414	7.20088	49.06906	5.75505
32.32265	7.20239	49.5041	5.67446
32.33634	7.20275	53.622	5.110
32.47899	7.20605		
32.76177	7.21261		
32.79807	7.21348		
33.1989	7.22214		
33.63747	7.23120		
34.07282	7.24020		
34.4962	7.24804		
35.31709	7.25393		
36.03146	7.24999		
37.21264	7.22474		
38.31478	7.18044		

Table 3. Concluded.

(f) P12 Inlet Cowl

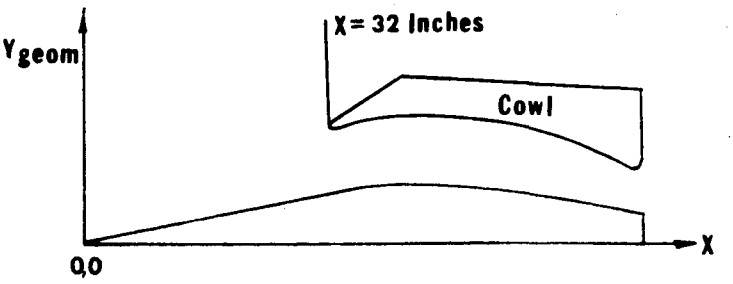

X, In.	Y_{geom}, In.	X, In.	Y_{geom}, In.
32.	7.21656		
32.01109	7.19727	39.20993	7.12987
32.01262	7.19647	40.08112	7.06796
32.01386	7.19592	41.12656	6.97741
32.01569	7.19528	42.15666	6.87073
32.01884	7.19458	43.04127	6.76367
32.02458	7.19440	44.16081	6.60679
32.0626	7.19524	45.16441	6.44345
32.07511	7.19565	46.20122	6.24863
32.10012	7.19644	47.13150	6.04526
32.12650	7.19723	47.54993	5.94367
32.15498	7.19804	47.9706	5.83766
32.18418	7.19883	48.11090	5.8021
32.21677	7.19968	48.4965	5.70662
32.26414	7.20088	49.0257	5.57674
32.32265	7.20239	49.5651	5.44441
32.33634	7.20275	49.9425	5.35183
32.47899	7.20605	50.2061	5.28605
32.76177	7.21261	53.622	4.730
32.79807	7.21348		
33.19890	7.22214		
33.63747	7.23120		
34.07282	7.24020		
34.49620	7.24804		
35.31709	7.25393		
36.03146	7.24999		
37.21264	7.22474		
38.31478	7.18044		

Table 4. Surface Instrumentation Locations for Inlet Models.

(a) Basic Wedge

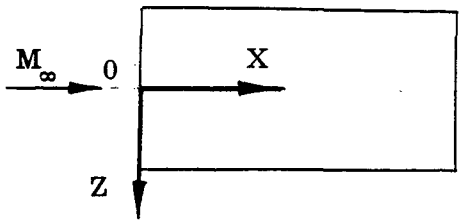

(28) Pressure Transducers

X, In.	Z, In.
32.0	+5.56
32.25	+5.38
31.75	+3.92
32.25	+3.92
31.75	+2.46
32.25	+2.46
31.75	+1.0
32.25	+1.0
1.5	0
4.0	0
6.0	0
8.0	0
10.0	0
14.0	0
18.0	0
22.0	0
25.0	0
28.0	0
31.75	0
32.25	0
31.75	-1.0
32.25	-1.0
31.75	-3.19
32.25	-3.19
31.75	-4.65
32.25	-4.65
32.25	-5.38
32.0	-5.56

(18) Thermocouples

X, In.	Z, In.
32.0	+5.38
32.0	+1.0
3.0	- .5
5.0	- .5
7.0	- .5
9.0	- .5
12.0	- .5
16.0	- .5
20.0	- .5
24.0	- .5
30.0	- .5
32.0	- .5
32.0	-3.19
32.0	-5.38

Table 4. Continued.

(b) P2 Inlet Centerbody

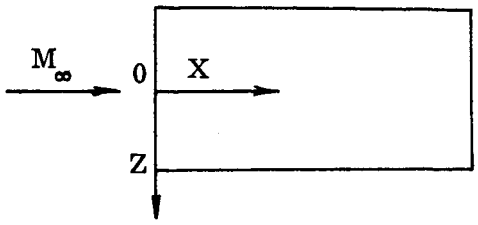

(53) Pressure Transducers				(23)Heat Transfer Gages		(14) Thermocouples	
X, In.	Z, In.	X, In.	Z, In.	X, In.	Z, In.	X, In.	Z, In.
45.9	+5.38	38.0	-2.095	44.16	+4.65	46.48	+5.38
47.0	+5.38	39.0	-2.095	45.32	+4.65	46.48	+3.92
39.0	+5.26	40.0	-2.095	47.0	+4.65	46.48	+2.46
43.0	+5.26	41.0	-2.095	44.16	+3.19	40.0	0
43.0	+3.92	42.0	-2.095	45.32	+3.19	42.0	0
45.9	+3.92	42.5	-2.095	47.0	+3.19	43.4	0
47.0	+3.92	43.15	-2.095	45.32	+ .5	44.45	0
43.0	+2.46	43.44	-2.095	47.0	+ .5	45.03	0
43.29	+2.46	43.73	-2.095	39.0	0	45.61	0
43.58	+2.46	44.02	-2.095	41.0	0	46.48	-1.0
43.87	+2.46	44.31	-2.095	43.0	0	46.48	-3.19
44.16	+2.46	45.5	-2.095	43.75	0	46.48	-4.65
44.45	+2.46	46.5	-2.095	44.75	0	46.48	-5.38
45.9	+2.46	43.0	-3.19	45.9	0		
47.0	+2.46	43.5	-3.19	45.3	- .5		
44.74	+1.0	44.5	-3.19	46.4	- .5		
45.32	+1.0	45.9	-3.19	47.0	- .5		
45.90	+1.0	47.0	-3.19	44.9	-2.095		
46.48	+1.0	43.0	-4.65	46.1	-2.095		
47.0	+1.0	45.9	-4.65	47.0	-2.095		
37.1	0	47.0	-4.65	44.16	-5.015		
46.48	0	39.0	-5.26	45.3	-5.015		
47.0	0	43.0	-5.26	47.0	-5.015		
44.6	-1.0	45.9	-5.38				
45.03	-1.0	47.0	-5.38				
45.61	-1.0						
46.0	-1.0						
47.0	-1.0						

Table 4. Continued

(c) P8 Inlet Centerbody

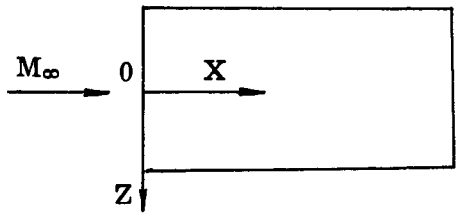

(60) Pressure Transducers				(23) Heat Transfer Gages		(14) Thermocouples	
X, In.	Z, In.	X, In.	Z, In.	X, In.	Z, In.	X, In.	Z, In.
43.0	+5.38	44.75	-1.0	45.0	+4.65	49.0	+5.38
48.0	+5.38	45.25	-1.0	47.0	+4.65	49.0	+3.92
49.5	+5.38	45.75	-1.0	49.5	+4.65	49.0	+2.46
39.0	+5.26	46.5	-1.0	45.0	+3.19	38.0	0
43.0	+3.92	47.5	-1.0	47.0	+3.19	40.0	0
48.0	+3.92	48.5	-1.0	49.5	+3.19	42.0	0
49.5	+3.92	49.5	-1.0	49.5	+ .5	44.0	0
41.5	+2.46	38.0	-2.095	39.0	0	45.5	0
42.0	+2.46	39.0	-2.095	41.0	0	46.5	0
42.5	+2.46	40.0	-2.095	43.0	0	47.5	0
43.0	+2.46	41.75	-2.095	43.6	0	49.0	-1.0
43.5	+2.46	42.25	-2.095	44.3	0	49.0	-3.19
44.0	+2.46	42.75	-2.095	45.0	0	49.0	-4.65
48.0	+2.46	43.25	-2.095	46.0	0	49.0	-5.38
49.5	+2.46	43.75	-2.095	47.0	0		
44.5	+1.0	44.25	-2.095	48.0	0		
45.0	+1.0	42.0	-3.19	49.5	- .5		
45.5	+1.0	42.5	-3.19	45.0	-2.095		
46.0	+1.0	43.0	-3.19	47.0	-2.095		
47.0	+1.0	43.5	-3.19	49.5	-2.095		
48.0	+1.0	44.0	-3.19	45.0	-5.015		
49.0	+1.0	44.5	-3.19	47.0	-5.015		
49.5	+1.0	45.0	-3.19	49.5	-5.015		
37.12	0	45.5	-3.19				
49.0	0	46.0	-3.19				
49.5	0	48.0	-3.19				
		49.5	-3.19				
		43.0	-4.65				
		48.0	-4.65				
		49.5	-4.65				
		39.0	-5.26				
		43.62	-5.38				
		48.0	-5.38				
		49.5	-5.38				

Table 4. Continued

(d) P12 Inlet Centerbody

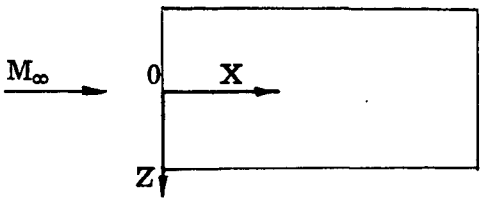

(48) Pressure Transducers				(23) Heat Transfer Gages		(14) Thermocouples	
X, In.	Z, In.	X, In.	Z, In.	X, In.	Z, In.	X, In.	Z, In.
43.0	+5.38	44.75	-1.0	45.0	+4.65	49.0	+5.38
48.0	+5.38	45.25	-1.0	47.0	+4.65	49.0	+3.92
49.9	+5.38	45.75	-1.0	49.9	+4.65	49.0	+2.46
39.0	+5.26	46.5	-1.0	45.0	+3.19	38.0	0
43.0	+3.92	47.5	-1.0	47.0	+3.19	40.0	0
48.0	+3.92	48.5	-1.0	49.9	+3.19	42.0	0
49.9	+3.92	49.9	-1.0	49.9	+ .5	44.0	0
41.5	+2.46	41.75	-2.095	39.0	0	45.5	0
42.0	+2.46	42.25	-2.095	41.0	0	46.5	0
42.5	+2.46	42.75	-2.095	43.0	0	47.5	0
43.0	+2.46	43.25	-2.095	43.6	0	49.0	-1.0
43.5	+2.46	43.75	-2.095	44.3	0	49.0	-3.19
44.0	+2.46	44.25	-2.095	45.0	0	49.0	-4.65
48.0	+2.46	48.0	-3.19	46.0	0	49.0	-5.38
49.9	+2.46	49.9	-3.19	47.0	0		
44.5	+1.0	43.0	-4.65	48.0	0		
45.0	+1.0	48.0	-4.65	49.9	- .5		
45.5	+1.0	49.9	-4.65	45.0	-2.095		
46.0	+1.0	39.0	-5.26	47.0	-2.095		
47.0	+1.0	43.62	-5.38	49.9	-2.095		
48.0	+1.0	48.0	-5.38	45.0	-5.015		
49.0	+1.0	49.9	-5.38	47.0	-5.015		
49.9	+1.0			49.9	-5.015		
37.12	0						
49.0	0						
49.9	0						

Table 4. Continued.

(e) P2 Inlet Cowl

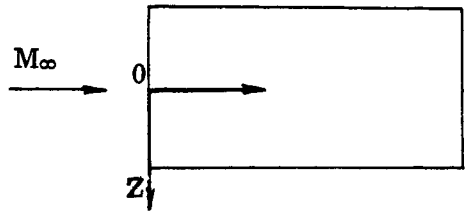

(66) Pressure Transducers				(27) Heat Transfer Gages		(16) Thermocouples	
X, In.	Z, In.	X, In.	Z, In.	X, In.	Z, In.	X, In.	Z, In.
34.38	+5.38	32.8	-1.0	35.85	+4.65	35.68	+5.38
45.4	+5.38	36.19	-1.0	39.55	+4.65	46.48	+5.38
47.04	+5.38	37.02	-1.0	47.04	+4.65	38.84	+5.26
37.86	+5.26	39.54	-1.0	35.85	+3.19	42.05	+5.26
41.25	+5.26	40.37	-1.0	39.55	+3.19	46.48	+3.92
34.38	+3.92	32.9	-1.0	47.04	+3.19	46.48	+2.46
37.86	+3.92	33.72	-1.0	35.85	+1.73	36.2	0
41.25	+3.92	34.9	-1.0	39.55	+1.73	37.4	0
45.4	+3.92	36.0	-1.0	47.04	+1.73	38.82	0
47.04	+3.92	37.04	-1.0	47.04	+ .5	40.33	0
34.38	+2.46	38.0	-1.0	35.25	0	42.05	0
37.86	+2.46	39.0	-1.0	36.85	0	44.74	0
41.25	+2.46	40.0	-1.0	37.86	0	46.48	-1.0
45.4	+2.46	41.0	-1.0	39.55	0	46.48	-3.19
47.04	+2.46	42.0	-1.0	41.25	0	46.48	-4.65
34.38	+1.0	45.5	-1.0	43.0	0	46.48	-5.38
35.68	+1.0	34.38	-3.19	45.4	0		
37.86	+1.0	37.86	-3.19	47.04	+ .5		
38.84	+1.0	41.25	-3.19	35.85	-2.095		
41.25	+1.0	42.5	-3.19	39.55	-2.095		
42.05	+1.0	43.0	-3.19	47.04	-2.095		
44.2	+1.0	43.5	-3.19	35.85	-3.92		
45.4	+1.0	44.0	-3.19	39.55	-3.92		
46.48	+1.0	44.5	-3.19	47.04	-3.92		
47.04	+1.0	45.0	-3.19	35.85	-5.015		
33.68	0	45.4	-3.19	39.55	-5.015		
46.48	0	47.04	-3.19	47.04	-5.015		
47.04	0	46.5	-3.39				
		34.38	-4.65				
		37.86	-4.65				
		41.25	-4.65				
		45.4	-4.65				
		47.04	-4.65				
		37.86	-5.26				
		41.25	-5.26				
		34.38	-5.38				
		45.4	-5.38				
		47.04	-5.38				

Table 4. Continued.

(f) P8 Inlet Cowl

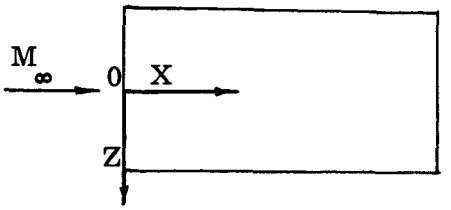

(69) Pressure Transducers				(27) Heat Transfer Gages		(16) Thermocouples	
X, In.	Z, In.	X, In.	Z, In.	X, In.	Z, In.	X, In.	Z, In.
35.8	+5.38	32.75	-1.0	35.8	+4.65	36.0	+5.38
44.0	+5.38	37.0	-1.0	41.0	+4.65	46.0	+5.38
48.0	+5.38	38.0	-1.0	49.66	+4.65	49.0	+5.38
49.66	+5.38	39.6	-1.0	35.8	+3.19	40.0	+5.26
39.0	+5.26	41.0	-1.0	41.0	+3.19	49.0	+3.92
35.8	+3.92	42.0	-1.0	49.66	+3.19	49.0	+2.46
39.0	+3.92	43.55	-1.0	35.8	+1.73	36.32	0
43.0	+3.92	44.55	-1.0	41.0	+1.73	38.0	0
48.0	+3.92	45.0	-1.0	49.66	+1.73	40.0	0
49.66	+3.92	46.0	-1.0	49.66	+ .5	42.0	0
35.8	+2.46	47.0	-1.0	36.0	0	44.0	0
39.0	+2.46	48.5	-1.0	37.0	0	46.0	0
43.0	+2.46	49.66	-1.0	39.0	0	49.0	-1.0
48.0	+2.46	35.8	-3.19	41.0	0	49.0	-3.19
49.66	+2.46	39.0	-3.19	43.0	0	49.0	-4.65
35.8	+1.0	40.0	-3.19	45.0	0	49.0	-5.38
37.45	+1.0	41.0	-3.19	48.0	0		
39.0	+1.0	42.0	-3.19	49.66	- .5		
40.0	+1.0	43.5	-3.19	35.8	-2.095		
41.52	+1.0	44.0	-3.19	41.0	-2.095		
43.0	+1.0	44.5	-3.19	49.66	-2.095		
44.0	+1.0	45.5	-3.19	35.8	-3.92		
45.5	+1.0	46.5	-3.19	41.0	-3.92		
46.5	+1.0	47.5	-3.19	49.66	-3.92		
47.5	+1.0	48.0	-3.19	35.8	-5.015		
48.0	+1.0	49.5	-3.19	41.0	-5.015		
49.0	+1.0	49.66	-3.19	49.66	-5.015		
49.66	+1.0	49.0	-3.39				
33.5	0	35.8	-4.65				
49.5	0	39.0	-4.65				
49.66	0	41.0	-4.65				
		48.0	-4.65				
		49.66	-4.65				
		39.0	-5.26				
		35.8	-5.38				
		41.62	-5.38				
		48.0	-5.38				
		49.66	-5.38				

Table 4. Concluded.

(g) P12 Inlet Cowl

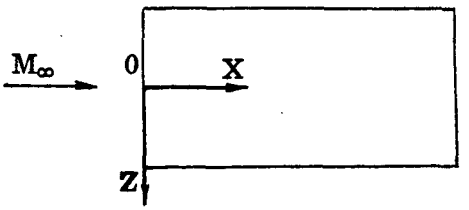

(59) Pressure Transducers				(27) Heat Transfer Gages		(16) Thermocouples	
X, In.	Z, In.	X, In.	Z, In.	X, In.	Z, In.	X, In.	Z, In.
35.8	+5.38	32.75	-1.0	35.8	+4.65	36.0	+5.38
44.0	+5.38	37.0	-1.0	41.0	+4.65	46.0	+5.38
48.0	+5.38	38.0	-1.0	50.08	+4.65	49.0	+5.38
50.08	+5.38	39.6	-1.0	35.8	+3.19	40.0	+5.26
39.0	+5.26	41.0	-1.0	41.0	+3.19	49.0	+3.92
35.8	+3.92	42.0	-1.0	50.08	+3.19	49.0	+2.46
39.0	+3.92	43.55	-1.0	35.8	+1.73	36.32	0
43.0	+3.92	44.55	-1.0	41.0	+1.73	38.0	0
48.0	+3.92	45.0	-1.0	50.08	+1.73	40.0	0
50.08	+3.92	46.0	-1.0	50.08	+ .5	42.0	0
35.8	+2.46	47.0	-1.0	36.0	0	44.0	0
39.0	+2.46	48.5	-1.0	37.0	0	46.0	0
43.0	+2.46	50.08	-1.0	39.0	0	49.0	-1.0
48.0	+2.46	35.8	-3.19	41.0	0	49.0	-3.19
50.08	+2.46	39.0	-3.19	43.0	0	49.0	-4.65
35.8	+1.0	41.0	-3.19	45.0	0	49.0	-5.38
37.45	+1.0	48.0	-3.19	48.0	0		
39.0	+1.0	50.08	-3.19	50.08	- .5		
40.0	+1.0	35.8	-4.65	35.8	-2.095		
41.52	+1.0	39.0	-4.65	41.0	-2.095		
43.0	+1.0	41.0	-4.65	50.08	-2.095		
44.0	+1.0	48.0	-4.65	35.8	-3.92		
45.5	+1.0	50.08	-4.65	41.0	-3.92		
46.5	+1.0	39.0	-5.26	50.08	-3.92		
47.5	+1.0	35.8	-5.38	35.8	-5.015		
48.0	+1.0	43.62	-5.38	41.0	-5.015		
49.0	+1.0	48.0	-5.38	50.08	-5.015		
50.08	+1.0	50.08	-5.38				
33.5	0						
49.5	0						
50.08	0						

Table 5. Heat-Transfer and Skin-Friction Data.

P2 Inlet Model Cowl

Station X = 47.0 In.

		τ_w, lb/ft^2	$\dot{q}$, BTU/sec-ft^2
Analysis:	Laminar	0.32	0.36
	Turbulent	2.89	5.80
Experiment		0.45 - 0.50	0.73 - 0.76

P8 Inlet Model Cowl

Station X = 47.25 In.

		τ_w, lb/ft^2	$\dot{q}$, BTU/sec-ft^2
Analysis:	Laminar	0.32	0.83
	Turbulent	9.54	20.1
Experiment		4.62	9.3

3

Table 6. Effective Coordinates for Wedge Forebody and Cowl Surfaces, Final Analysis.

(a) Wedge Forebody

X, In.	ϵ, Deg.	Y, In.
0.1	7.9500	0.016585
0.2	7.5147	0.030163
0.4	7.2028	0.055992
0.6	7.0629	0.081020
0.8	6.9805	0.105654
1.0	6.9260	0.130045
1.2	6.8875	0.154272
1.6	6.8260	0.202371
1.8	6.8050	0.226274
2.0	6.7900	0.250114
3.0	6.7570	0.368888
4.0	6.7240	0.487078
5.0	6.7410	0.605126
6.0	6.7500	0.723404
7.0	6.7540	0.841797
8.0	6.7540	0.960226
9.0	6.7540	1.078650
10.0	6.7540	1.197080
12.0	6.7540	1.433940
14.0	6.7540	1.670800
16.0	6.7540	1.907650
16.8	6.7540	2.002400
21.0	7.0300	2.510060
25.2	7.0900	3.030220
28.0	7.15000	3.379998
29.0	7.15177	3.505456
30.0	7.15369	3.630947
31.0	7.15578	3.756474
32.0	7.15807	3.882039
33.0	7.16061	4.007647
34.0	7.16343	4.133303
35.0	7.16660	4.259011
36.0	7.17019	4.384780
37.0	7.17432	4.510616
38.0	7.17913	4.636532
39.0	7.18486	4.762540
40.0	7.19183	4.888661
41.0	7.20057	5.014920
42.0	7.21204	5.141356
43.0	7.22803	5.268032

Table 6. Continued.

(b) P2 Inlet Cowl

X, In.	ϵ, Deg.	Y, In.
32.00225	-64.15807	7.206758
32.00450	-53.13011	7.203066
32.00675	-44.42701	7.200498
32.00900	-36.86991	7.198566
32.01125	-30.00001	7.197080
32.01350	-23.57819	7.195944
32.01575	-17.45762	7.195102
32.01800	-11.53698	7.194521
32.02025	- 5.73919	7.194179
32.02250	- 0.00002	7.194066
33.0	0.13371	7.195143
34.0	0.32445	7.199051
35.0	0.58381	7.206870
36.0	0.91300	7.219842
37.0	1.28534	7.239000
38.0	1.64941	7.264668
39.0	1.95899	7.296268
40.0	2.19673	7.332654
41.0	2.36941	7.372606
42.0	2.38070	7.414773
43.0	2.19801	7.454697
44.0	2.04786	7.491725
45.0	1.92321	7.526360
46.0	1.81874	7.559000
47.0	1.73042	7.589961
48.0	1.65515	7.619497
49.0	1.59053	7.647815
50.0	1.53467	7.675082
51.0	1.48609	7.701440

Table 6. Continued.

(c) P8 Inlet Cowl

X, In.	ϵ, Deg.	Y, In.
32.00225	-64.15807	7.206758
32.00450	-53.13011	7.203066
32.00675	-44.42701	7.200498
32.00900	-36.86991	7.198566
32.01125	-30.00001	7.197080
32.01350	-23.57819	7.195944
32.01575	-17.45762	7.195102
32.01800	-11.53698	7.194521
32.02025	- 5.73919	7.194179
32.02250	- 0.00002	7.194066
33.0	0.13371	7.195143
34.0	0.32463	7.199051
35.0	0.58309	7.206870
36.0	0.00000	7.210000
37.0	- 0.95195	7.201997
38.0	- 2.10462	7.175585
39.0	- 3.40271	7.127628
40.0	- 4.73612	7.056437
41.0	- 5.97914	6.962438
42.0	- 7.20472	6.823004
43.0	- 7.85465	6.717253
44.0	- 8.61921	6.572355
45.0	- 9.26491	6.414798
46.0	- 9.76914	6.246941
47.0	-10.14602	6.071205
48.0	-10.42304	5.889624

Table 6. Concluded.

(d) P12 Inlet Cowl

X, In.	ϵ, Deg.	Y, In.
32.00225	-64.15807	7.206758
32.00450	-53.13011	7.203066
32.00675	-44.42701	7.200498
32.00900	-36.86991	7.198566
32.01125	-30.00001	7.197080
32.01350	-23.57819	7.195944
32.01575	-17.45762	7.195102
32.01800	-11.53698	7.194521
32.02025	- 5.73919	7.194179
32.02250	- 0.00002	7.194066
33.0	0.13371	7.195143
34.0	0.32463	7.199051
35.0	0.58309	7.206870
36.0	0.00000	7.210000
37.0	- 0.95195	7.201997
38.0	- 2.10462	7.175585
39.0	- 3.40271	7.127628
40.0	- 4.73612	7.056437
41.0	- 5.97914	6.962438
42.0	- 7.20472	6.823004
43.0	- 7.85465	6.717253
44.0	- 8.61921	6.572355
45.0	- 9.26491	6.414798
46.0	- 9.76914	6.246941
47.0	-12.66271	6.045754
48.0	-14.26508	5.805033

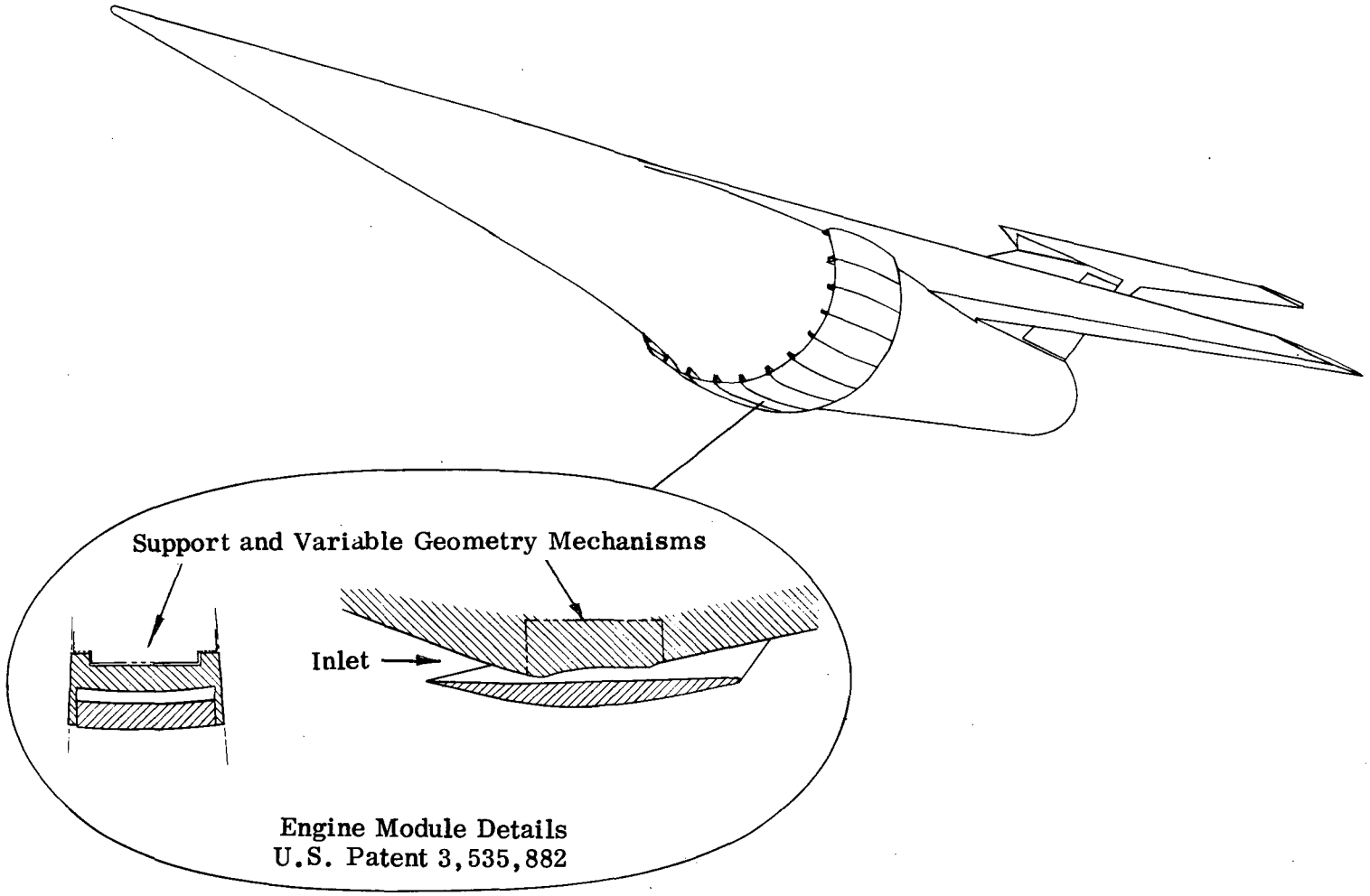

Figure 1. Hypersonic Cruise Vehicle for Mach 10 to 12 Range.

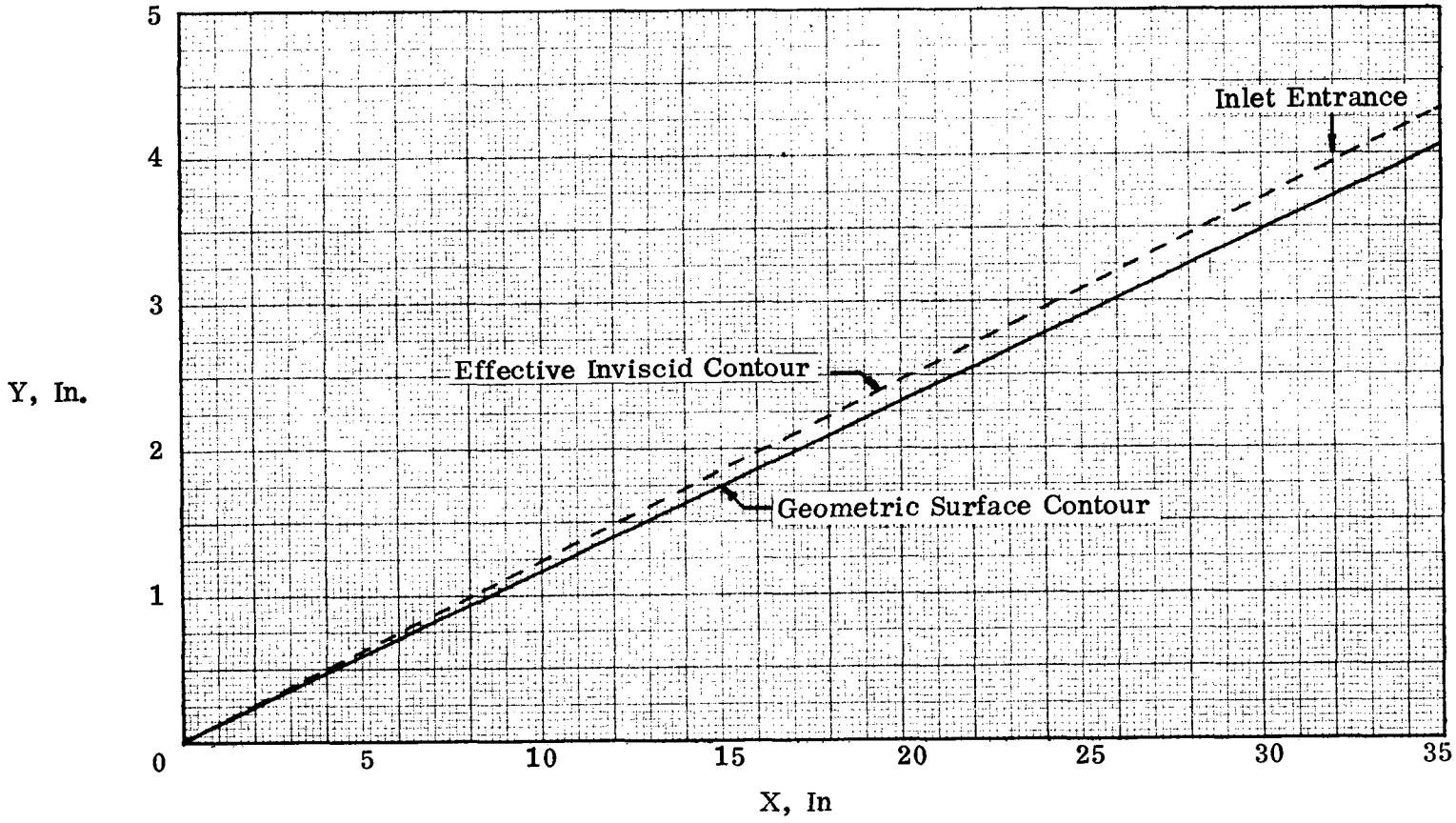

Figure 2. Effective and Geometric Coordinates for Wedge Forebody

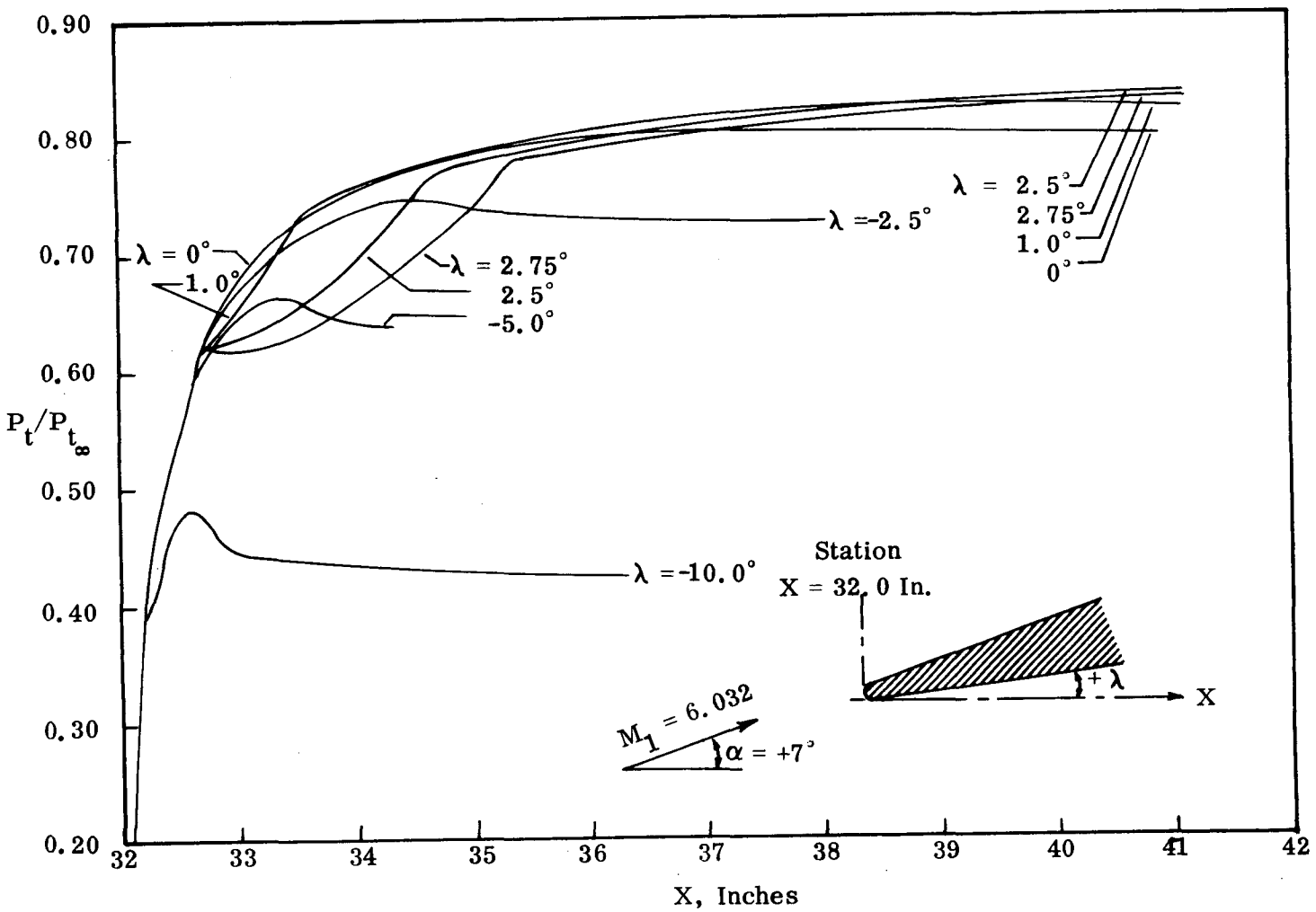

Figure 3. Total Pressure Recovery of Wedge-Forebody and Cowl Shock Waves.

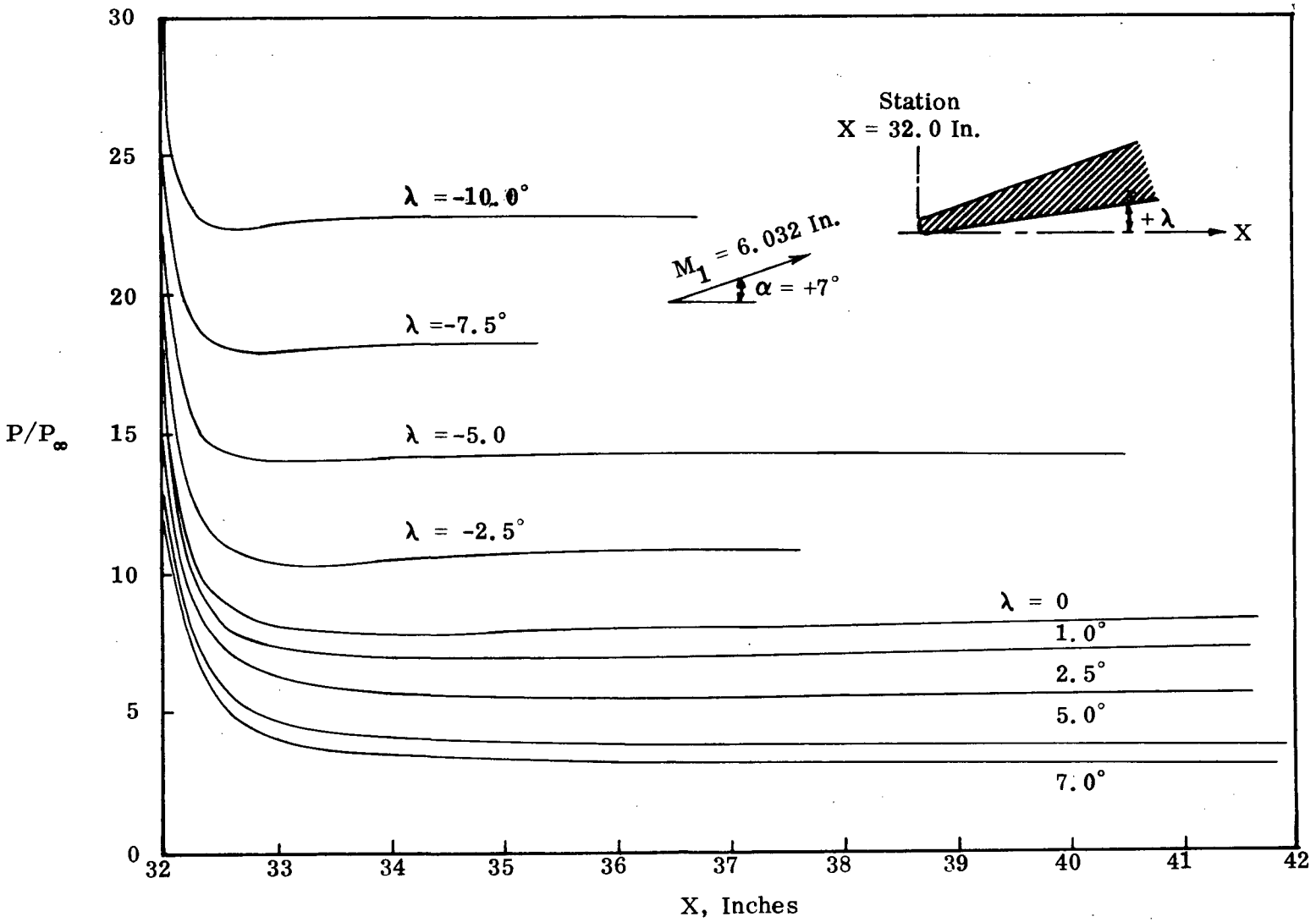

Figure 4. Surface Static-Pressure Distributions for Blunt Leading Edge.

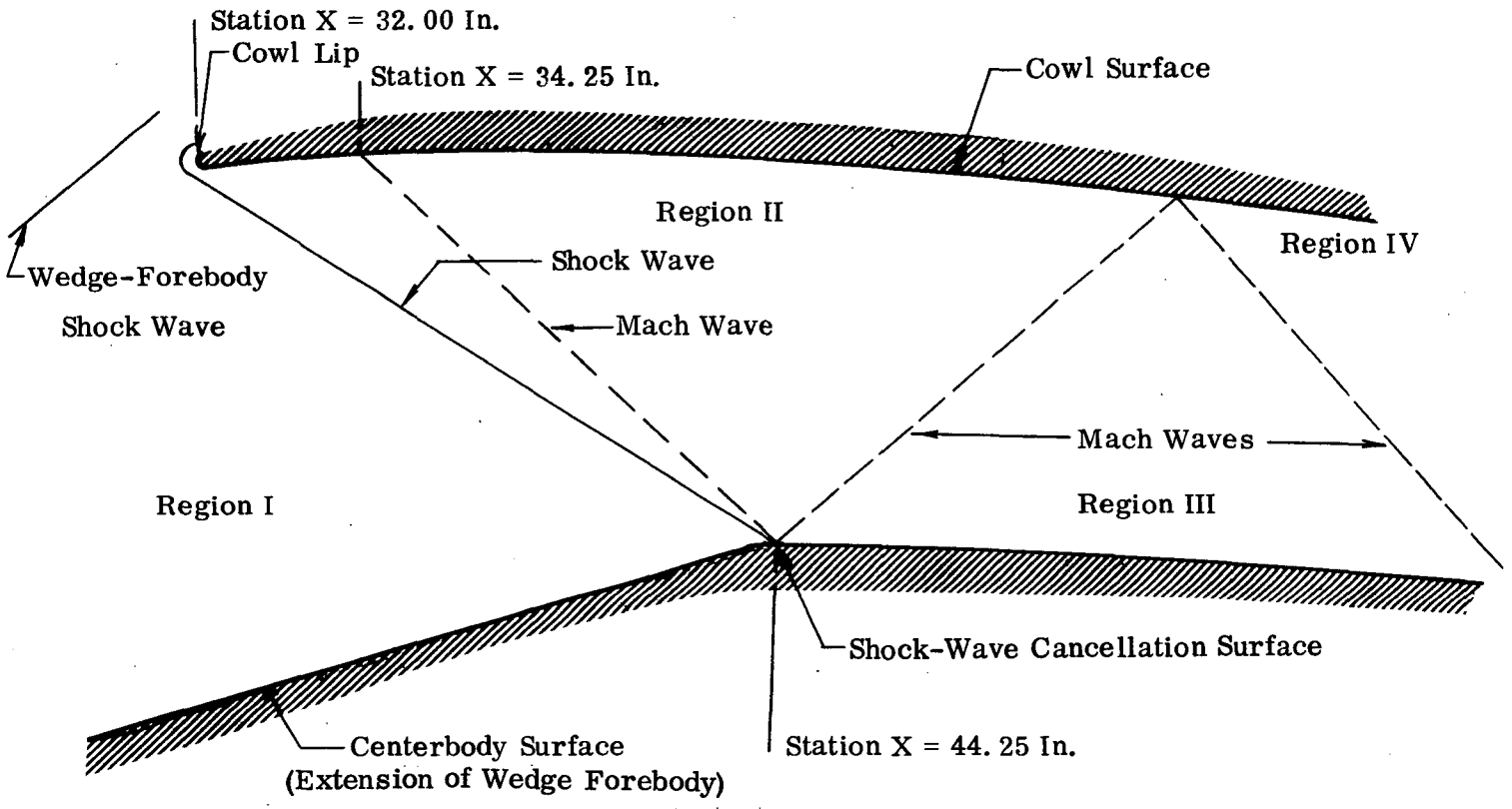

Figure 5. Region Specification for Internal Contour Design.

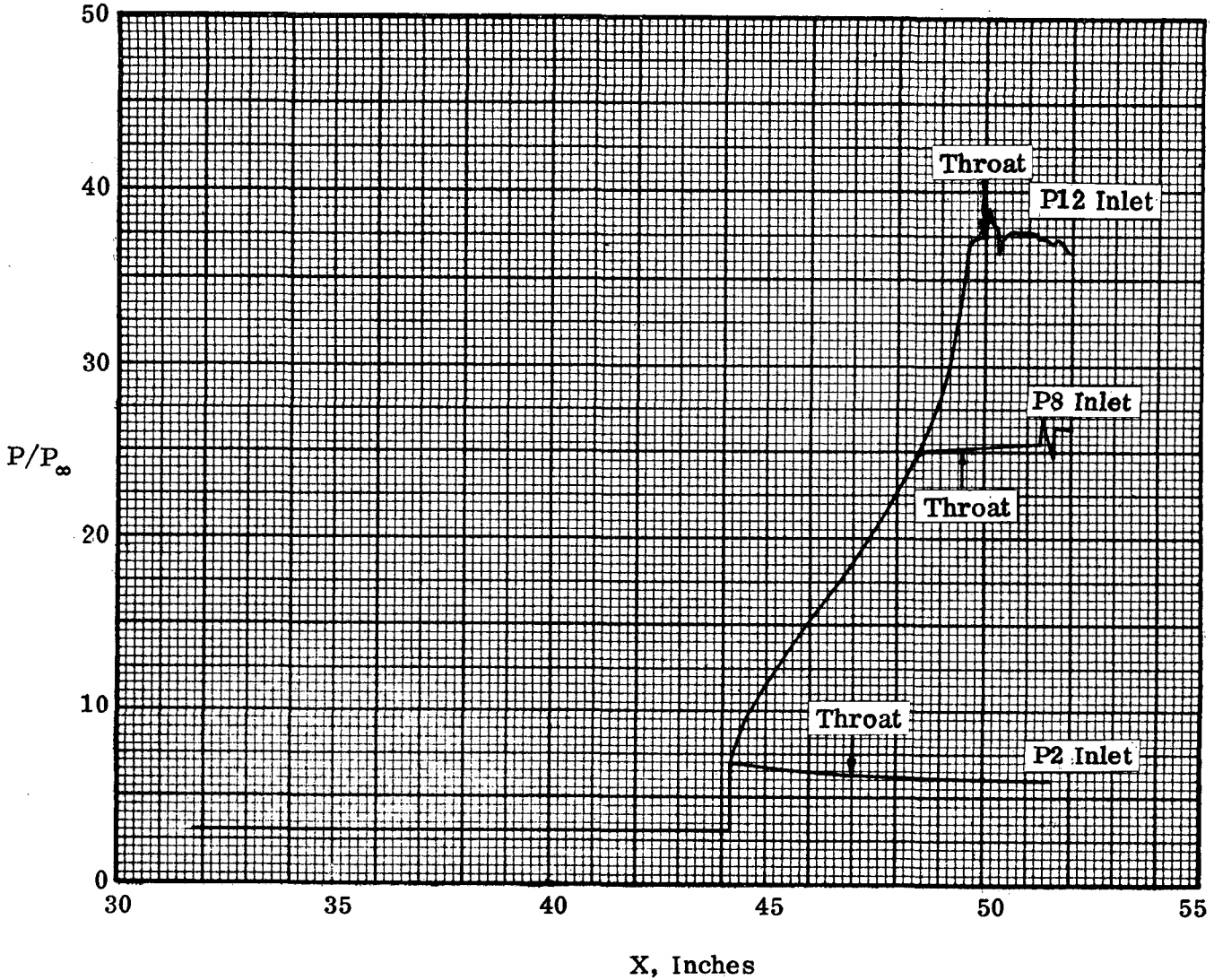

Figure 6. Predicted Surface Static-Pressure Distributions, Inlet Centerbodies.

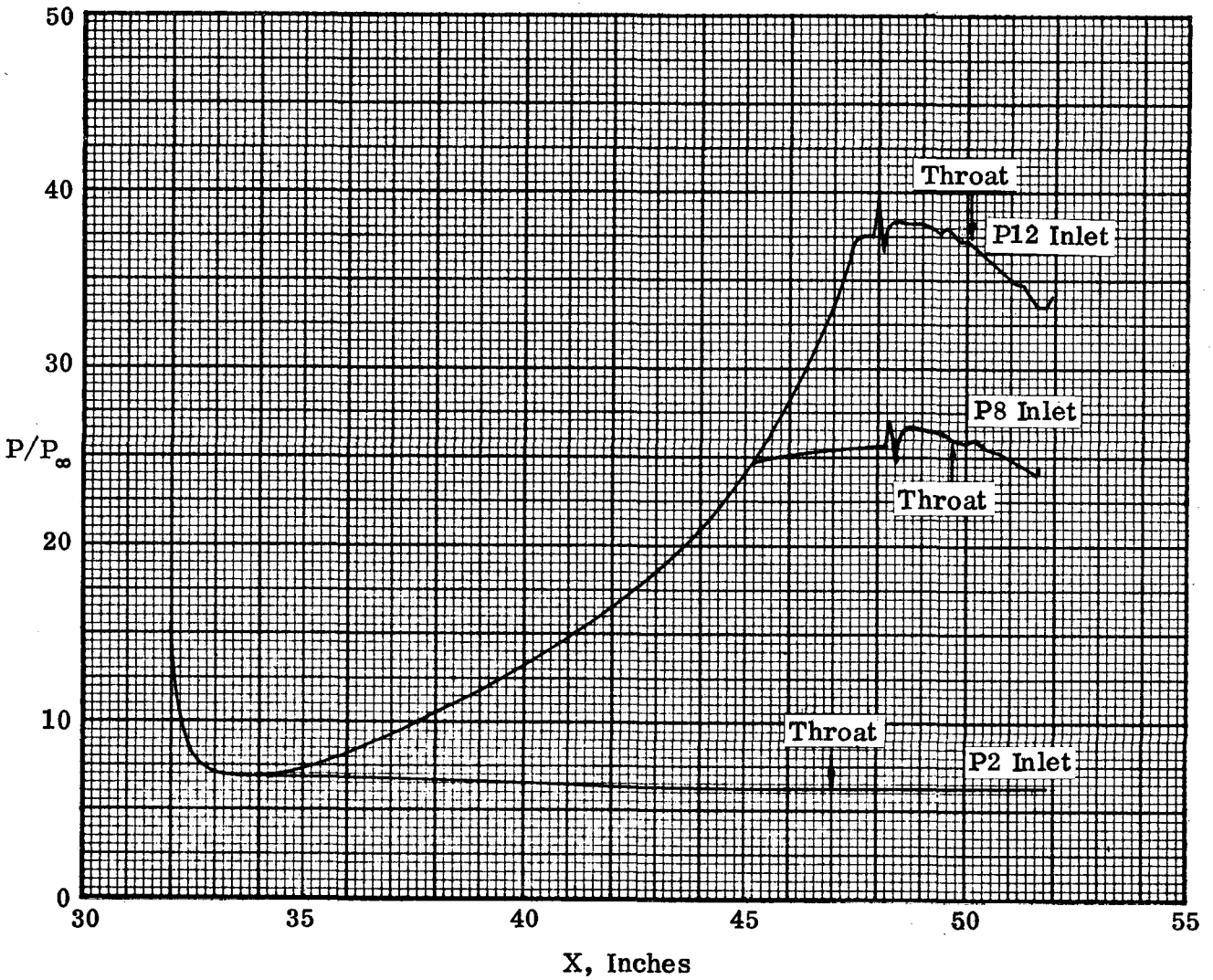

Figure 7. Predicted Surface Static-Pressure Distributions, Inlet Cowls.

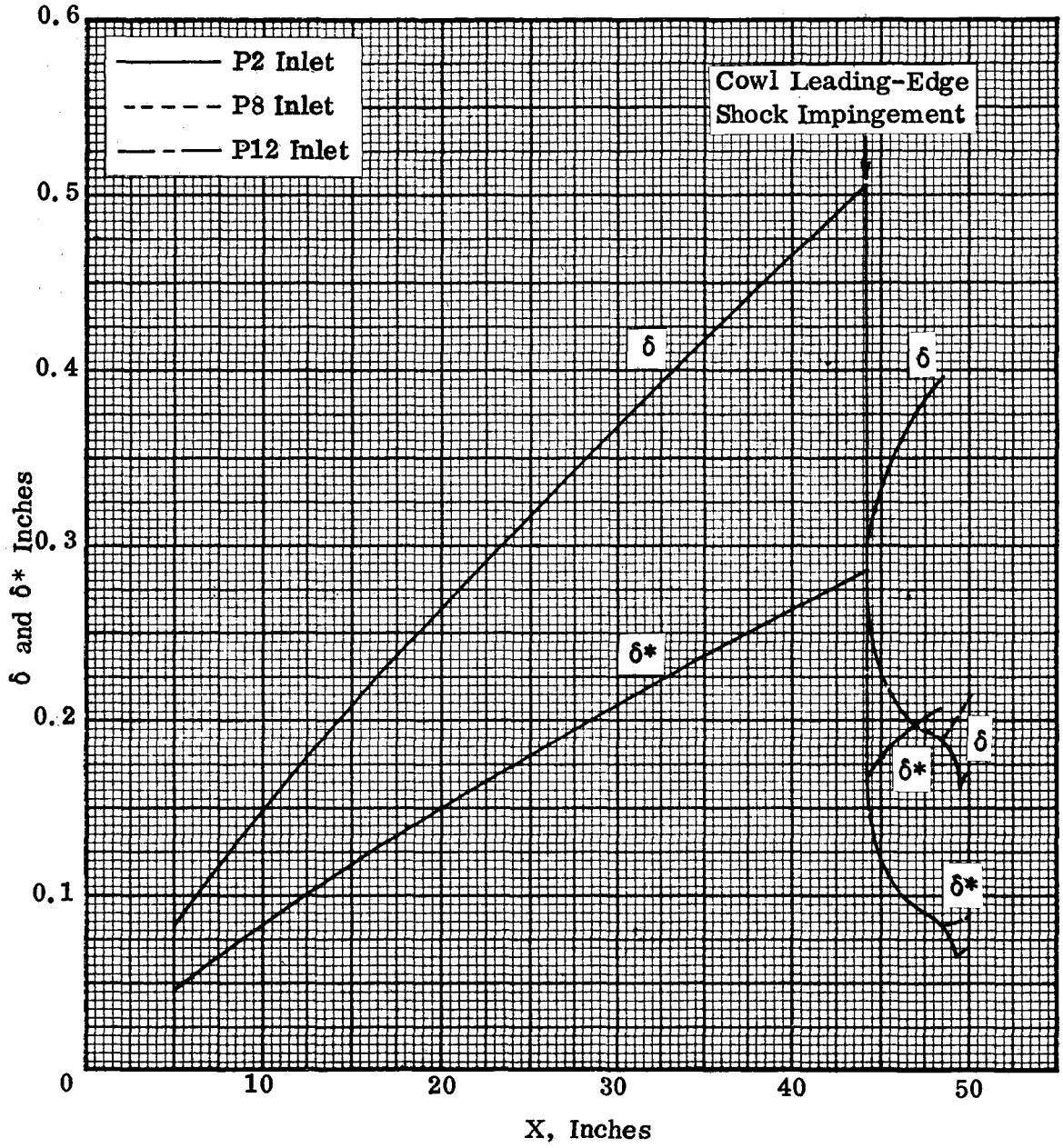

(a) Wedge Forebody

Figure 8. Wedge-Forebody and Centerbody Boundary-Layer Thickness Distributions.

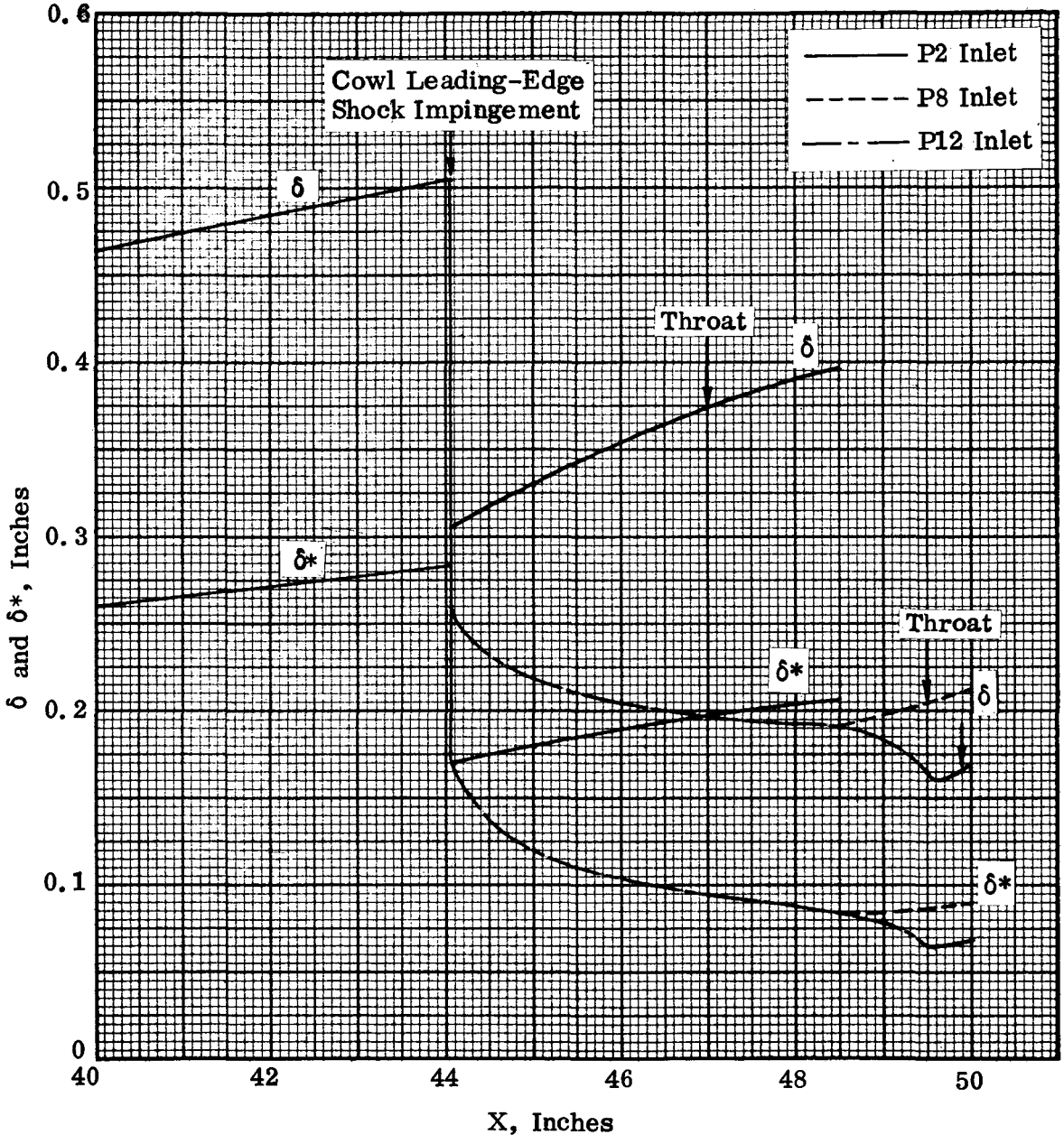

(b) Centerbodies

Figure 8. Concluded.

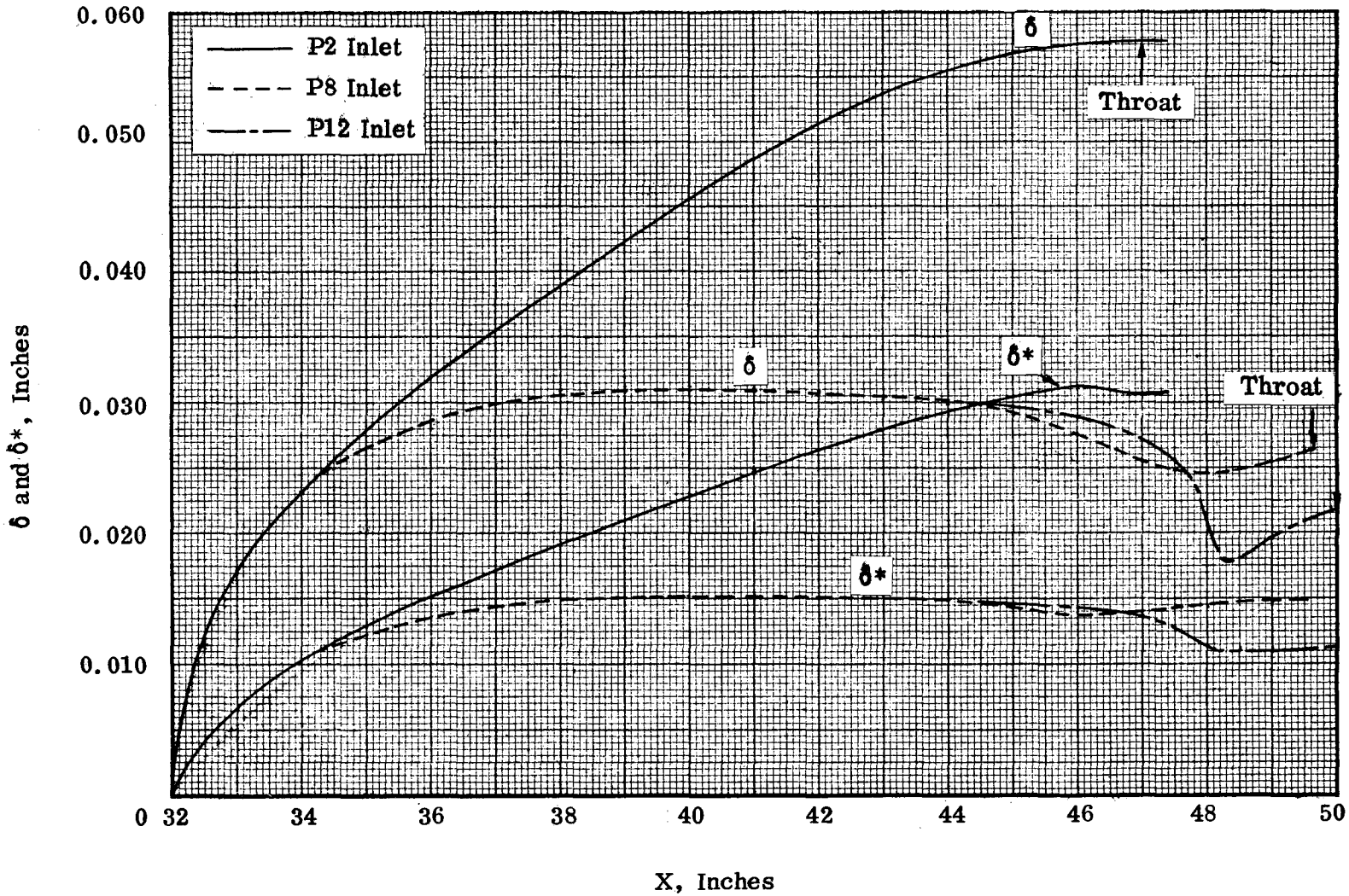

Figure 9. Cowl Boundary-Layer Thickness Distributions.

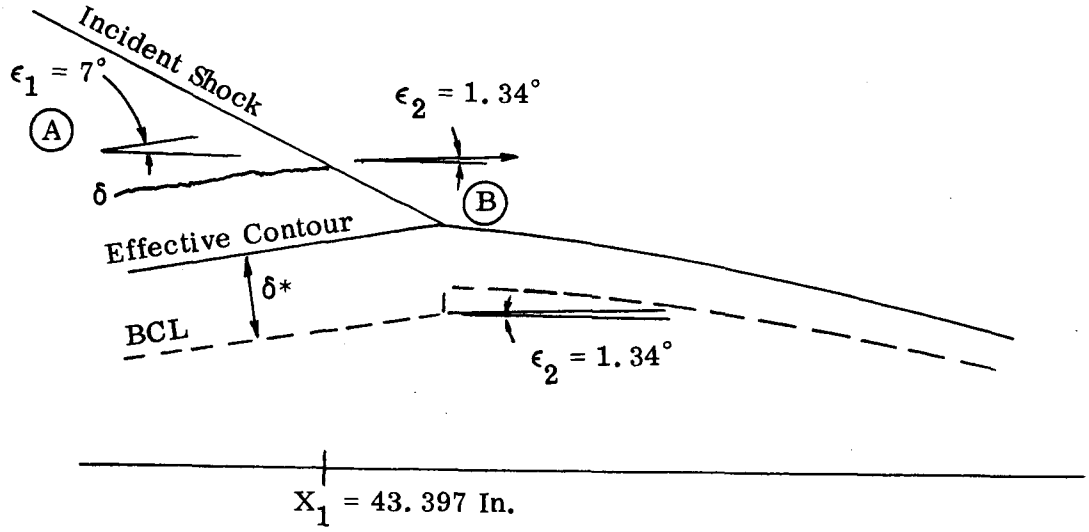

(a) Definition of Basic Contour Line and Angle ϵ_2

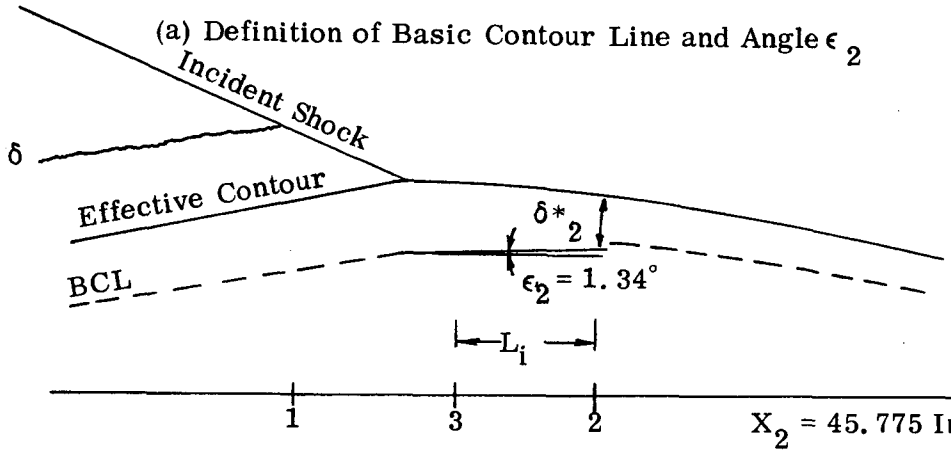

(b) Location of Stations 2 and 3

$X_2 = 45.775$ In. P12 Inlet
$X_2 = 45.749$ In. P8 Inlet
X_2 = Aft of Throat P2 Inlet

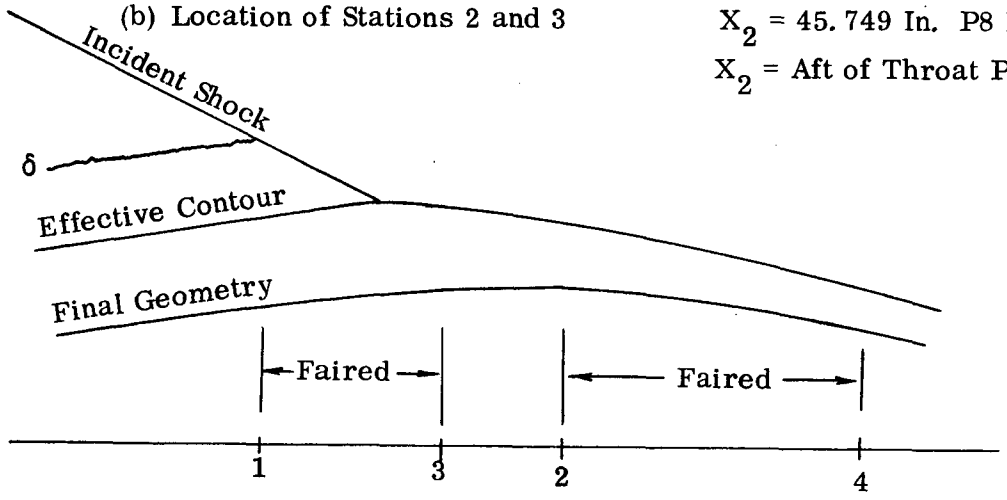

(c) Definition of Final Geometric Contour

Figure 10. Centerbody Contour Design Through Shock-Wave Cancellation Region.

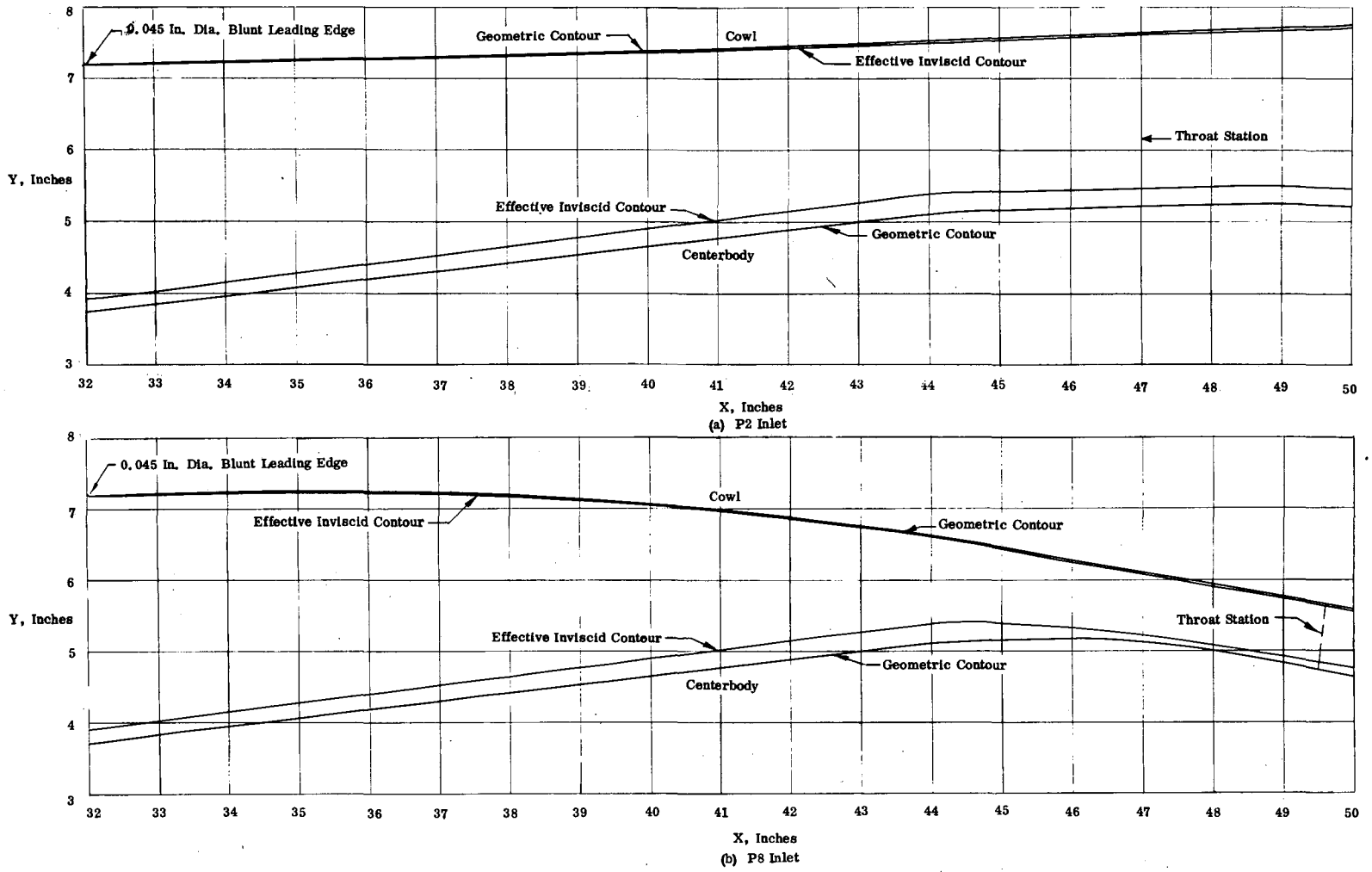

Figure 11. Effective and Geometric Coordinates for Internal Passages.

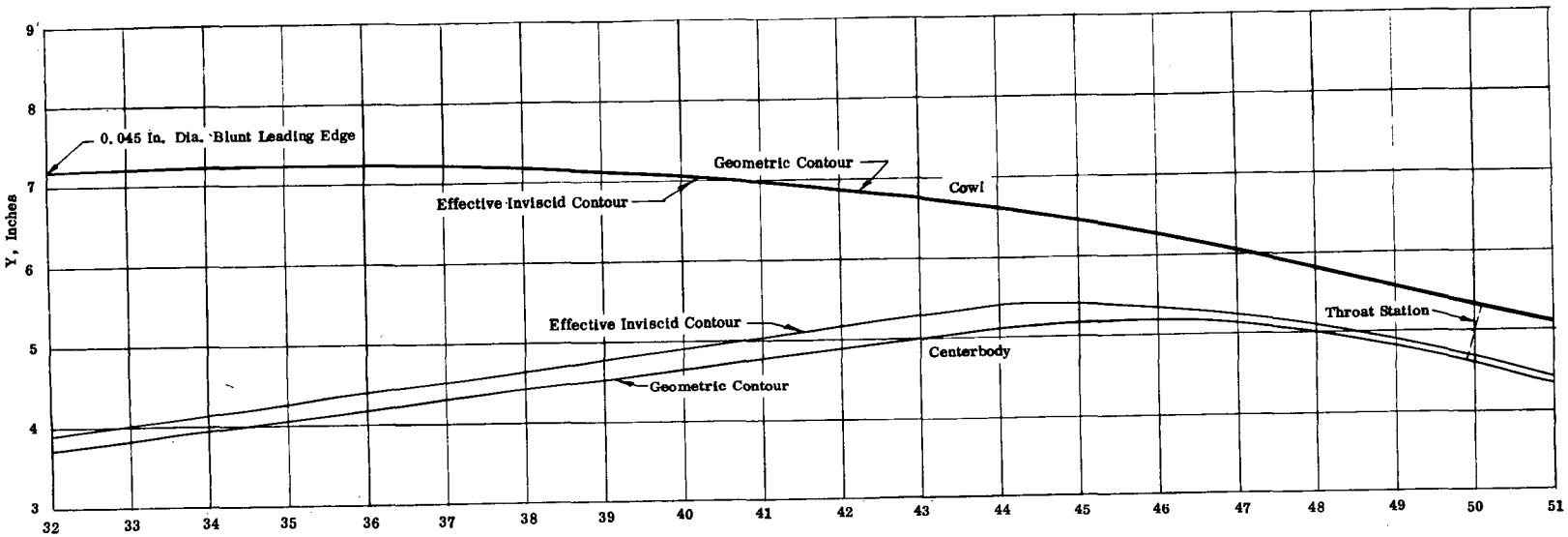

(c) P12 Inlet

Figure 11. Concluded.

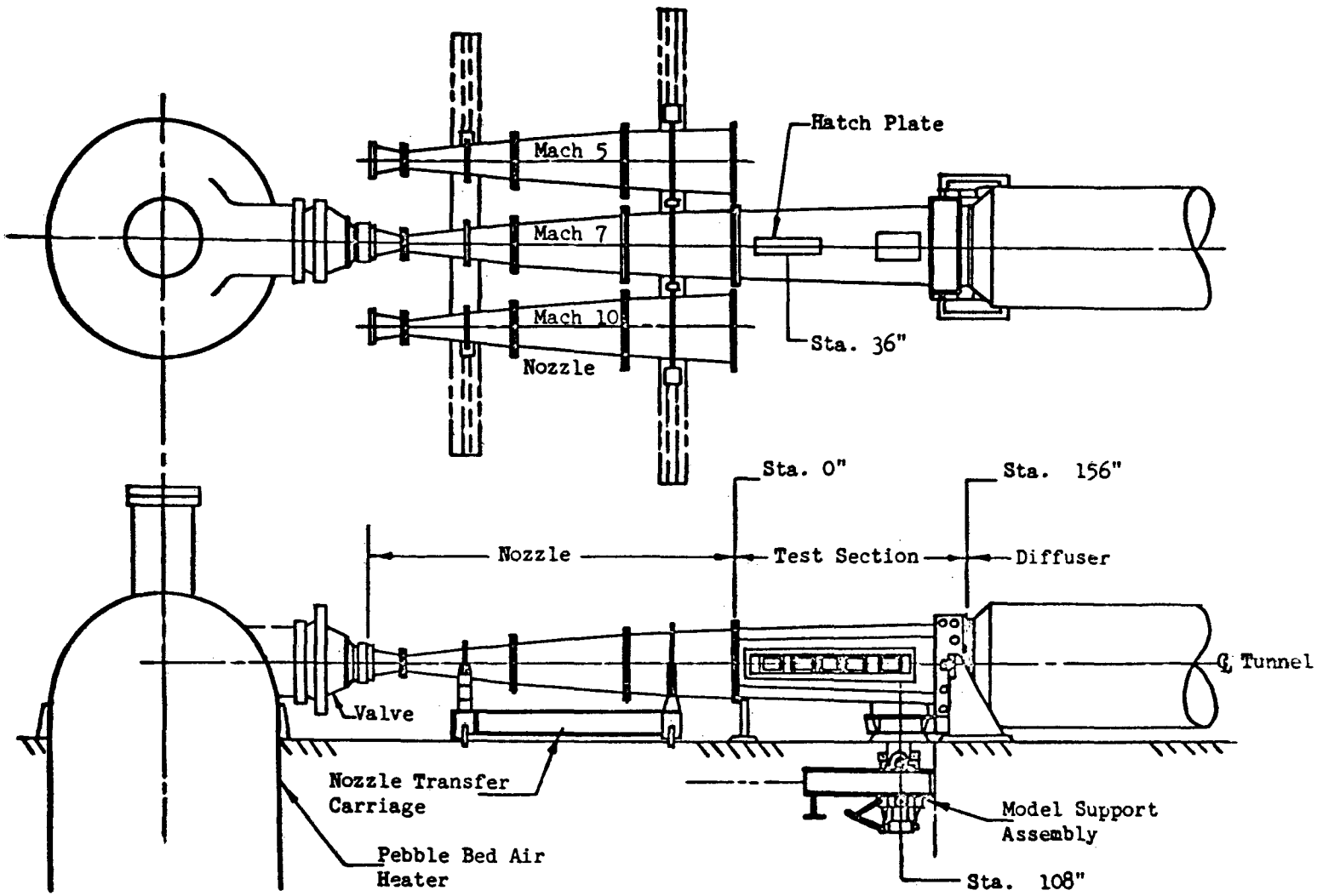

Figure 12. Schematic Representation of NASA-Ames 3.5-Foot Hypersonic Wind Tunnel.

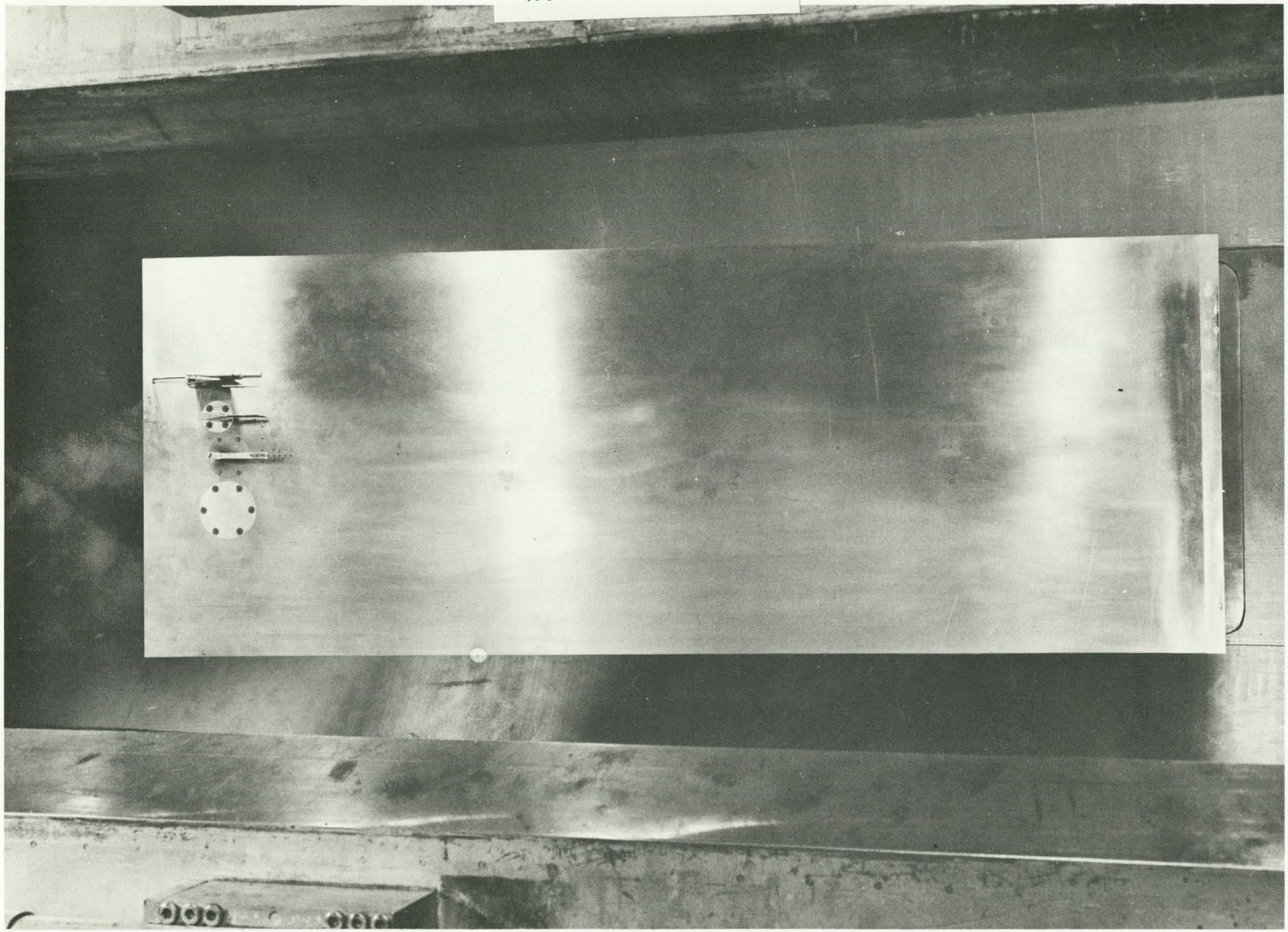

Figure 13. Calibration Plate Installed in 3.5-Foot Hypersonic Wind Tunnel.

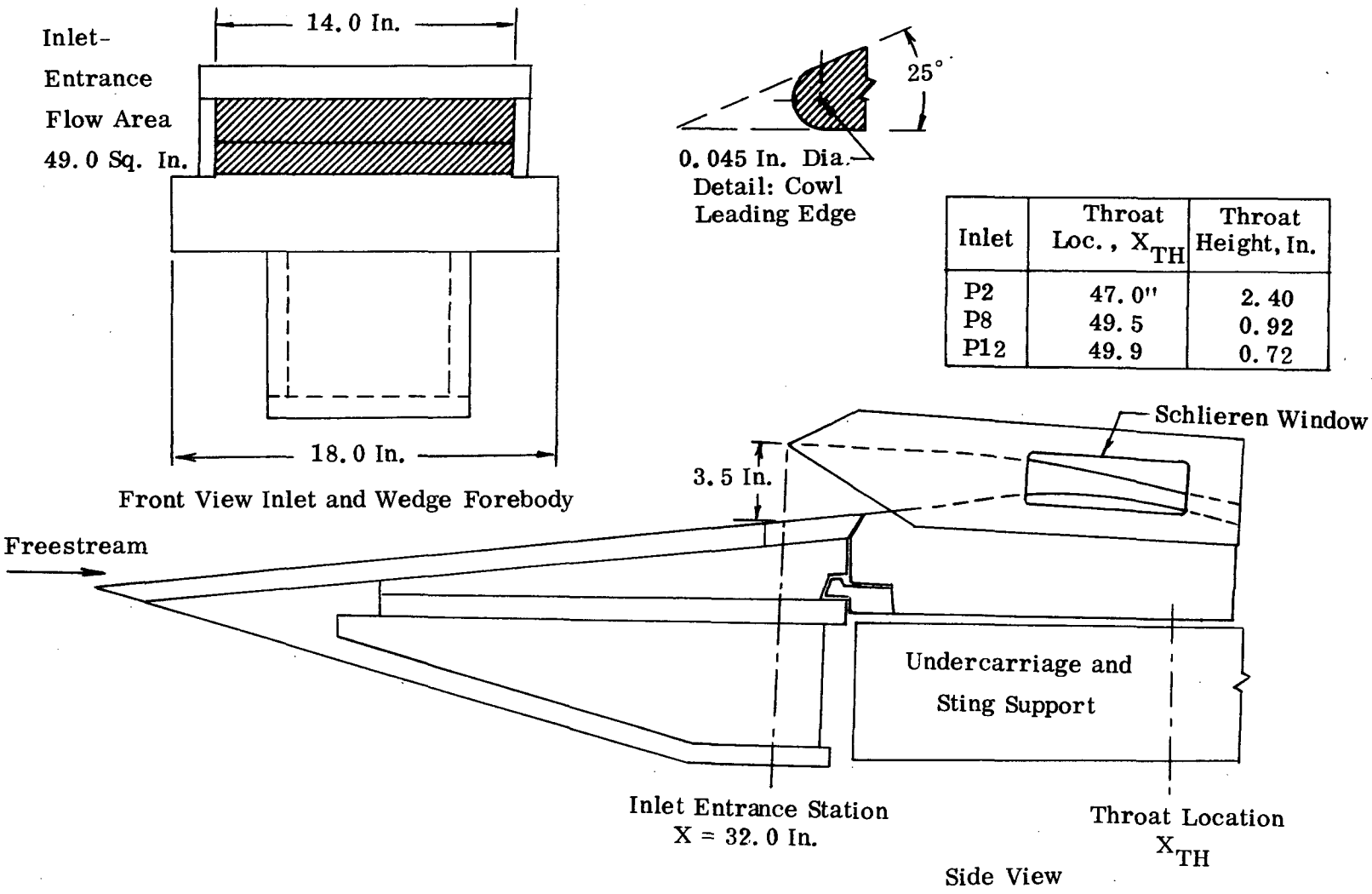

Figure 14. Schematic Representation of Inlet Model.

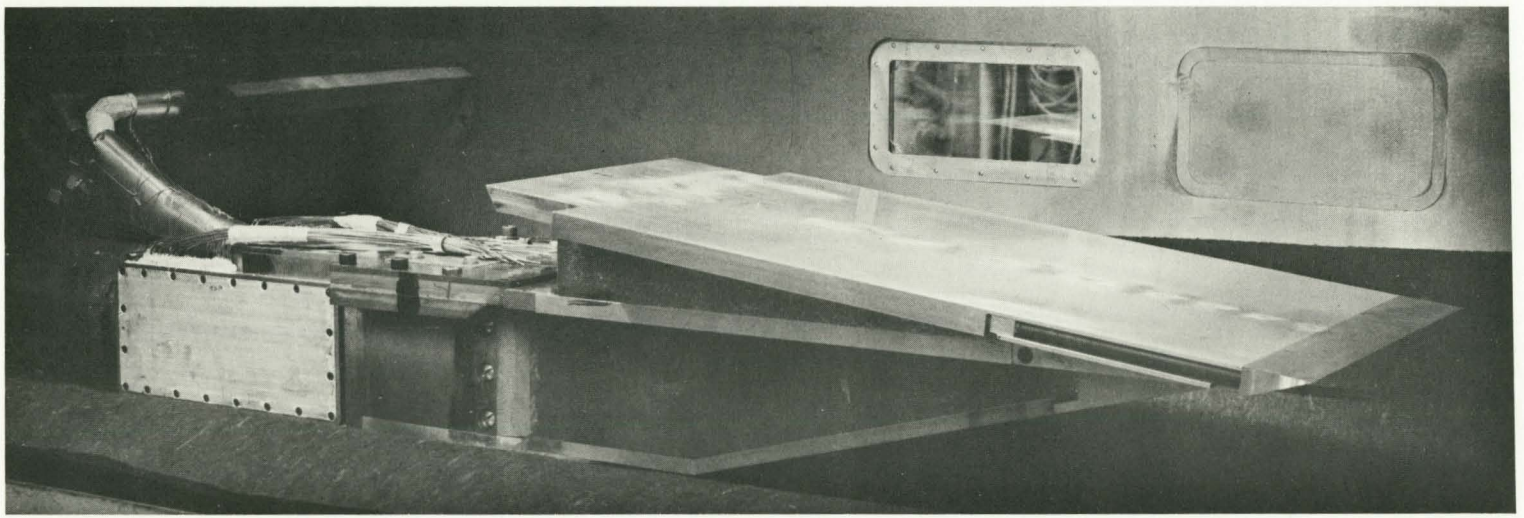

Figure 15. Basic Wedge-Forebody Model Mounted in 3.5-Foot Hypersonic Wind Tunnel.

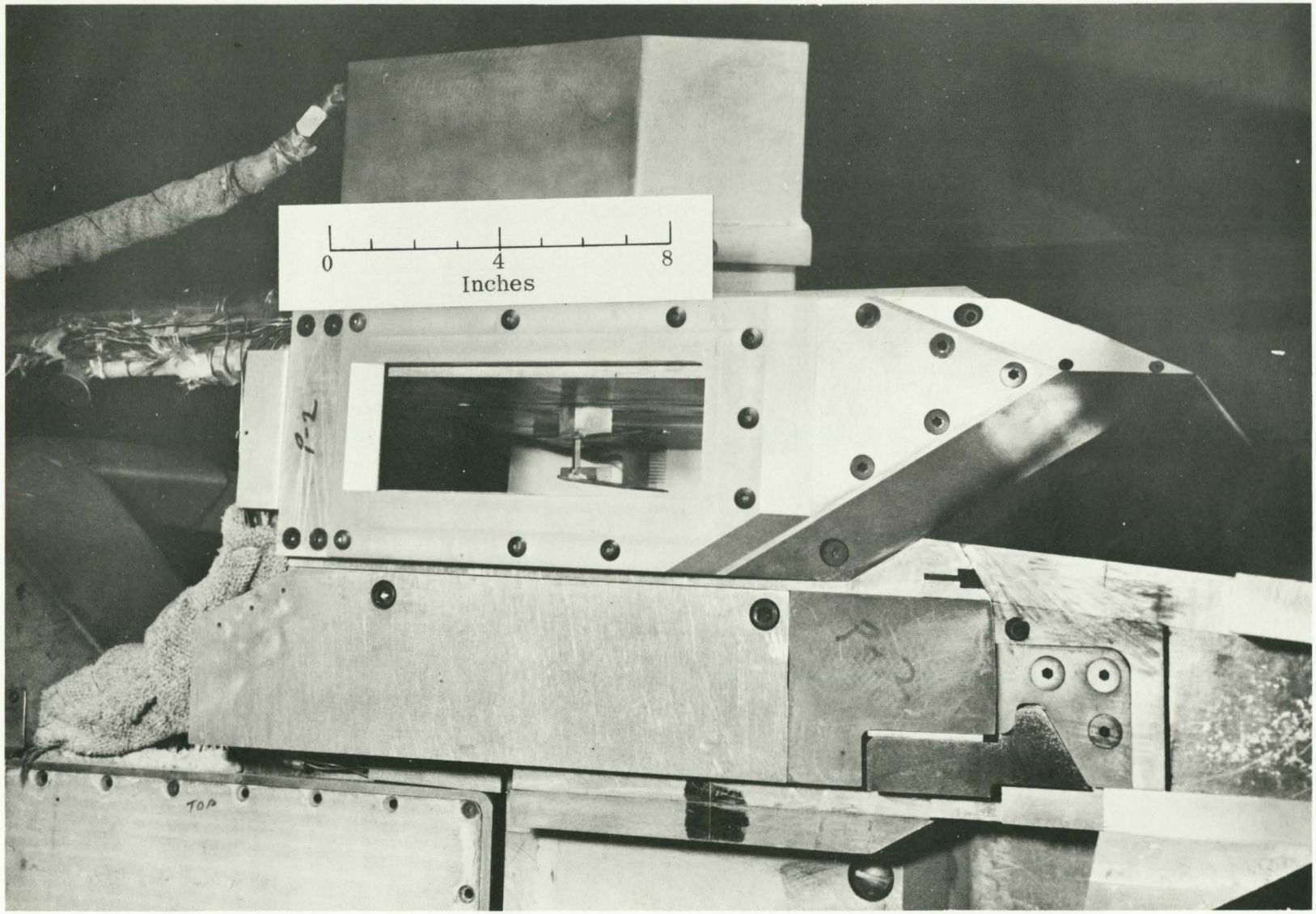

Figure 16. P2 Inlet Model Mounted in 3.5-Foot Hypersonic Wind Tunnel.

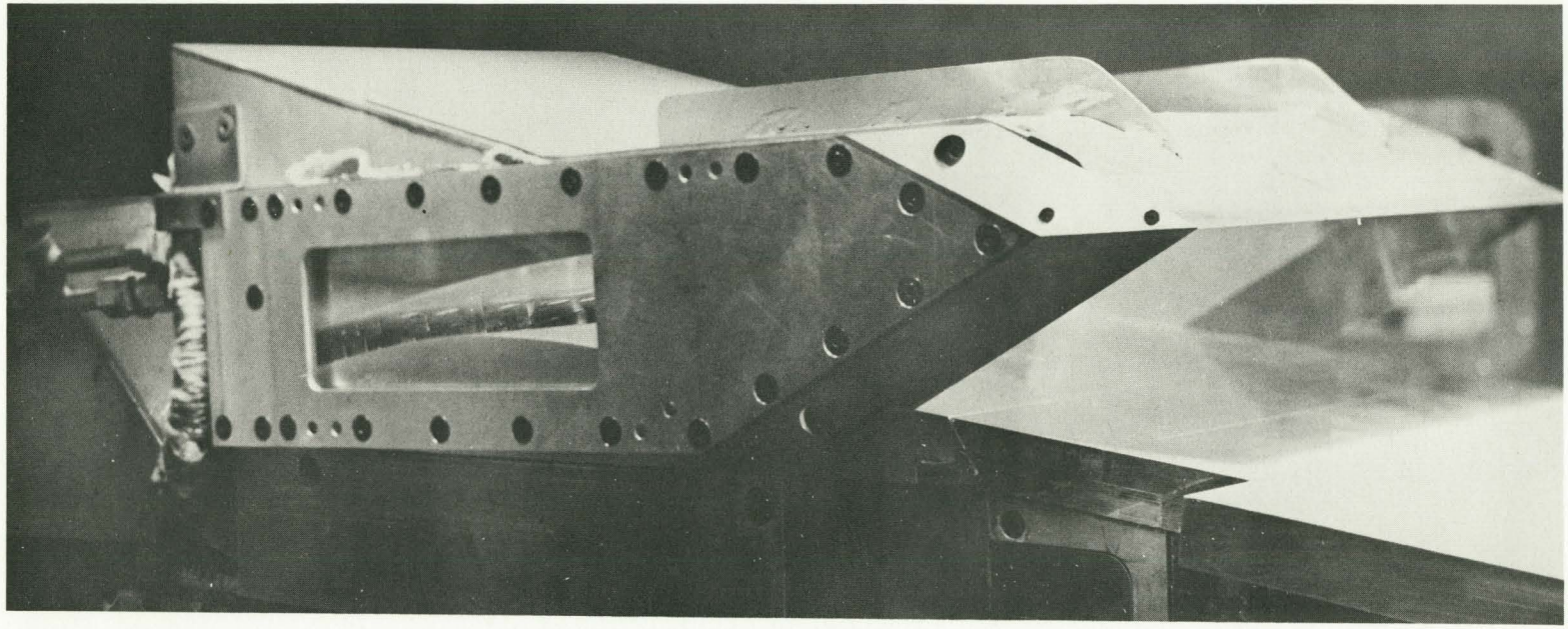

Figure 17. P8 Inlet Model Mounted in 3.5-Foot Hypersonic Wind Tunnel.

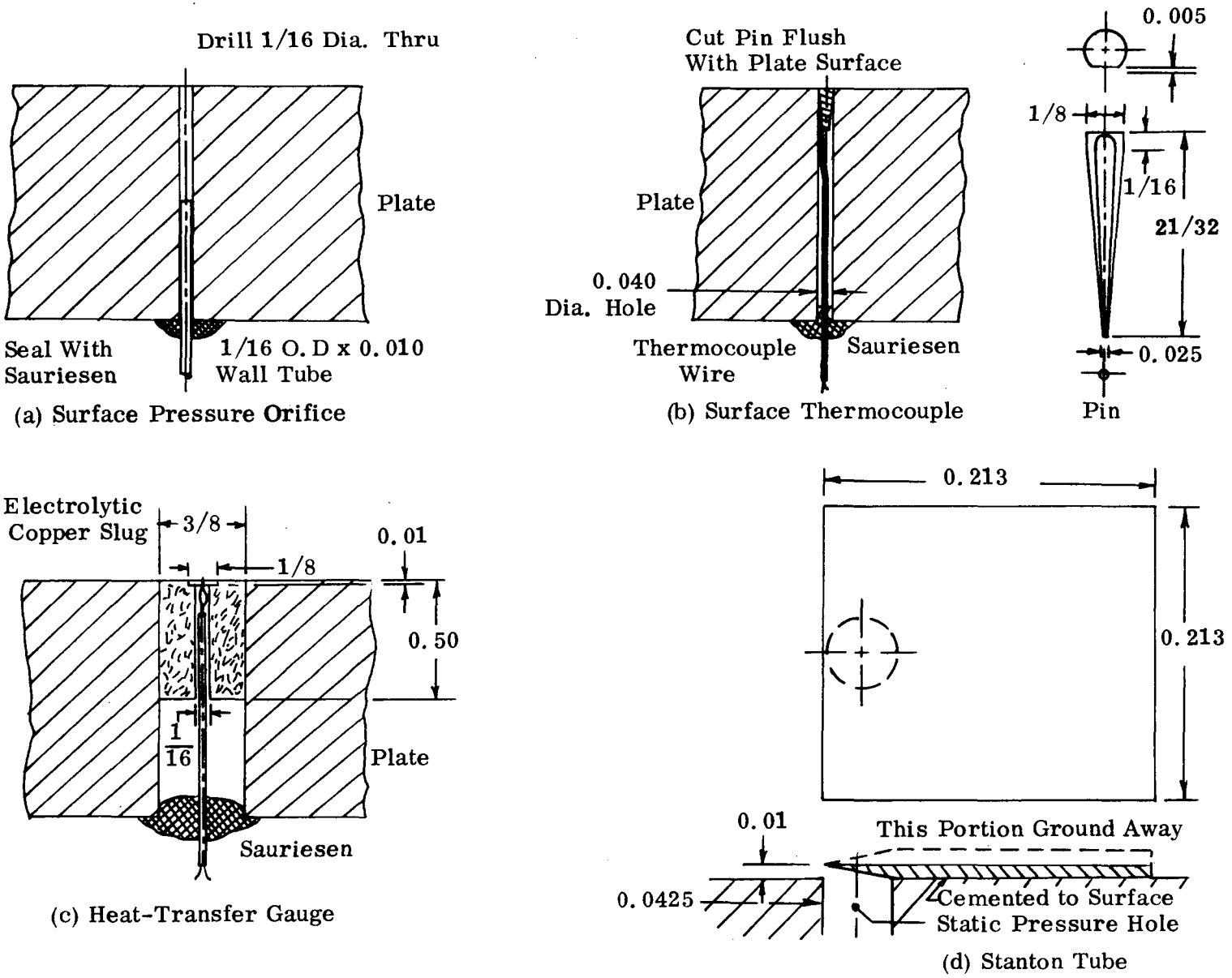

Figure 18. Surface Instrumentation.

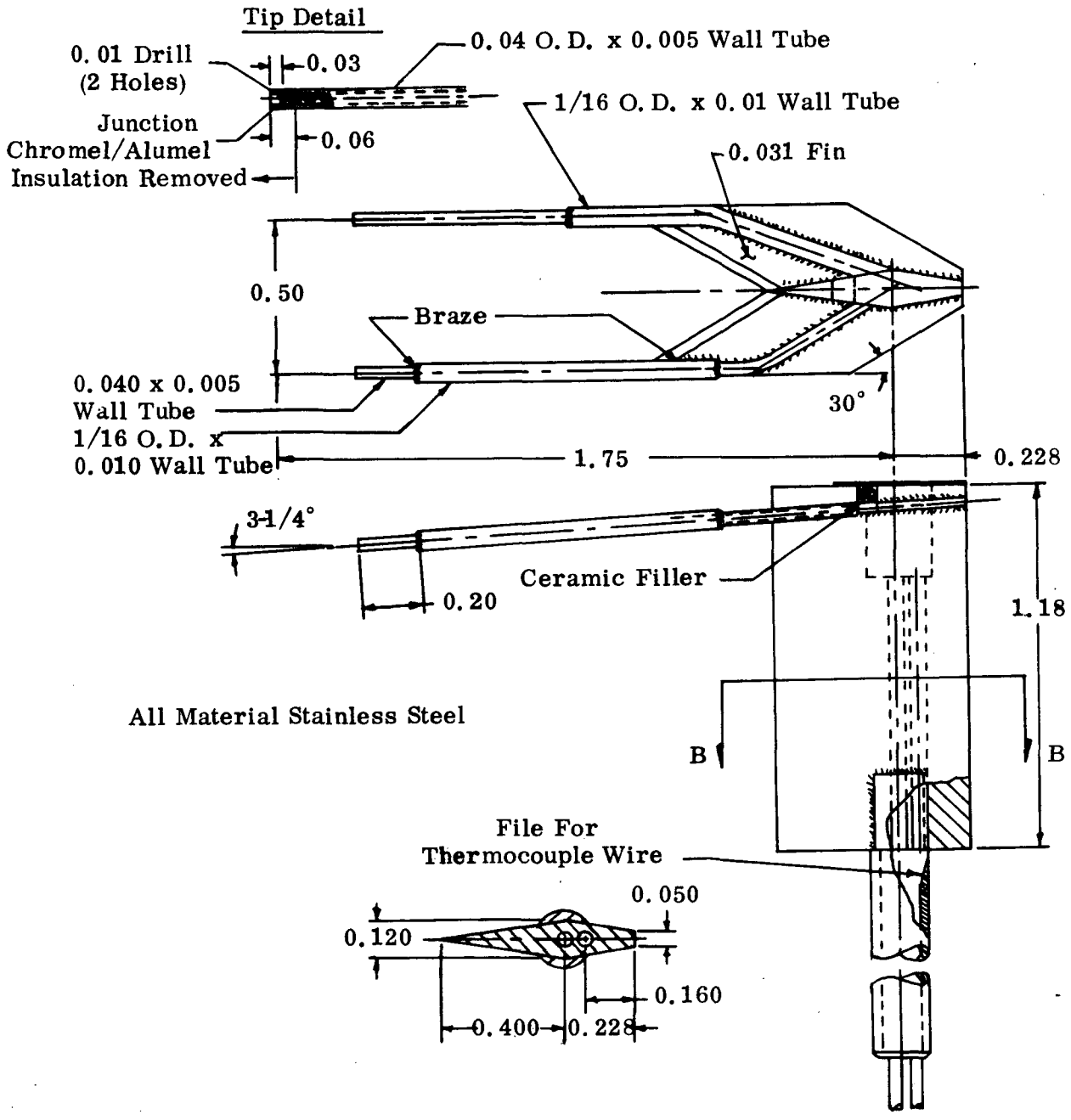

Figure 19. Combined Pitot Pressure and Singly Shielded Total-Temperature Probe.

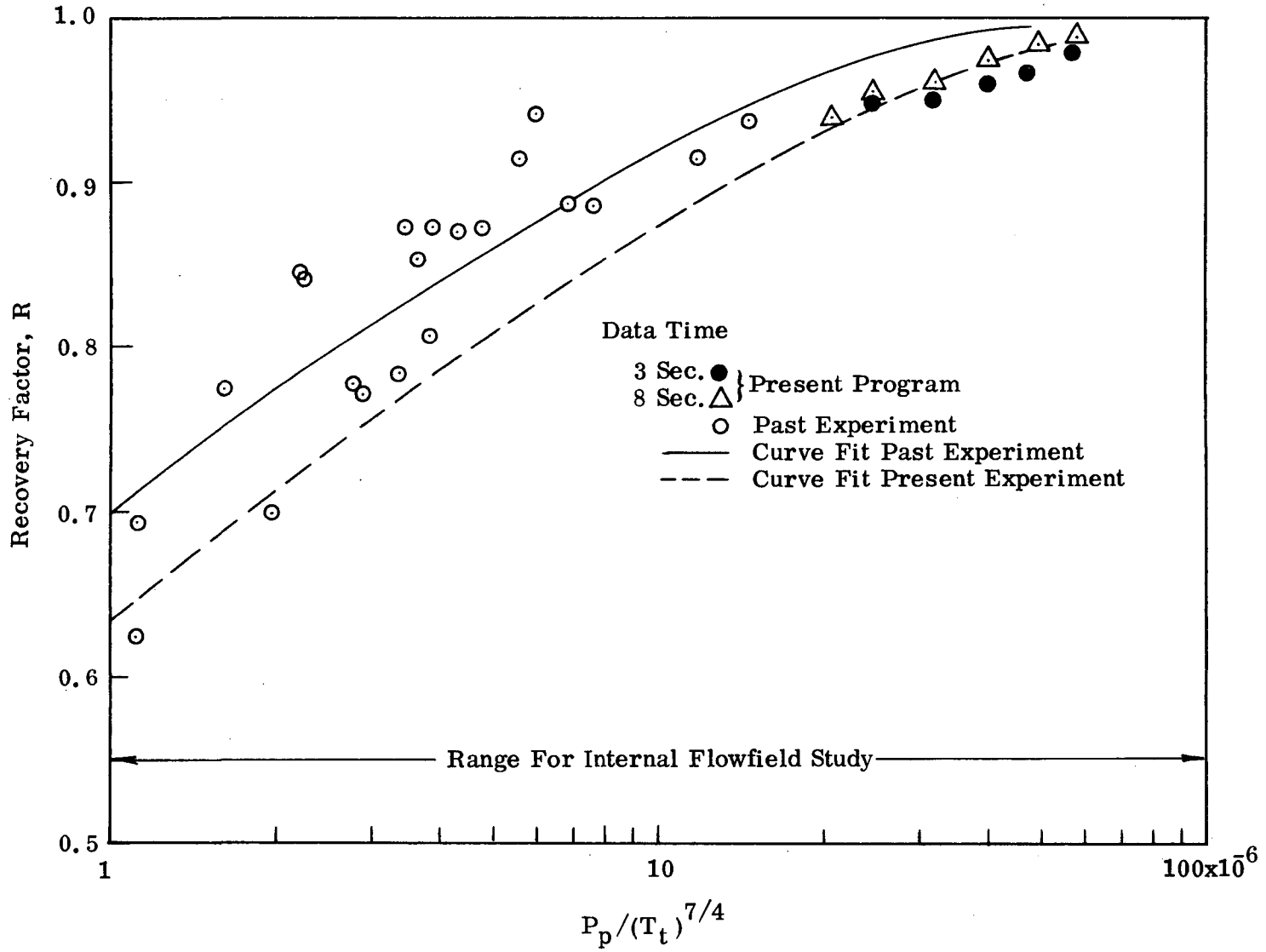

Figure 20. Calibration Data for Singly Shielded Total-Temperature Probes.

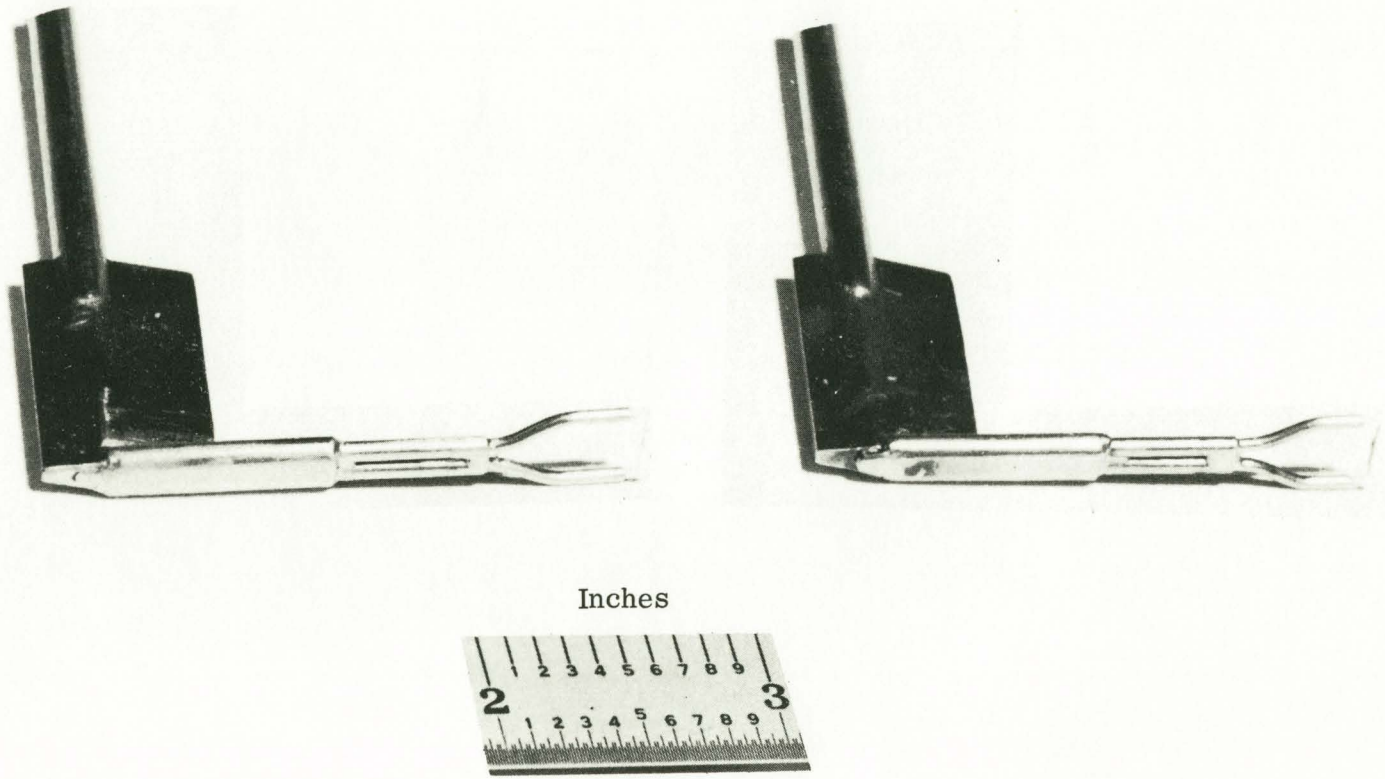

Figure 21. Exposed Thermocouple Probes (Early Design).

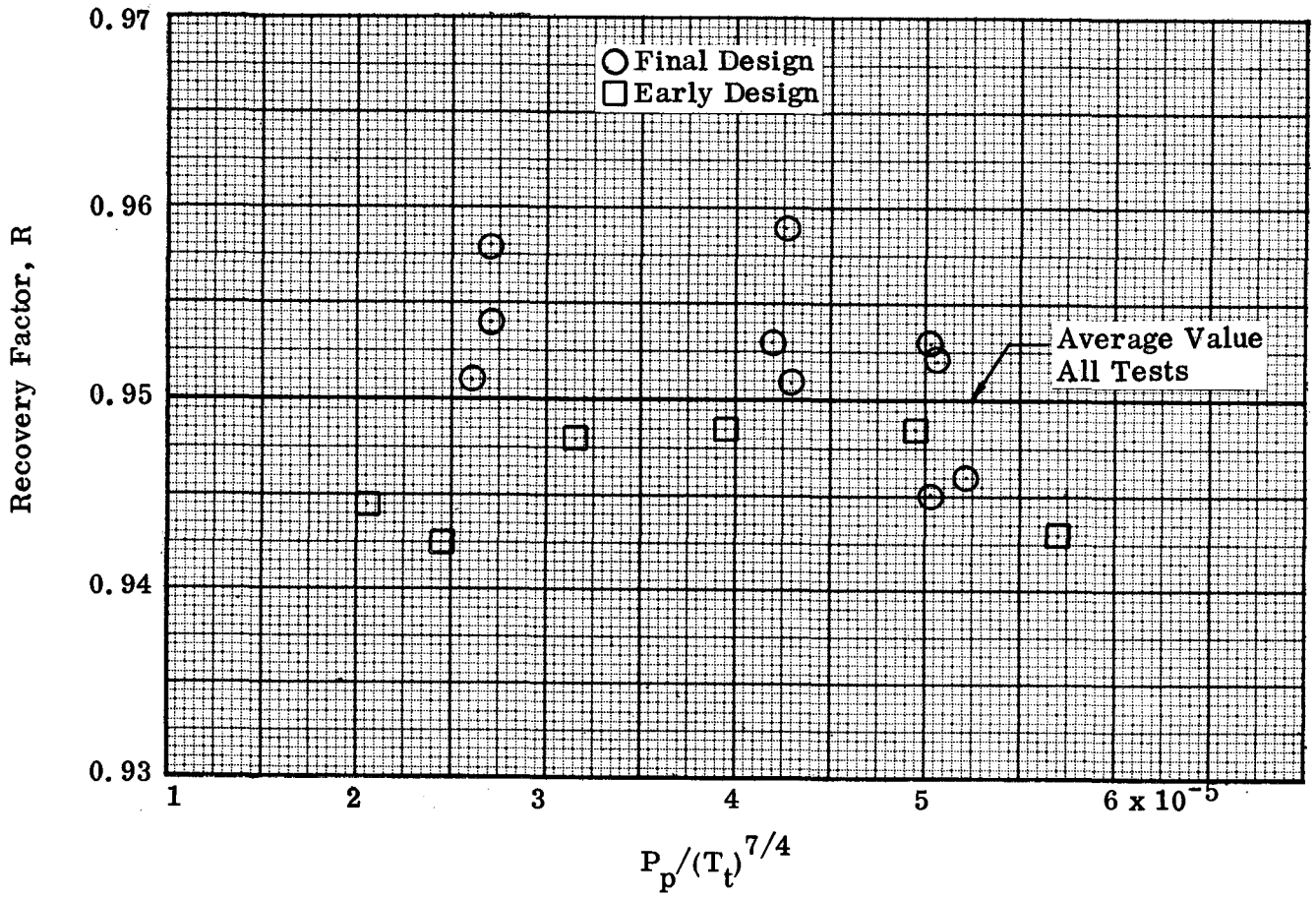

Figure 22. Recovery Factors for Exposed Thermocouple Probes.

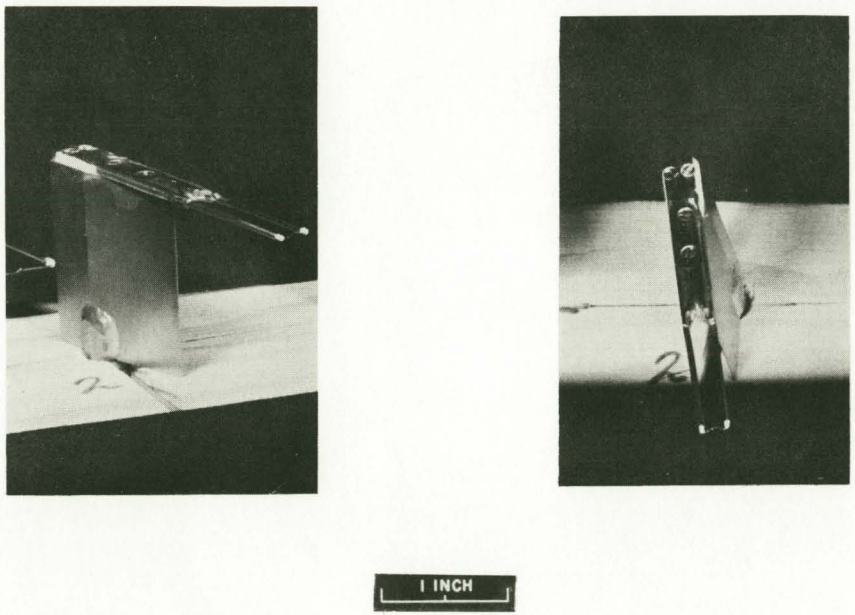

Figure 23. Exposed Thermocouple Probes (Revised Design).

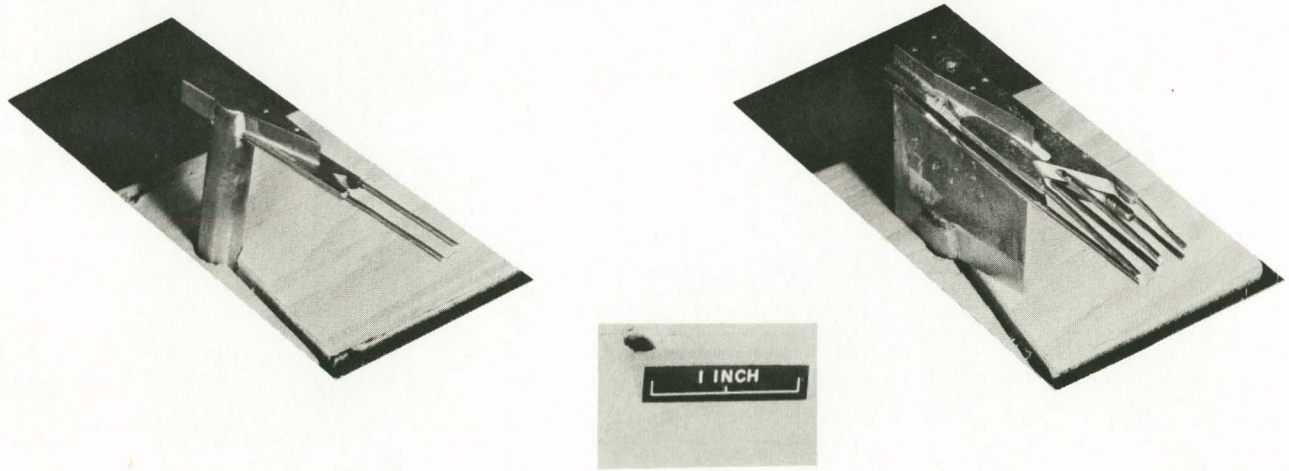

Round-Shaft Probe

Four-Element Probe

Figure 24. Special Purpose Exposed Thermocouple Probes.

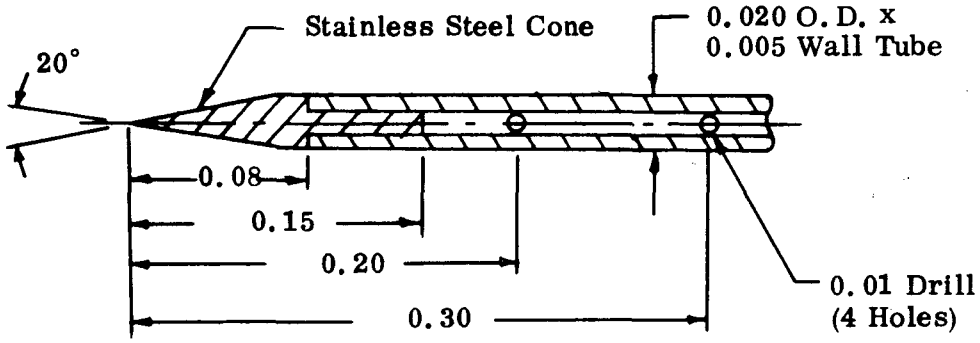

(a) Direct-Reading

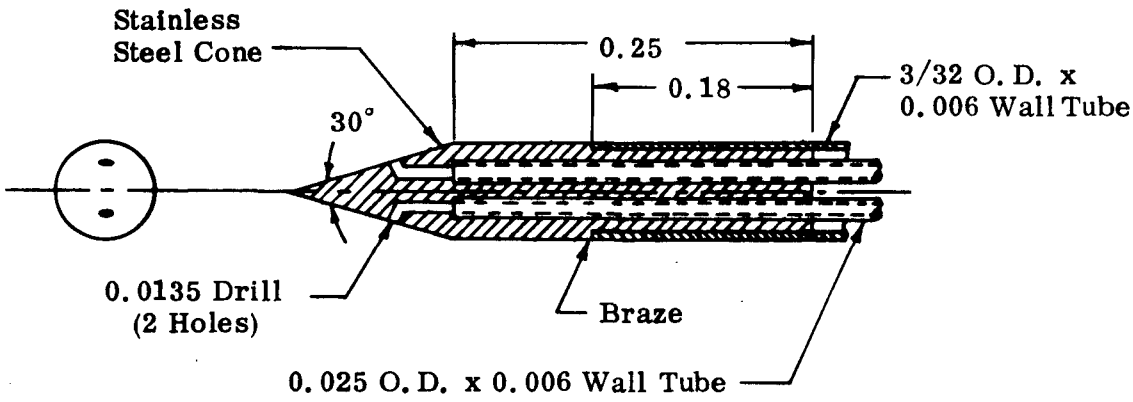

(b) Conical (Flow-Direction Sensitive)

Figure 25. Static Pressure Probes.

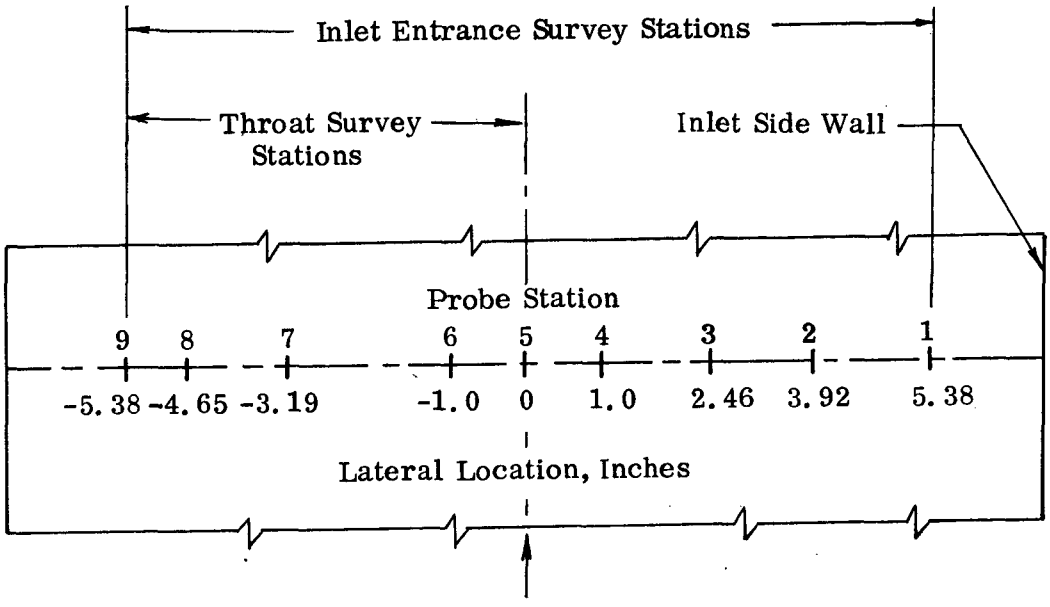

(a) Probe Locations - Plan View

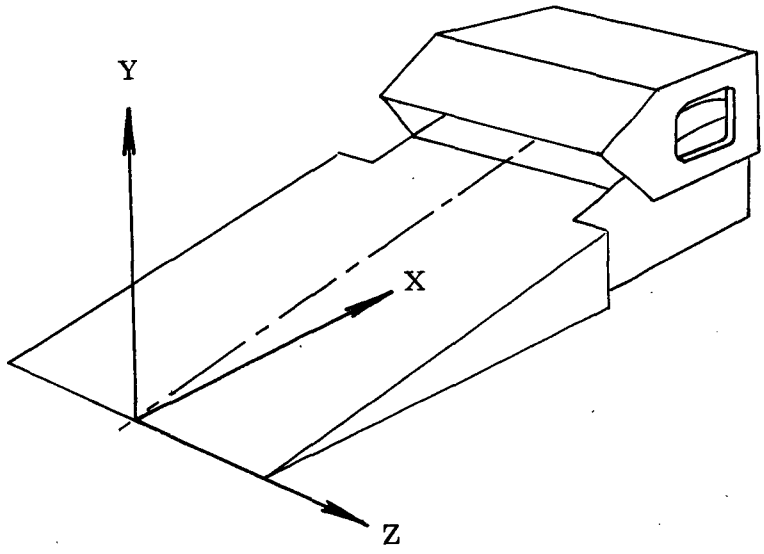

(b) Coordinate System

Figure 26. Lateral Survey Stations and Coordinate Axes.

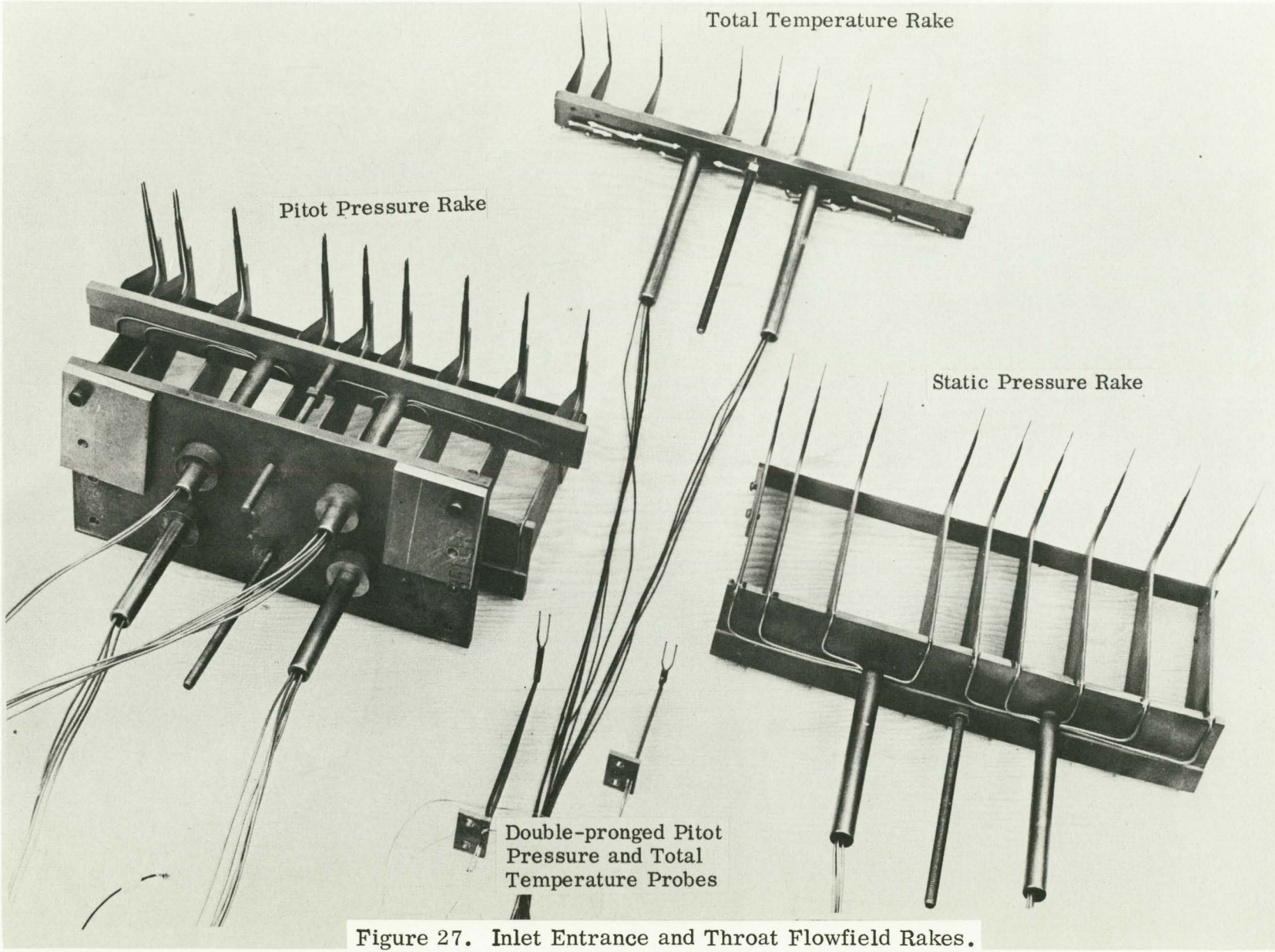

Figure 27. Inlet Entrance and Throat Flowfield Rakes.

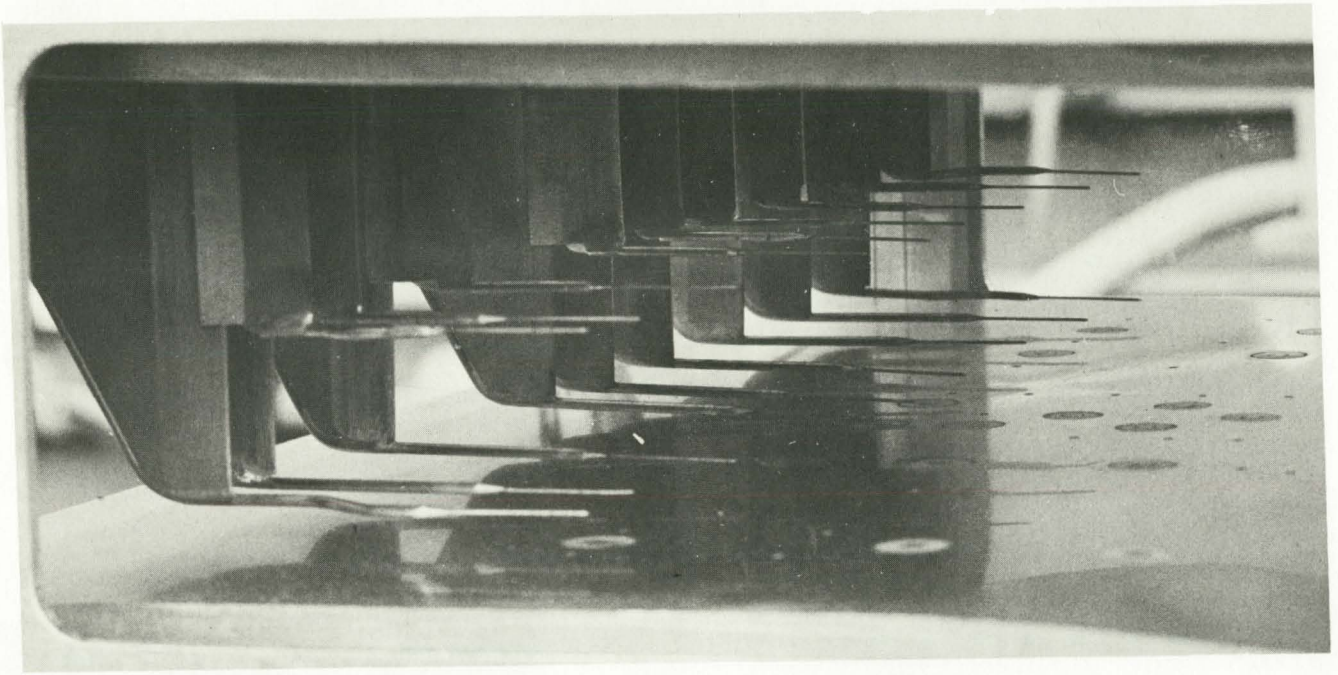

Figure 28. Static Pressure Probes Installed at Throat Station of P2 Inlet Model.

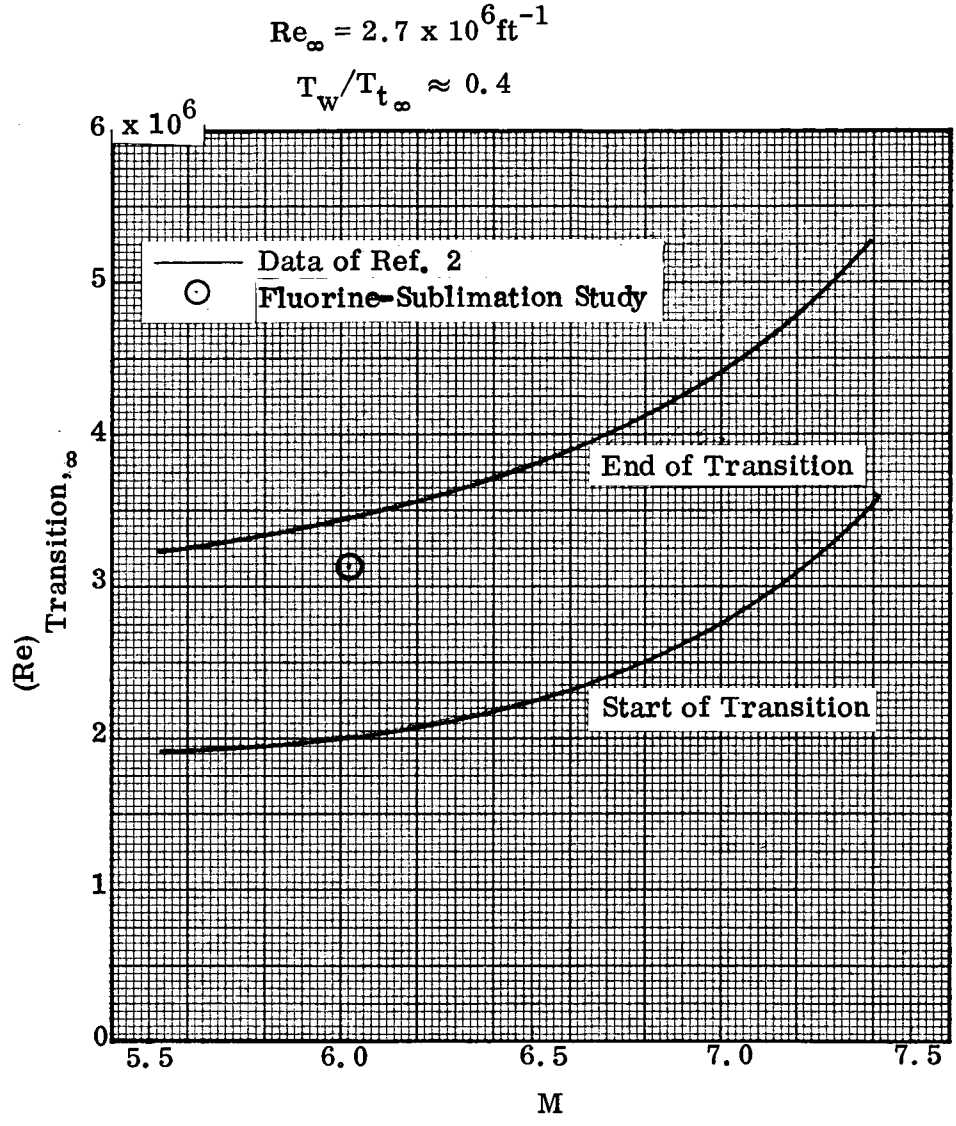

Figure 29. Comparison of Boundary-Layer Transition Data for Flat Plates.

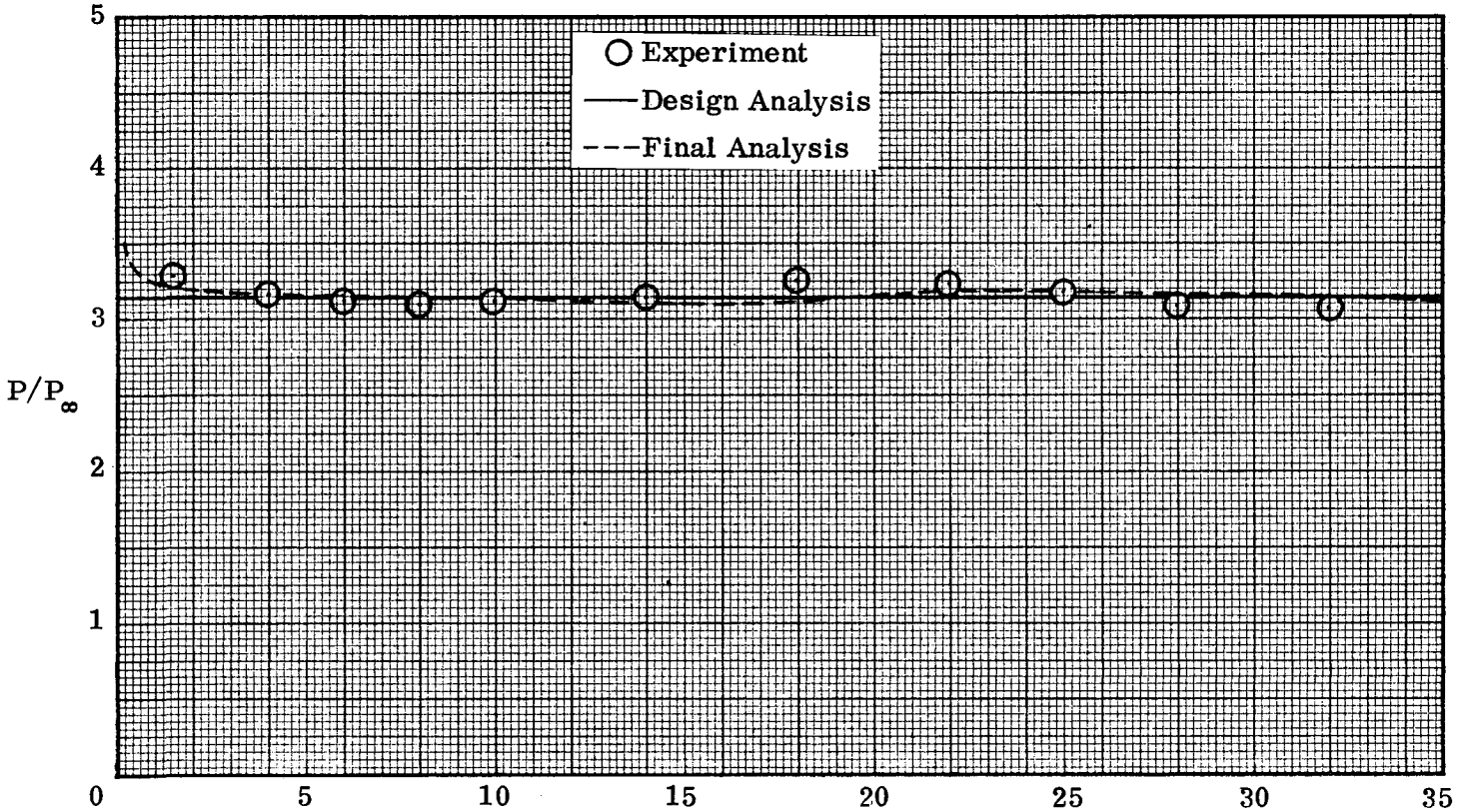

(a) Axial Distributions

Figure 30. Surface Static-Pressure Distributions, Wedge Forebody.

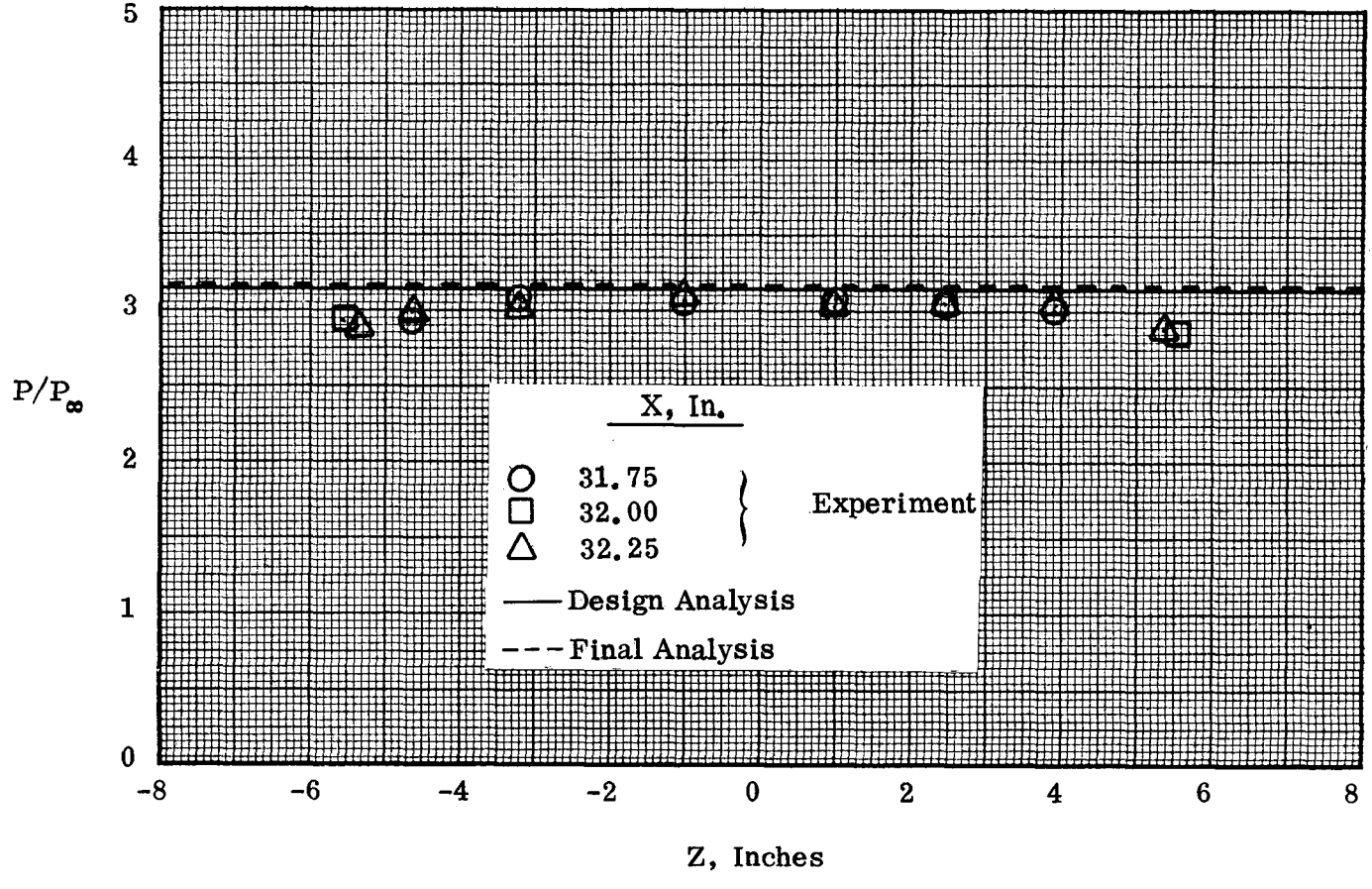

(b) Lateral Distributions

Figure 30. Concluded.

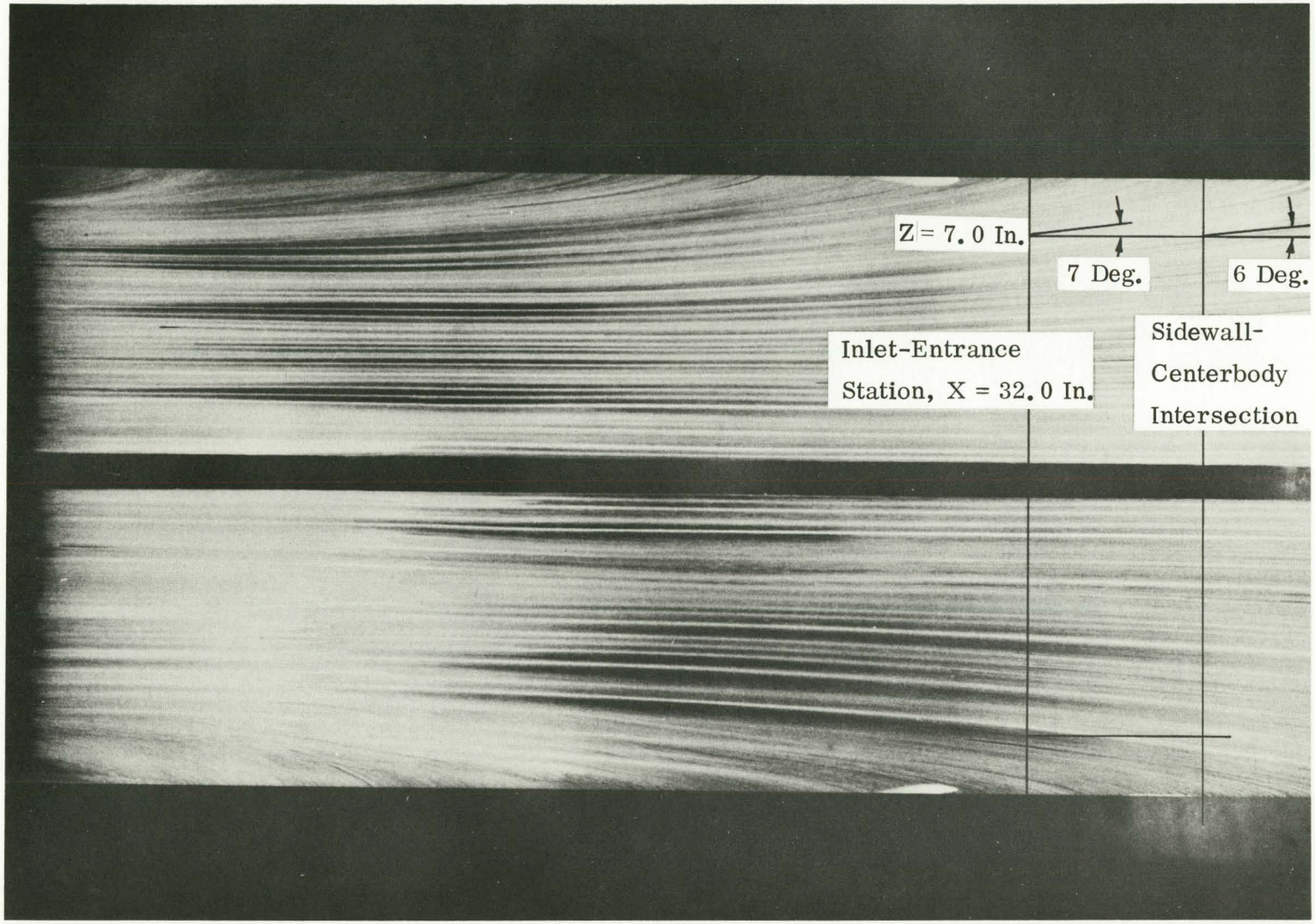

Figure 31. Surface Oil-Flow Photograph, Flat Plate at α = 6.4 Degrees.

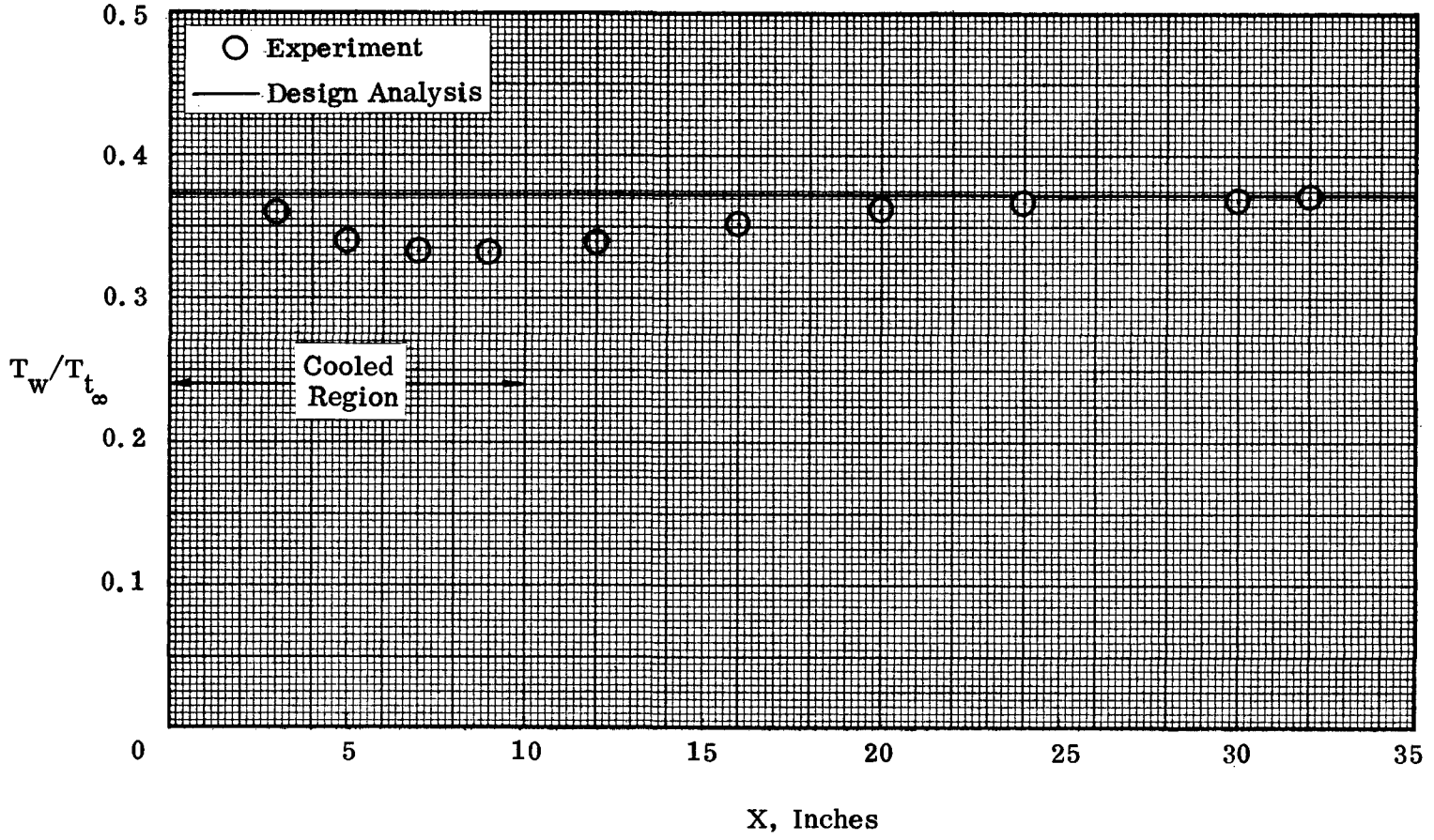

Figure 32. Surface Temperature Distribution , Wedge Forebody.

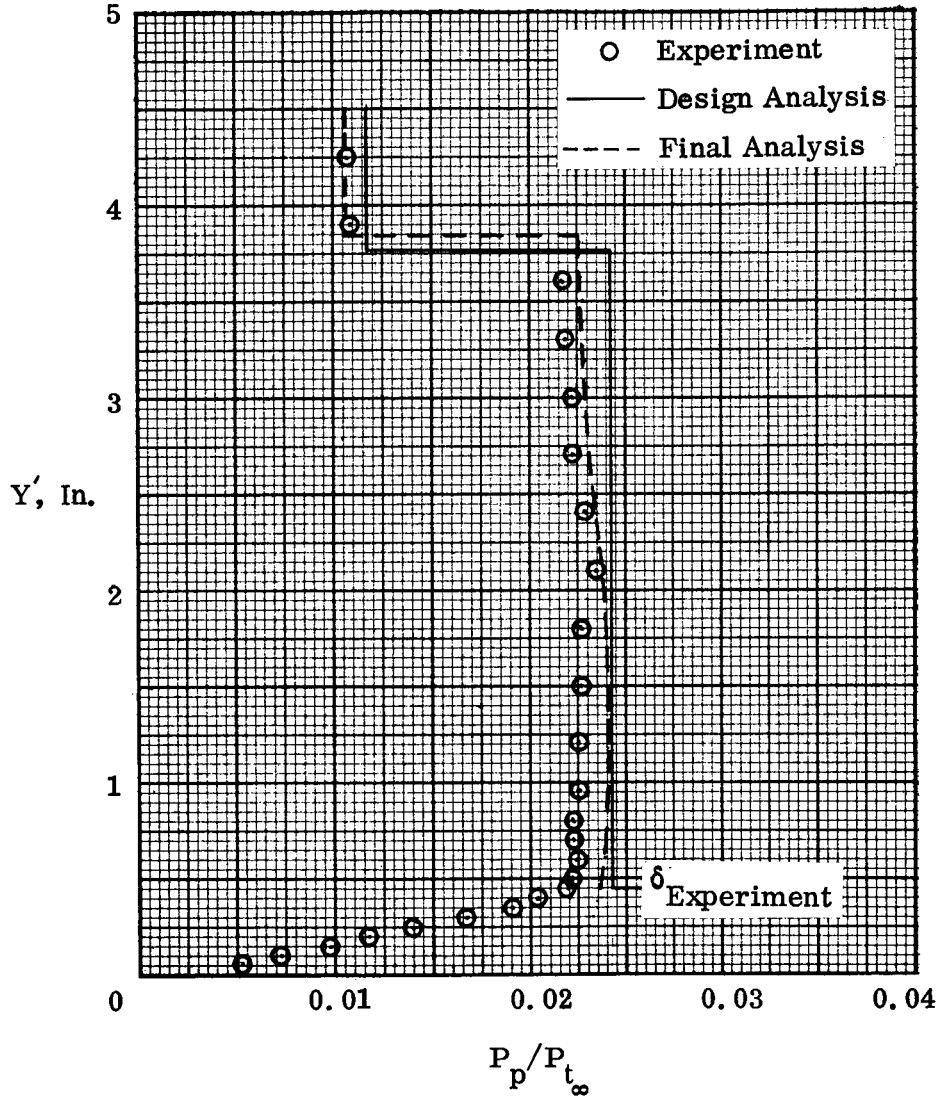

Figure 33. Pitot Pressure Distribution at Inlet-Entrance Station, Model Centerline.

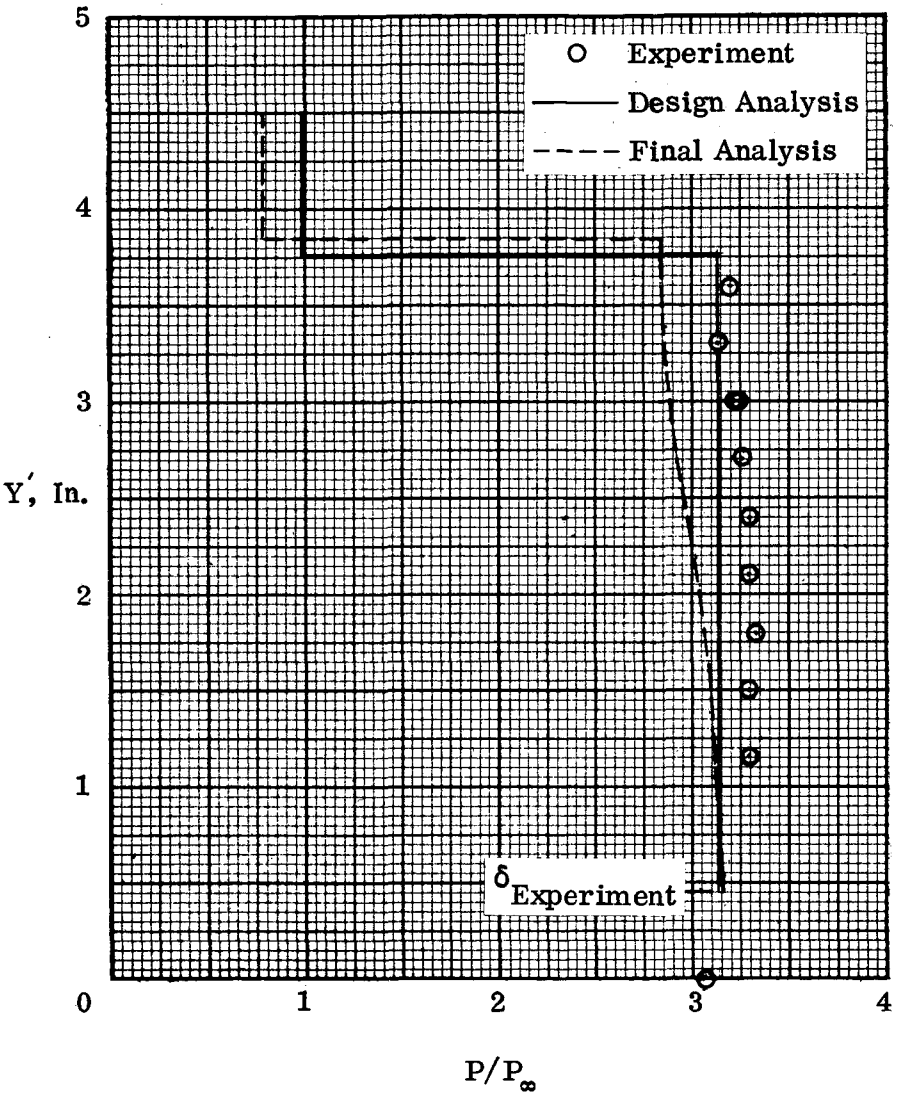

Figure 34. Static Pressure Distribution at Inlet-Entrance Station, Model Centerline.

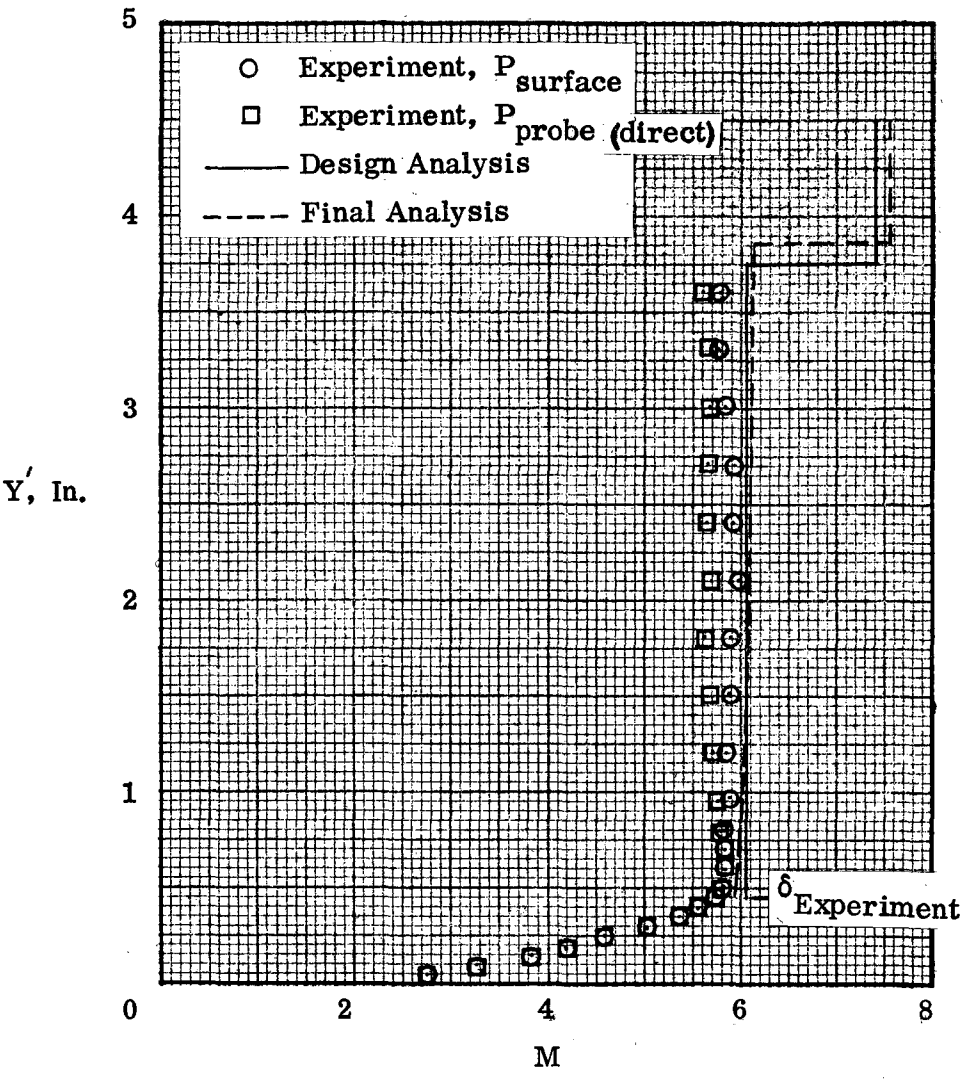

Figure 35. Mach Number Distribution at Inlet-Entrance Station, Model Centerline.

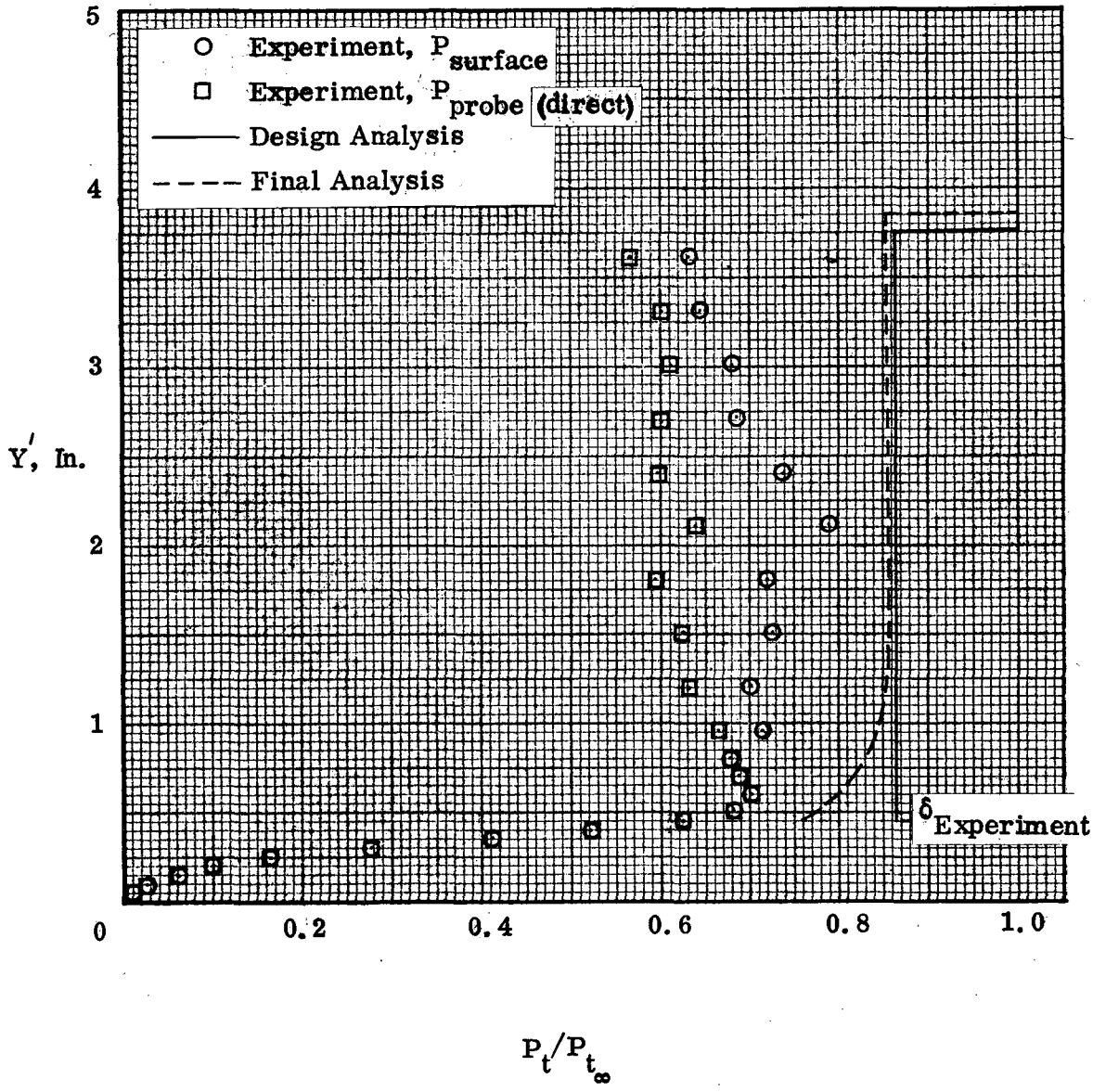

Figure 36. Total-Pressure Recovery Distribution at Inlet-Entrance Station, Model Centerline.

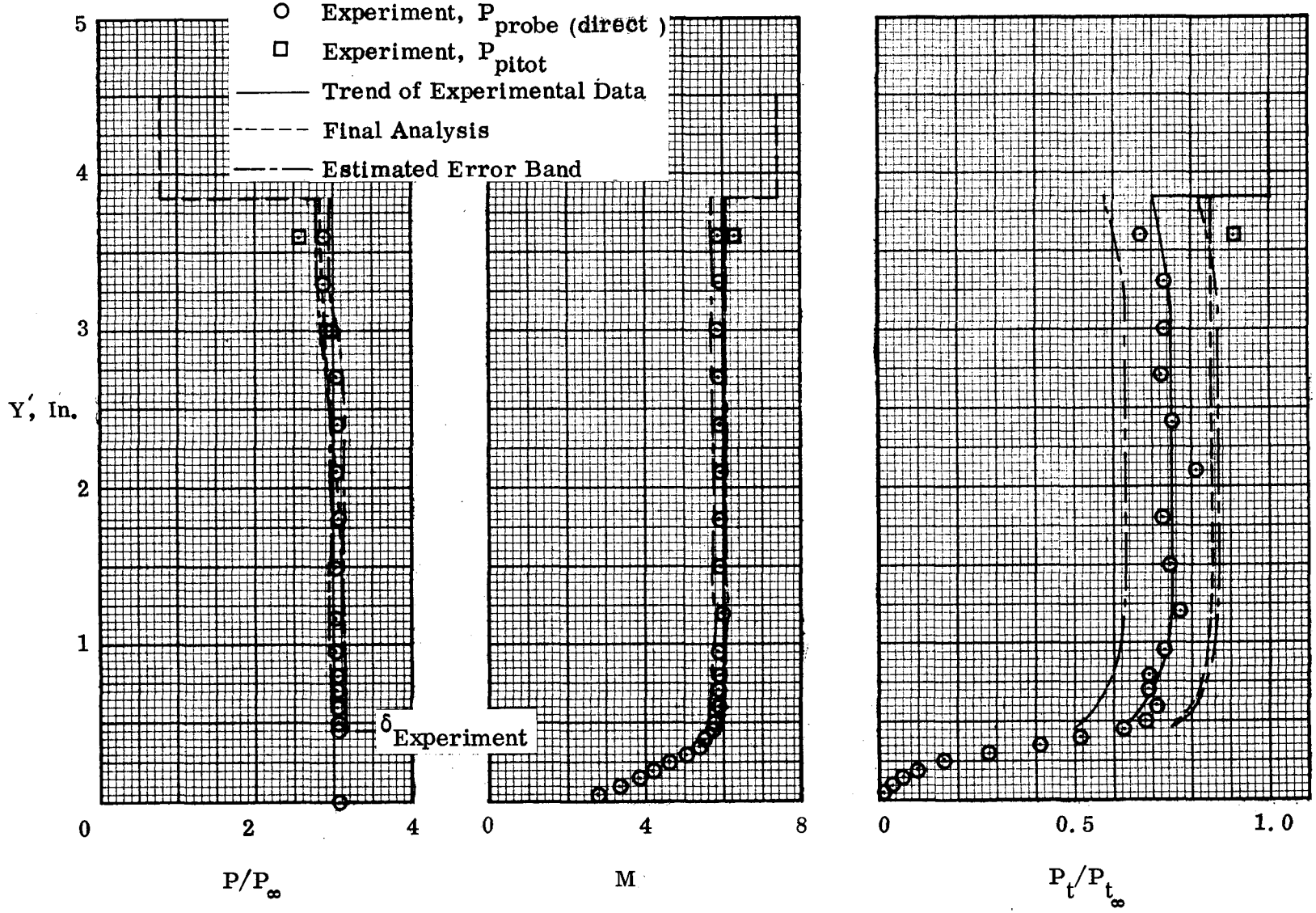

Figure 37. Flowfield Properties at Inlet-Entrance Station Using Corrected Static Pressures, Model Centerline.

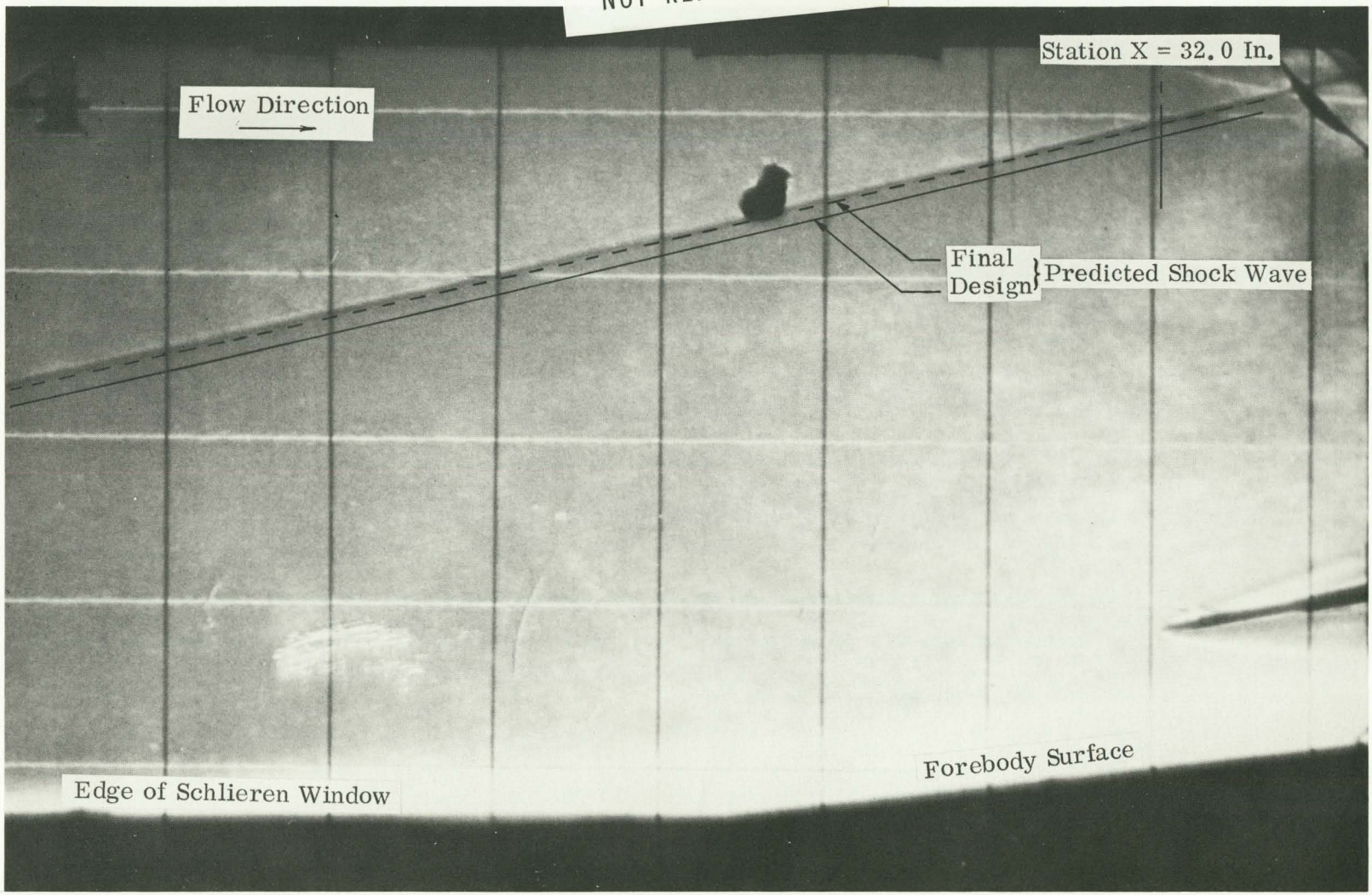

Figure 38. Wedge-Forebody Shock Wave at Inlet-Entrance Station.

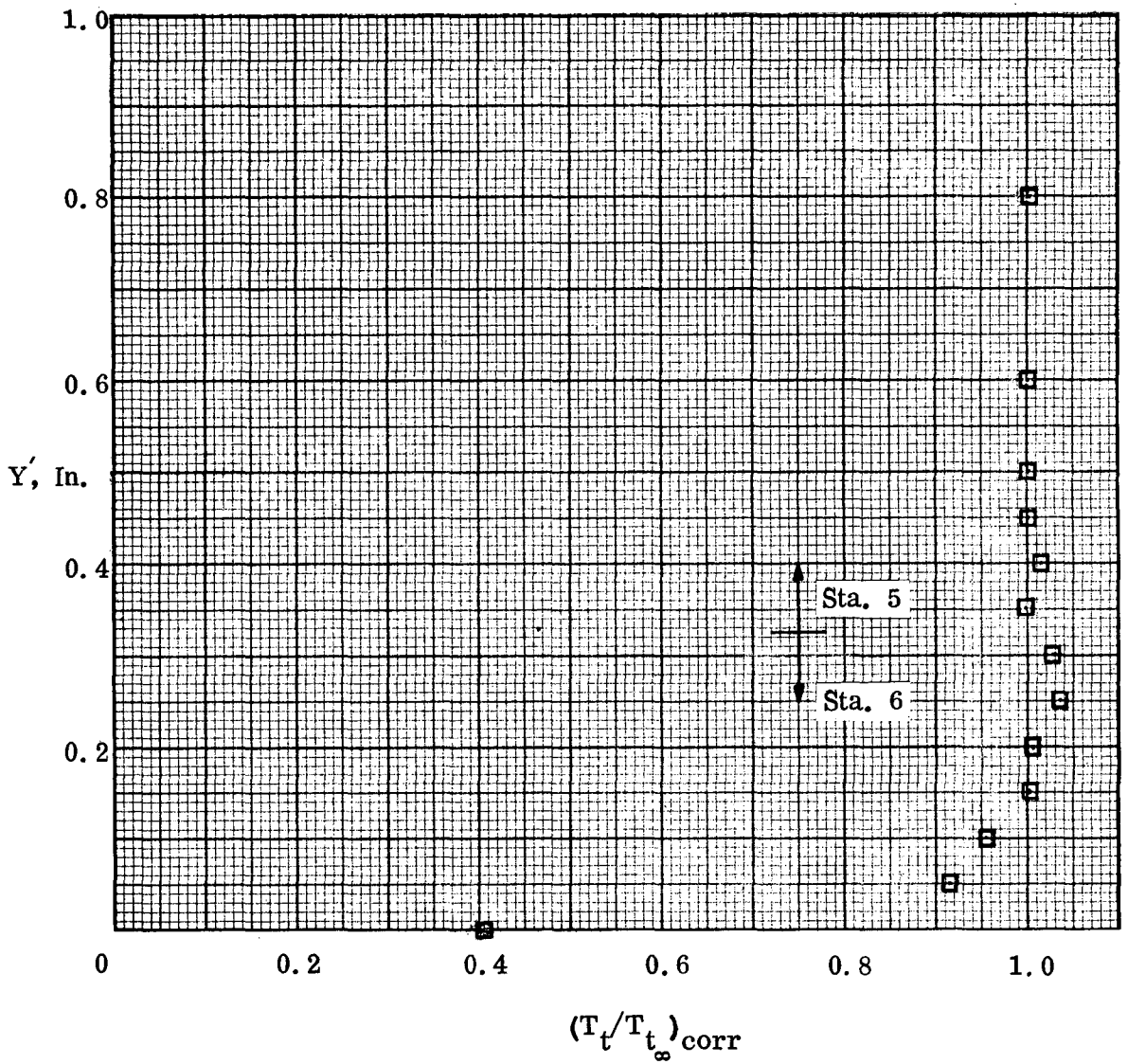

Figure 39. Total Temperature Distribution at Inlet-Entrance Station, Model Centerline.

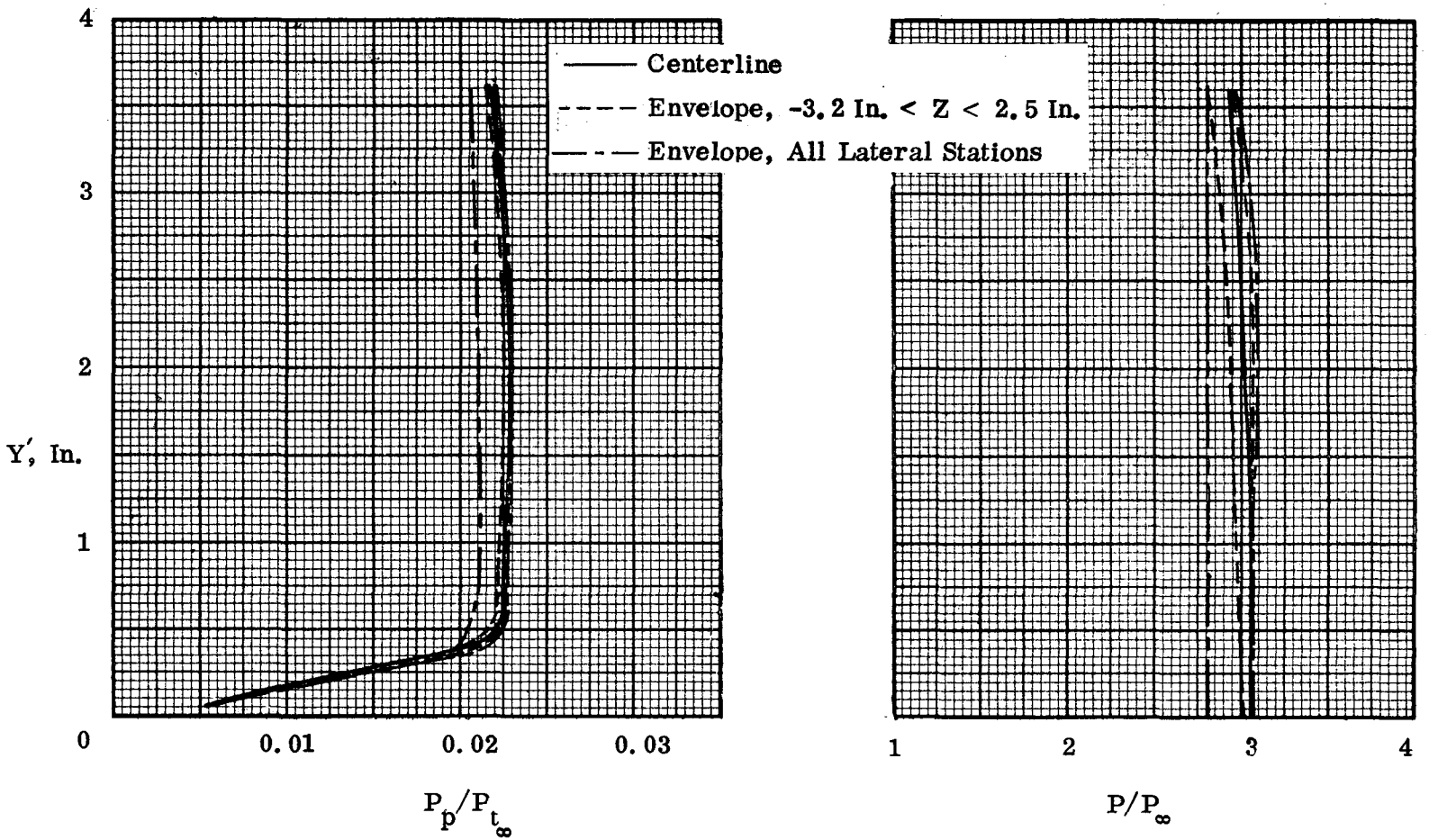

(a) Pitot Pressure and Static Pressure

Figure 40. Flowfield Properties at Inlet-Entrance Station, All Lateral Stations.

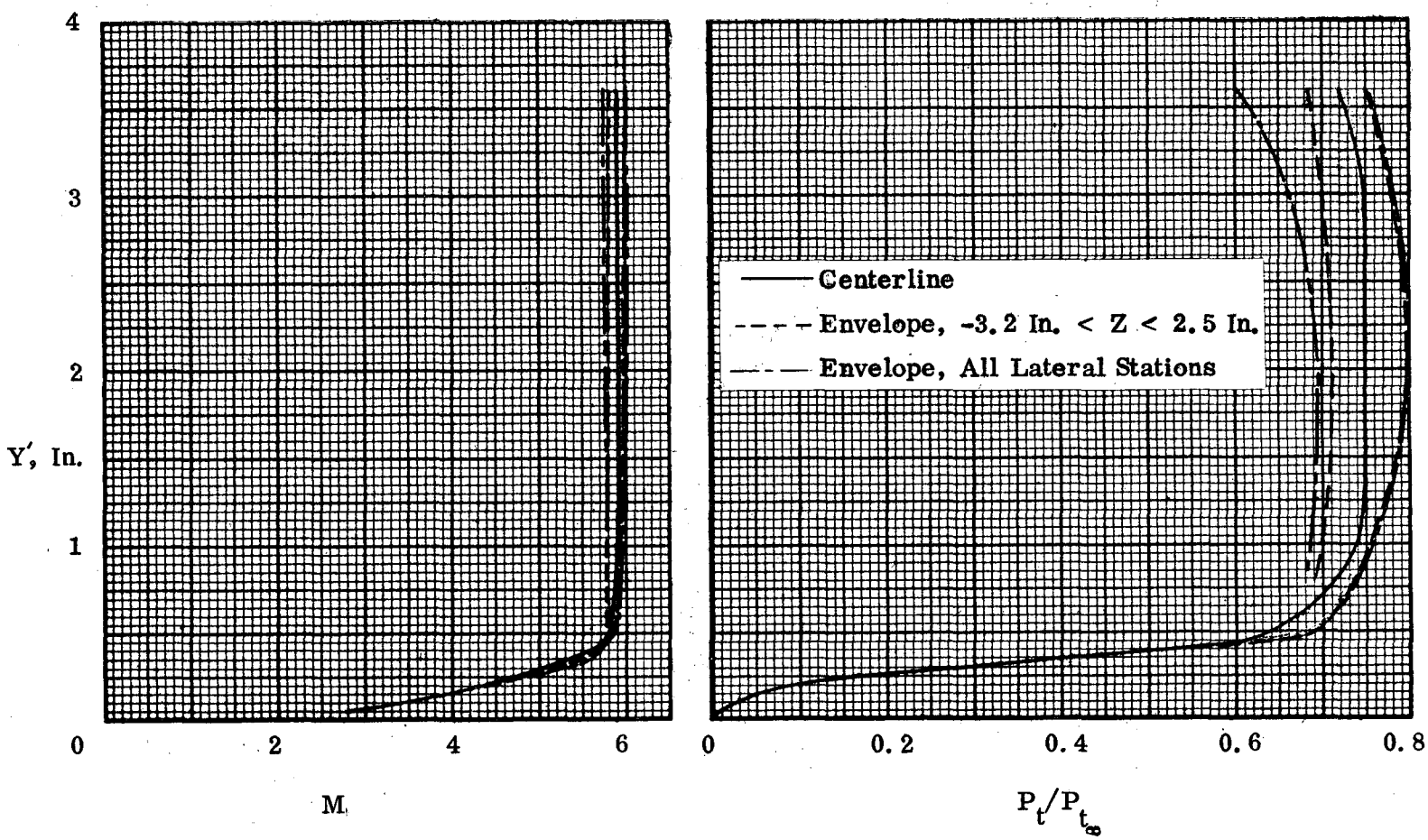

(b) Mach Number and Total Pressure Recovery

Figure 40. Continued.

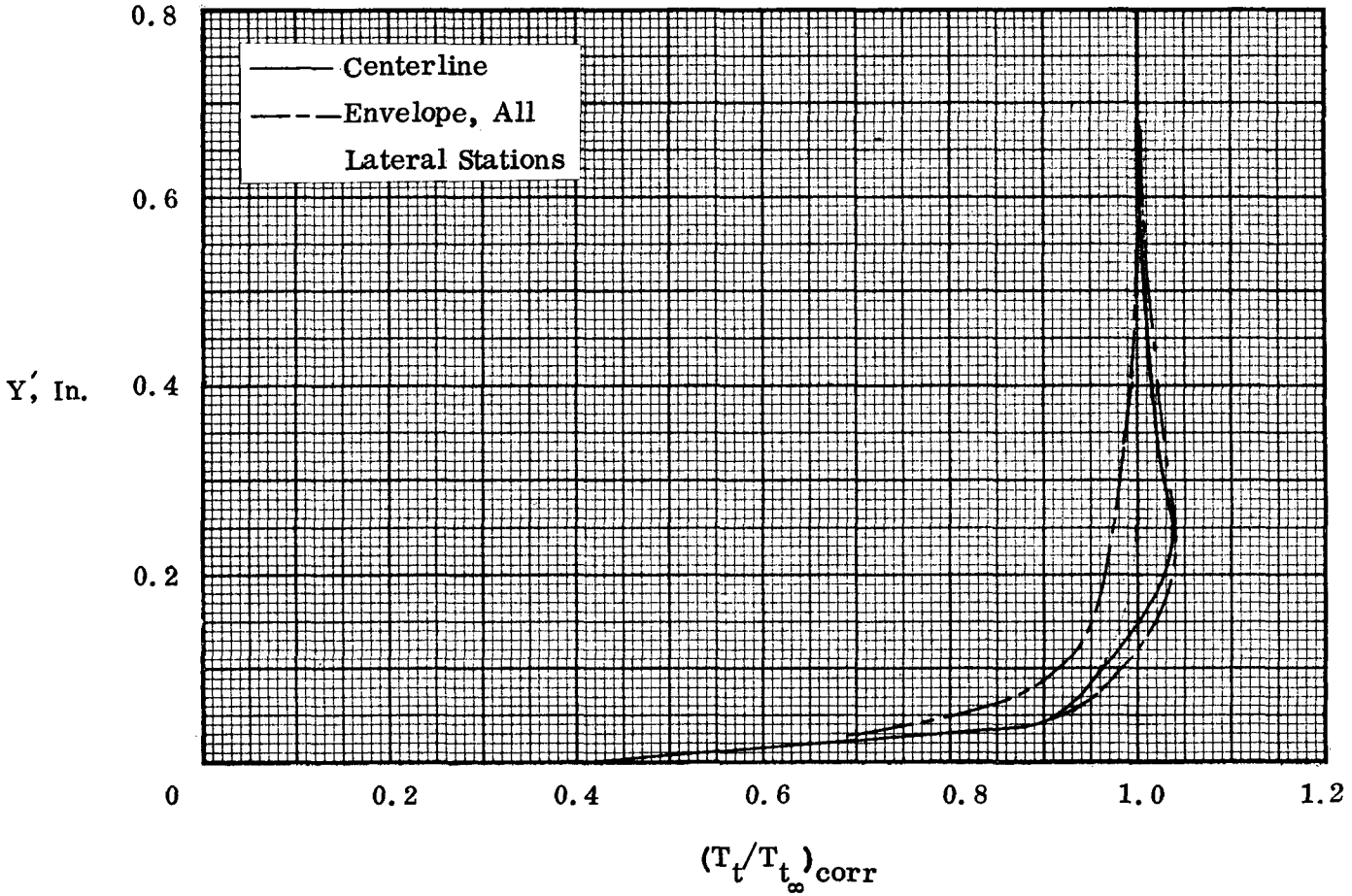

(c) Total Temperature

Figure 40. Concluded.

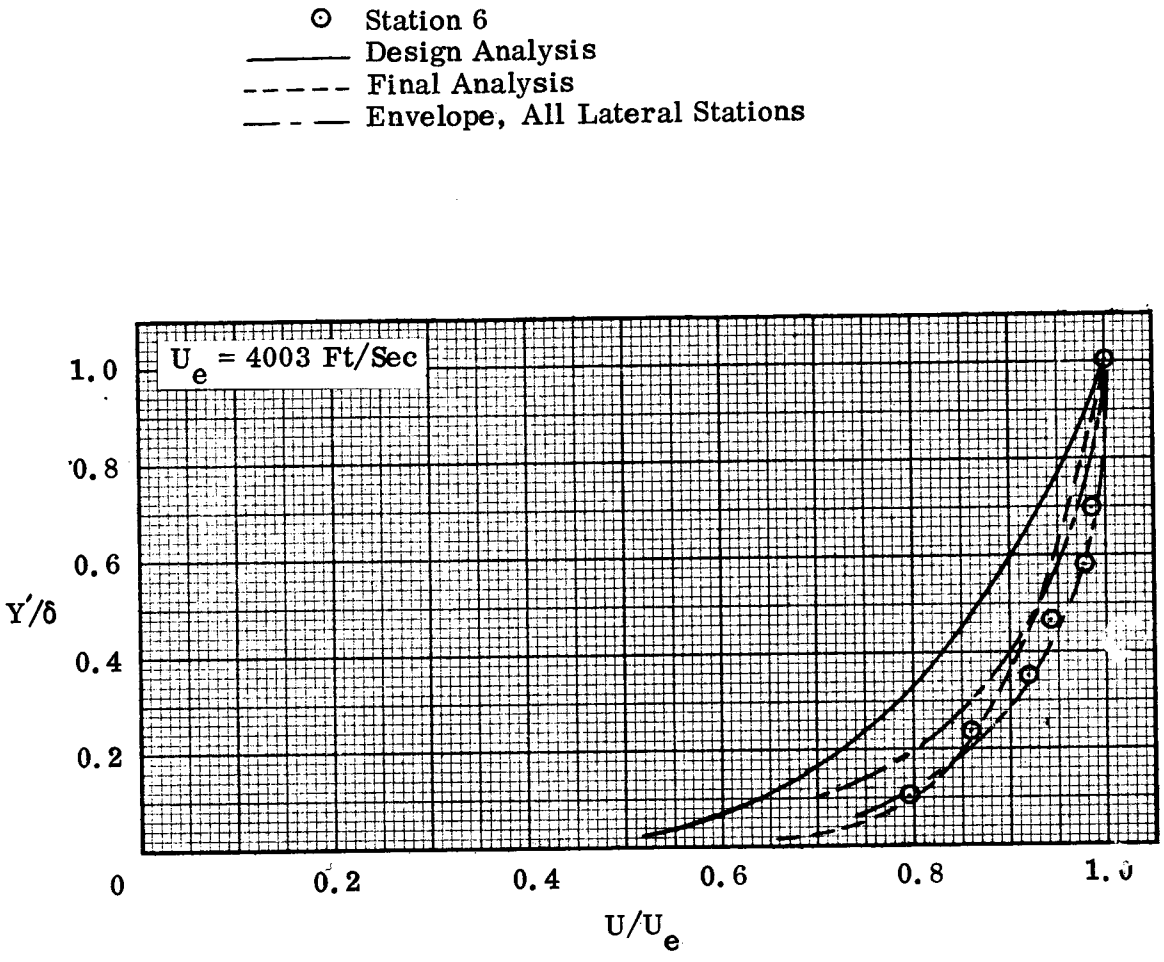

Figure 41. Boundary-Layer Velocity Profiles at Inlet-Entrance Station, All Lateral Stations.

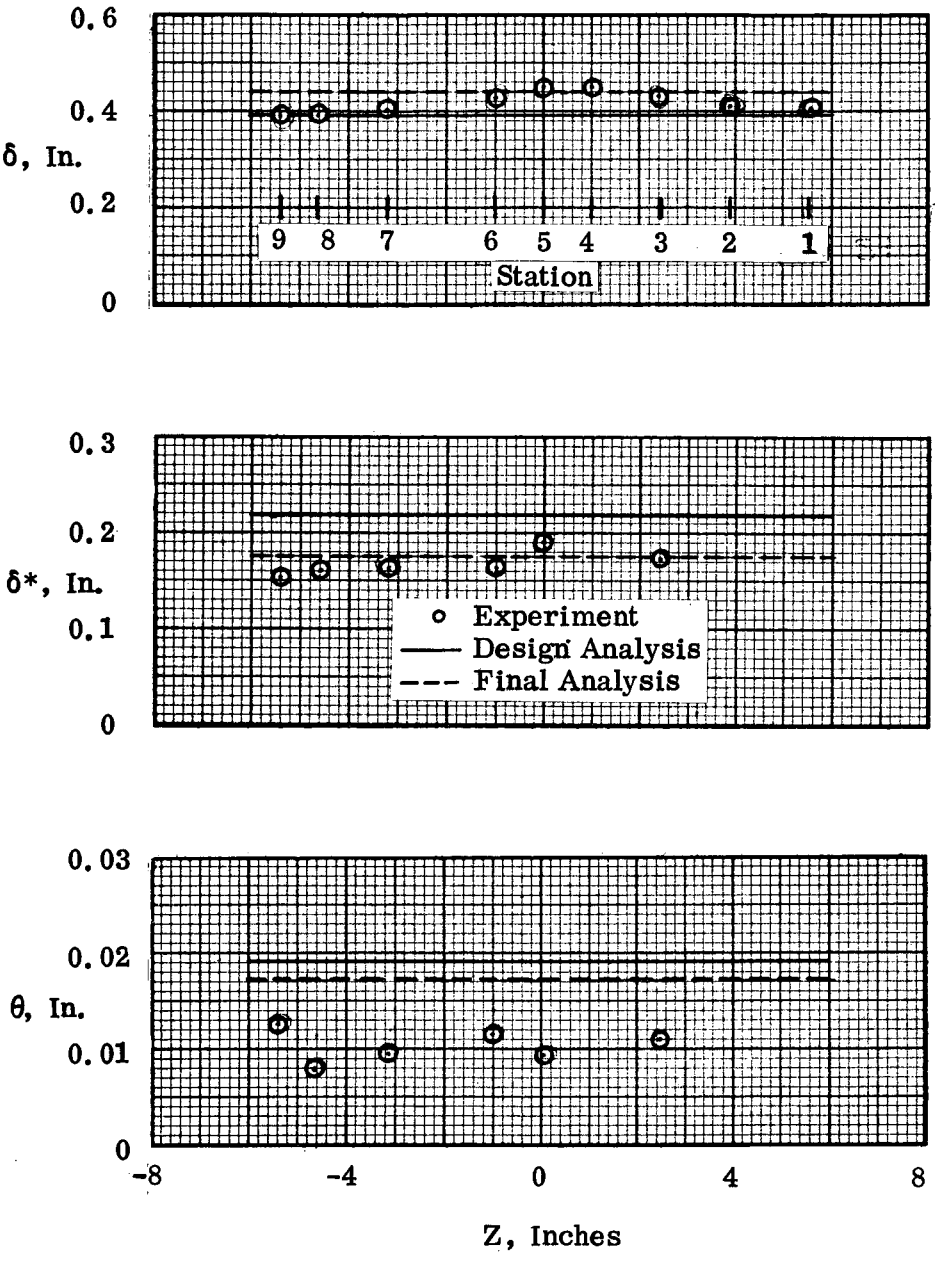

Figure 42. Boundary-Layer Integral Properties at Inlet-Entrance Station.

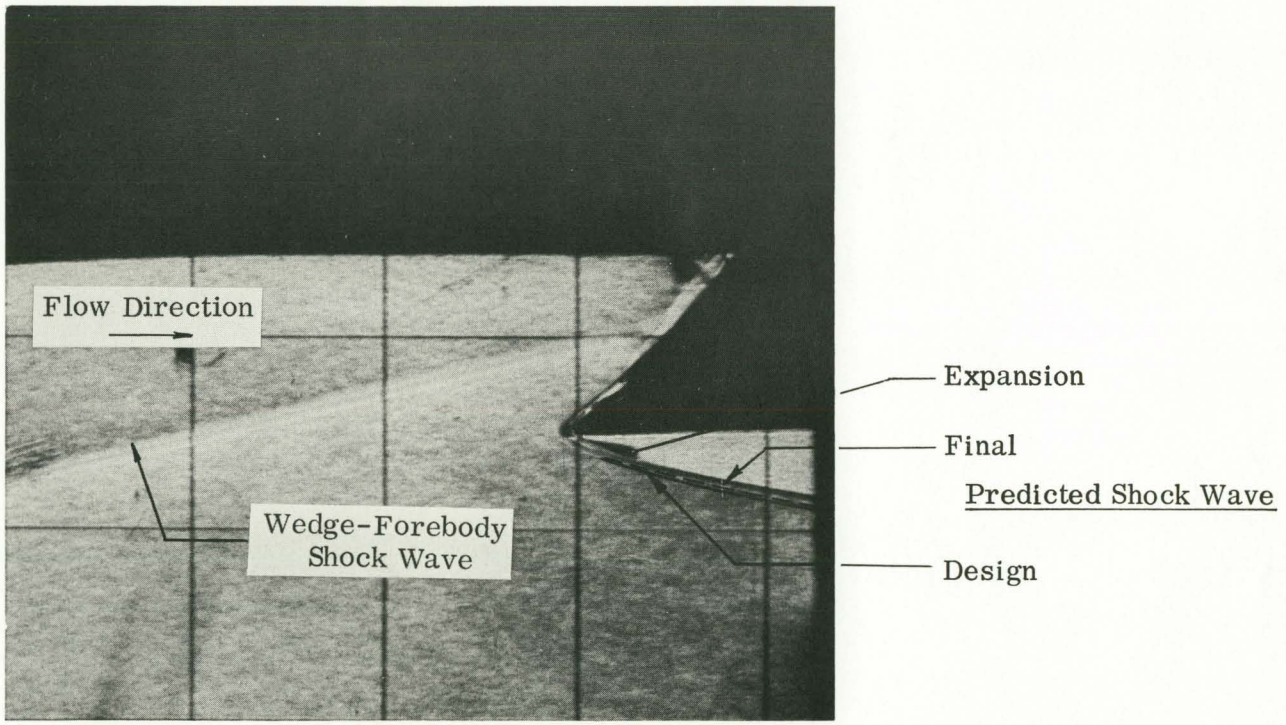

Figure 43. Cowl Shock Wave in Region of Cowl Leading Edge.

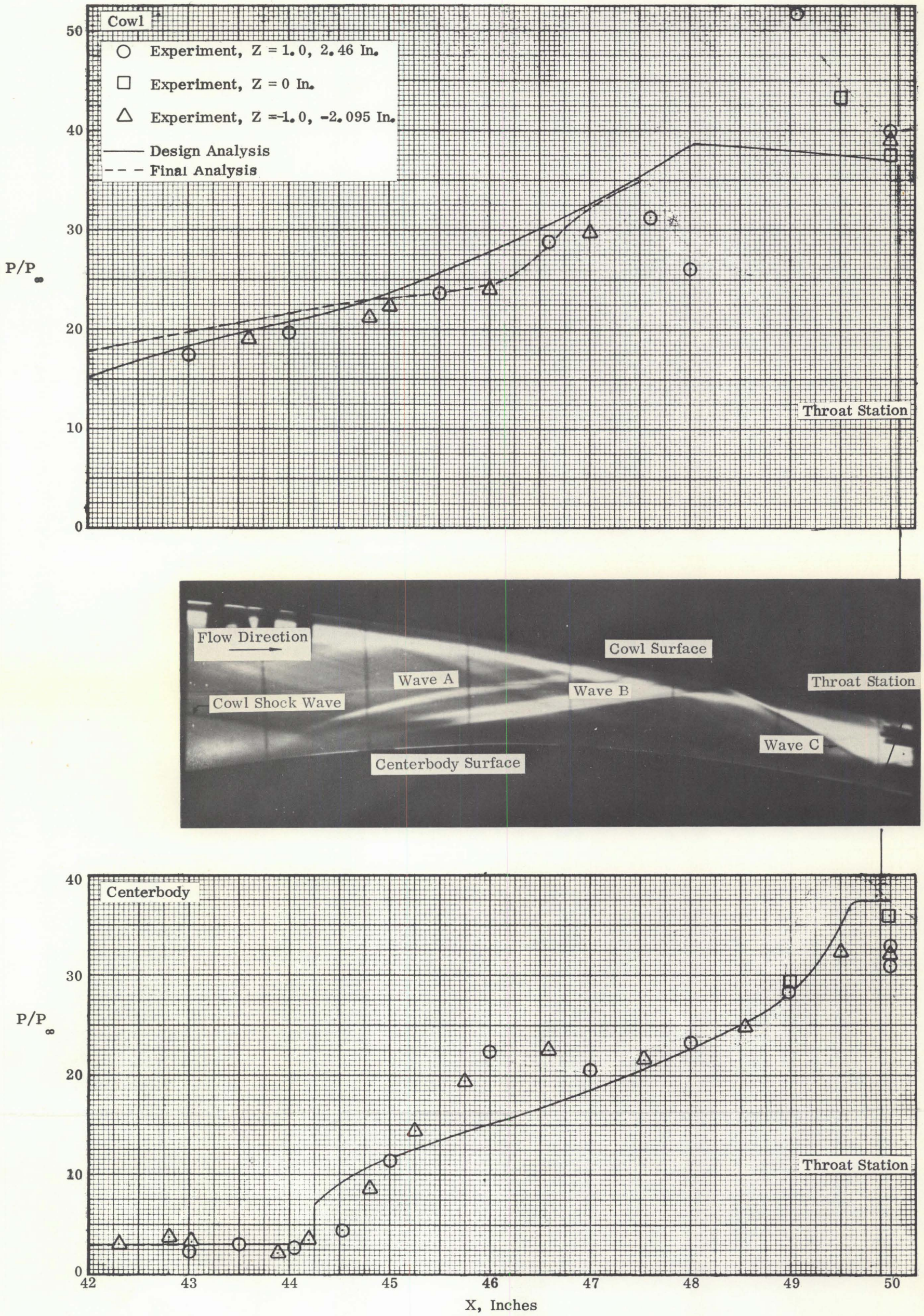

Figure 64. Surface Static-Pressure Distributions and Flowfield Pattern, P12 Inlet Model.

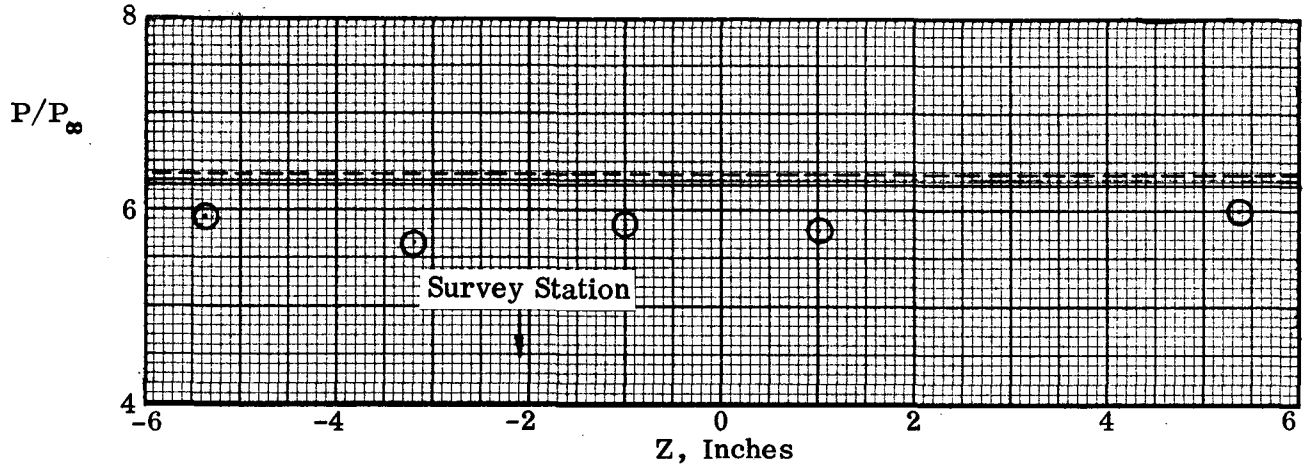

(a) Cowl Surface, Station X = 47.0 Inches

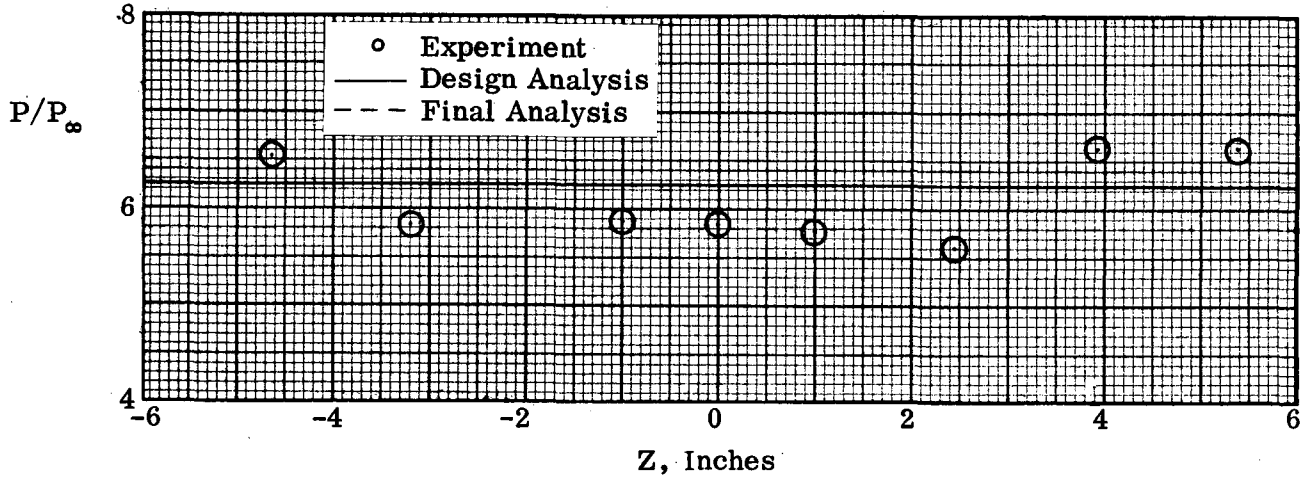

(b) Centerbody Surface, Station X = 47.0 Inches

Figure 45. Lateral Surface Static-Pressure Distributions at Throat Station, P2 Inlet Model.

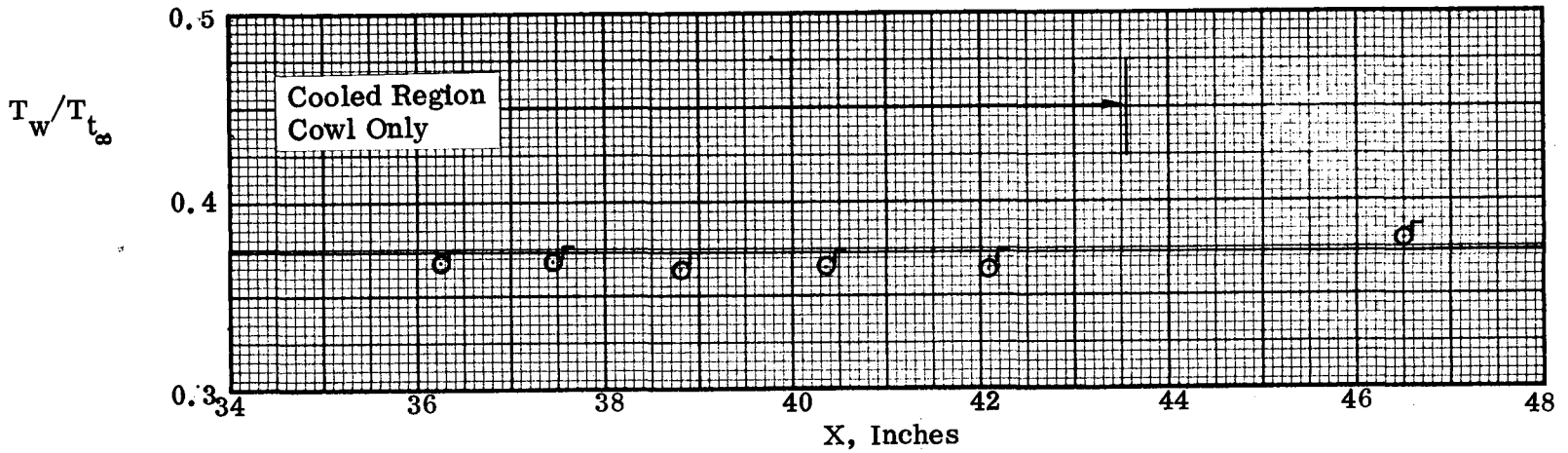

(a) Cowl Surface

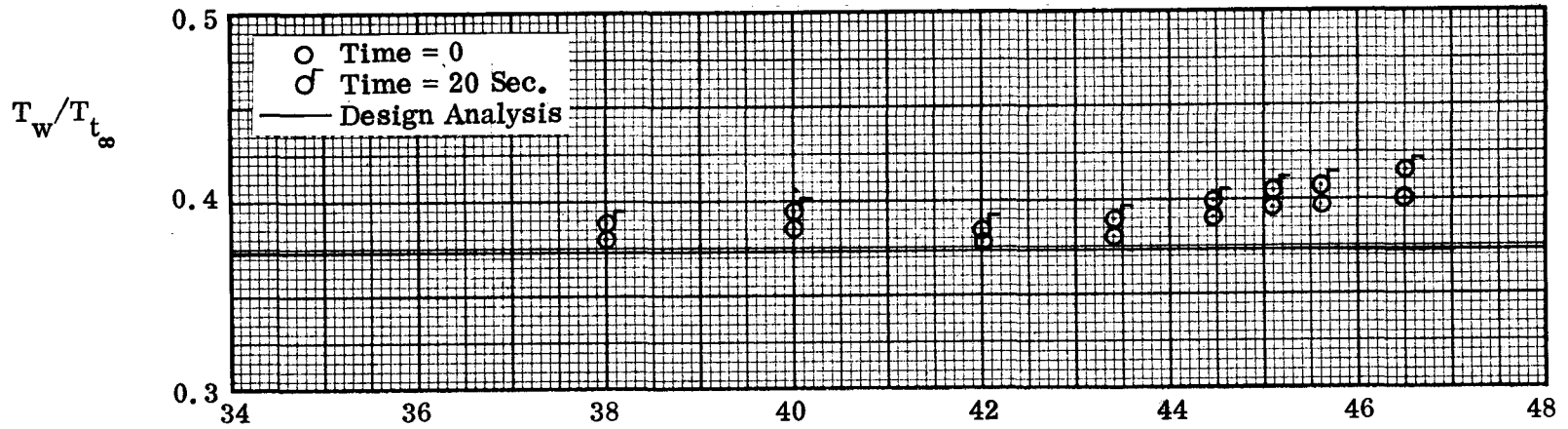

(b) Centerbody Surface

Figure 46. Surface Temperature Distributions, P2 Inlet Model.

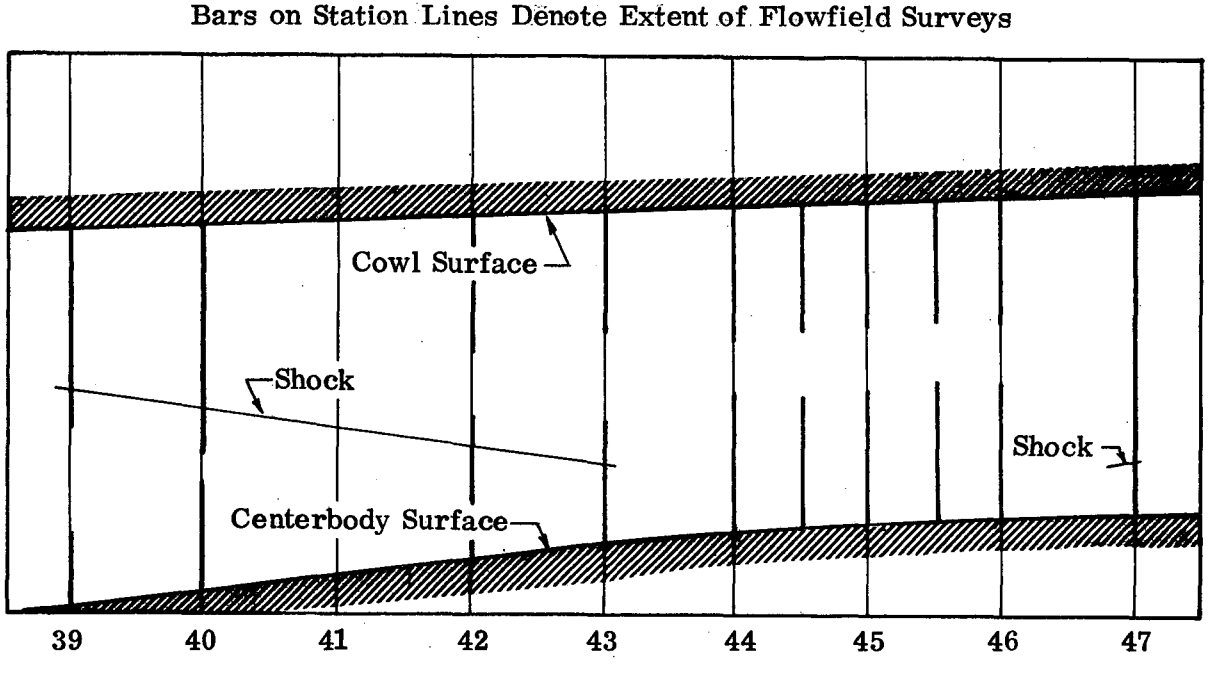

Figure 47. Probe Survey and Shock-Wave Locations, P2 Inlet Model.

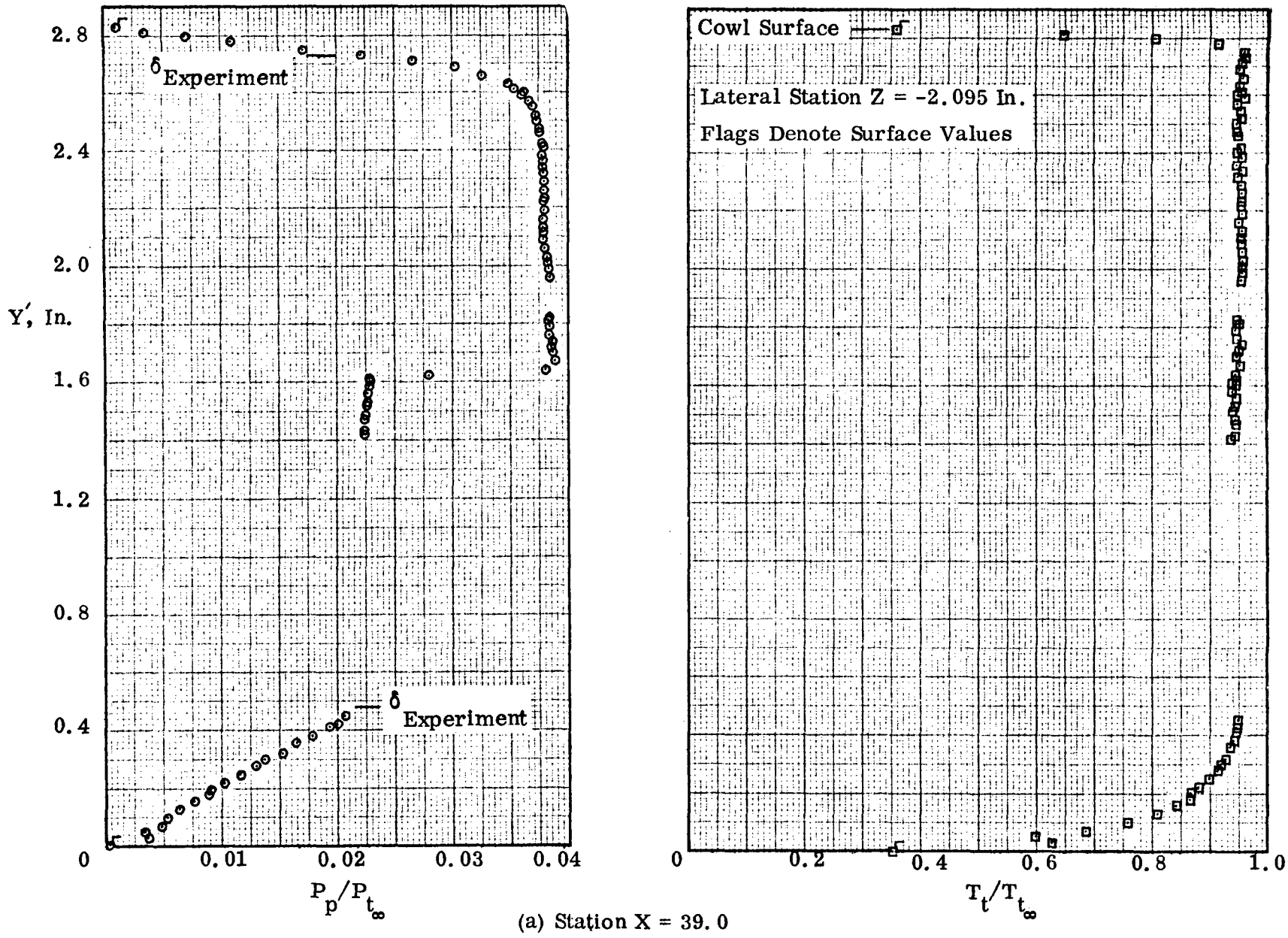

(a) Station X = 39.0

Figure 48. Pitot Pressure and Total Temperature Distributions, P2 Inlet Model.

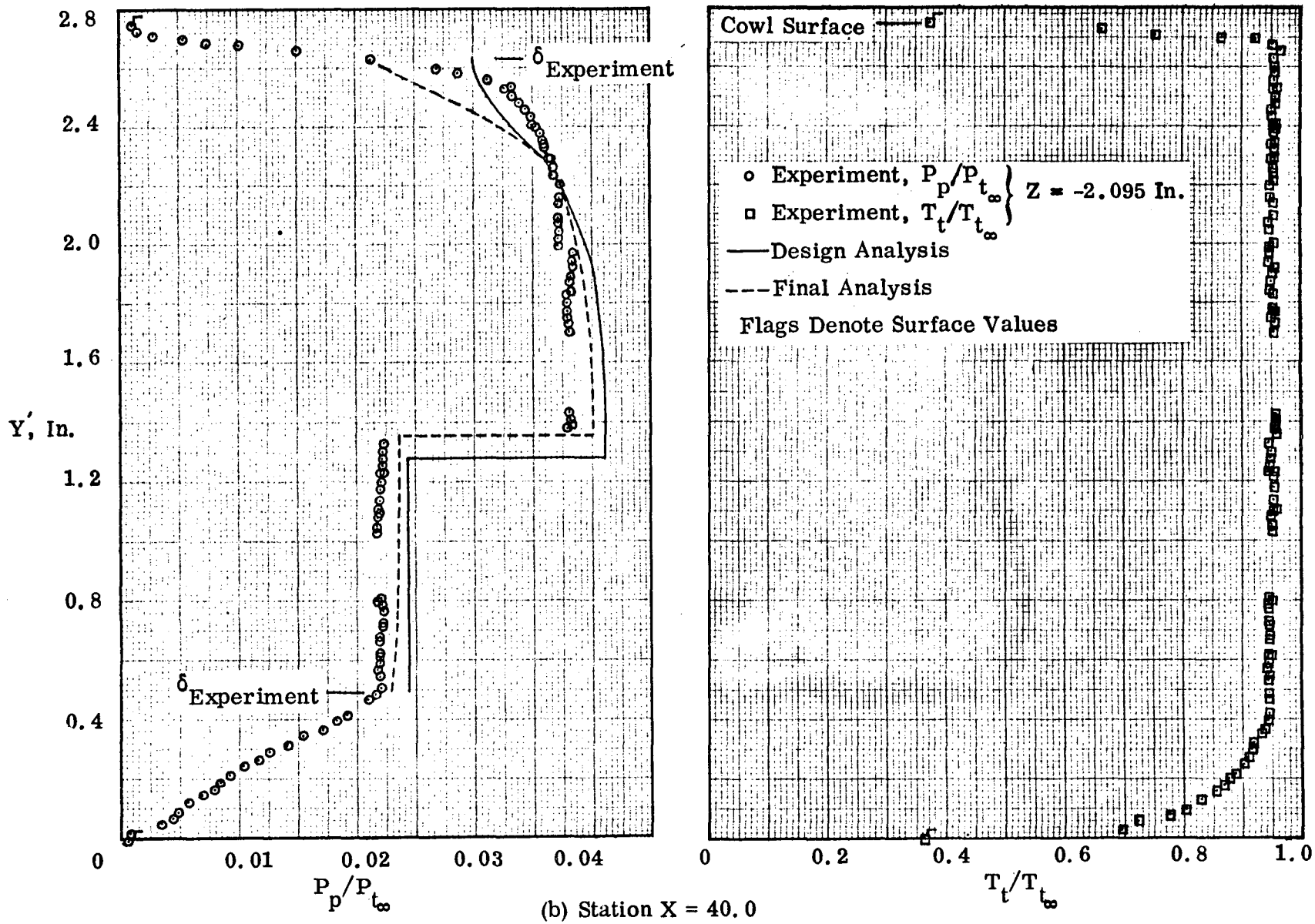

(b) Station X = 40.0

Figure 48. Continued.

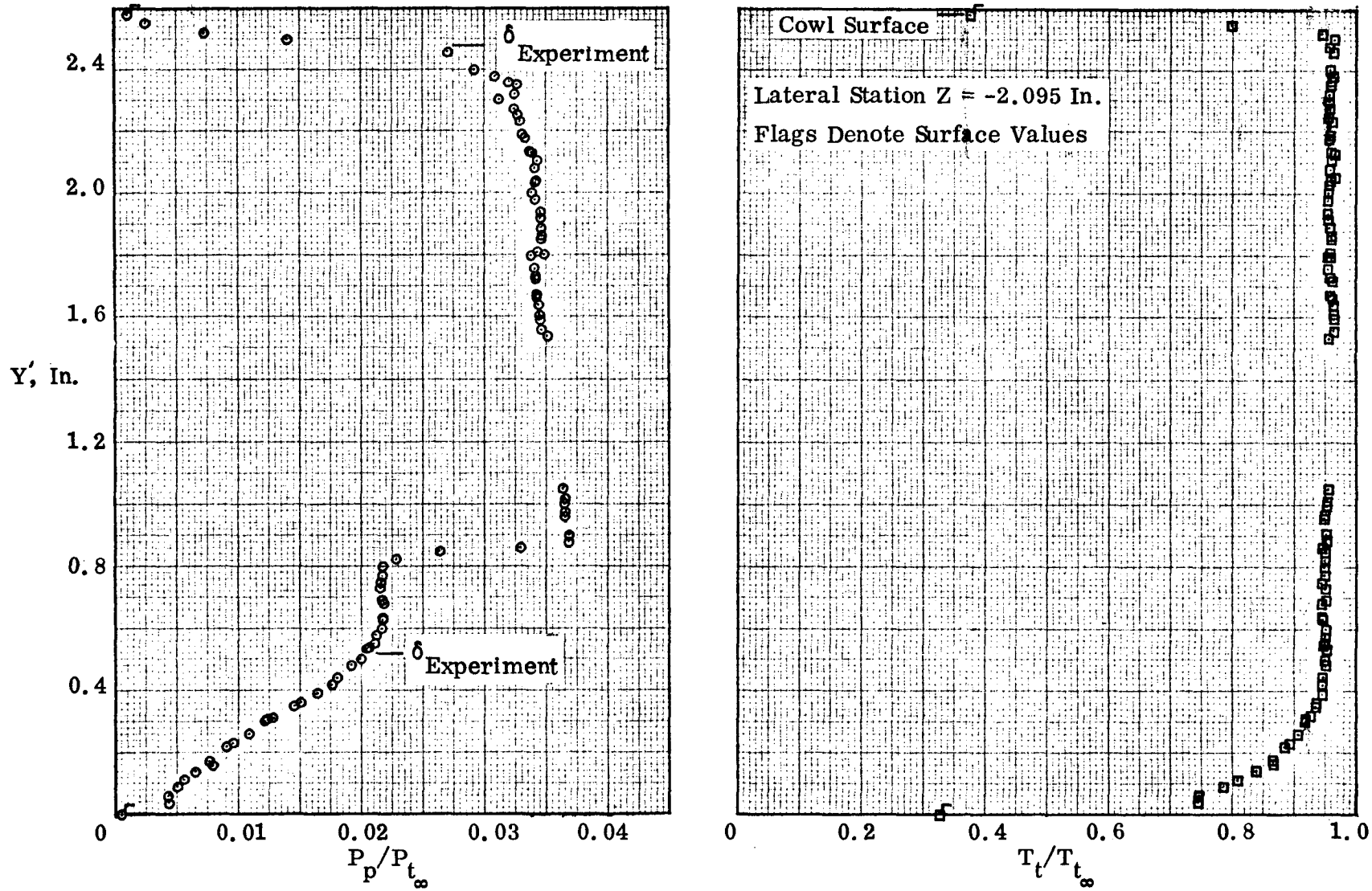

(c) Station X = 42.0

Figure 48. Continued.

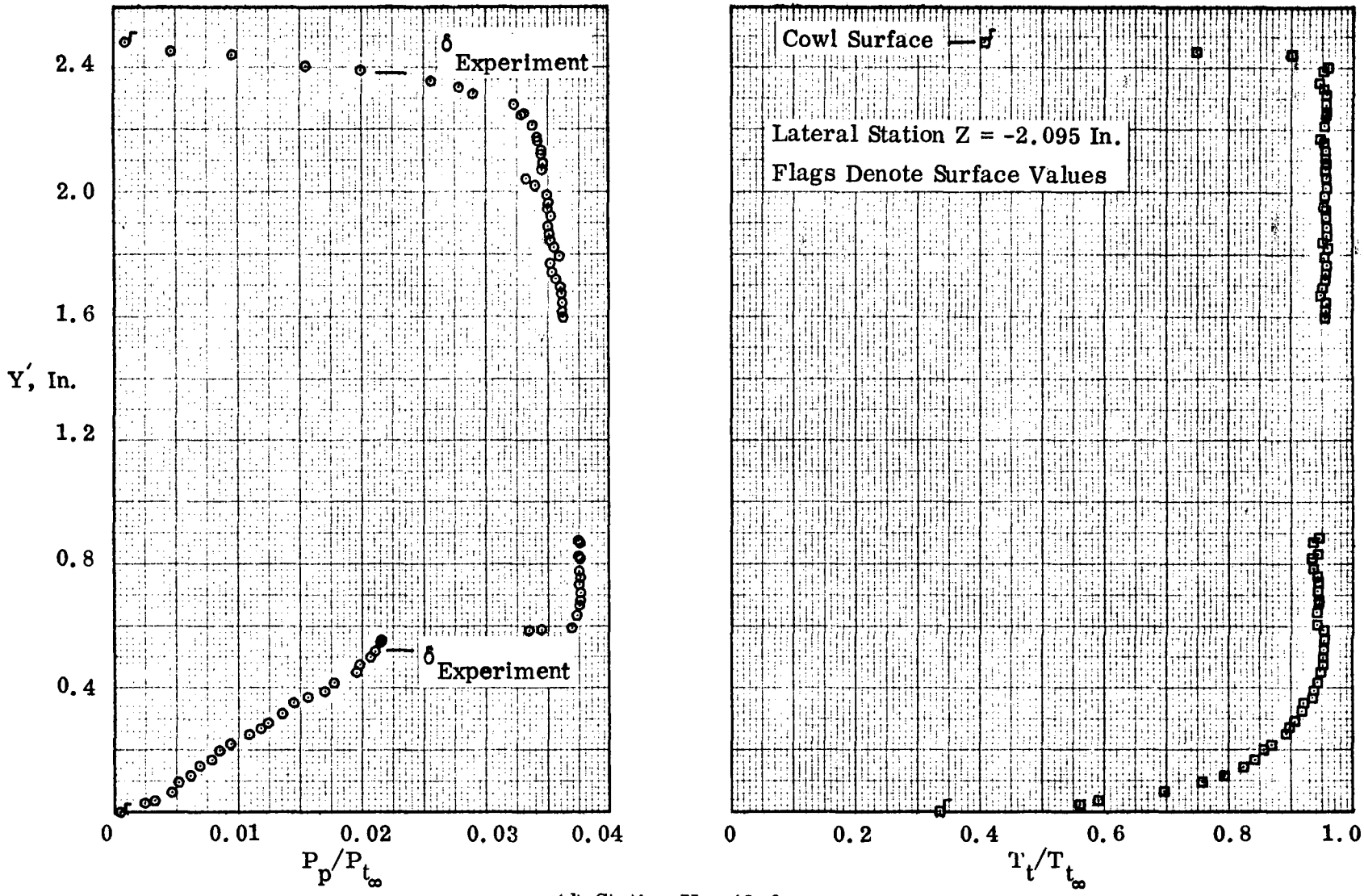

(d) Station X = 43.0

Figure 48. Continued.

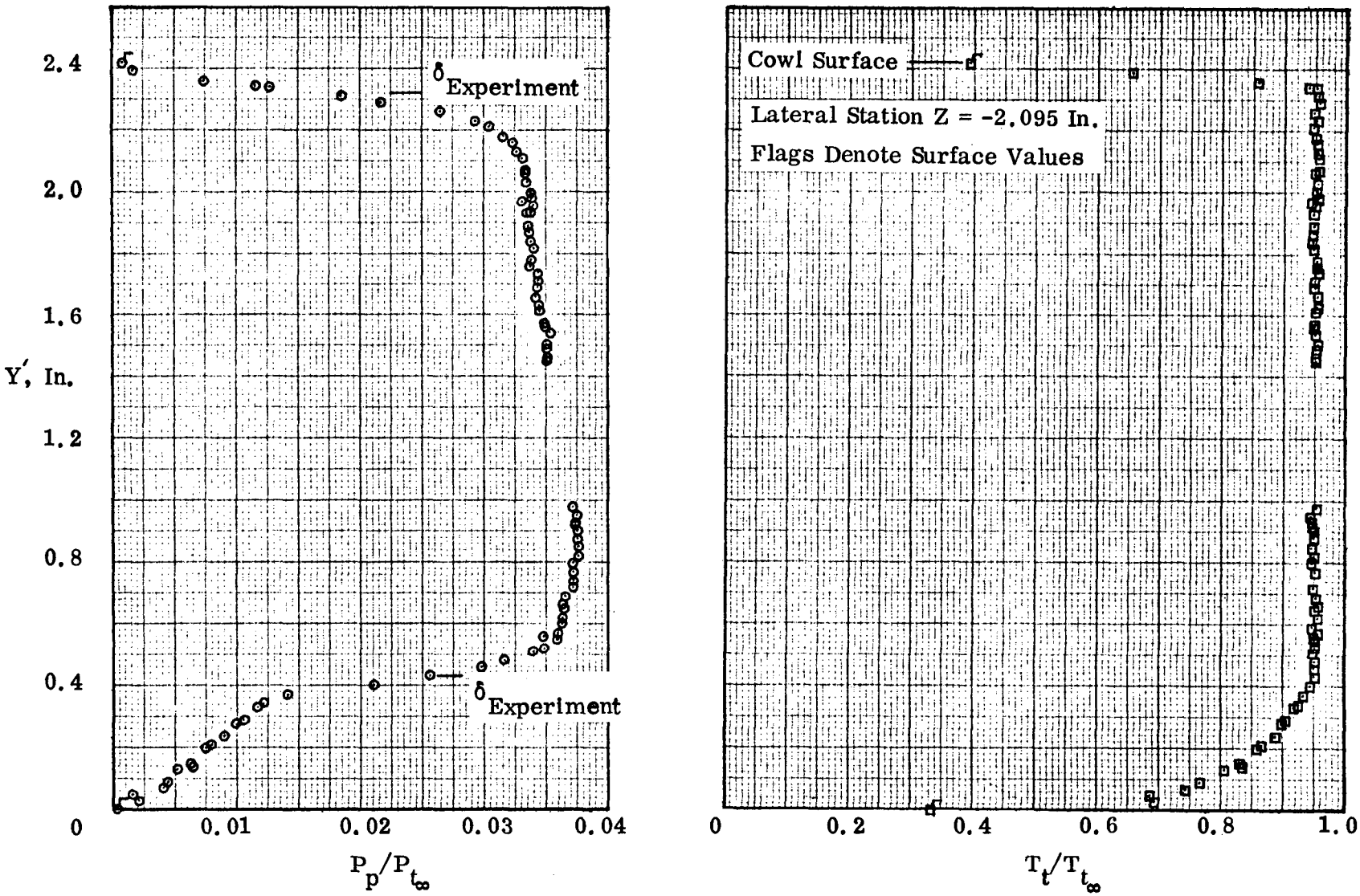

(e) Station X = 44.0

Figure 48. Continued.

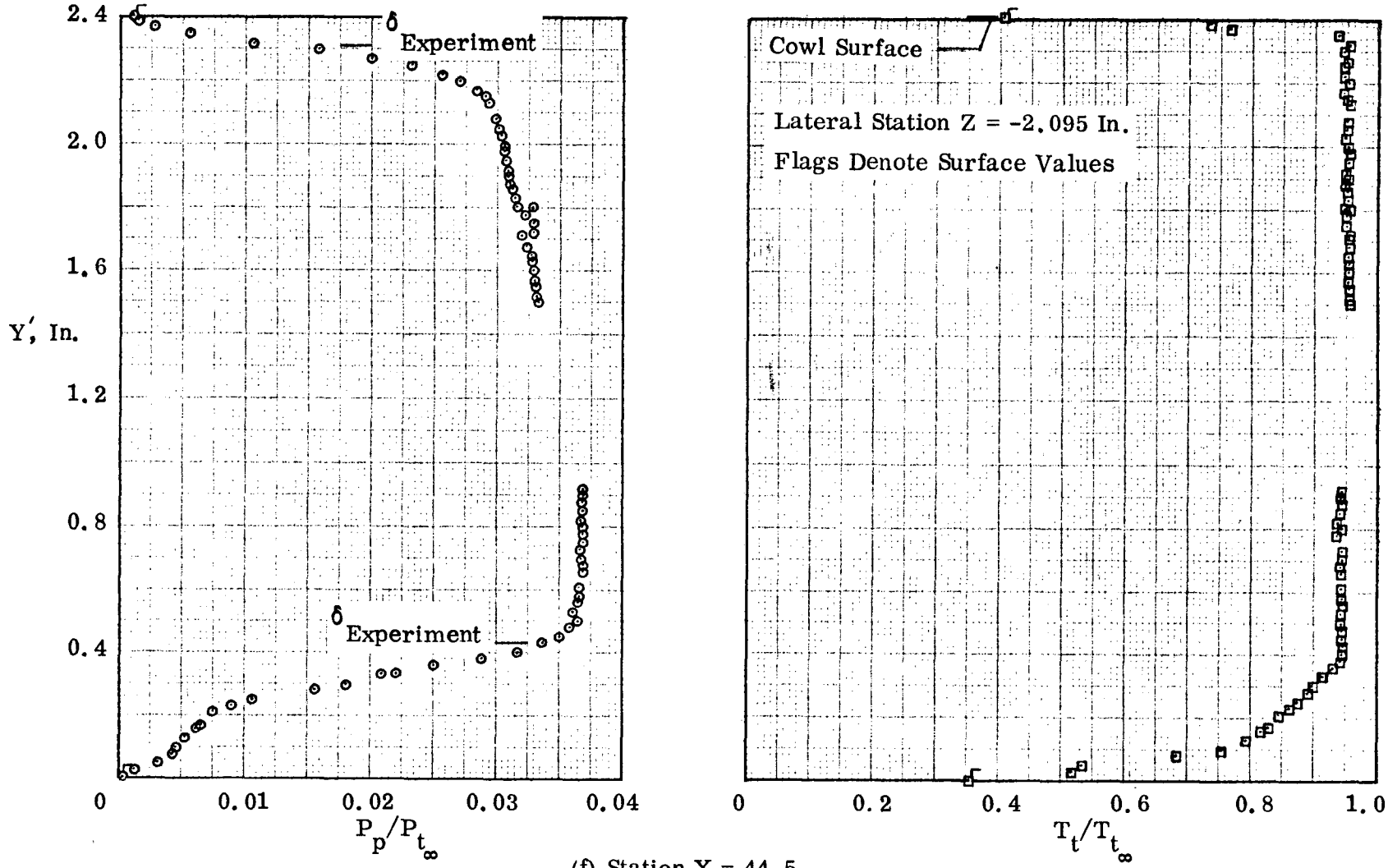

(f) Station X = 44.5

Figure 48. Continued.

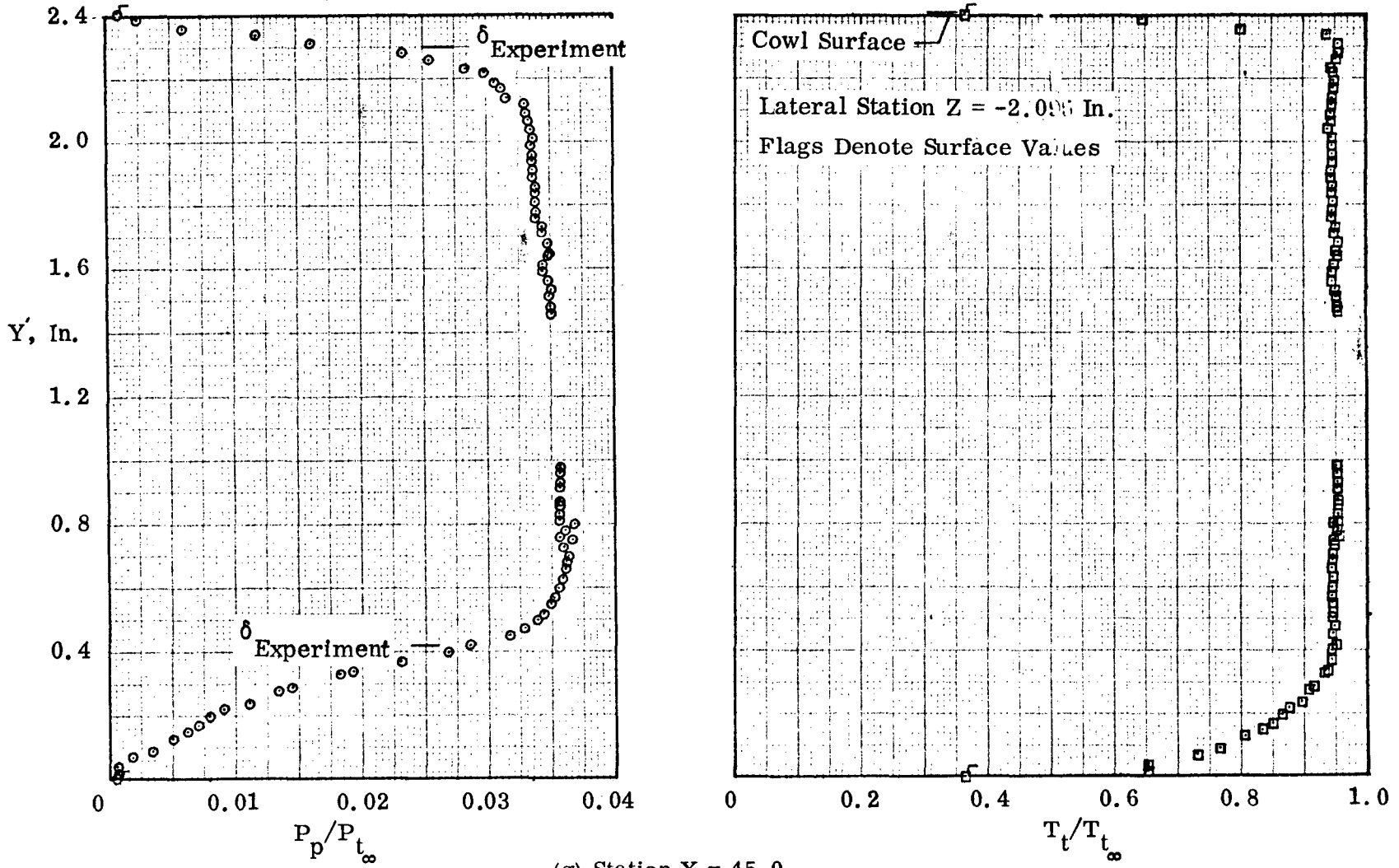

(g) Station X = 45.0

Figure 48. Continued.

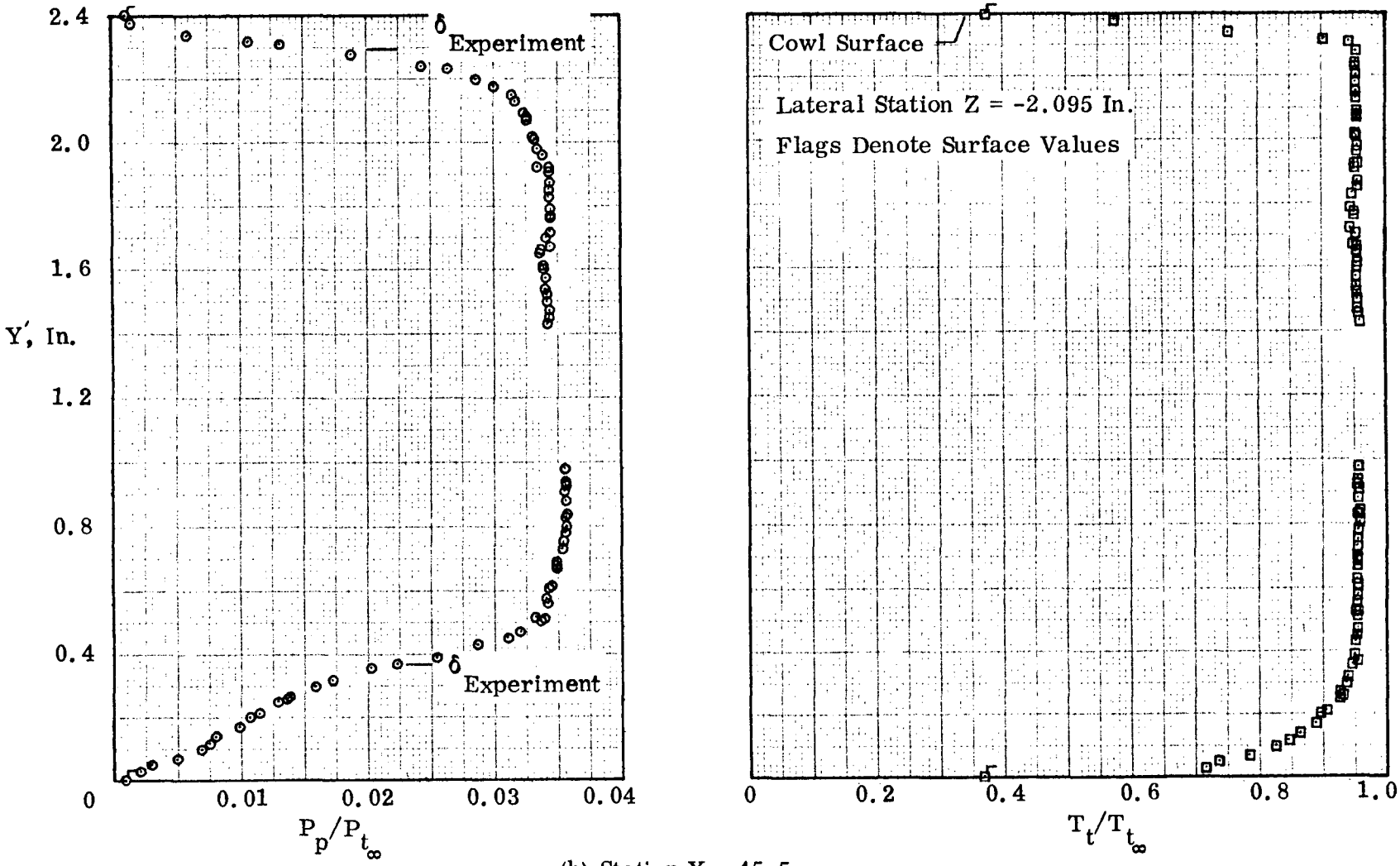

(h) Station X = 45.5

Figure 48. Continued.

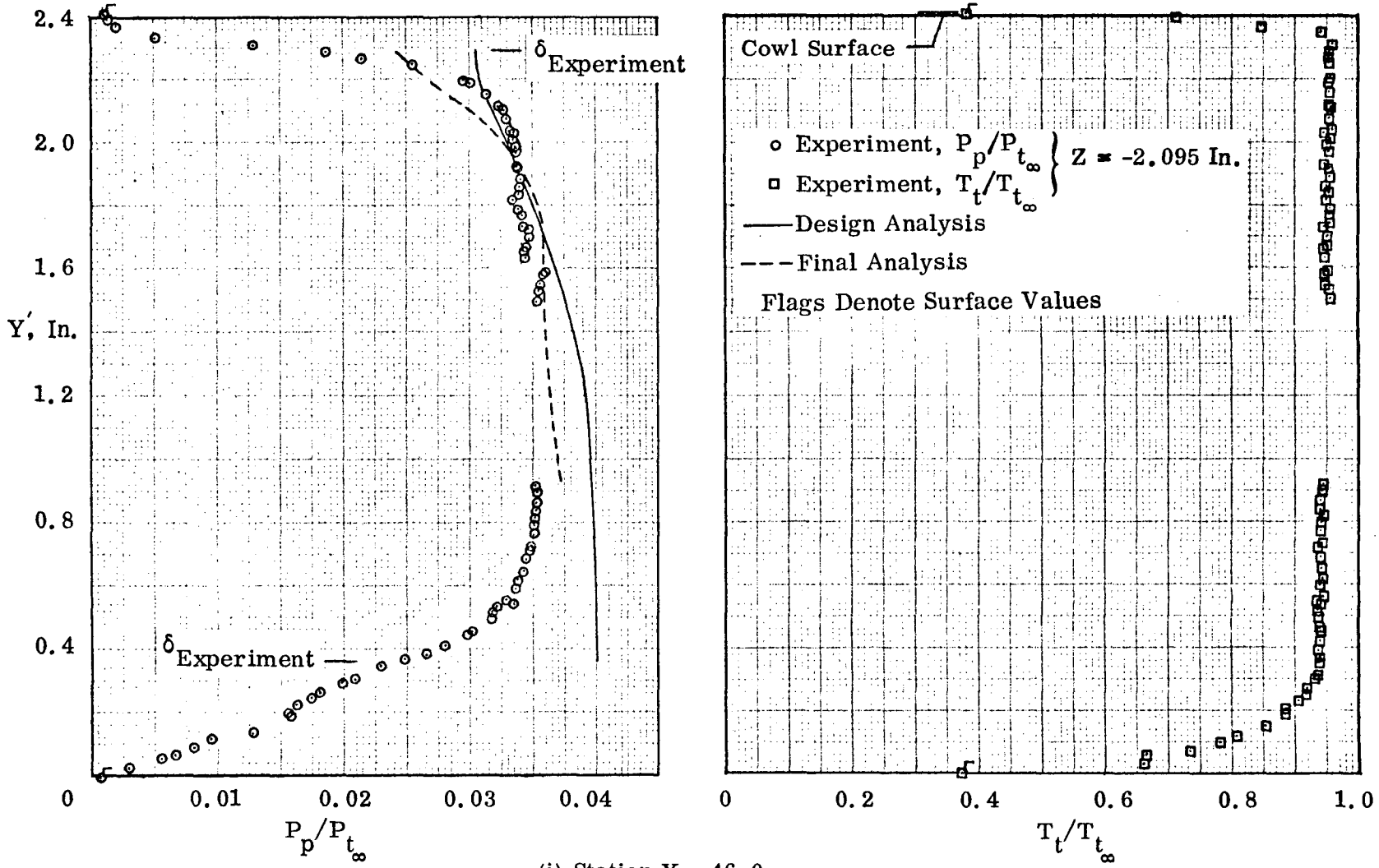

(i) Station X = 46.0

Figure 48. Continued.

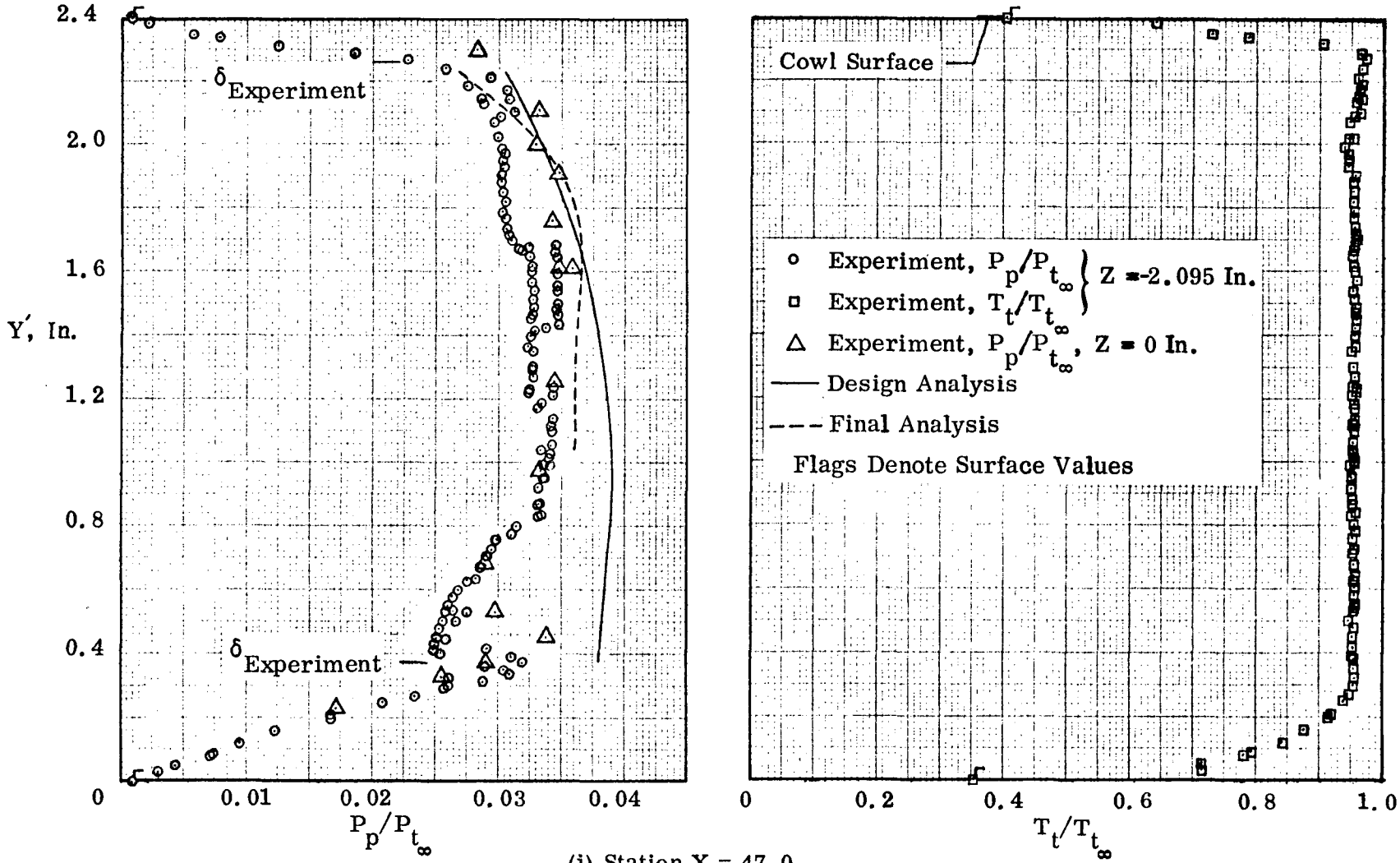

(j) Station X = 47.0

Figure 48. Concluded.

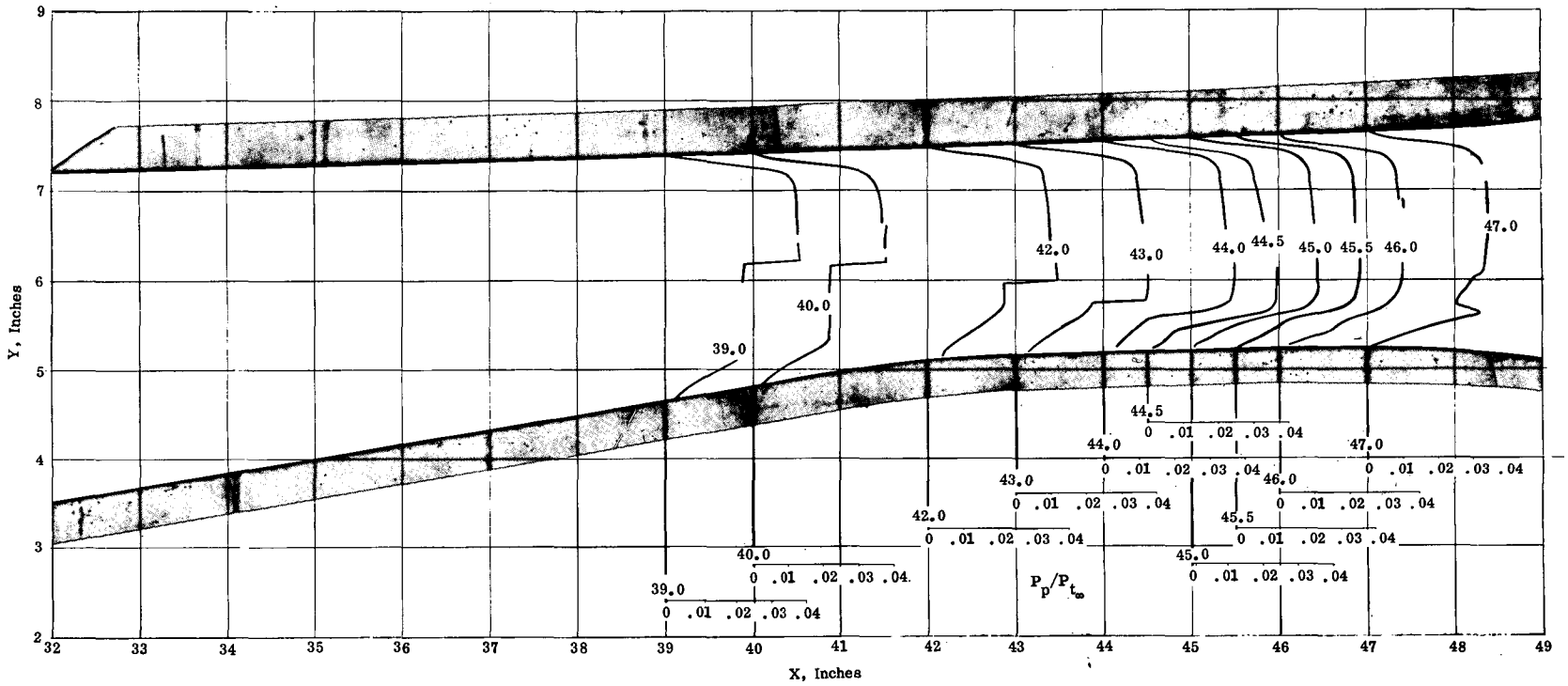

Figure 49. Summary of Pitot-Pressure Distributions, P2 Inlet Model.

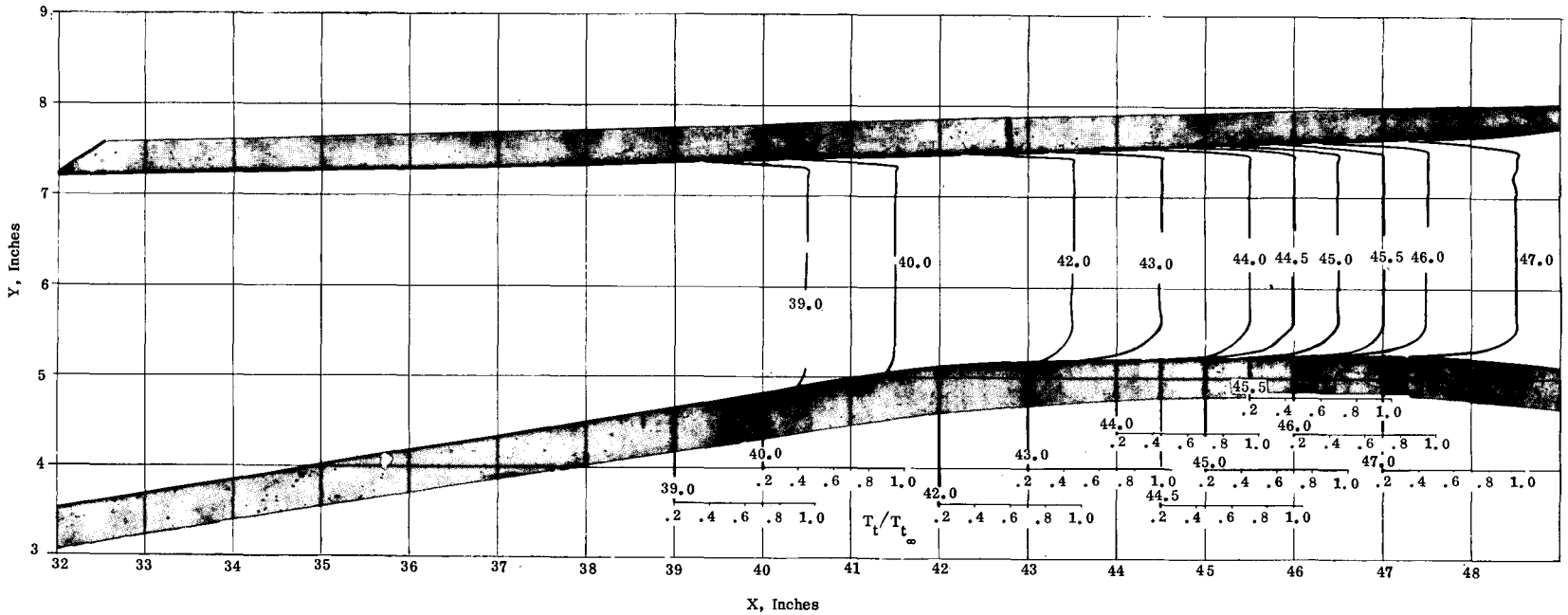

Figure 50. Summary of Total-Temperature Distributions, P2 Inlet Model.

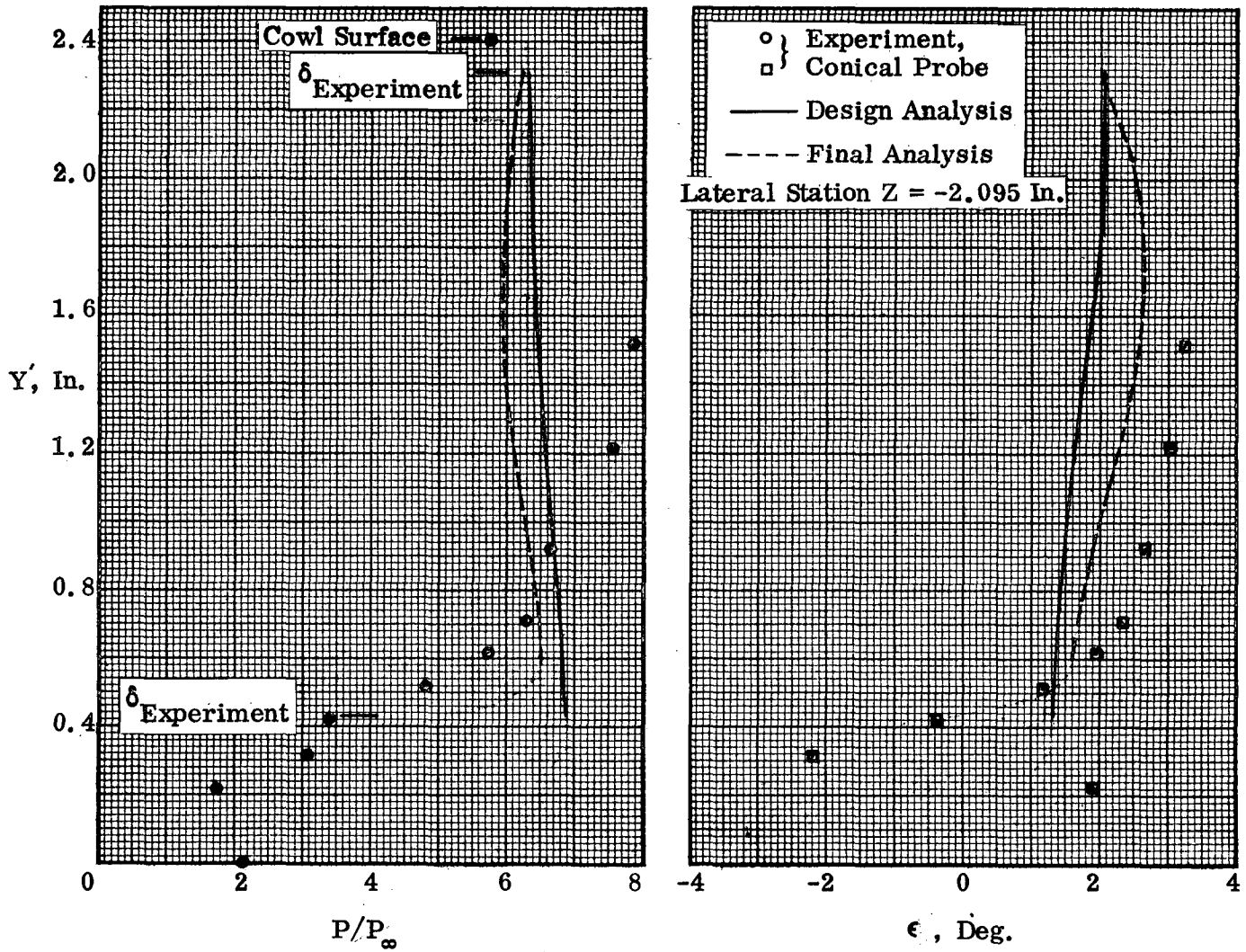

(a) Station X = 44.5 Inches

Figure 51. Static Pressure and Flow Angle Distributions, P2 Inlet Model.

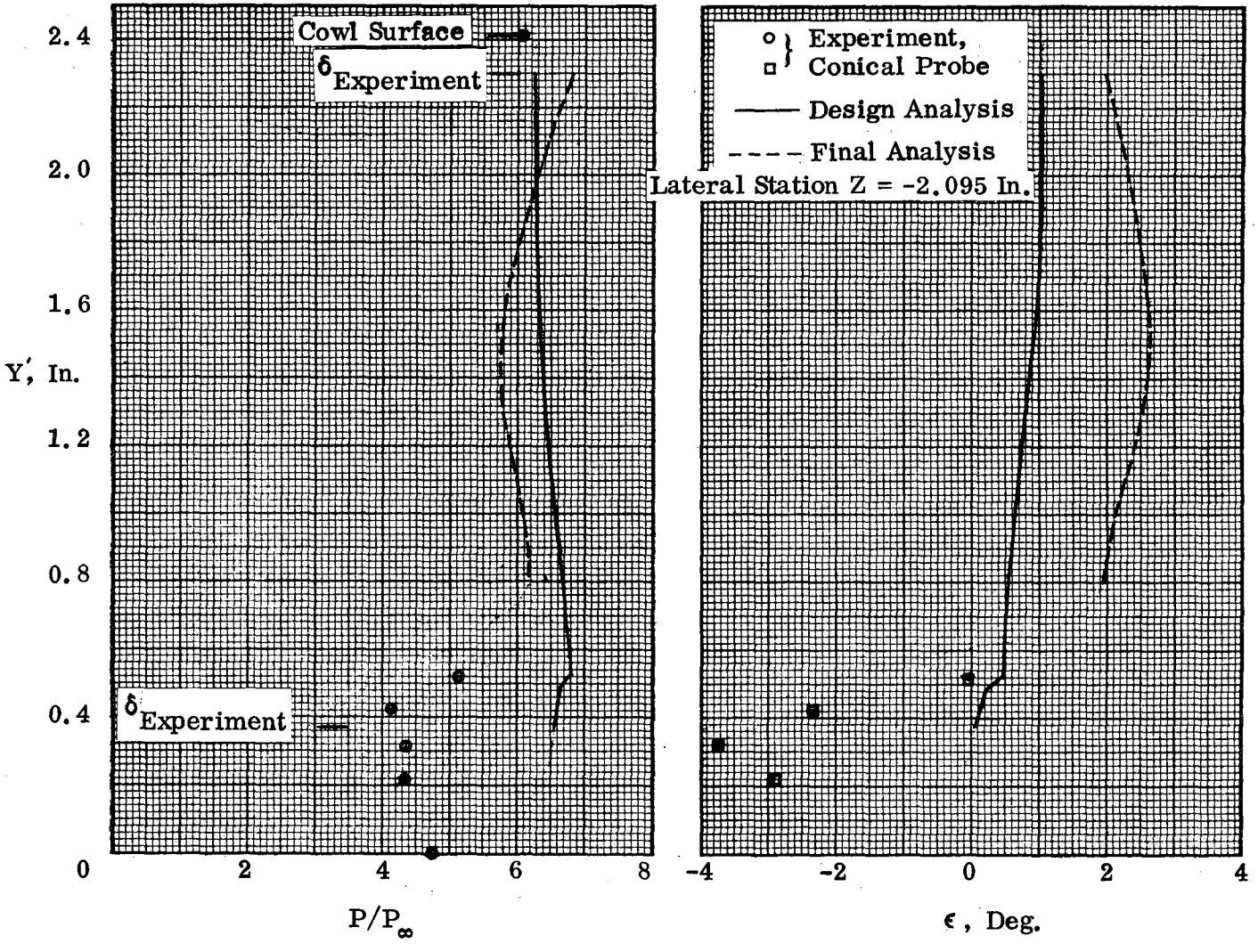

(b) Station X = 45.5 Inches

Figure 51. Continued.

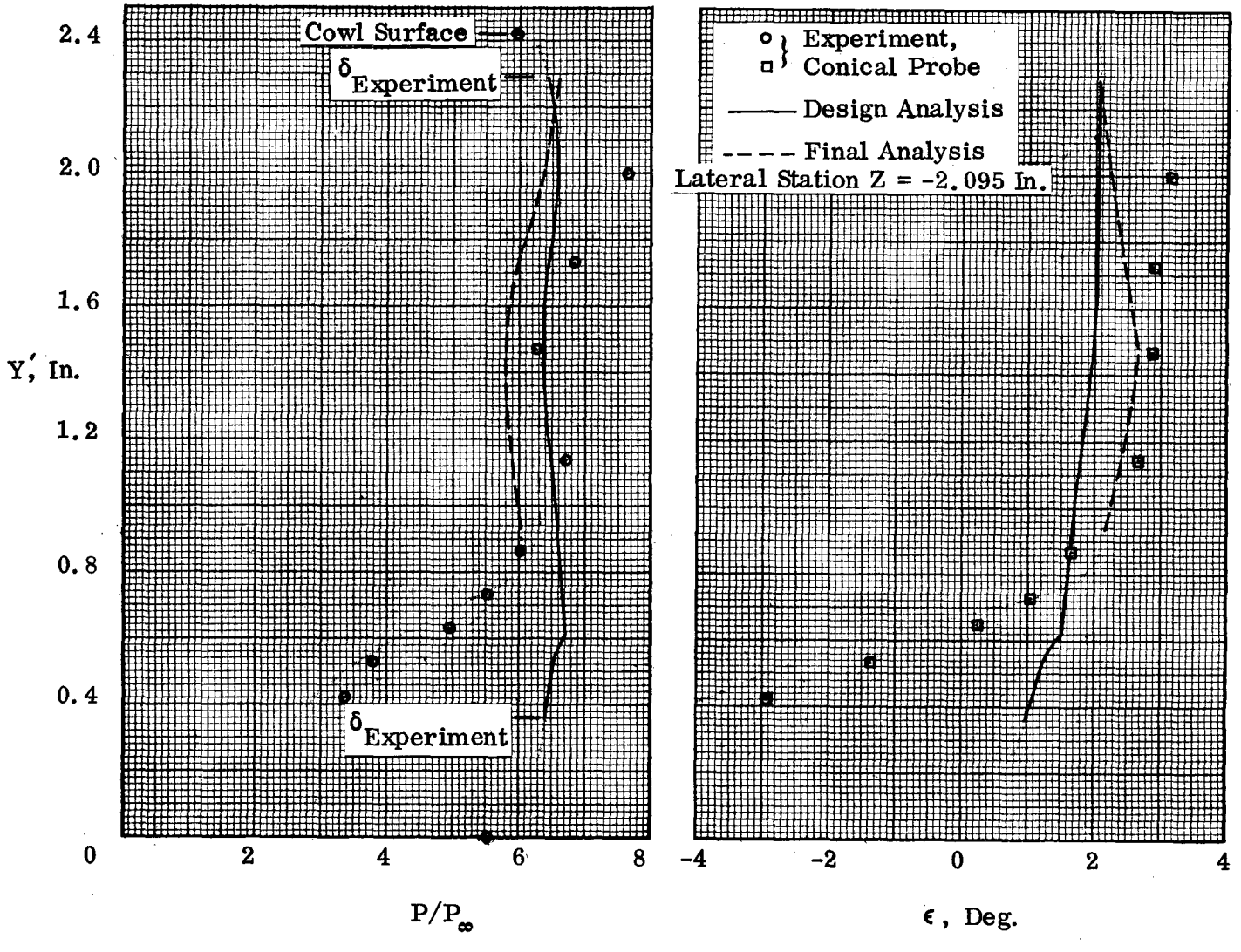

(c) Station X = 46.0 Inches

Figure 51. Continued.

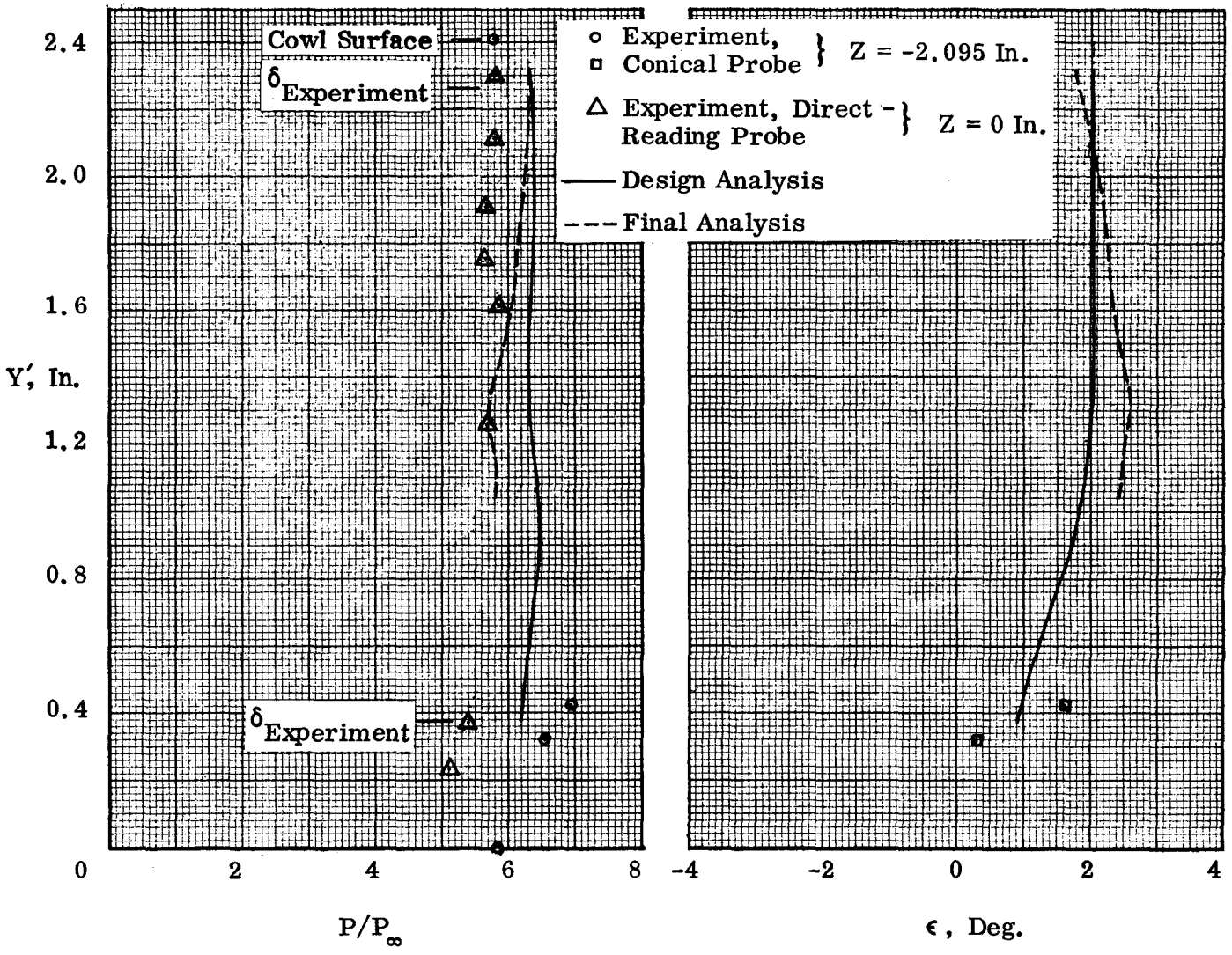

(d) Station X = 47.0 Inches

Figure 51. Concluded.

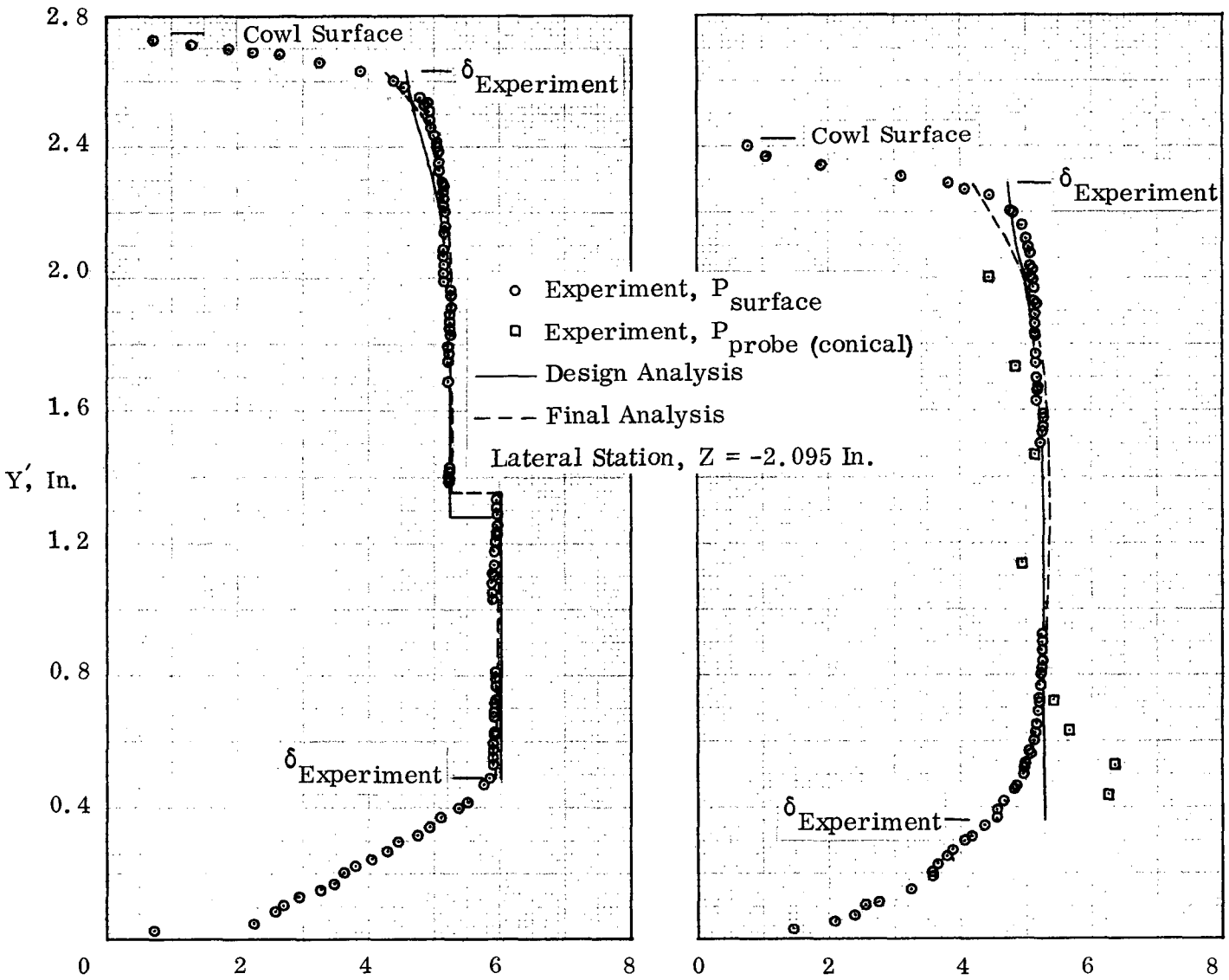

(a) Station X = 40.0 Inches

(b) Station X = 46.0 Inches

Figure 52. Mach Number Distributions, P2 Inlet Model.

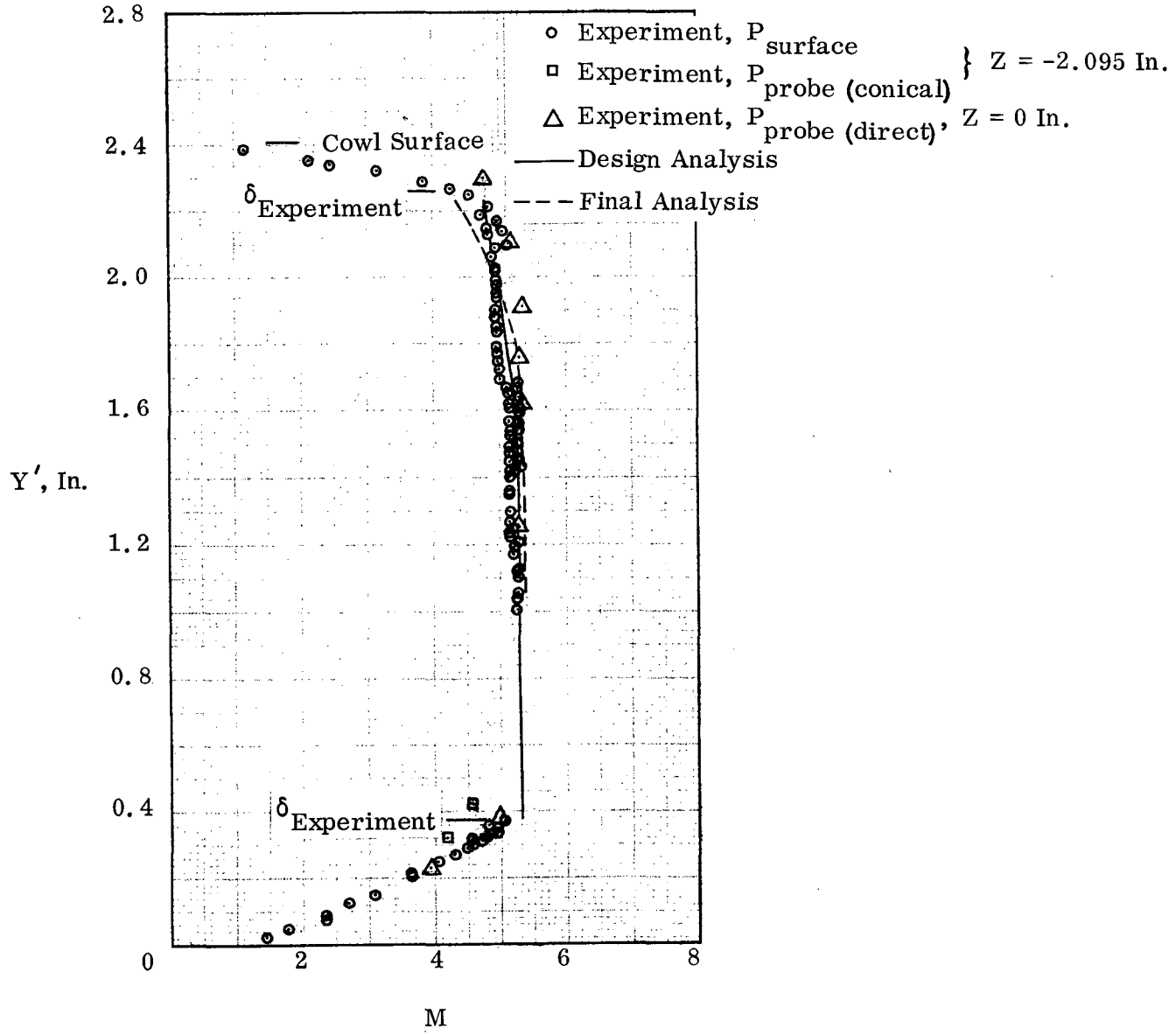

(c) Station X = 47.0 Inches

Figure 52. Concluded.

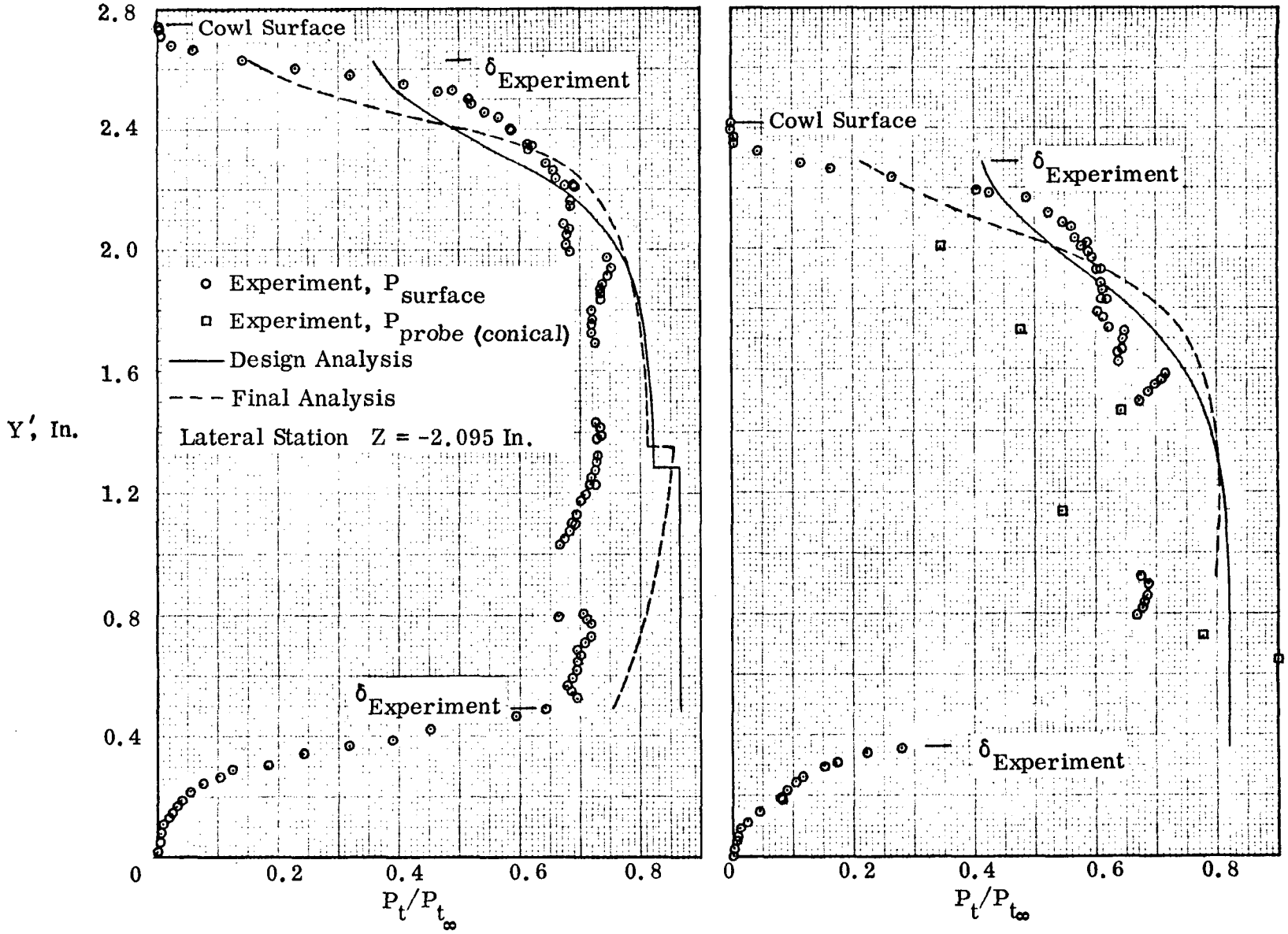

(a) Station X = 40.0 Inches

(b) Station X = 46.0 Inches

Figure 53. Total-Pressure Recovery Distributions, P2 Inlet Model.

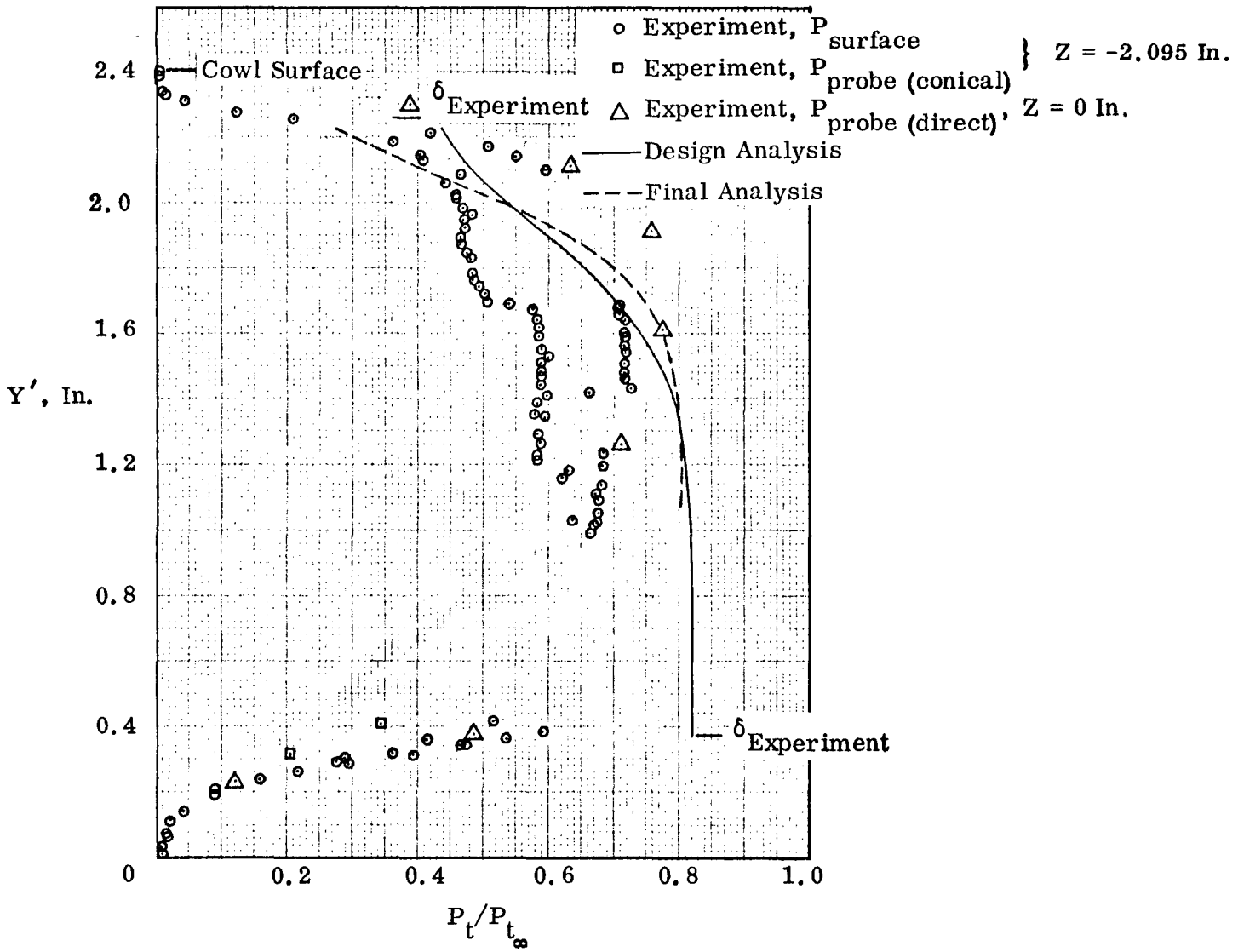

(c) Station X = 47 Inches

Figure 53. Concluded.

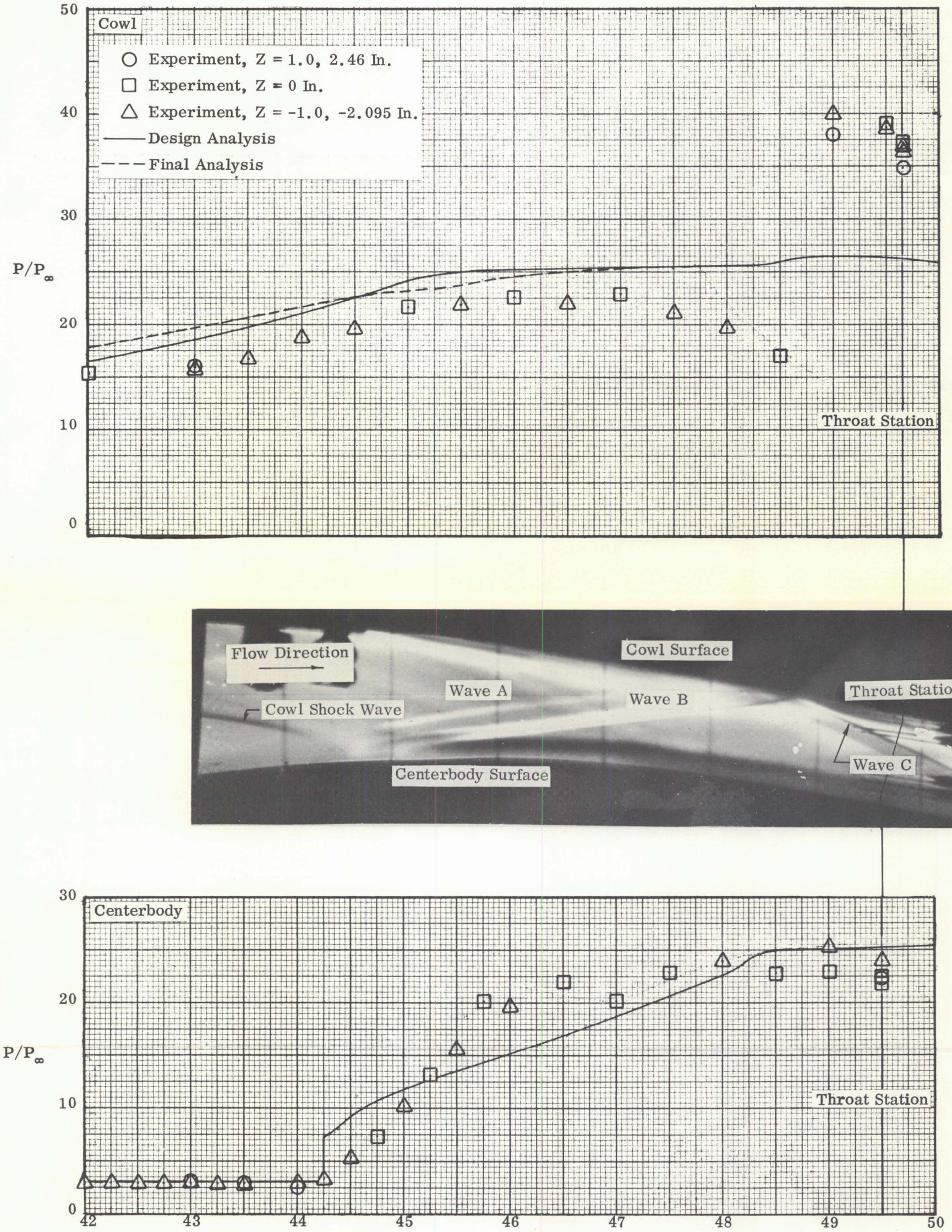

Figure 54. Surface Static-Pressure Distributions and Flowfield Pattern, P8 Inlet Model.

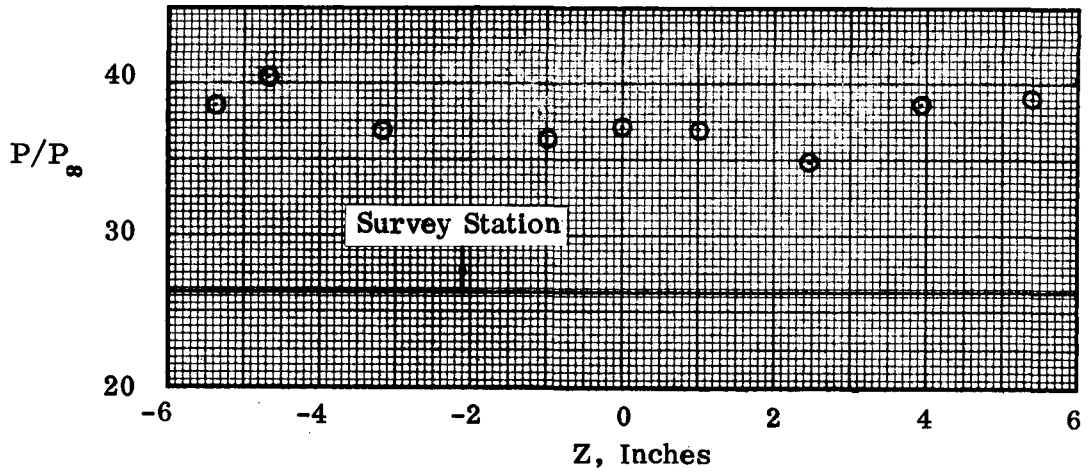

(a) Cowl Surface, Station X = 49.66 Inches

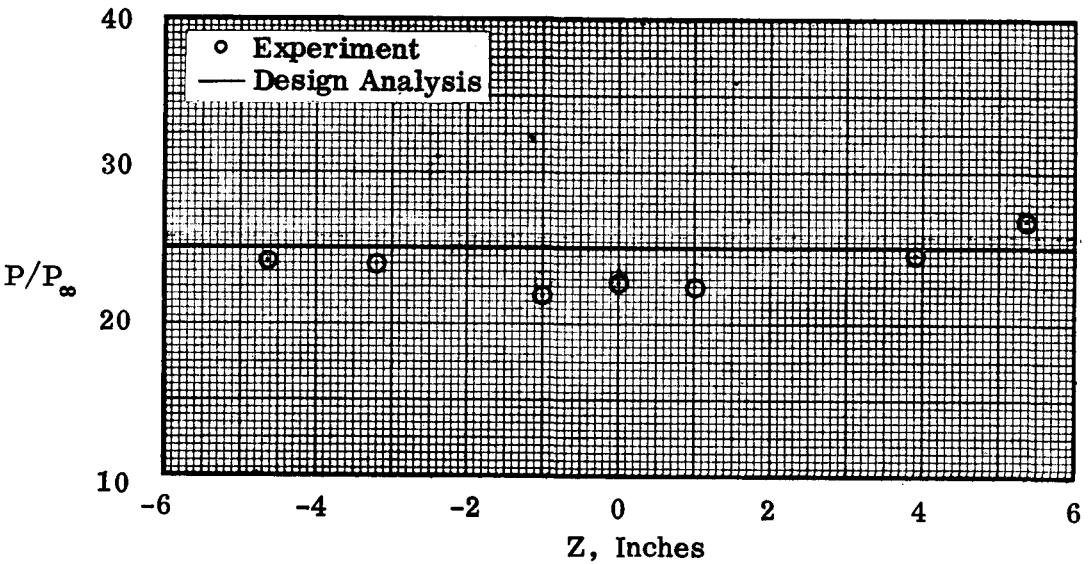

(b) Centerbody Surface, Station X = 49.5 Inches

Figure 55. Lateral Surface Static-Pressure Distributions at Throat Station, P8 Inlet Model.

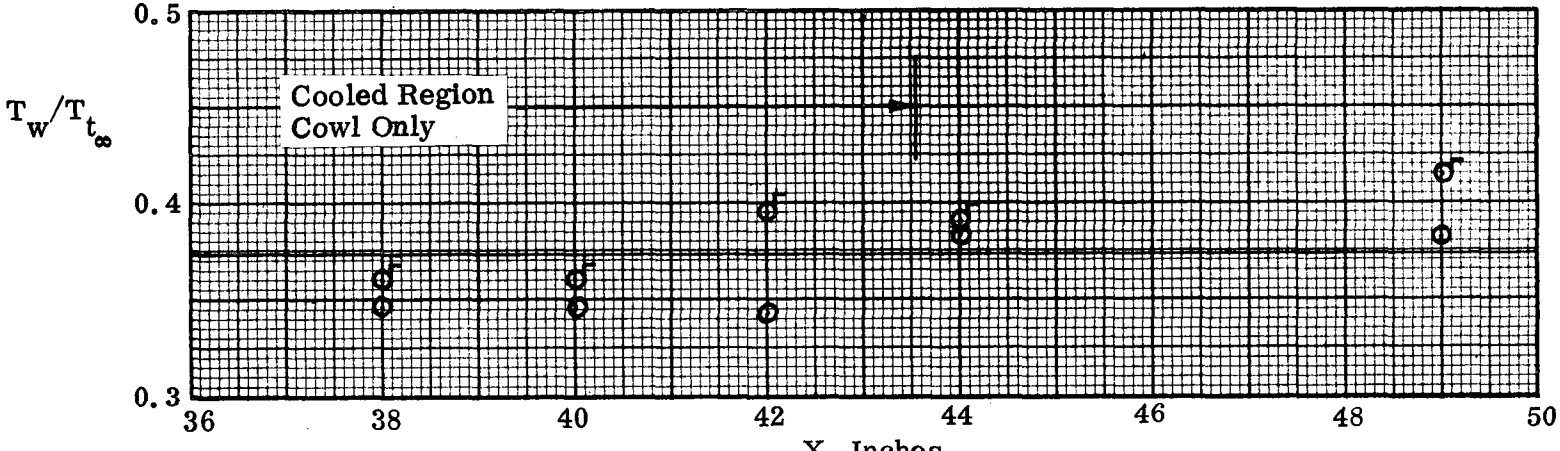

(a) Cowl Surface

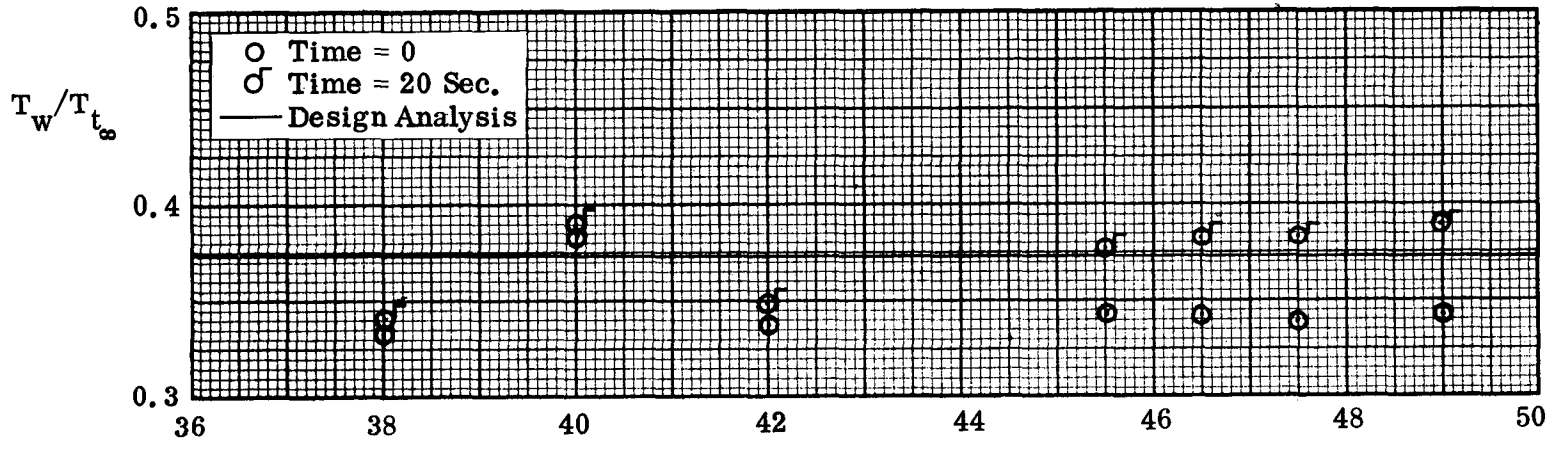

(b) Centerbody Surface

Figure 56. Surface Temperature Distributions, P8 Inlet Model.

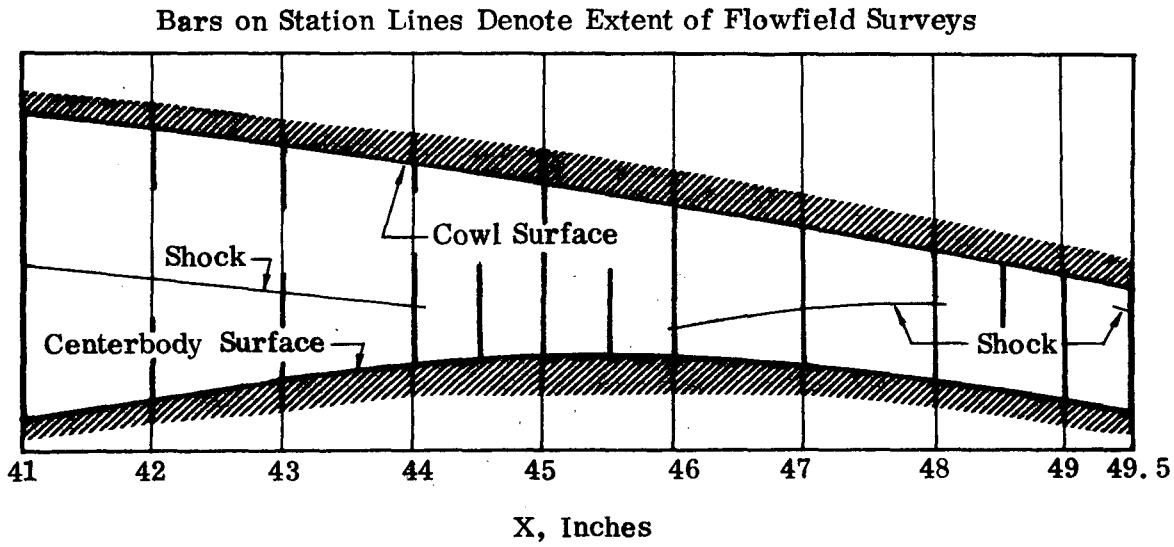

Figure 57. Probe Survey and Shock-Wave Locations, P8 Inlet Model.

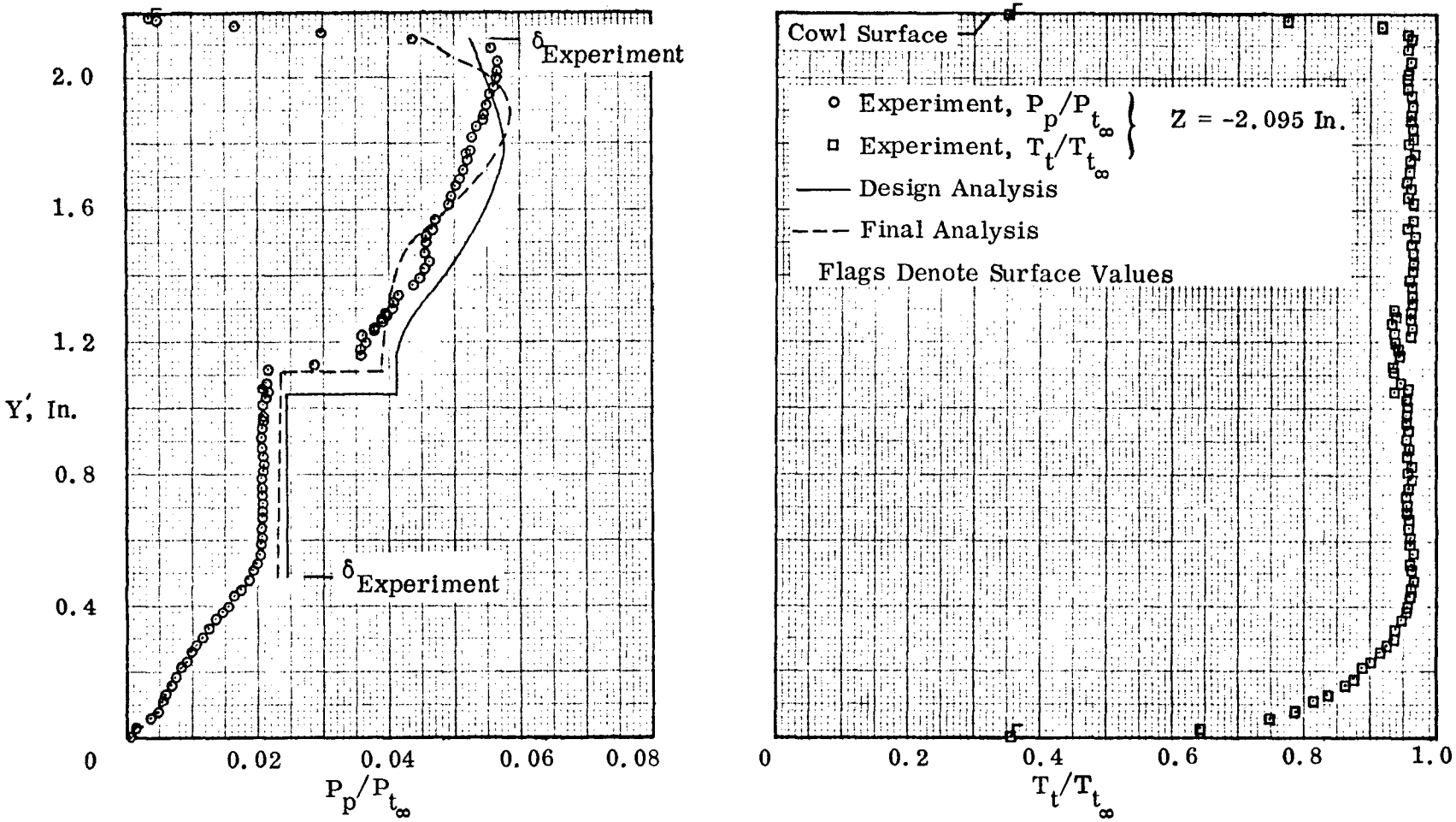

(a) Station X = 41.0

Figure 58. Pitot Pressure and Total Temperature Distributions, P8 Inlet Model.

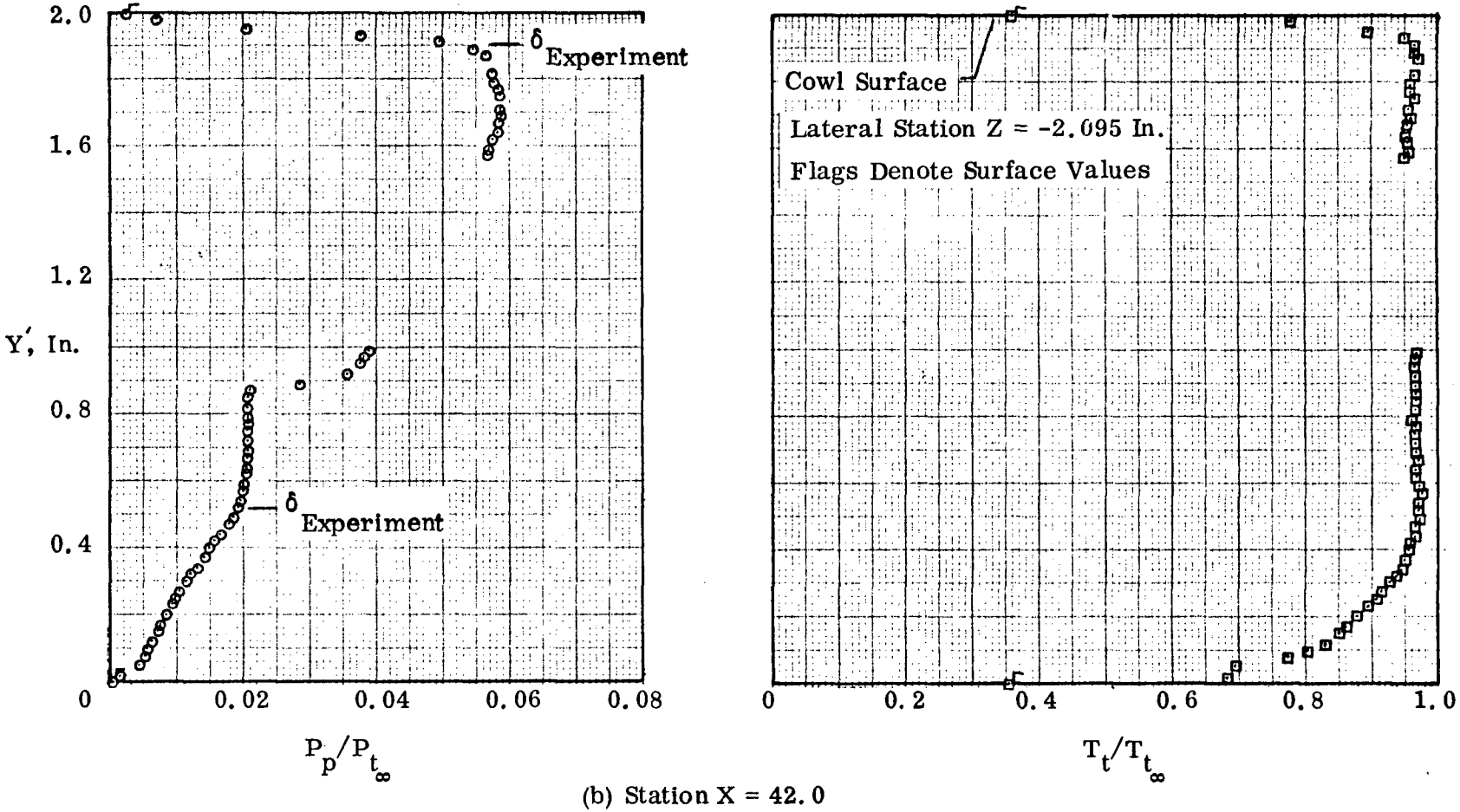

(b) Station X = 42.0

Figure 58. Continued.

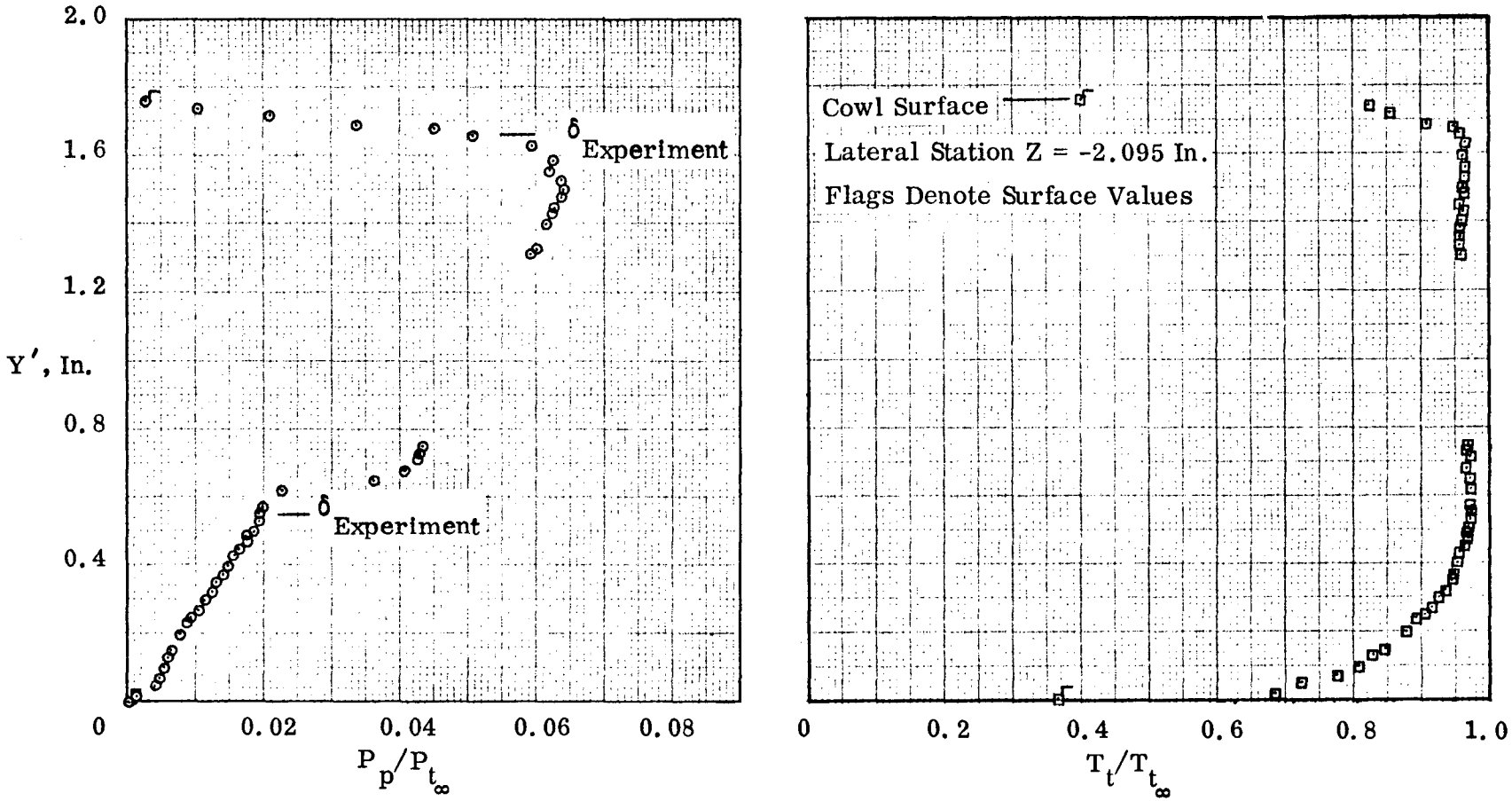

(c) Station X = 43.0

Figure 58. Continued.

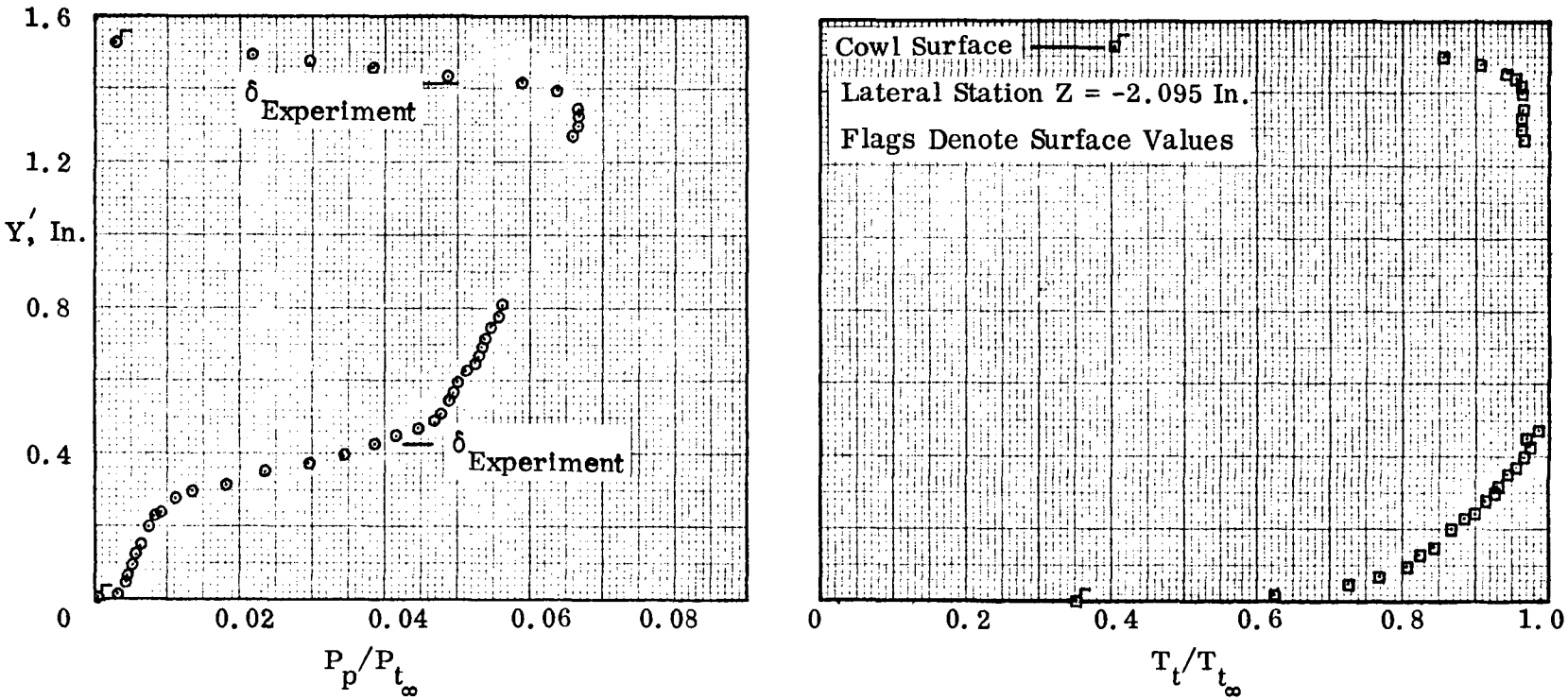

(d) Station X = 44.0

Figure 58. Continued.

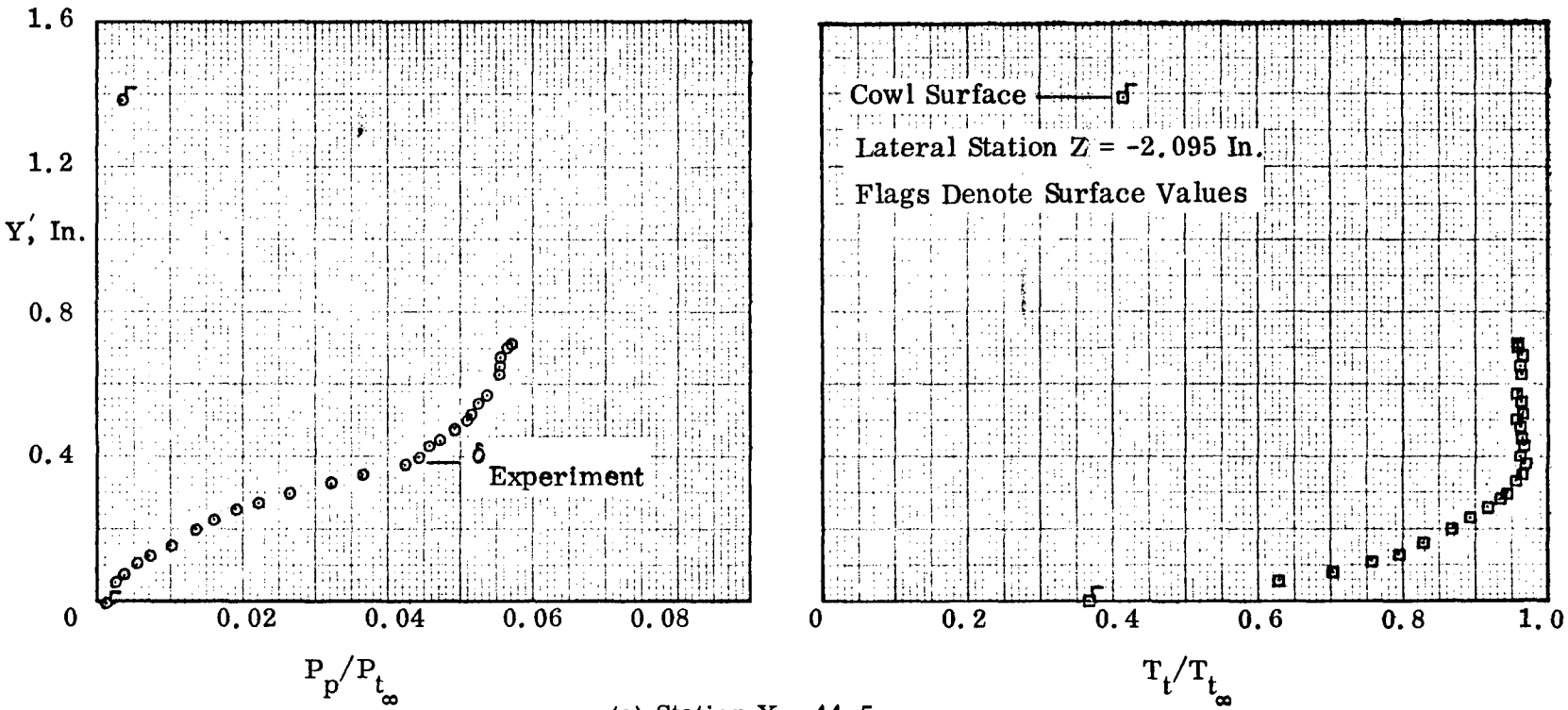

(e) Station X = 44.5

Figure 58. Continued.

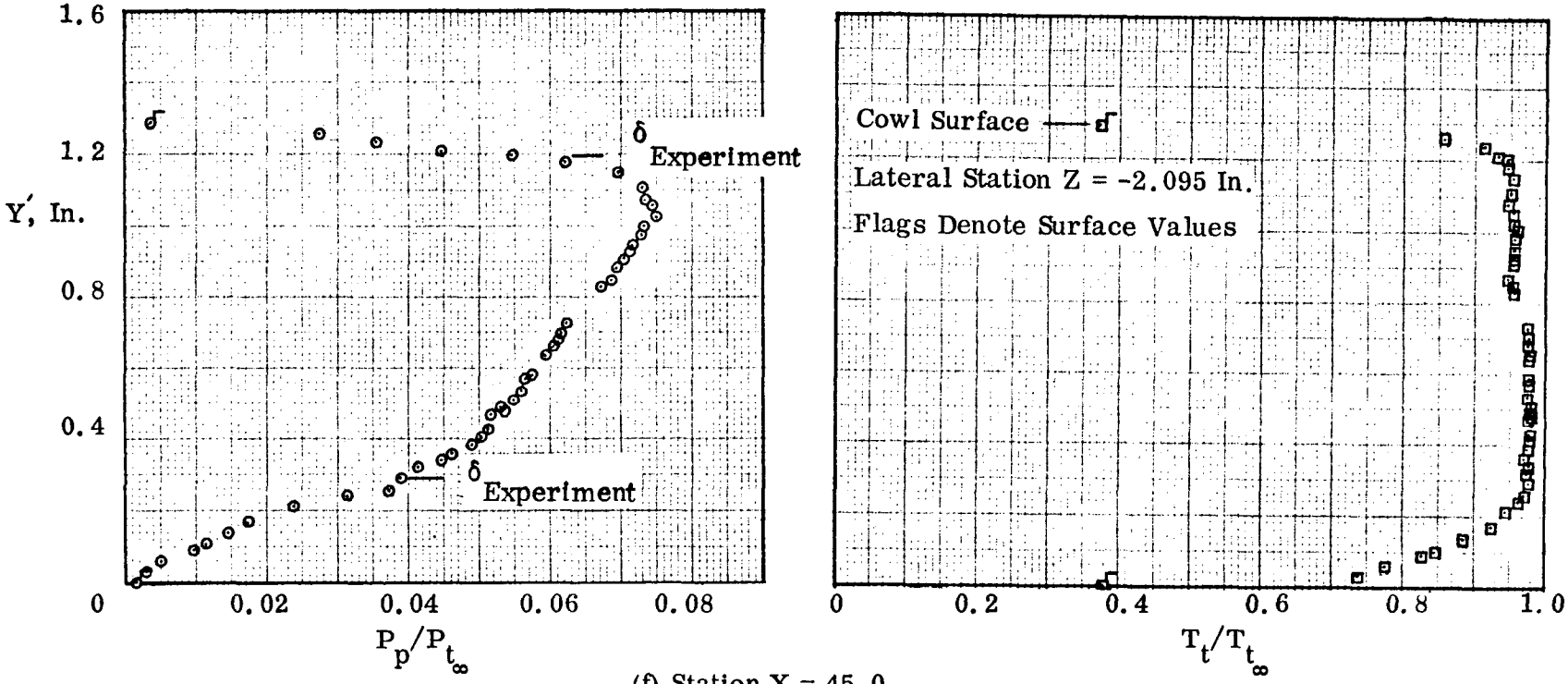

(f) Station X = 45.0

Figure 58. Continued.

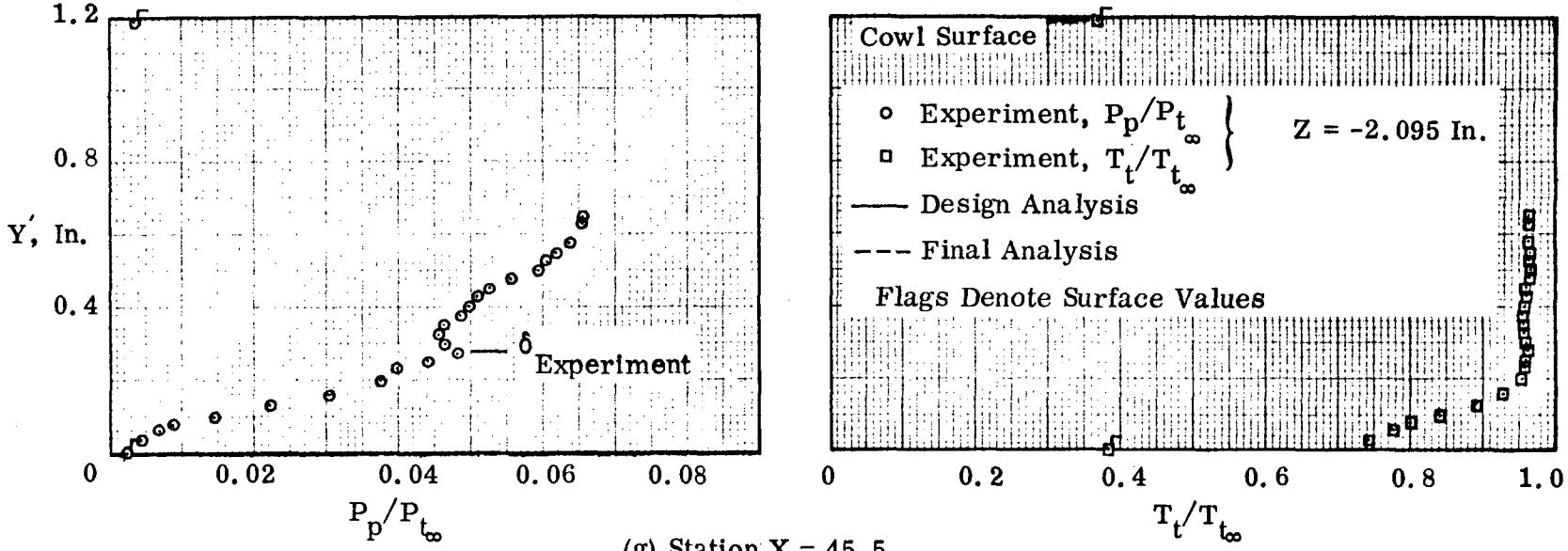

(g) Station X = 45.5

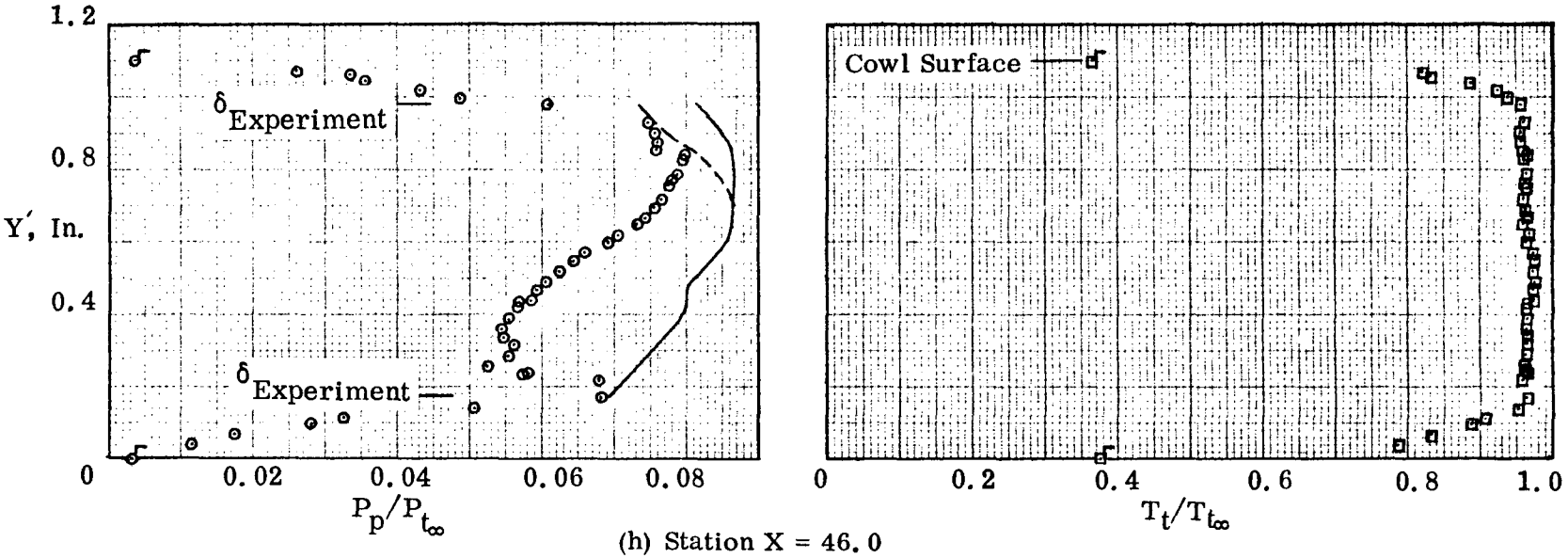

(h) Station X = 46.0

Figure 58. Continued.

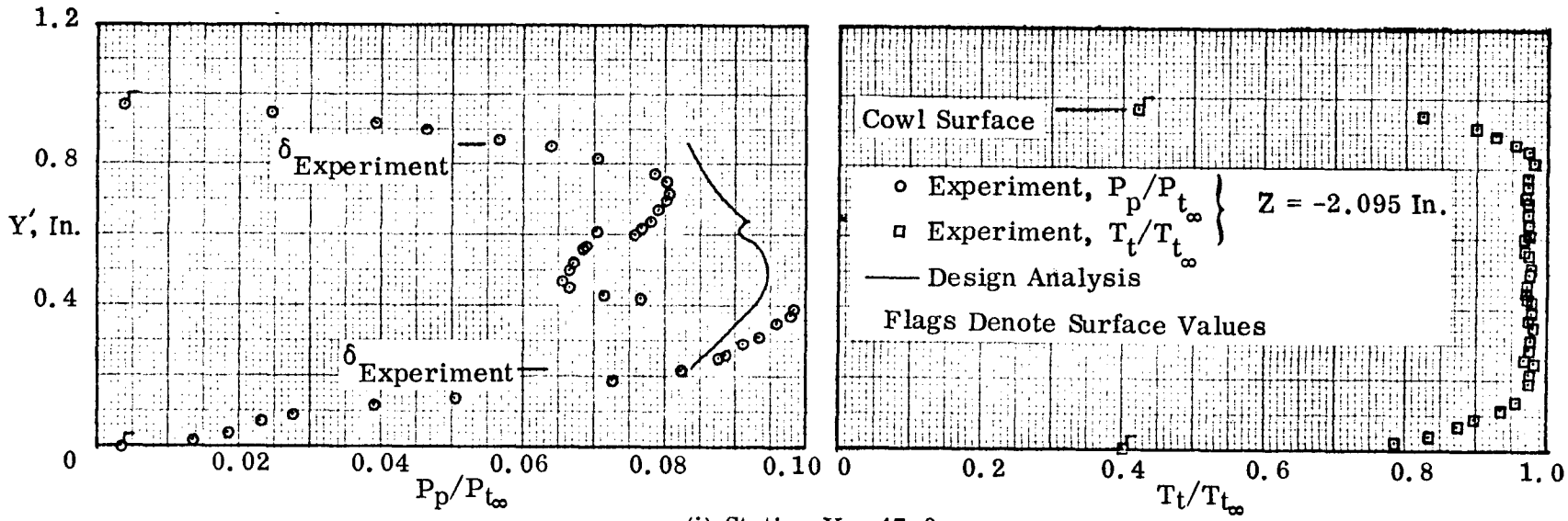

(i) Station X = 47.0

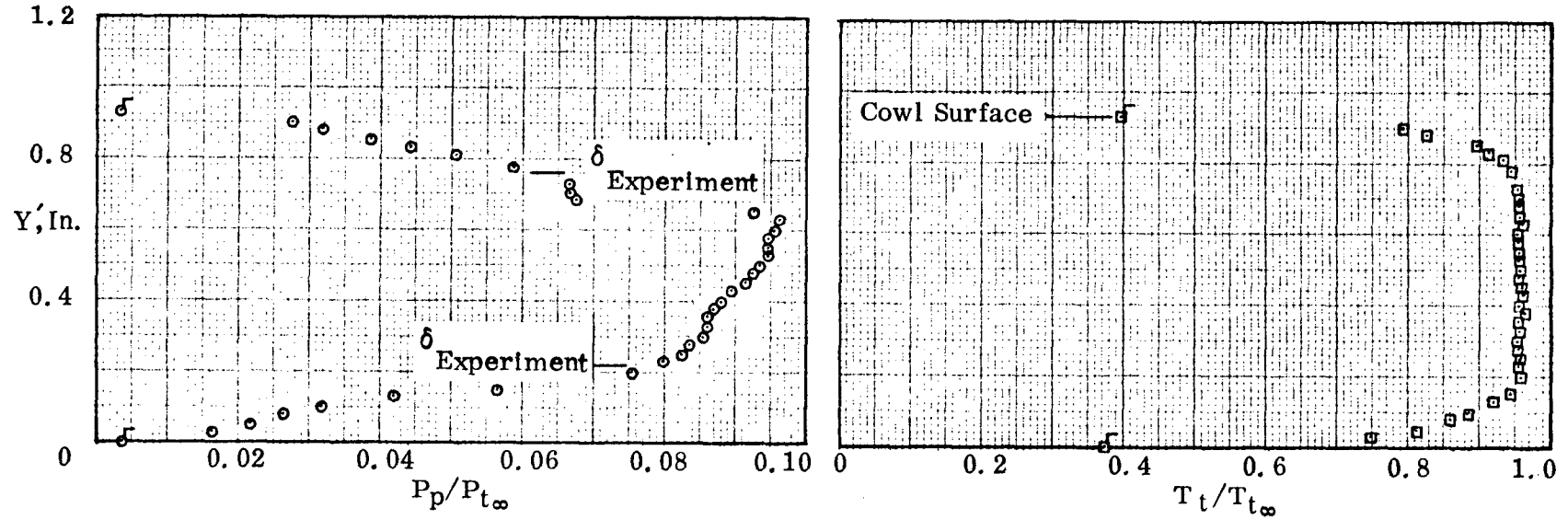

(j) Station X = 48.0

Figure 58. Continued.

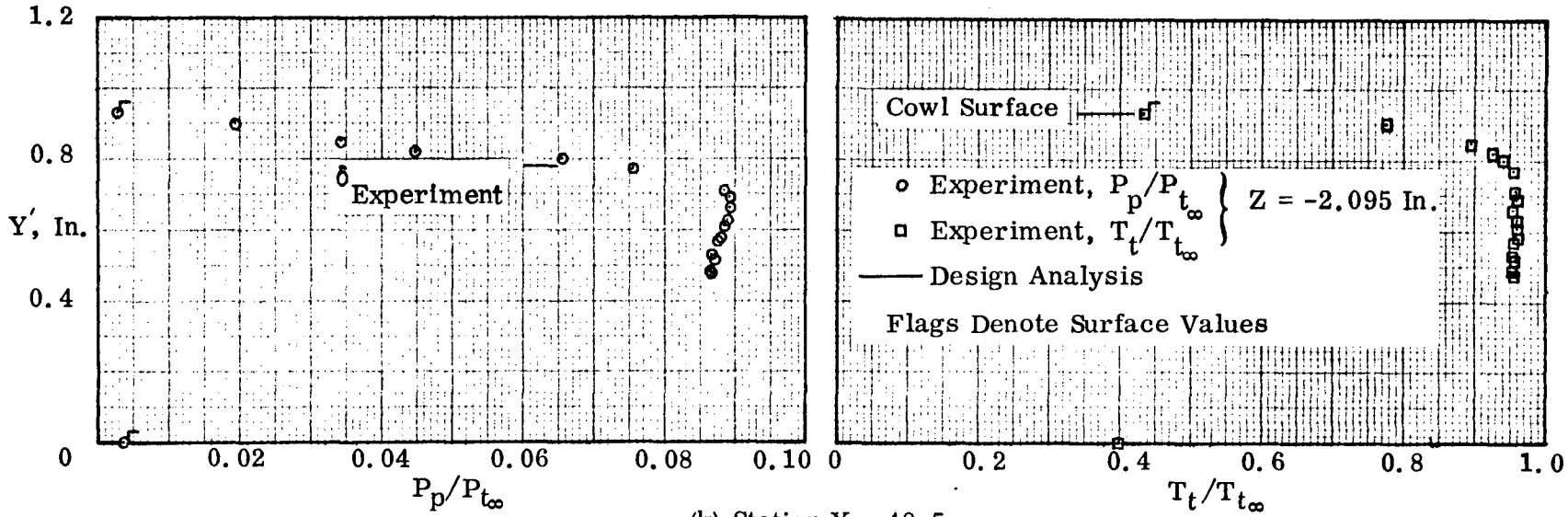

(k) Station X = 48.5

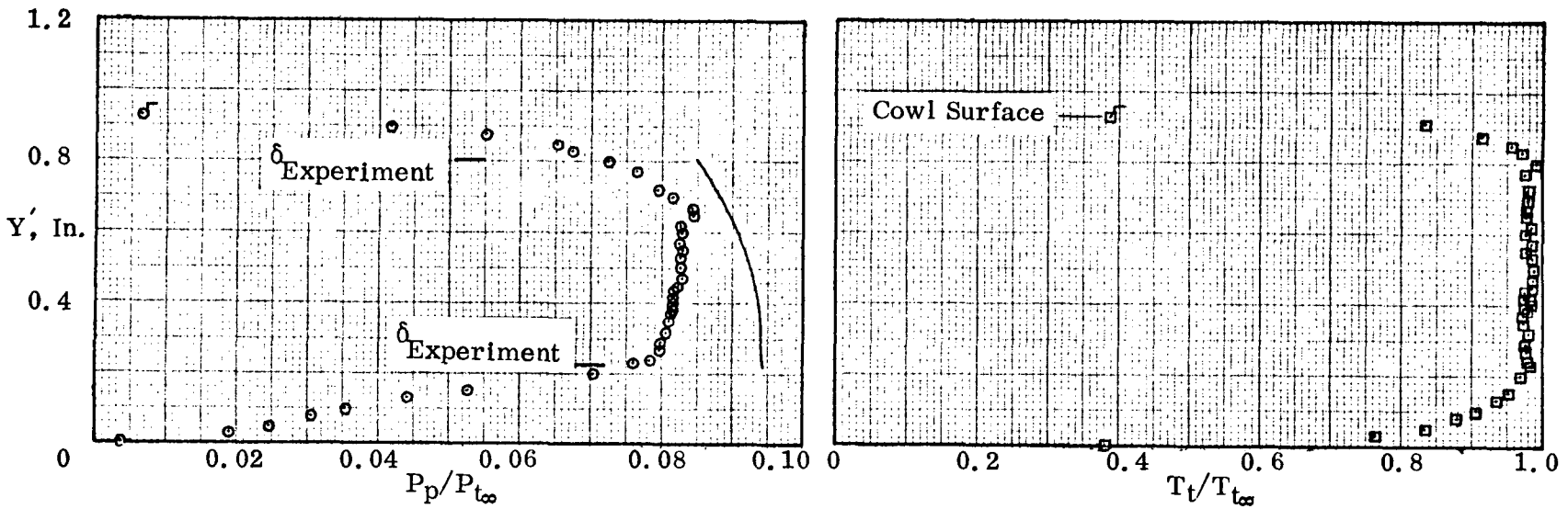

(l) Station X = 49.0

Figure 58. Continued.

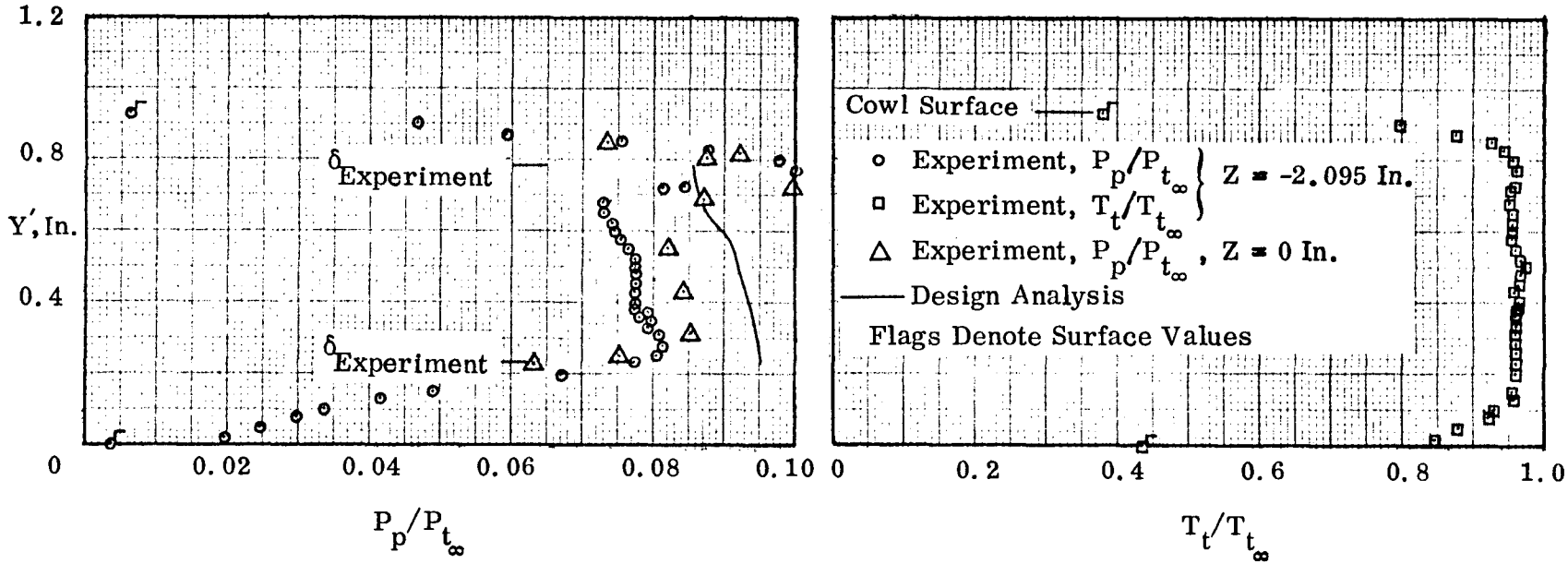

(m) Station X = 49.5

Figure 58. Concluded.

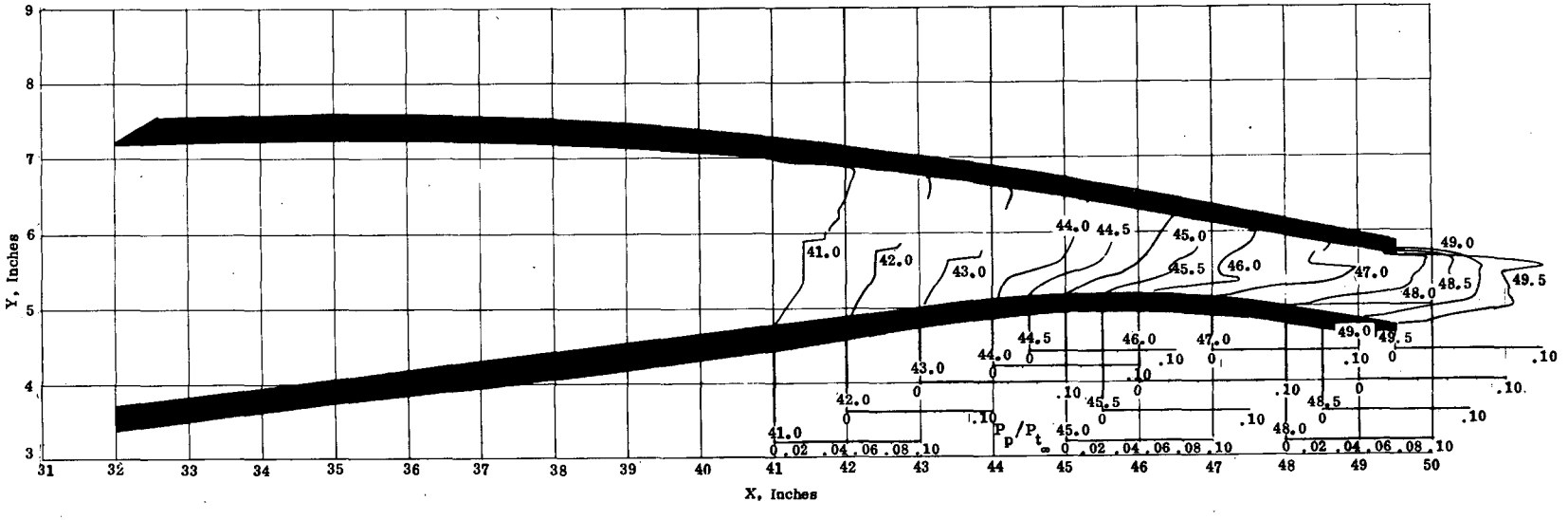

Figure 59. Summary of Pitot-Pressure Distributions, P8 Inlet Model.

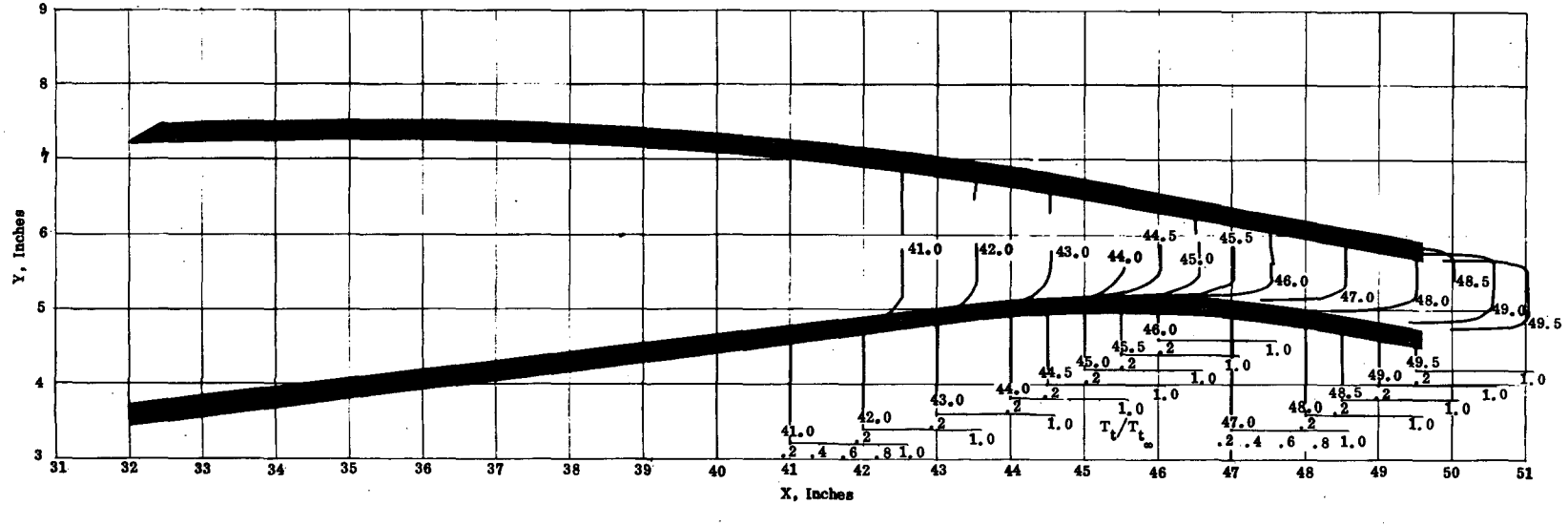

Figure 60. Summary of Total-Temperature Distributions, P8 Inlet Model.

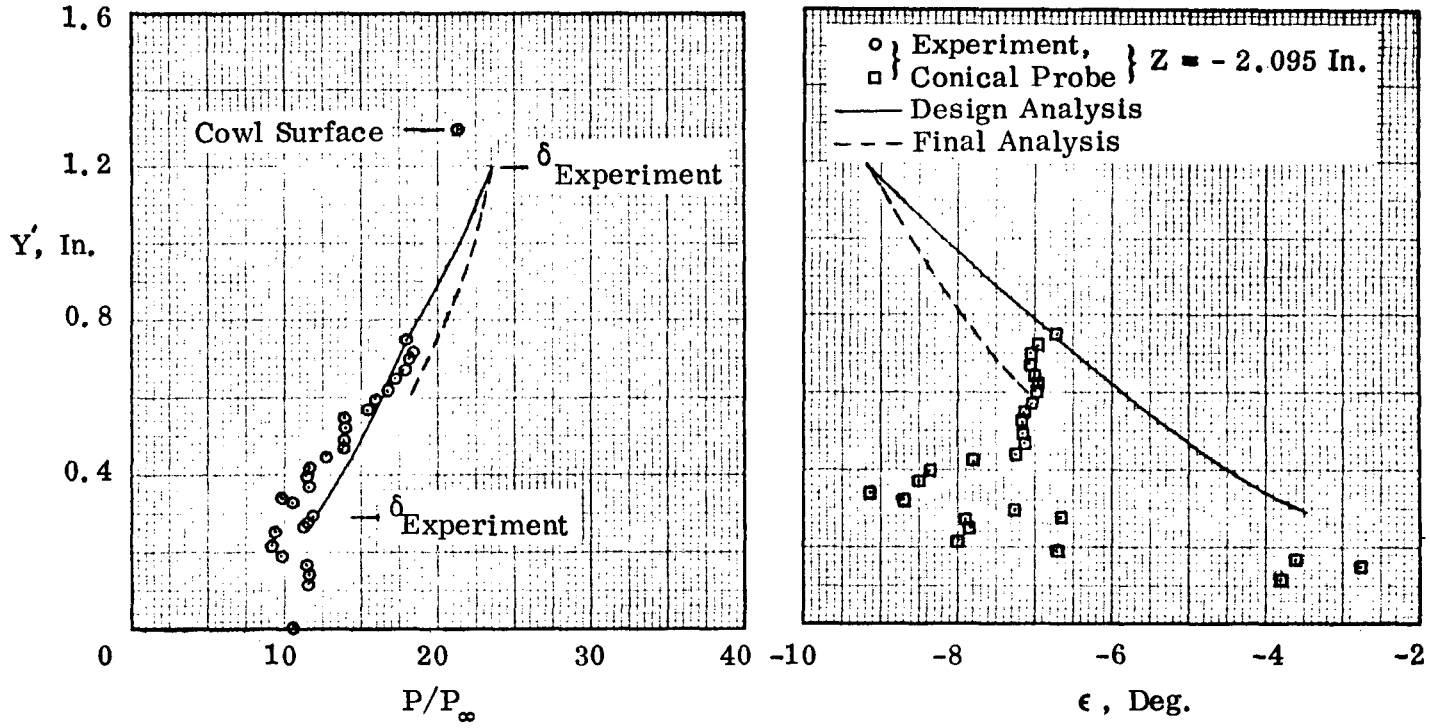

(a) Station X = 45.0

Figure 61. Static Pressure and Flow Angle Distributions, P8 Inlet Model.

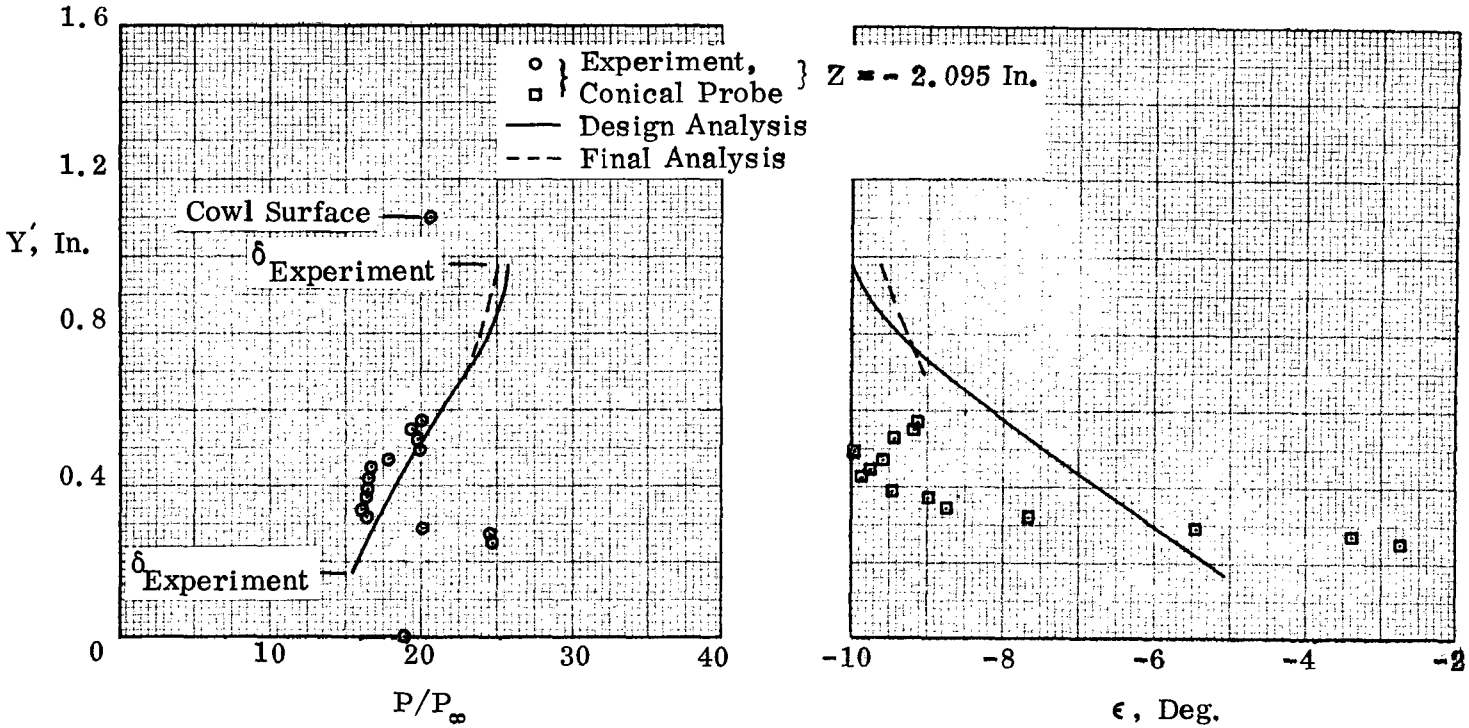

(b) Station X = 46.0 Inches

Figure 61. Continued.

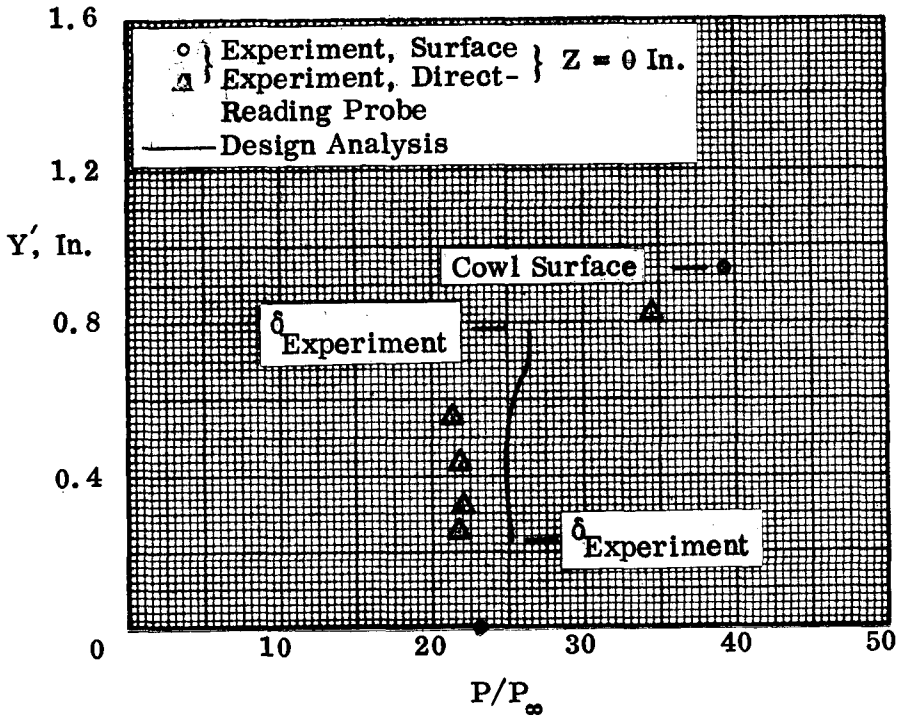

(c) Station X = 49.5 Inches

Figure 61. Concluded.

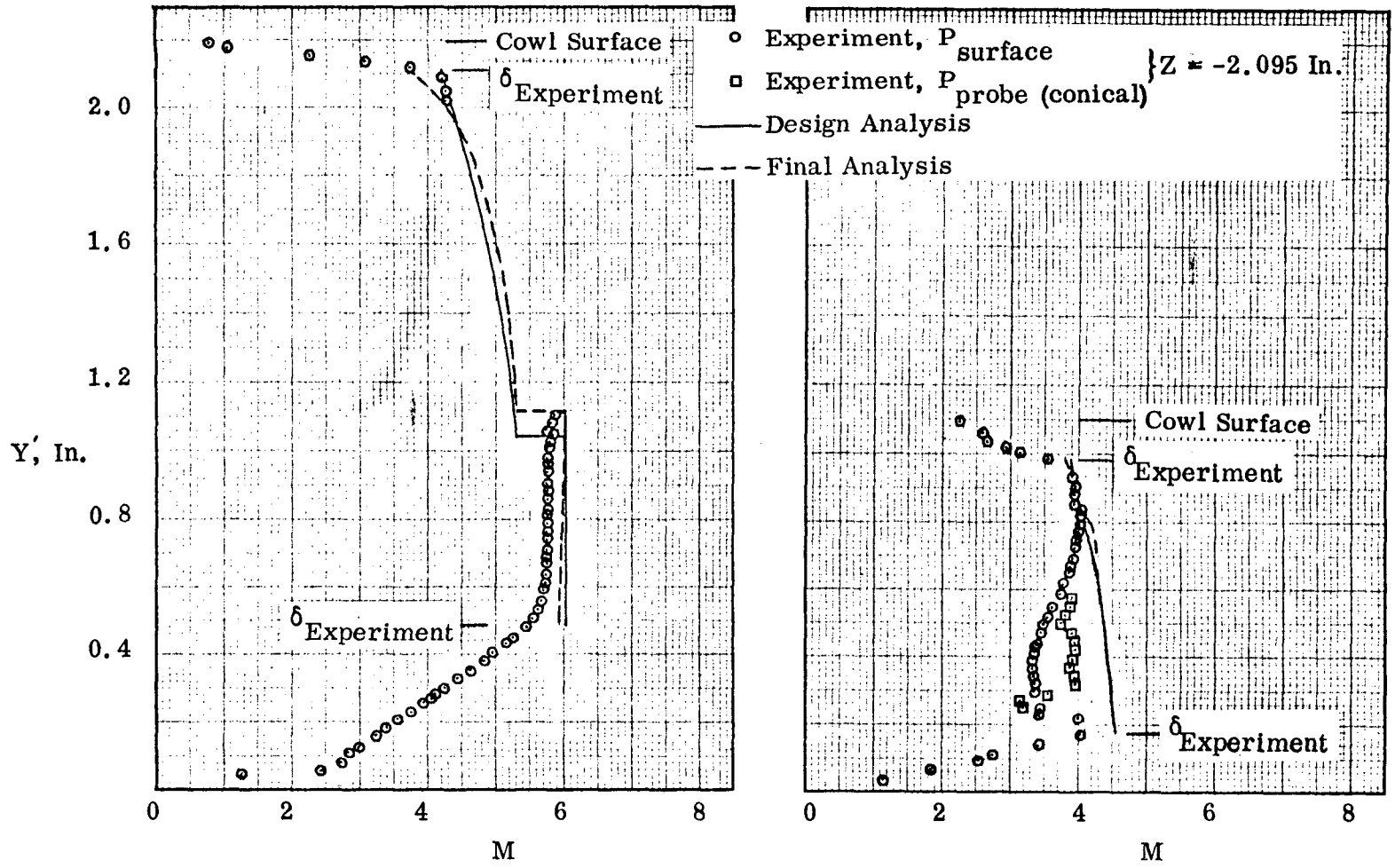

(a) Station X = 41.0 Inches

(b) Station X = 46.0 Inches

Figure 62. Mach Number Distributions, P8 Inlet Model.

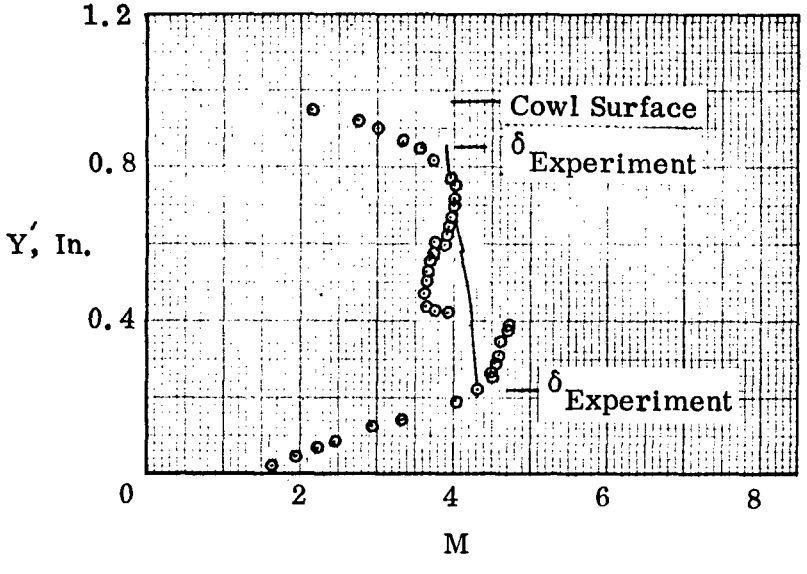

(c) Station X = 47.0 Inches

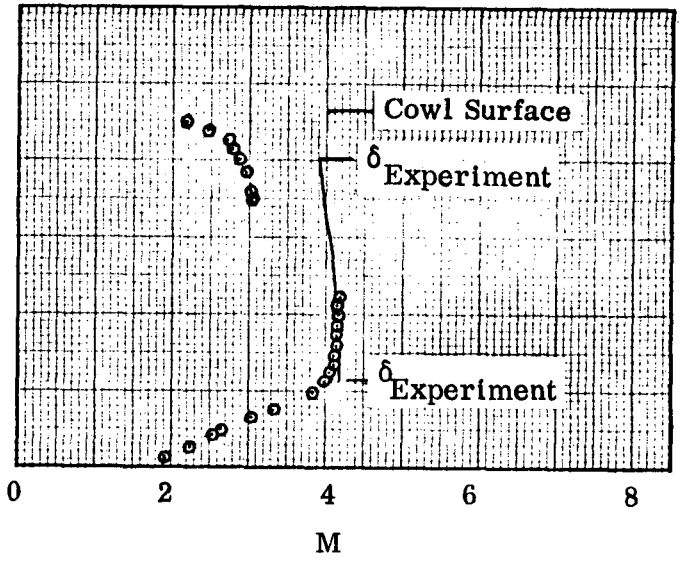

(d) Station X = 49.0 Inches

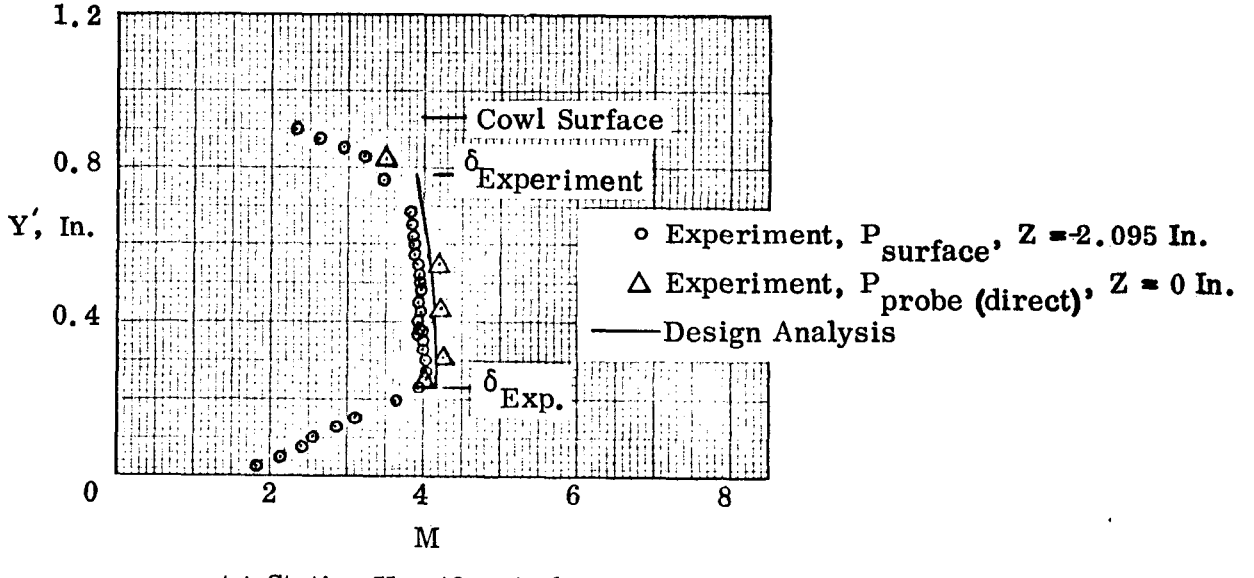

(e) Station X = 49.5 Inches

Figure 62. Concluded.

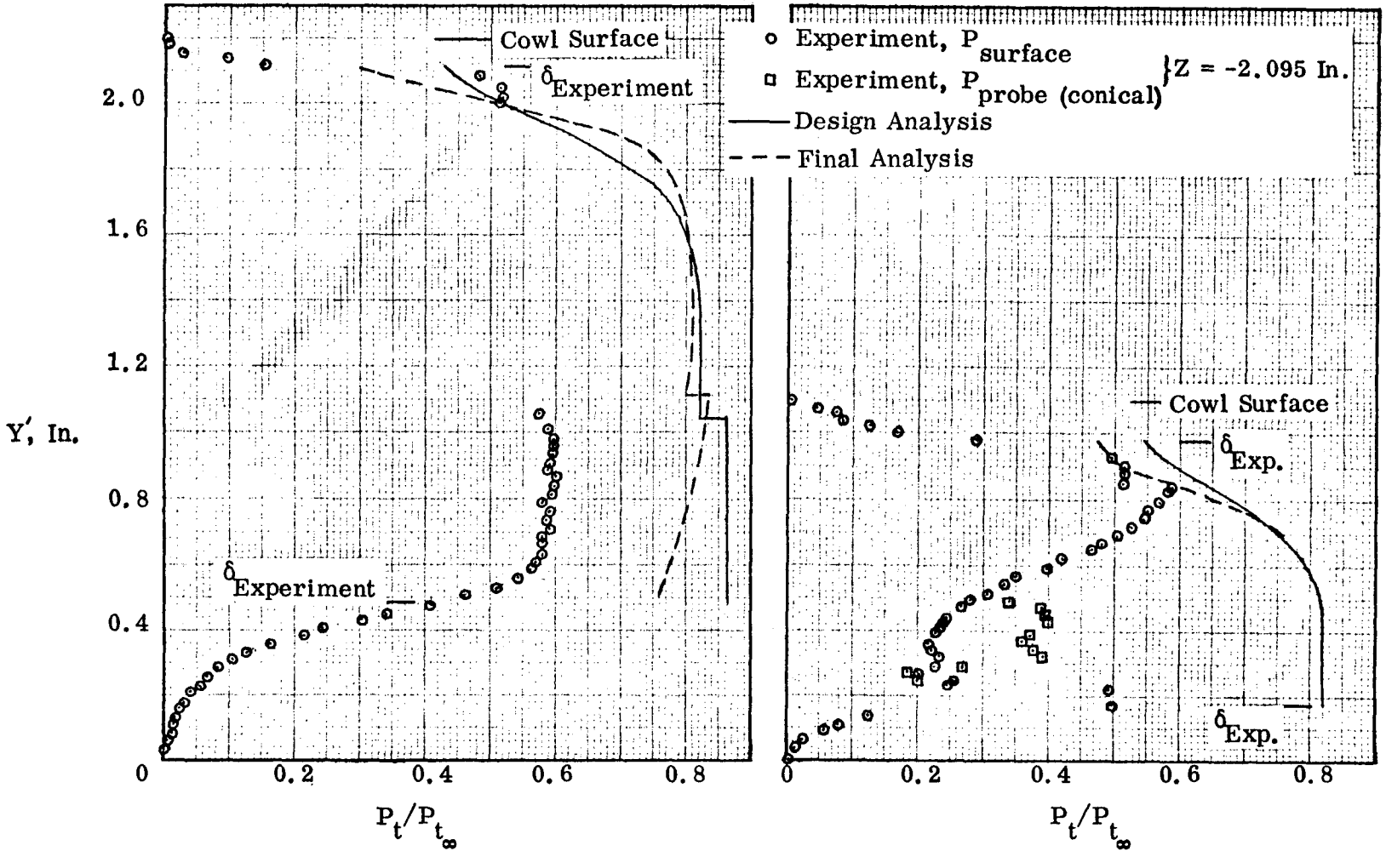

(a) Station X = 41.0 Inches

(b) Station X = 46.0 Inches

Figure 63. Total-Pressure Recovery Distributions, P8 Inlet Model.

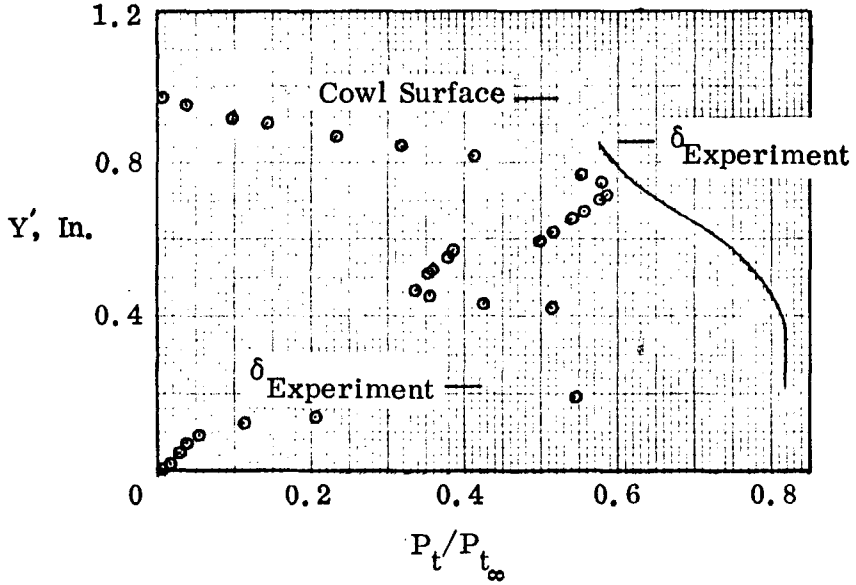

(c) Station X = 47.0 Inches

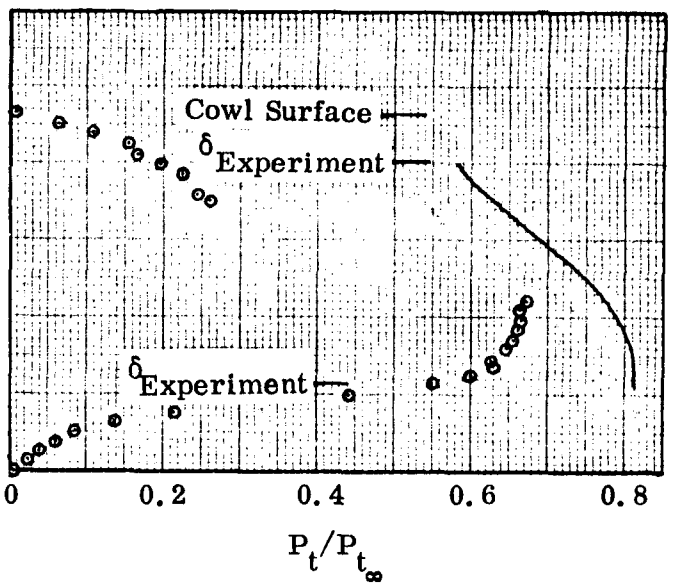

(d) Station X = 49.0 Inches

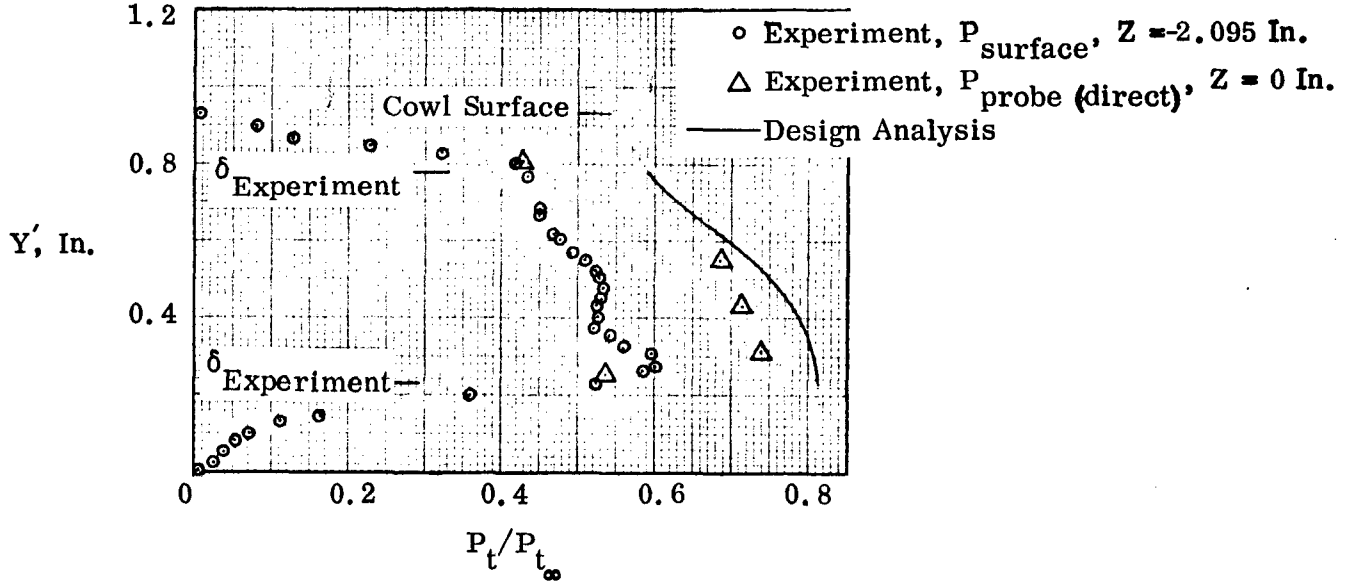

(e) Station X = 49.5 Inches

Figure 63. Concluded.

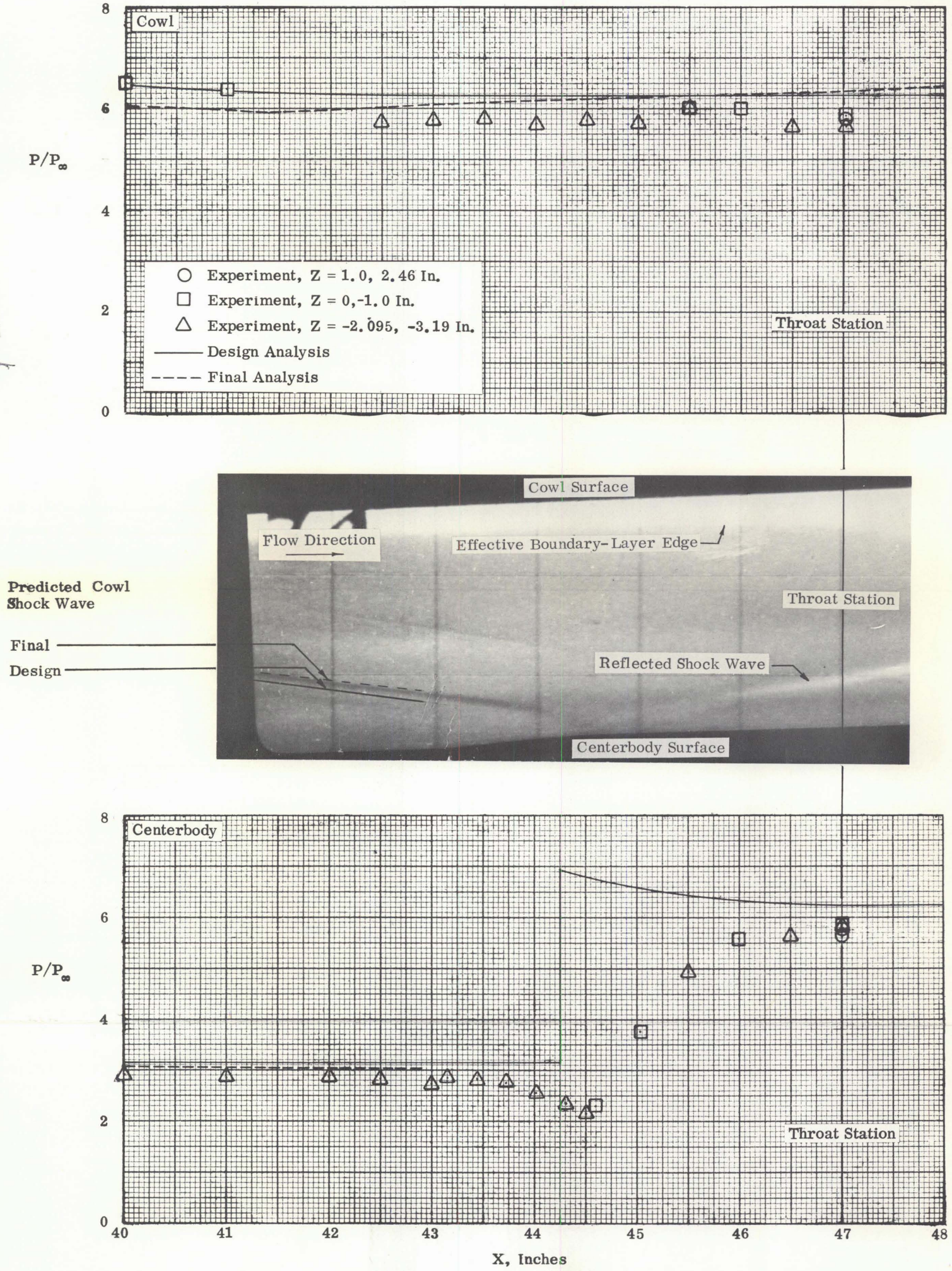

Figure 44. Surface Static-Pressure Distributions and Flowfield Pattern P2 Inlet Model.

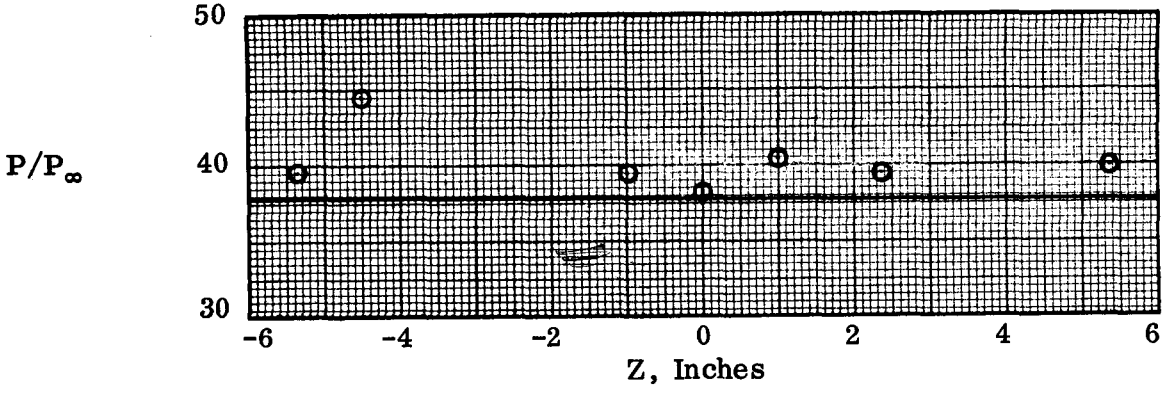

(a) Cowl Surface, Station X = 50.08 Inches

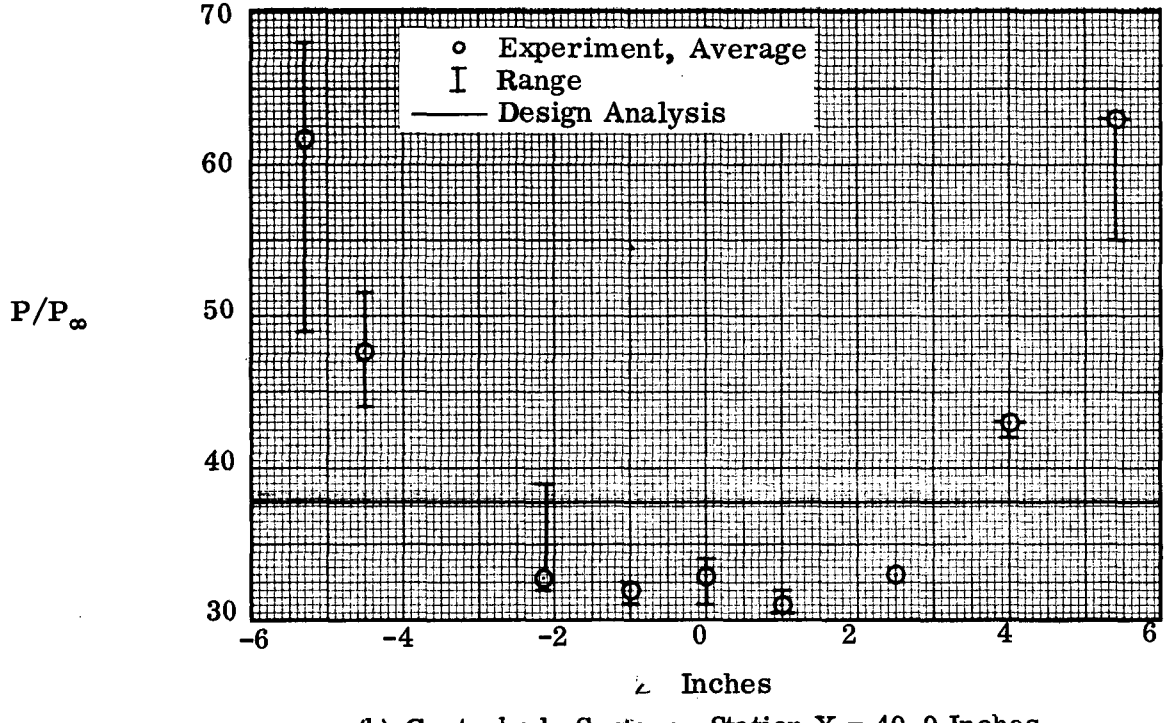

(b) Centerbody Surface, Station X = 49.9 Inches

Figure 65. Lateral Surface Static-Pressure Distribution at Throat Station, P12 Inlet Model.

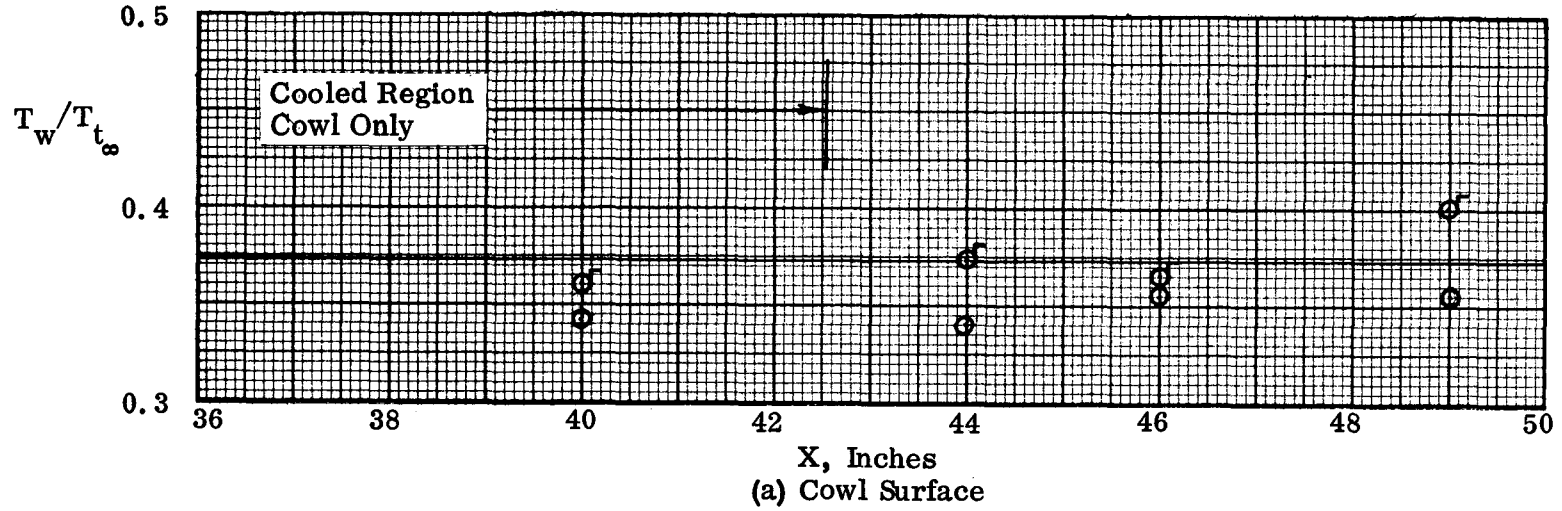

(a) Cowl Surface

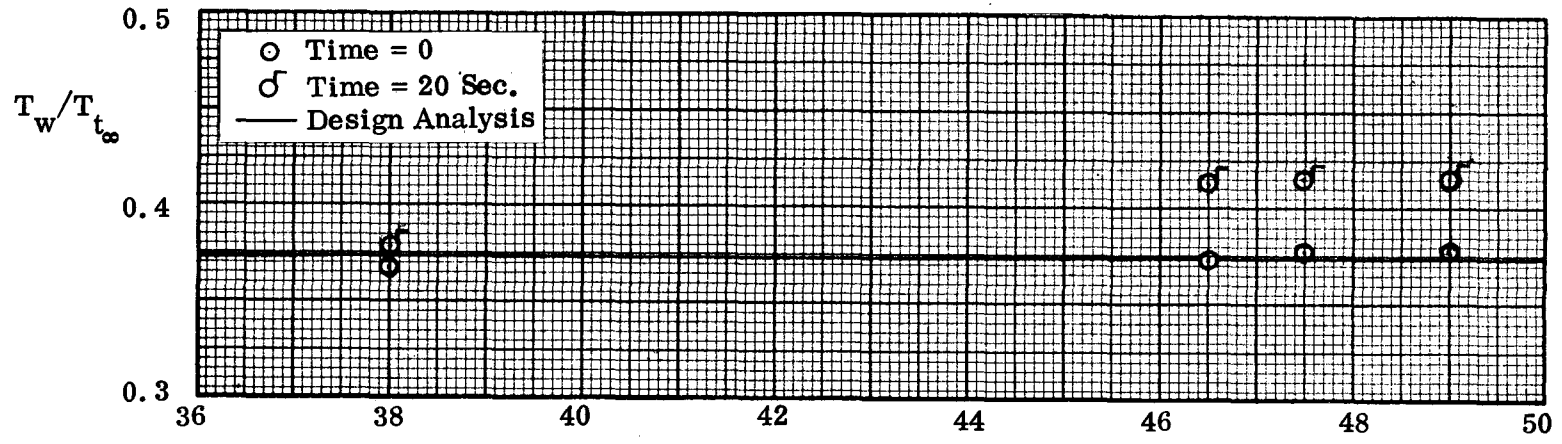

(b) Centerbody Surface

Figure 66. Surface Temperature Distributions, P12 Inlet Model.

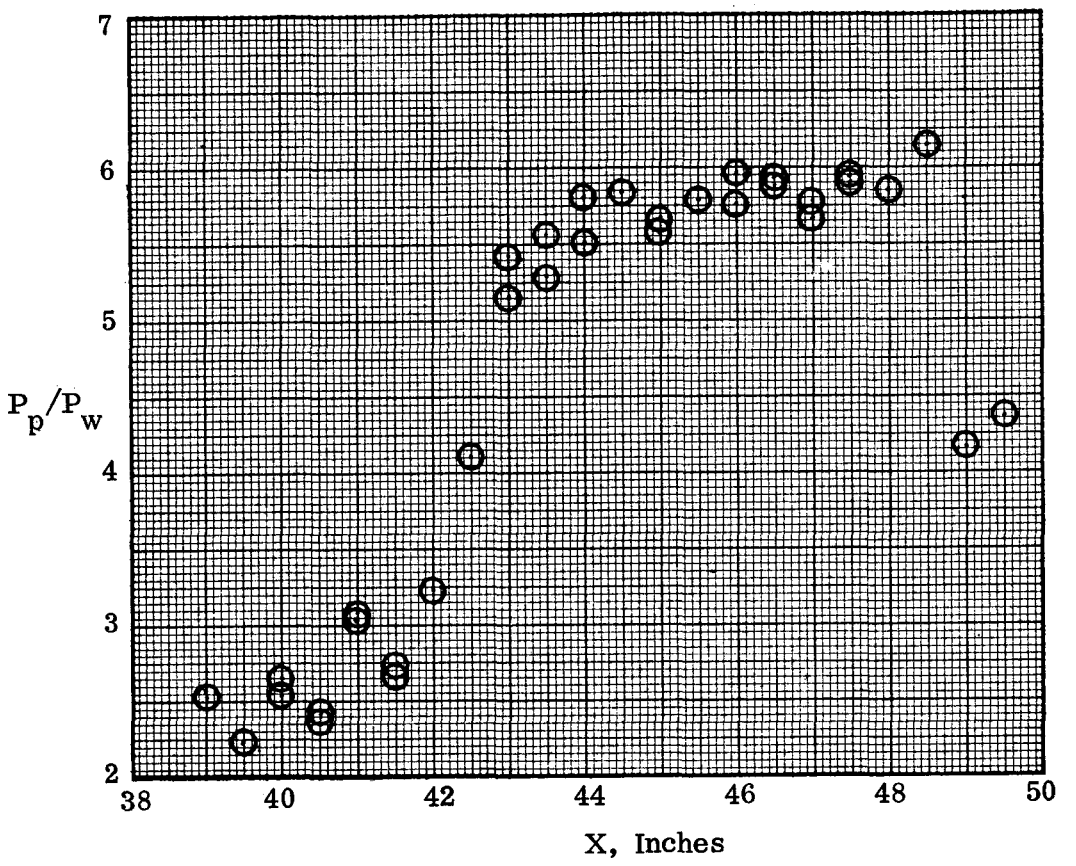

Figure 67. Surface Pitot-Pressure Distribution, P8 Inlet Model Cowl.

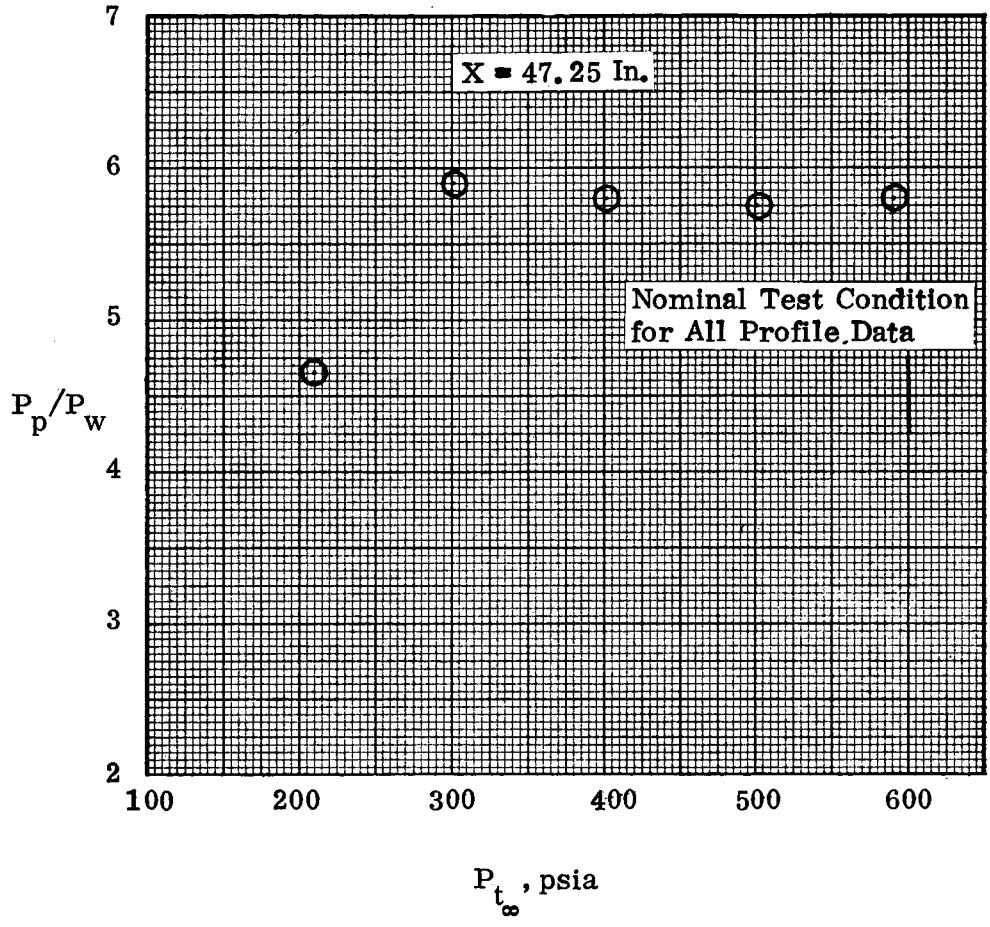

Figure 68. Effect of Freestream Total Pressure on Surface Pitot Pressure, P8 Inlet Model Cowl.

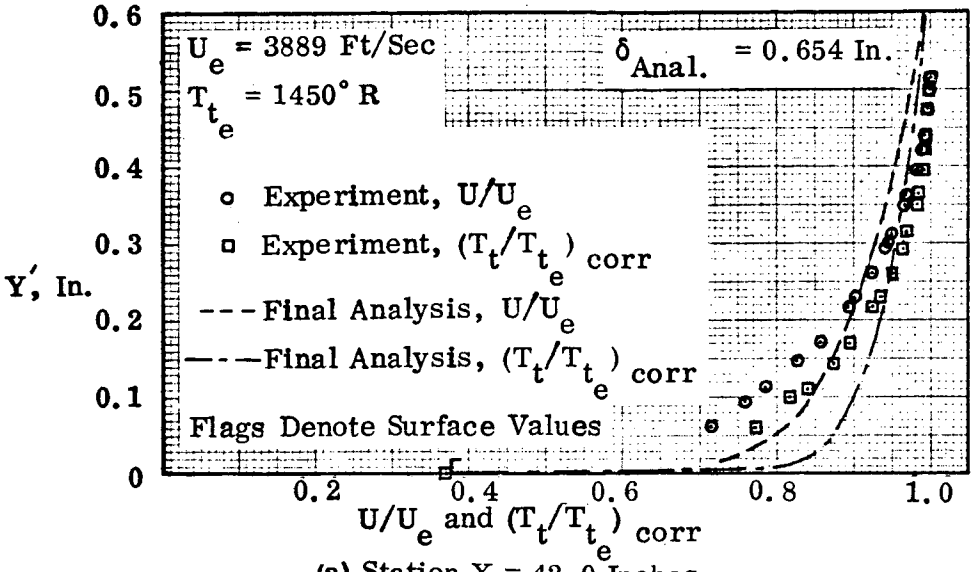

(a) Station X = 42.0 Inches

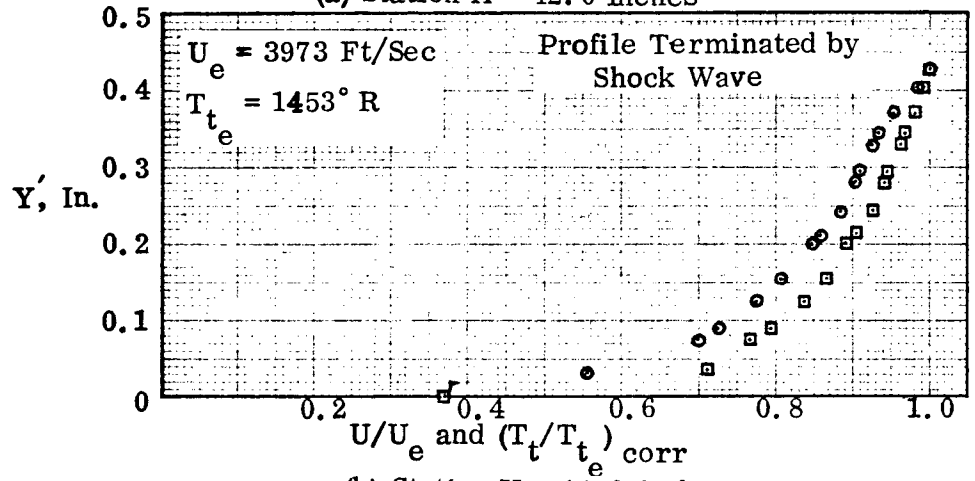

(b) Station X = 44.0 Inches

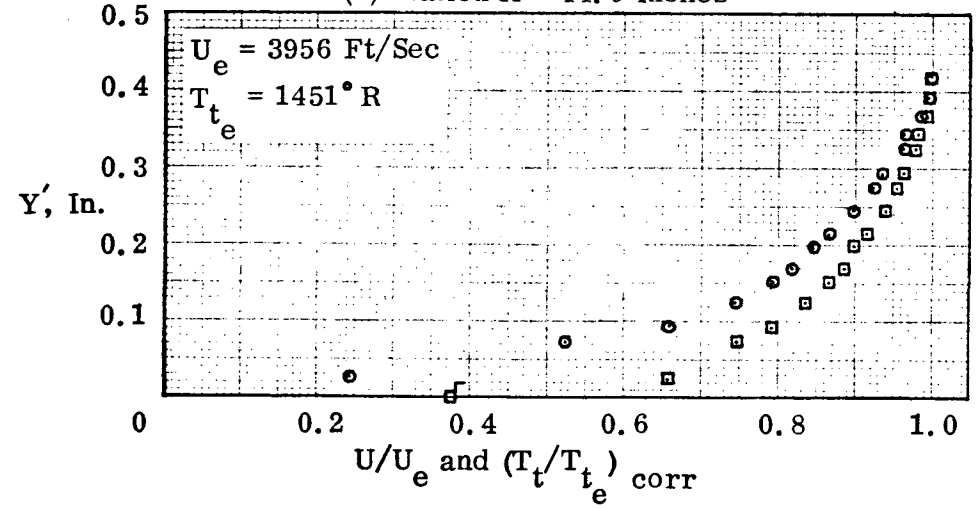

(c) Station X = 45.0 Inches

Figure 69. Boundary-Layer Velocity and Total Temperature Distributions, P2 Inlet Model Centerbody.

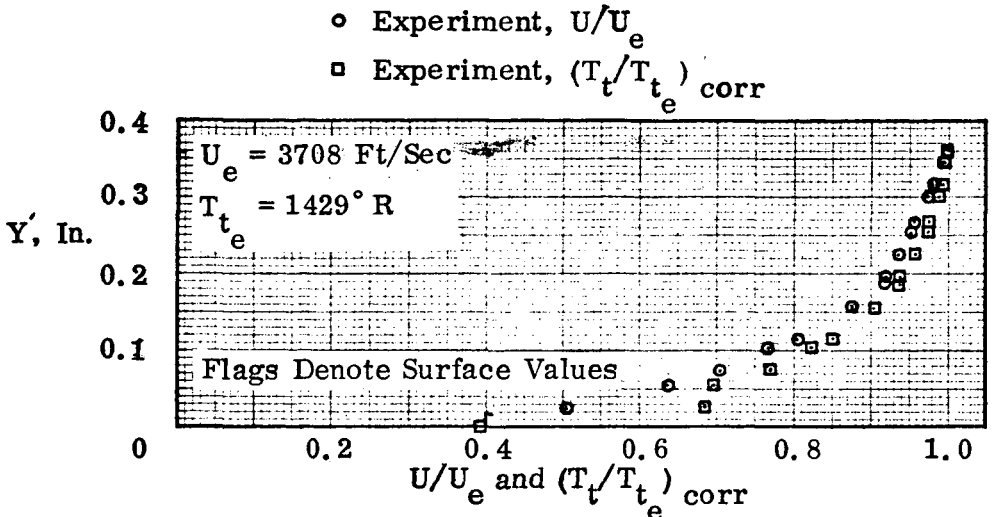

(d) Station X = 46.0 Inches

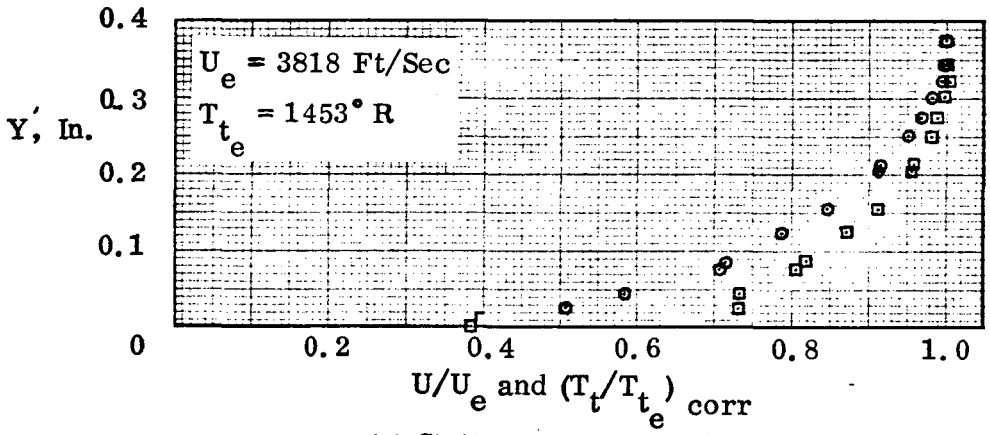

(e) Station X = 47.0 Inches

Figure 69. Concluded.

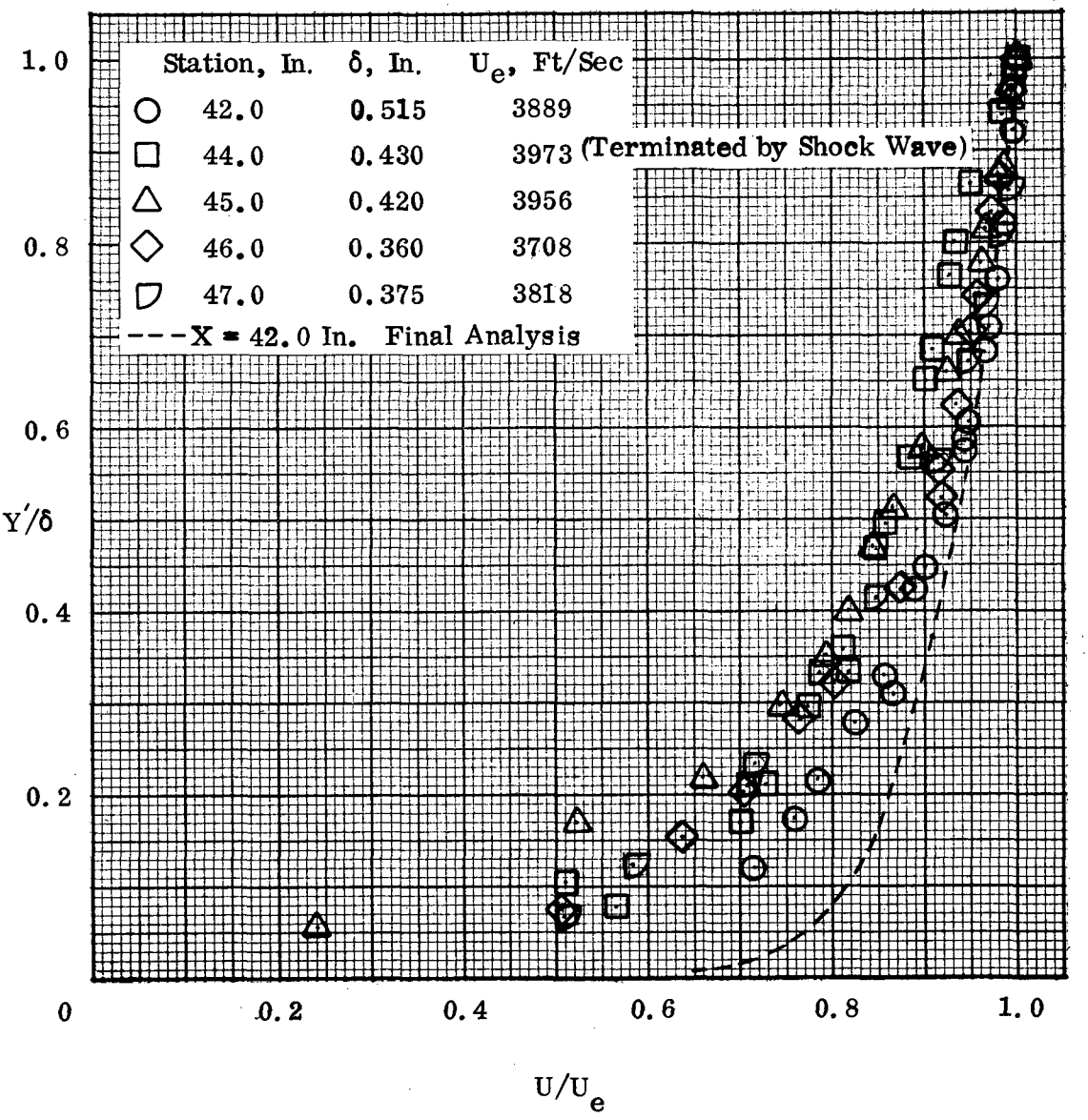

Figure 70. Summary of Velocity Distributions, P2 Inlet Model Centerbody.

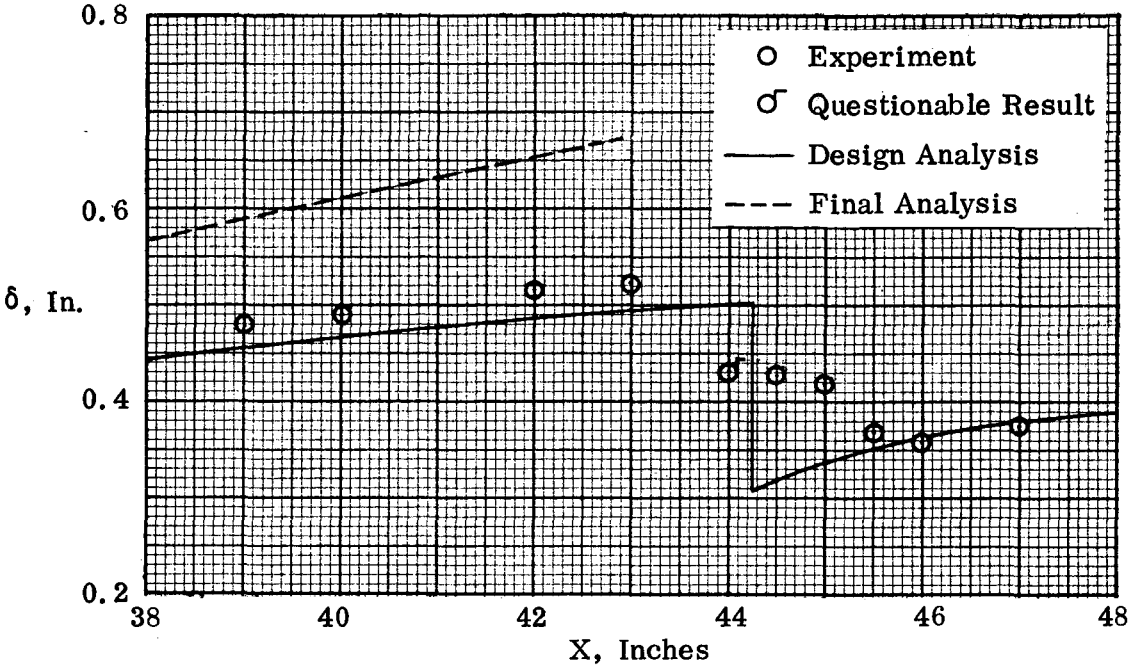

(a) Boundary-Layer Thickness

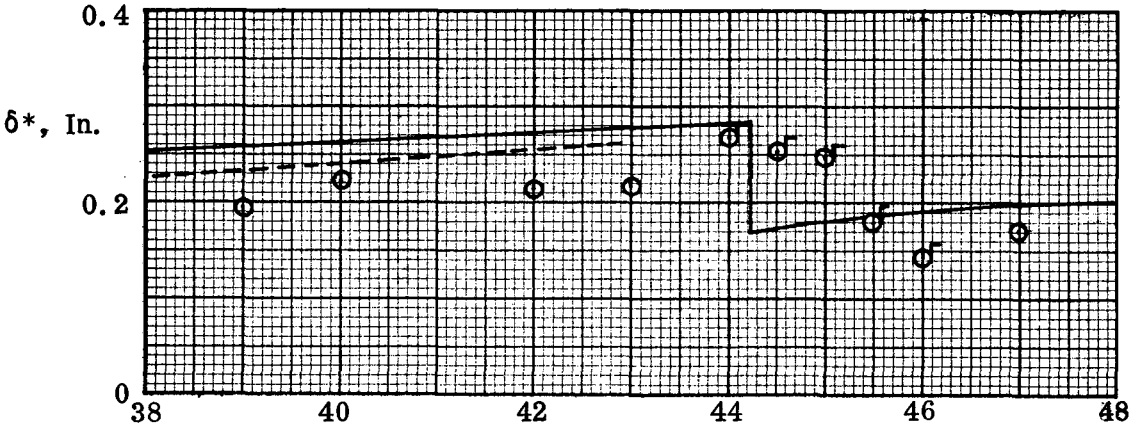

(b) Displacement Thickness

Figure 71. Boundary-Layer Properties, P2 Inlet Model Centerbody.

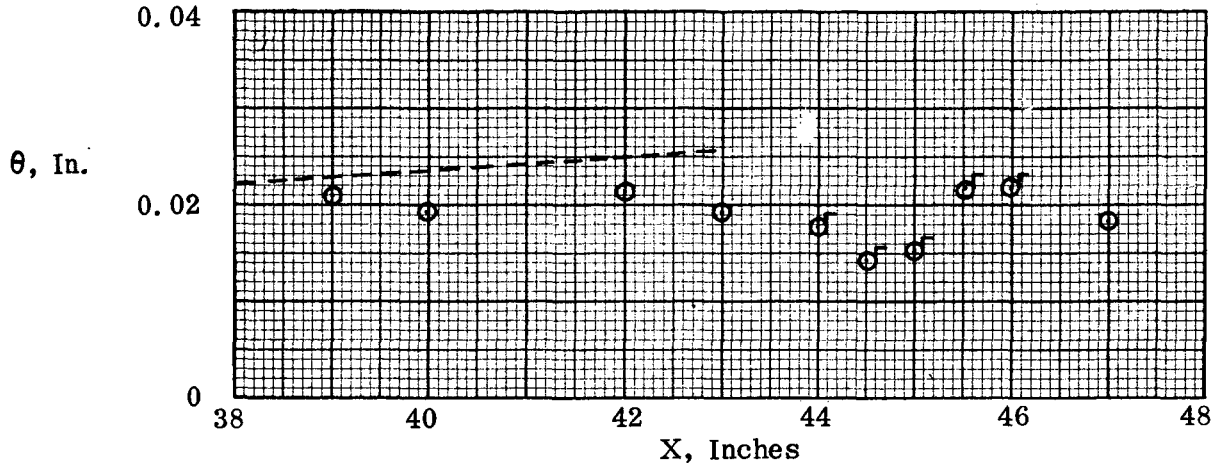

(c) Momentum Thickness

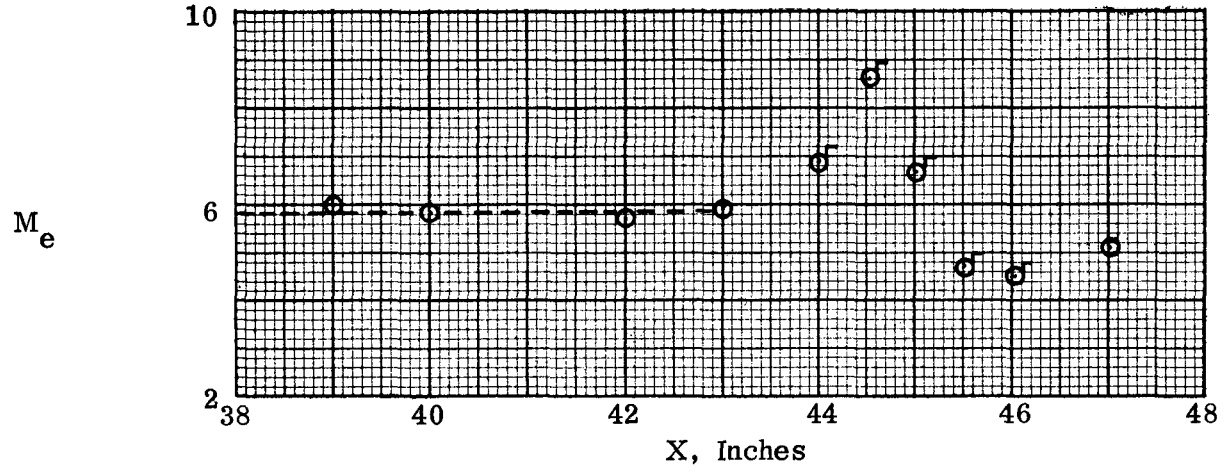

(d) Mach Number

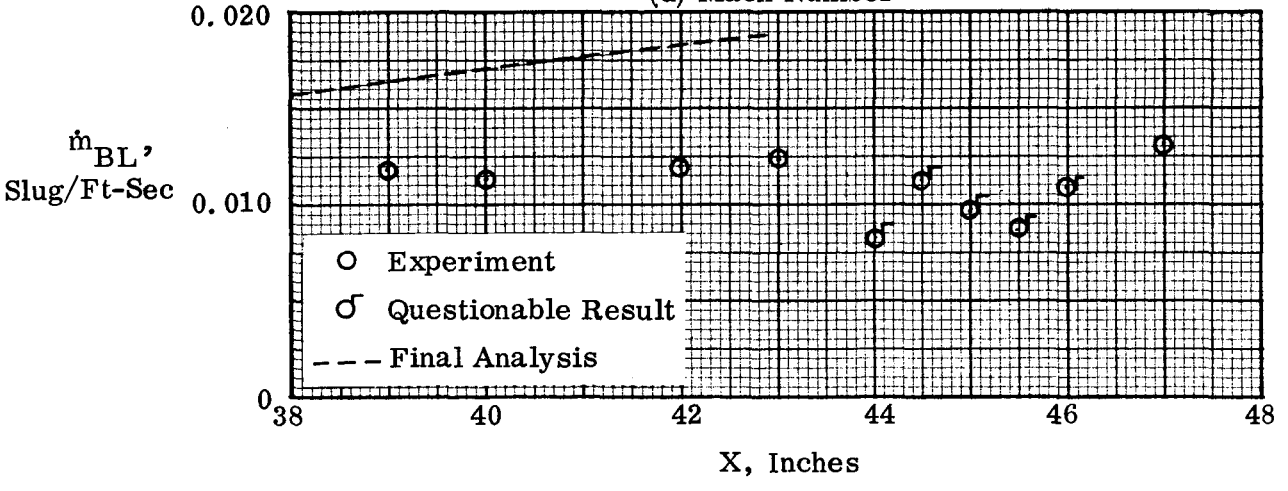

(e) Mass Flow

Figure 71. Concluded.

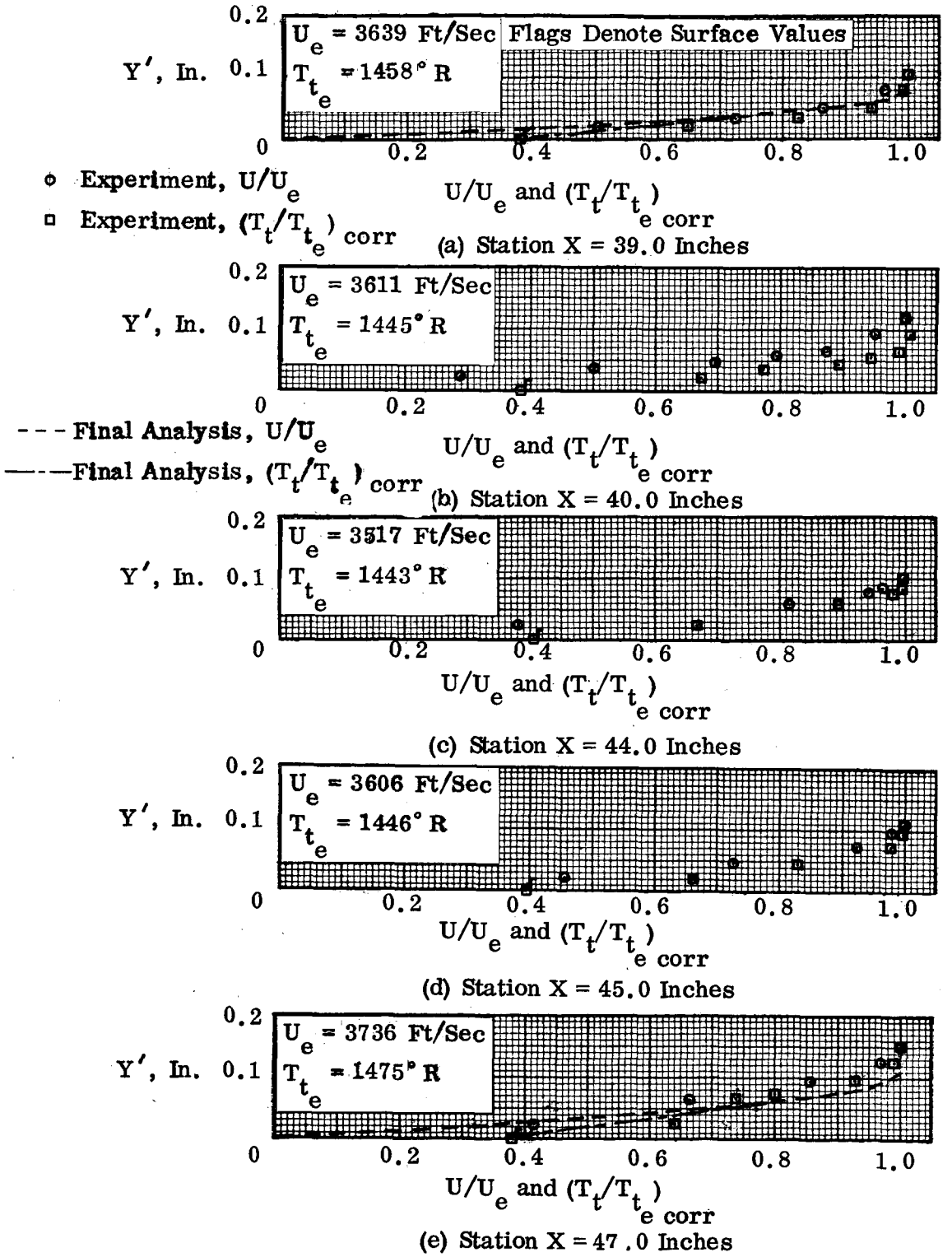

Figure 72. Boundary-Layer Velocity and Total Temperature Distributions, P2 Inlet Model Cowl.

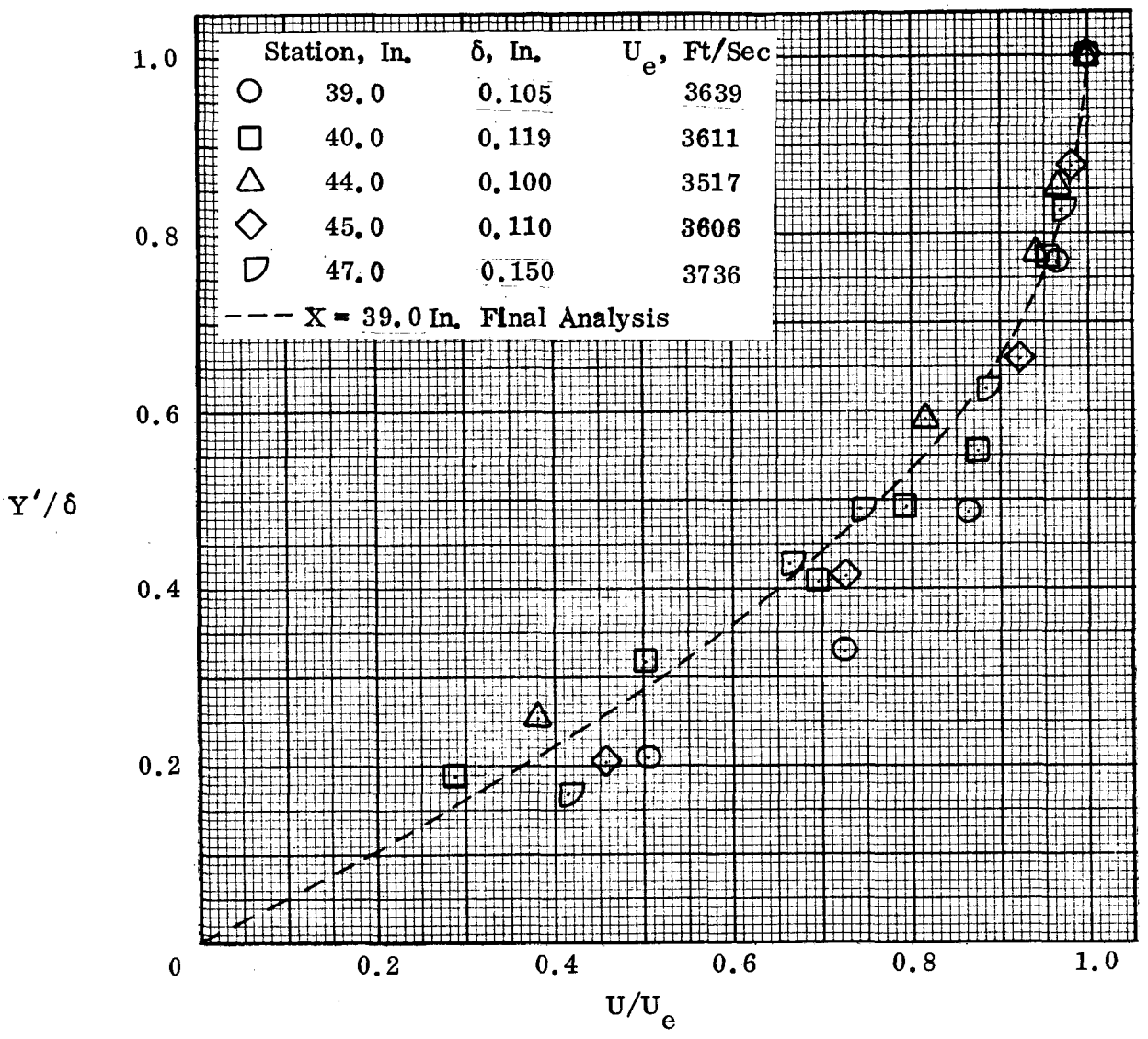

Figure 73. Summary of Velocity Distributions, P2 Inlet Model Cowl.

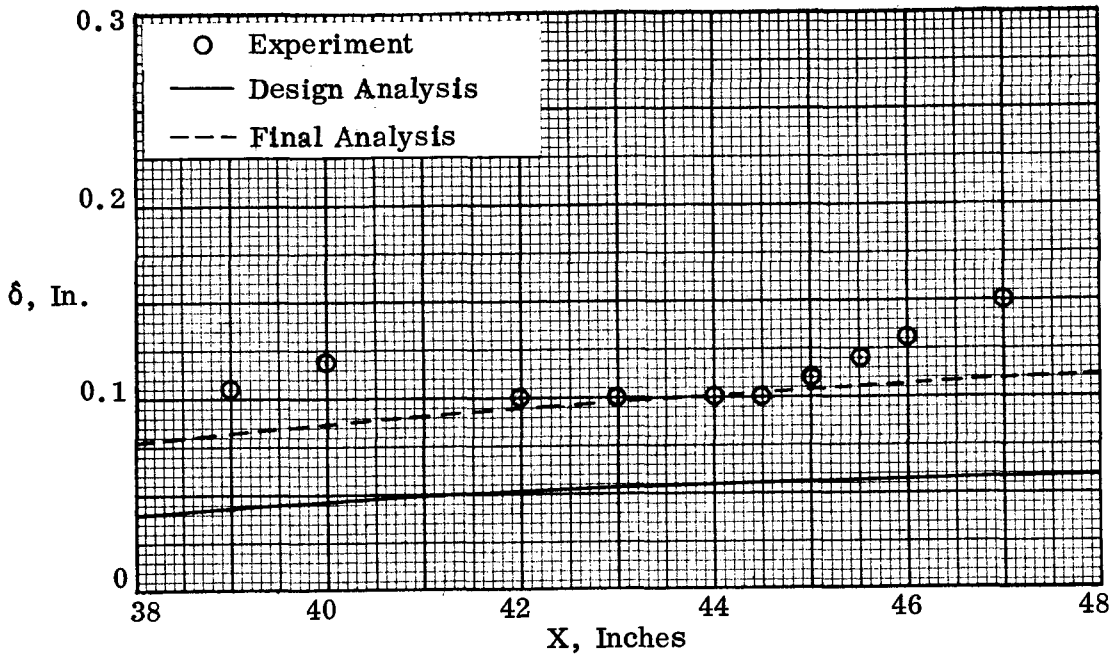

(a) Boundary-Layer Properties

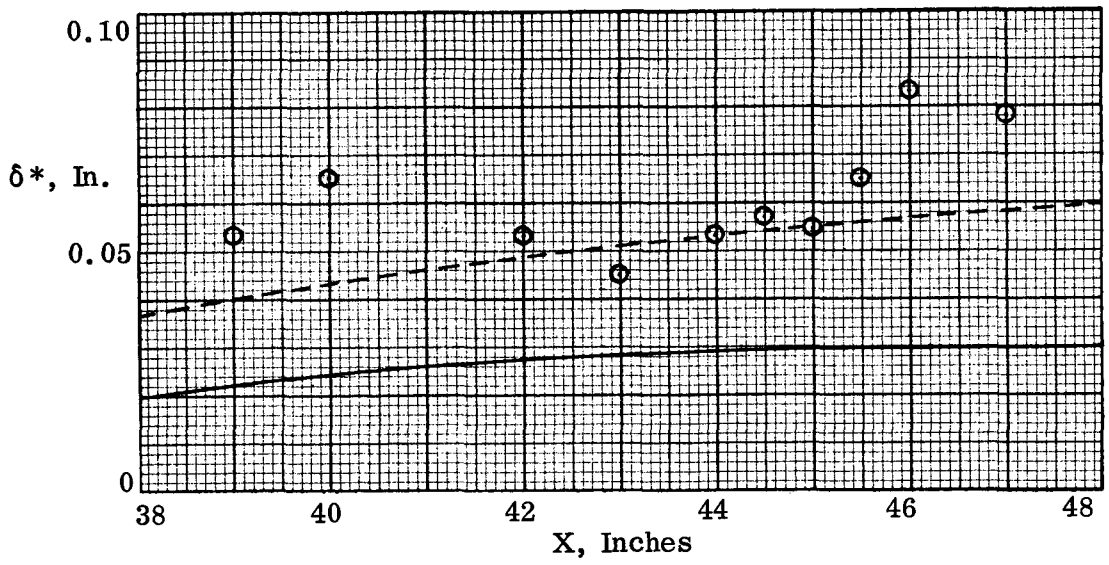

(b) Displacement Thickness

Figure 74. Boundary-Layer Properties, P2 Inlet Model Cowl.

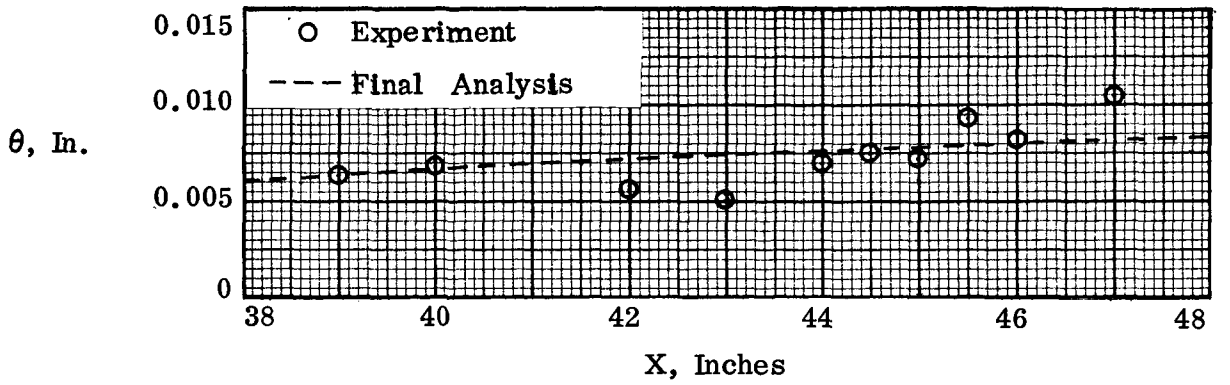

(c) Momentum Thickness

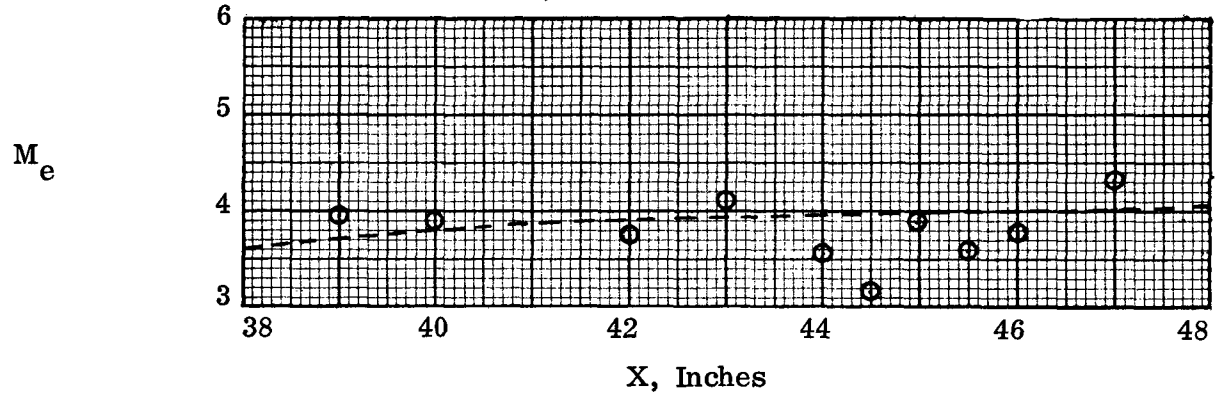

(d) Mach Number

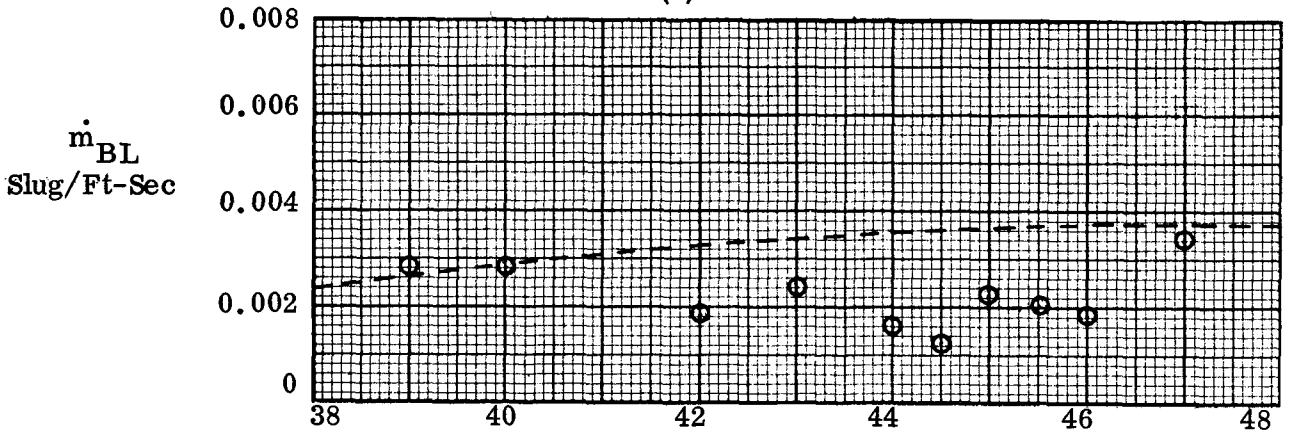

(e) Mass Flow

Figure 74. Concluded.

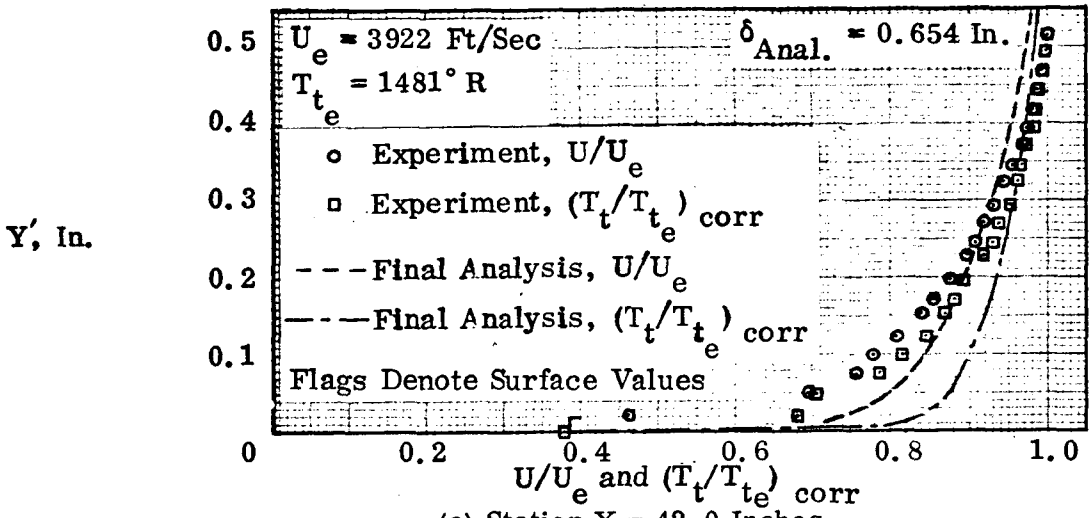

(a) Station X = 42.0 Inches

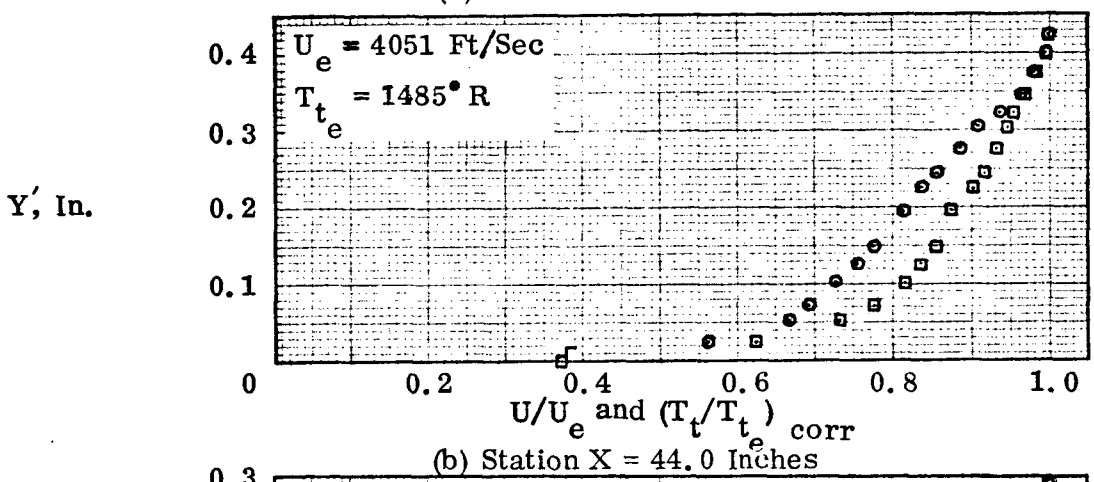

(b) Station X = 44.0 Inches

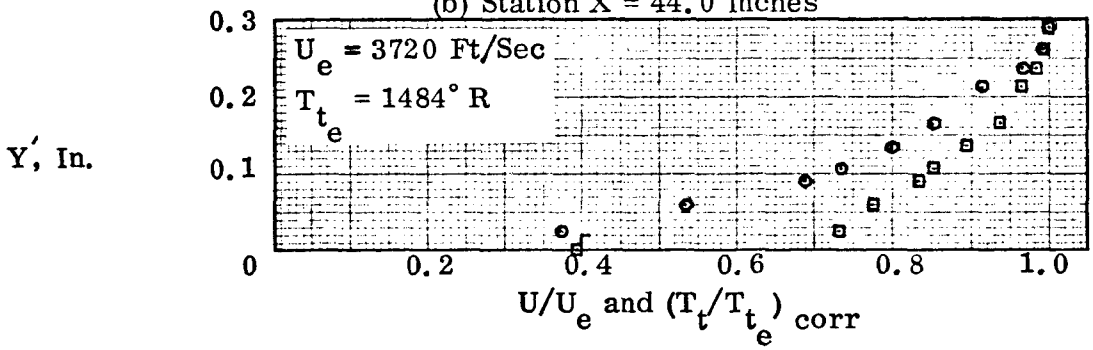

(c) Station X = 45.0 Inches

Figure 75. Boundary-Layer Velocity and Total Temperature Distributions, P8 Inlet Model Centerbody.

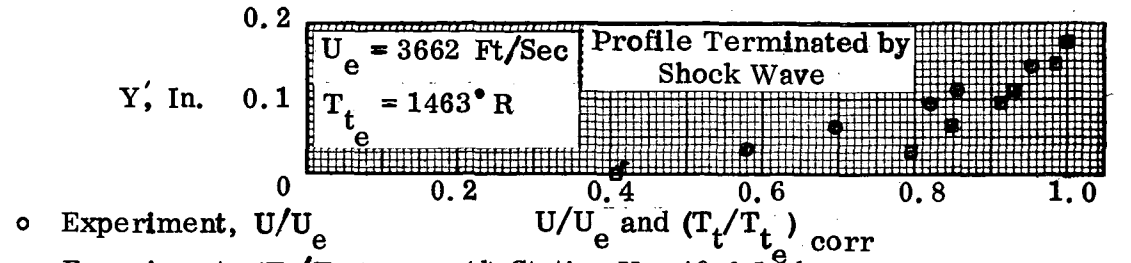

o Experiment, U/U_e

□ Experiment, $(T_t/T_{t_e})_{corr}$

(d) Station X = 46.0 Inches

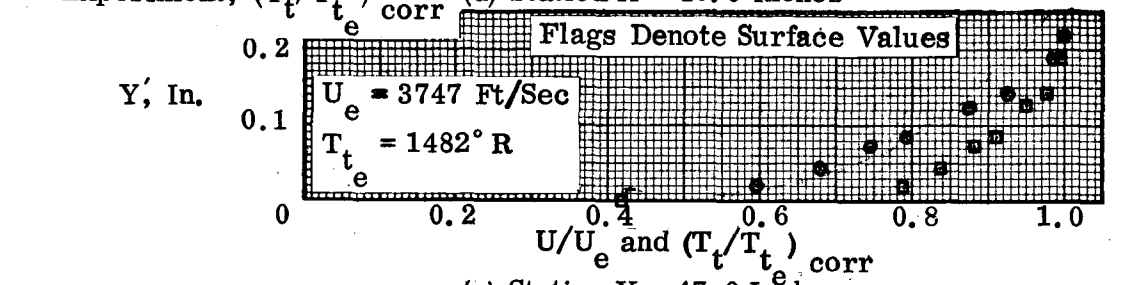

(e) Station X = 47.0 Inches

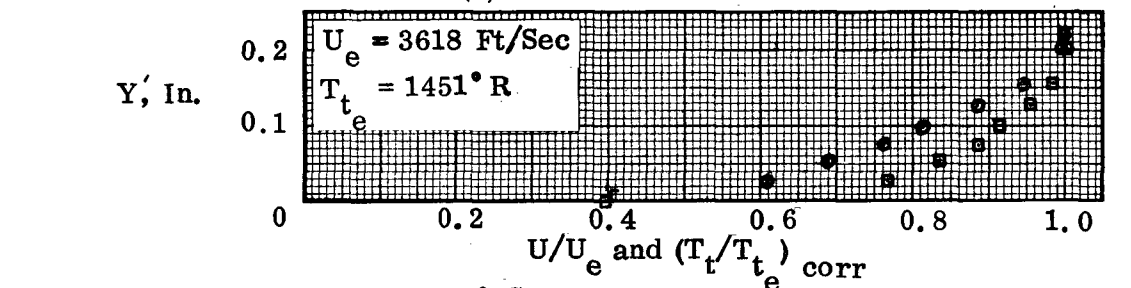

(f) Station X = 48.0 Inches

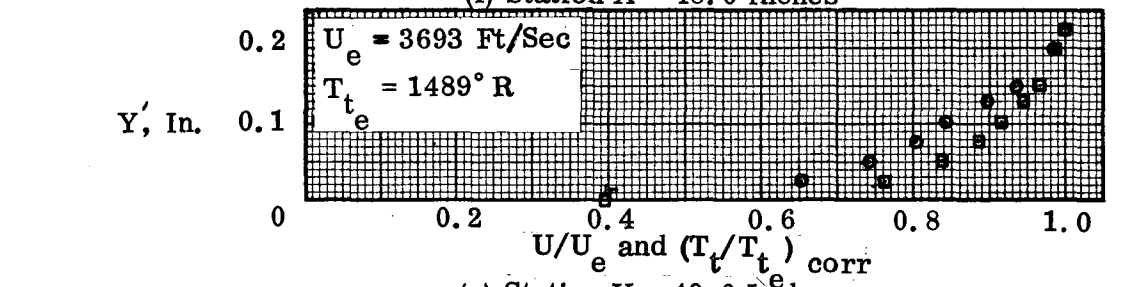

(g) Station X = 49.0 Inches

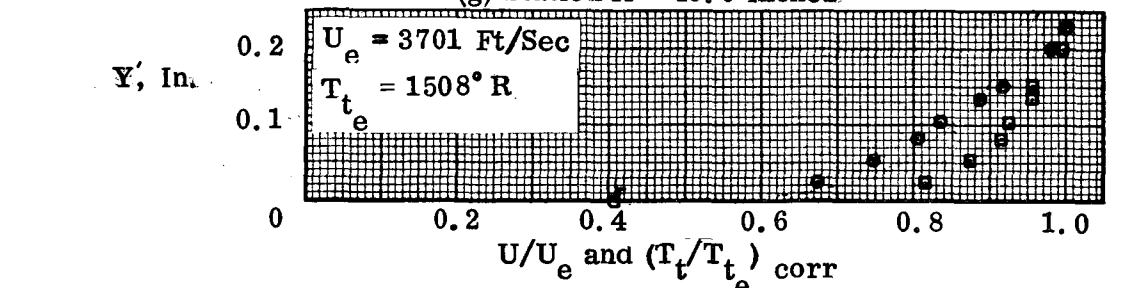

(h) Station X = 49.5 Inches

Figure 75. Concluded.

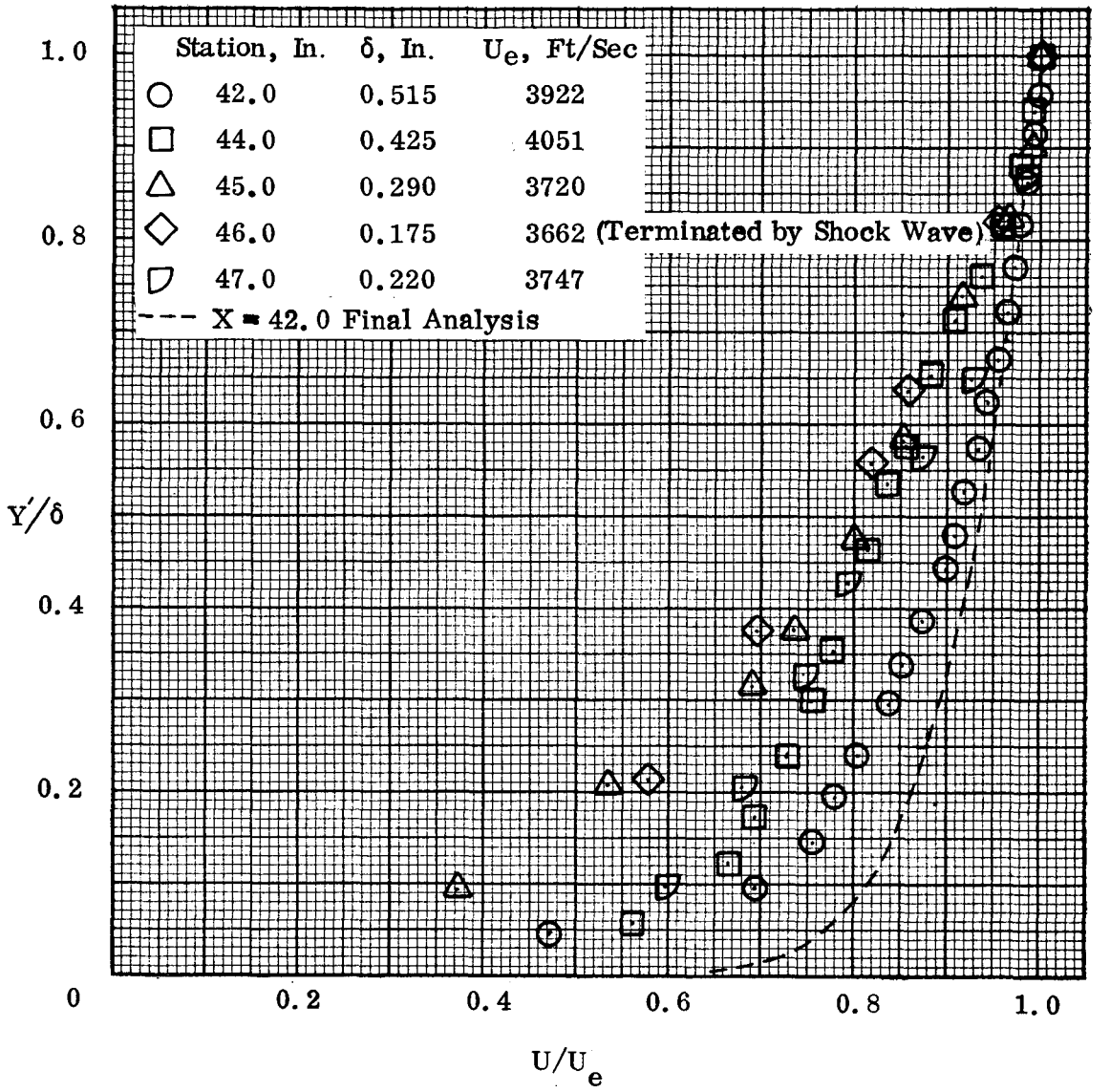

(a) Stations Upstream and Within Interaction Region

Figure 76. Summary of Velocity Distributions, P8 Inlet Model Centerbody.

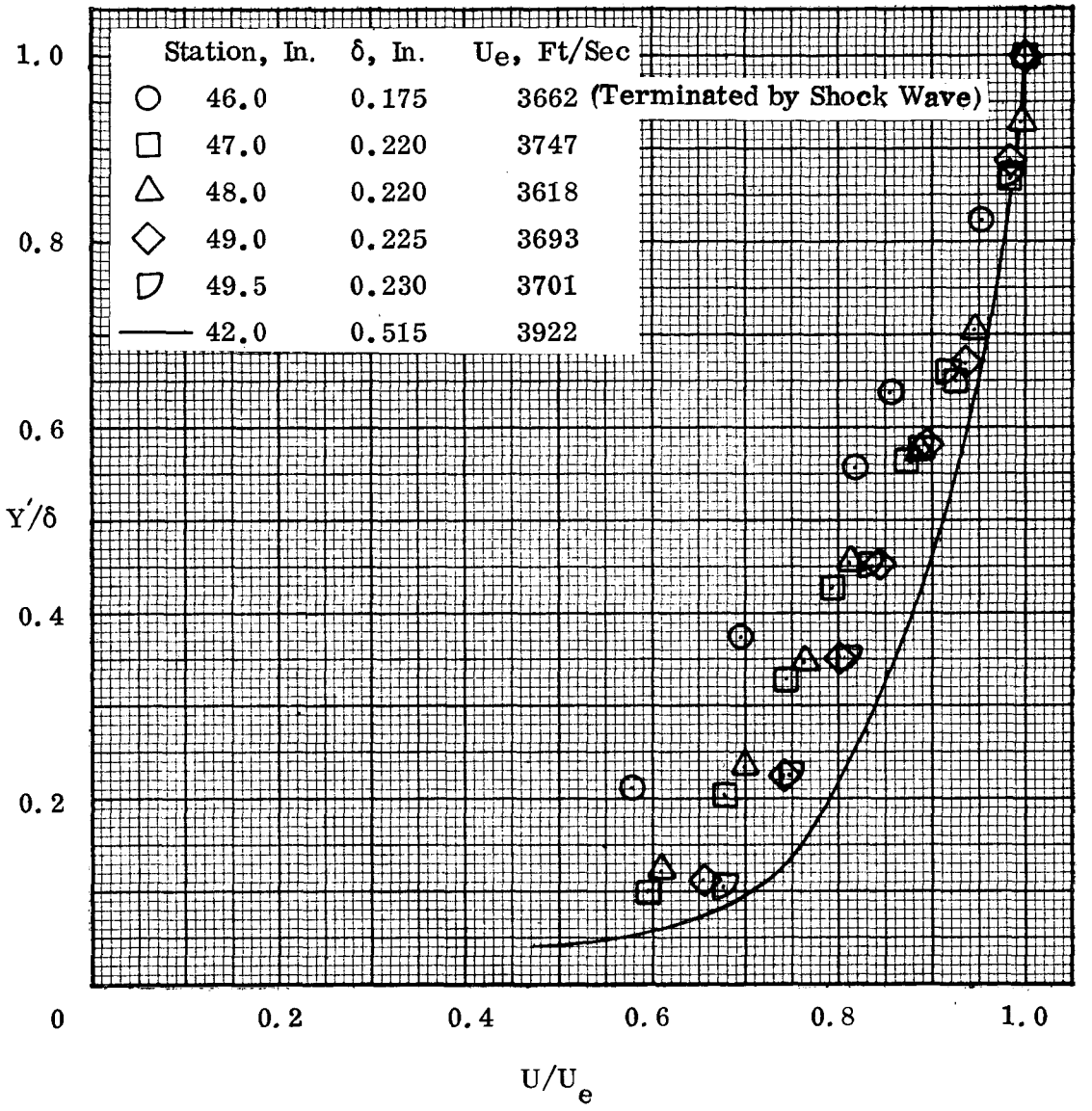

(b) Stations Downstream of Interaction Region

Figure 76. Concluded.

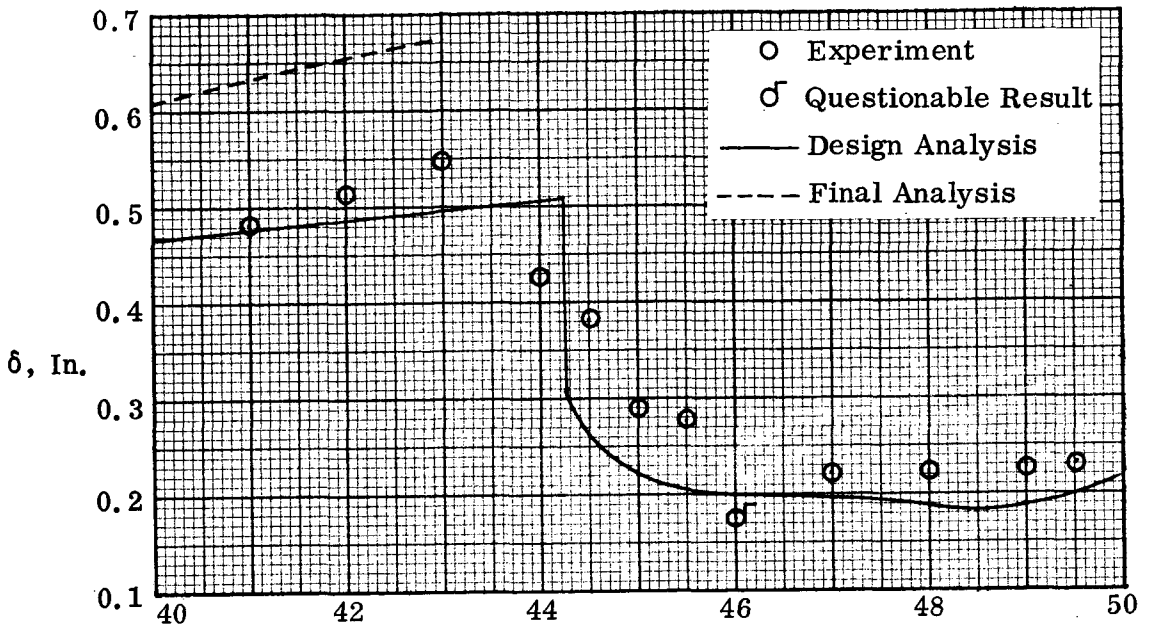

(a) Boundary-Layer Thickness

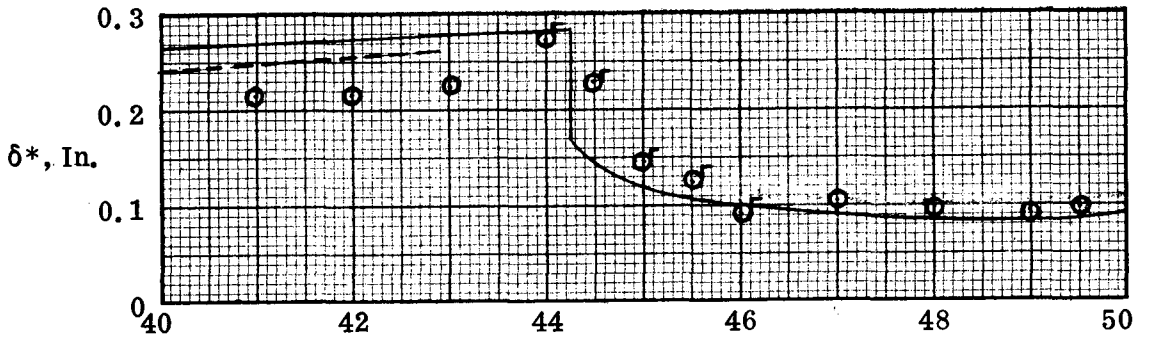

(b) Displacement Thickness

Figure 77. Boundary Layer Properties, P8 Inlet Model Centerbody.

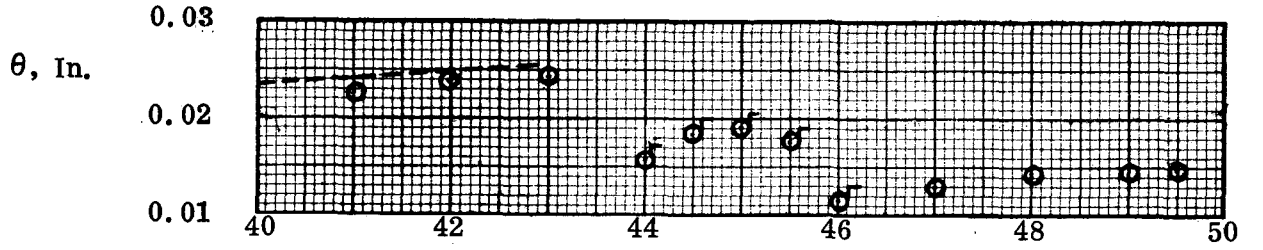

X, Inches

(c) Momentum Thickness

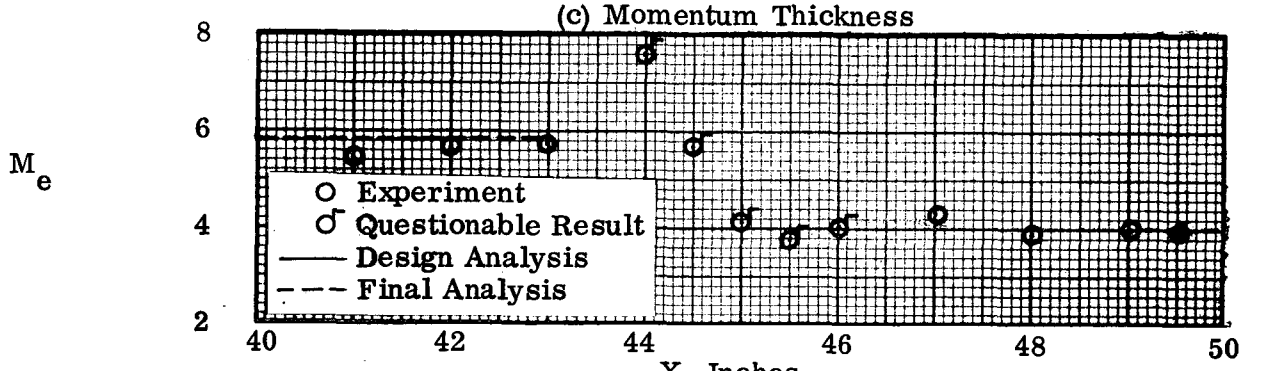

X, Inches

(d) Mach Number

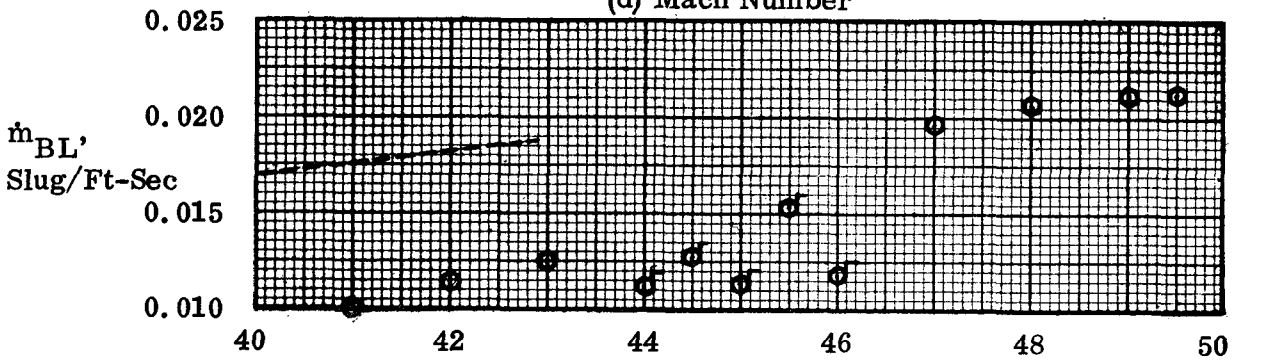

X, Inches

(e) Mass Flow

Figure 77. Concluded.

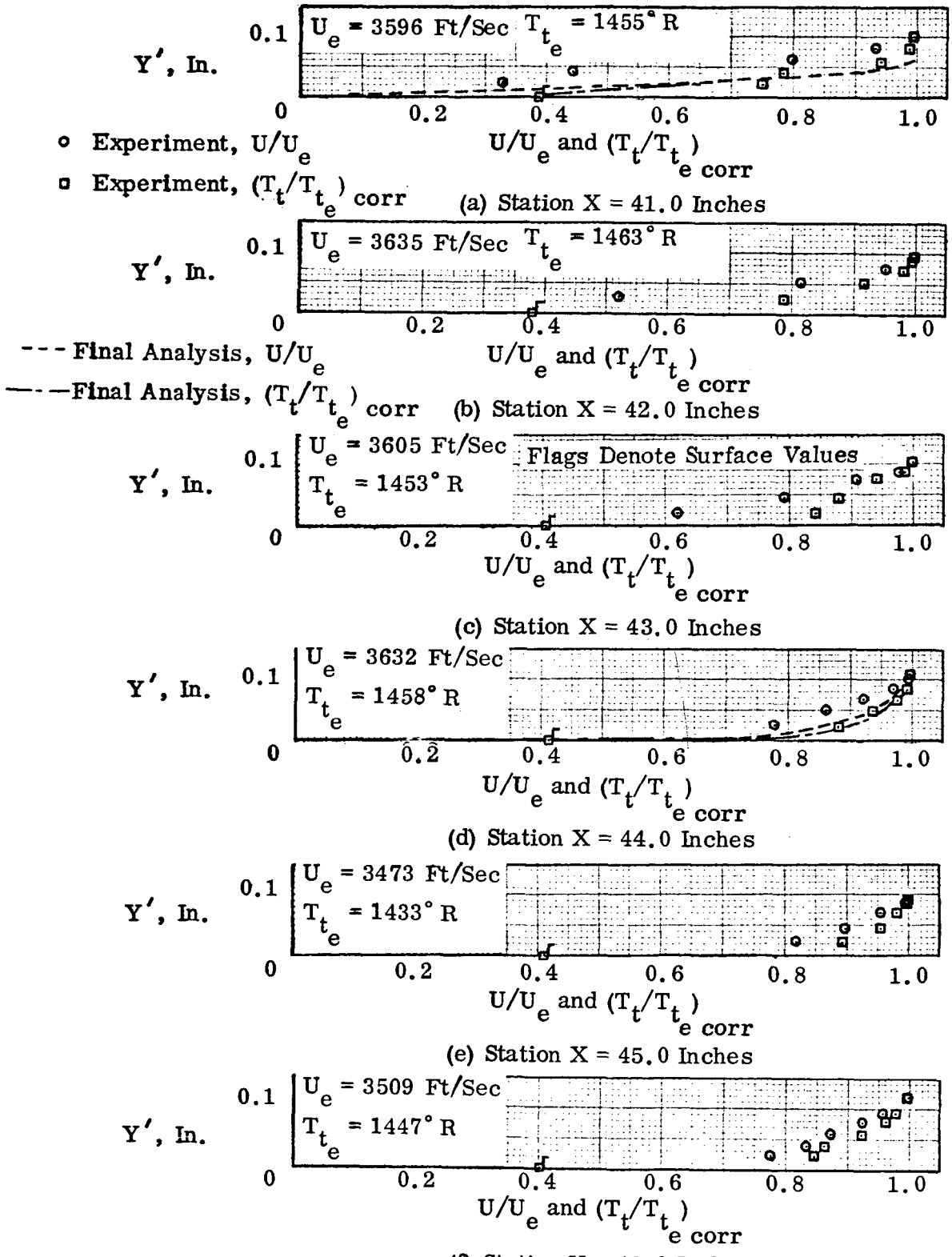

Figure 78. Boundary-Layer Velocity and Total Temperature Distributions, P8 Inlet Model Cowl.

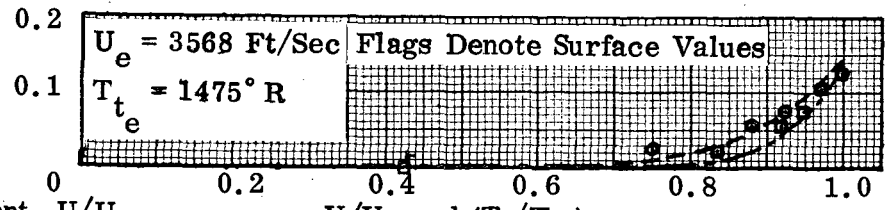

o Experiment, U/U_e

□ Experiment, $(T_t/T_{t_e})_{corr}$ (g) Station X = 47.0 Inches

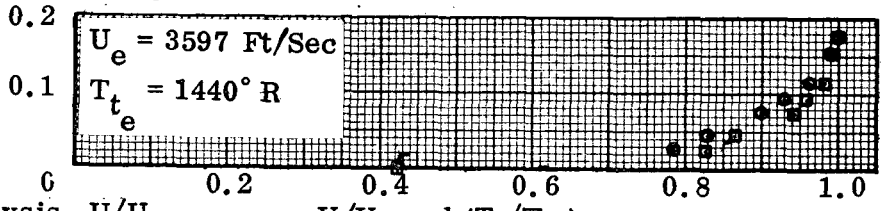

– – – Final Analysis, U/U_e

———Final Analysis, $(T_t/T_{t_e})_{corr}$ (h) Station X = 48.0 Inches

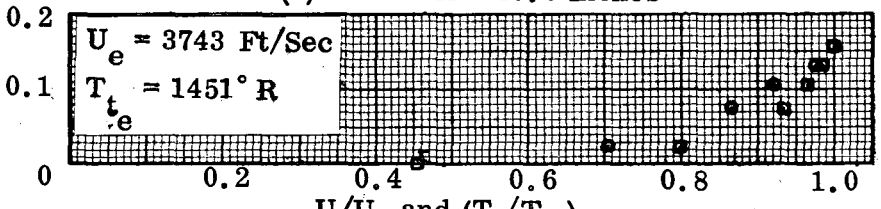

(i) Station X = 48.5 Inches

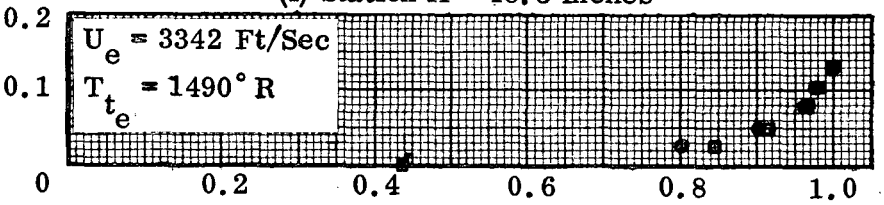

(j) Station X = 49.0 Inches

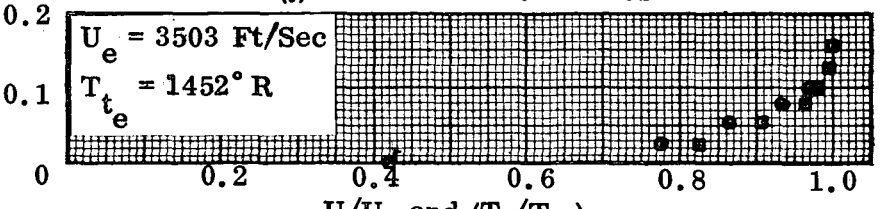

(k) Station X = 49.5 Inches

Figure 78. Concluded.

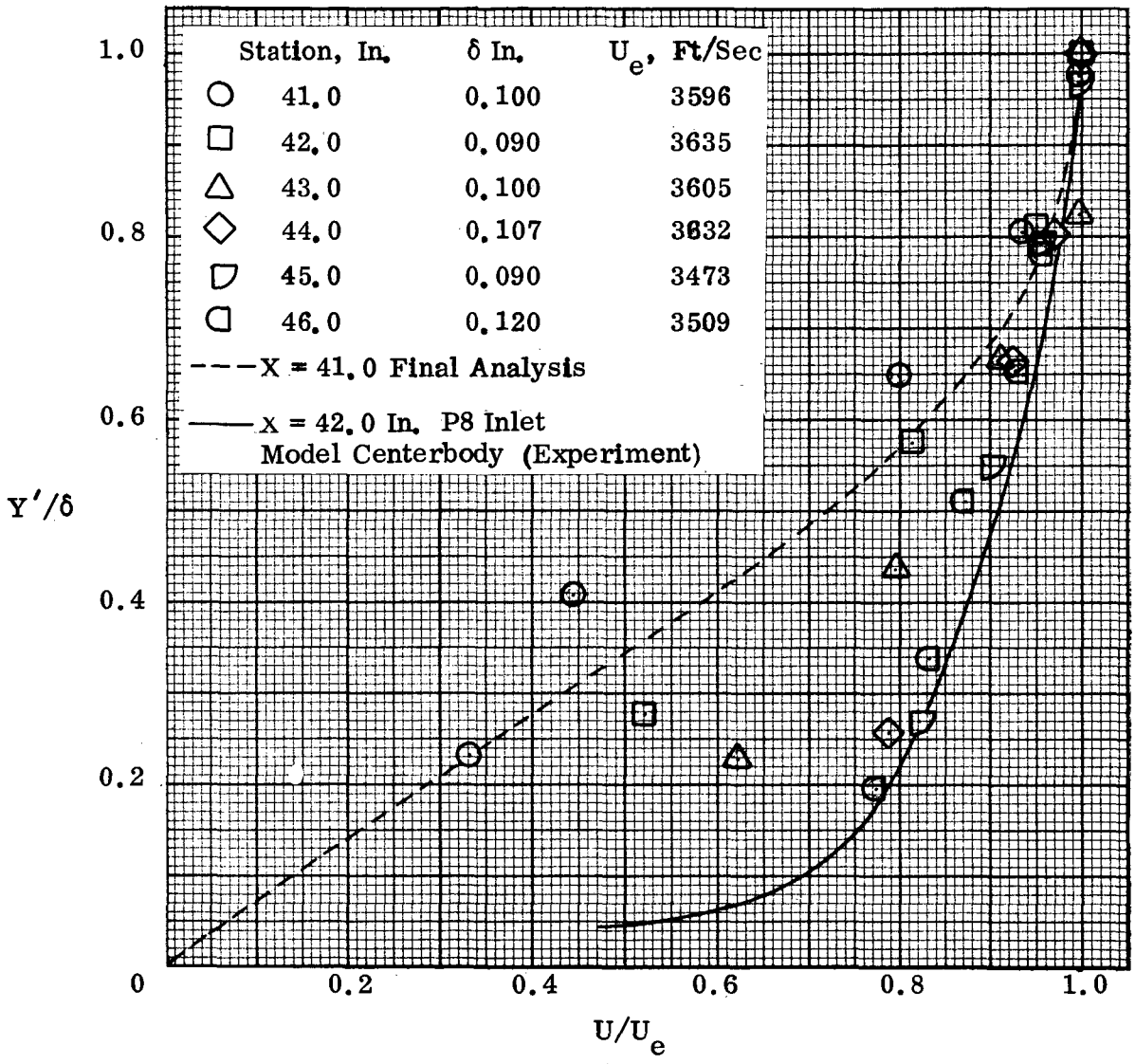

(a) Upstream Stations

Figure 79. Summary of Velocity Distributions, P8 Inlet Model Cowl.

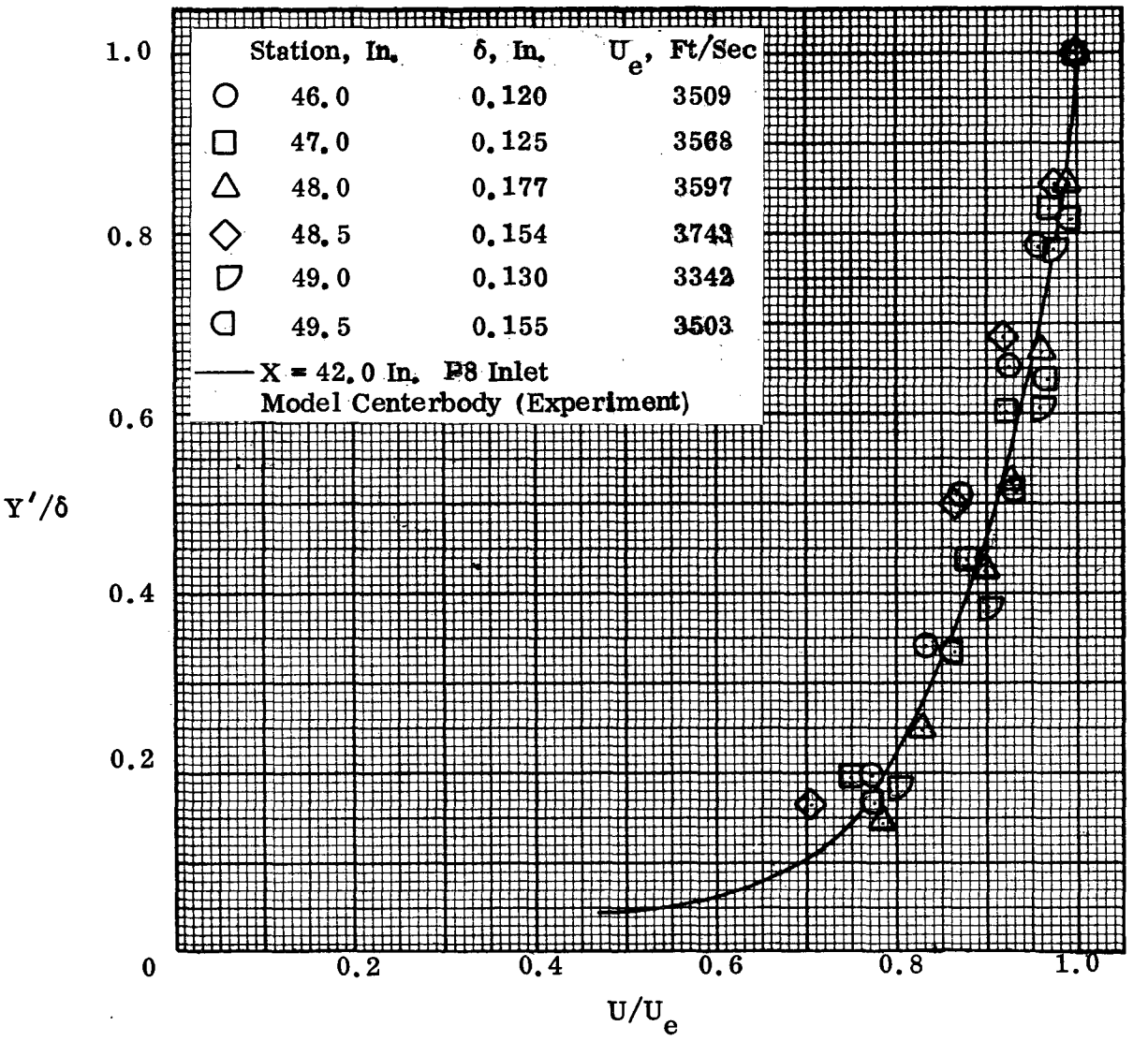

(b) Downstream Stations

Figure 79. Concluded.

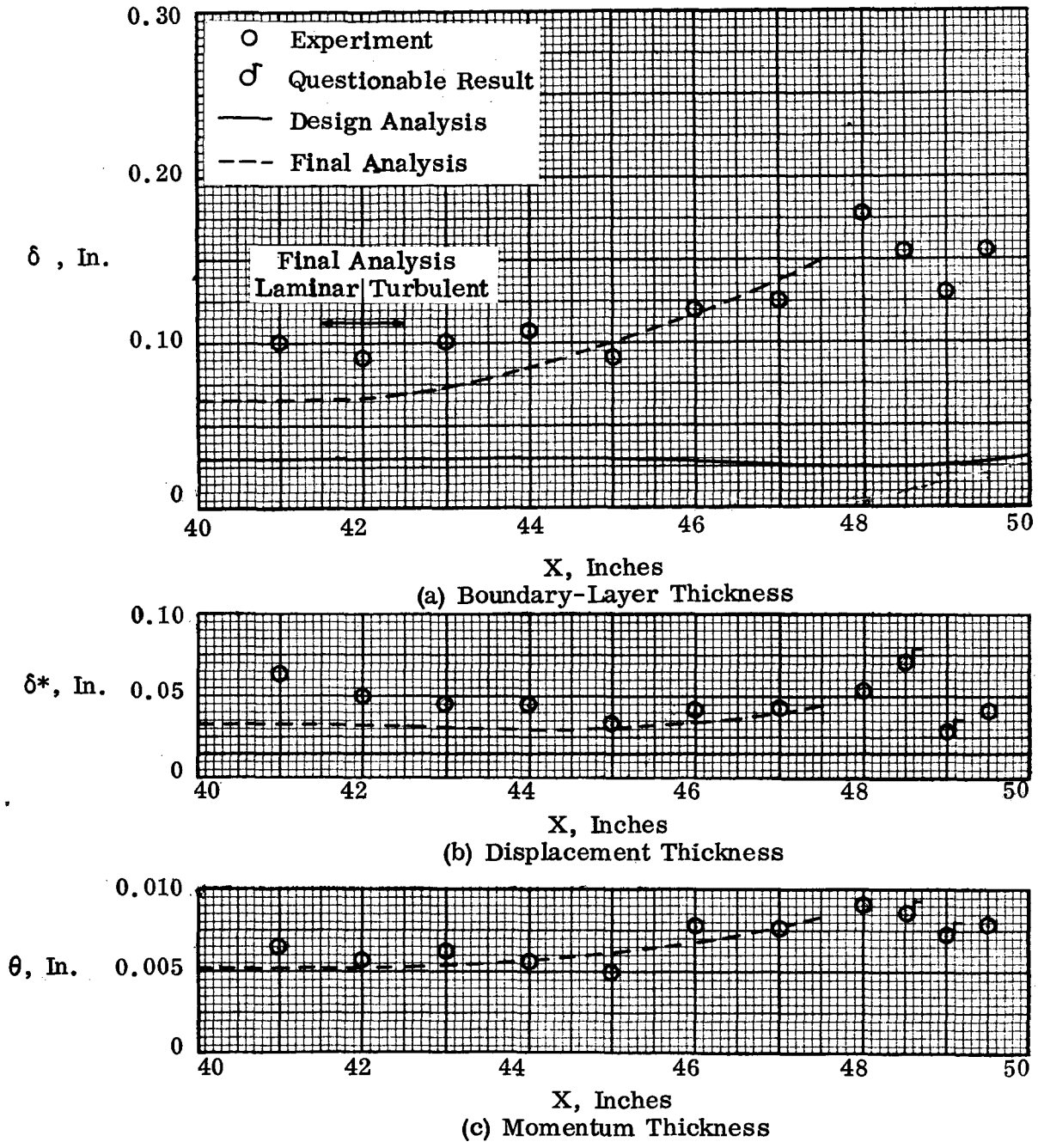

Figure 80. Boundary-Layer Properties, P8 Inlet Model Cowl.

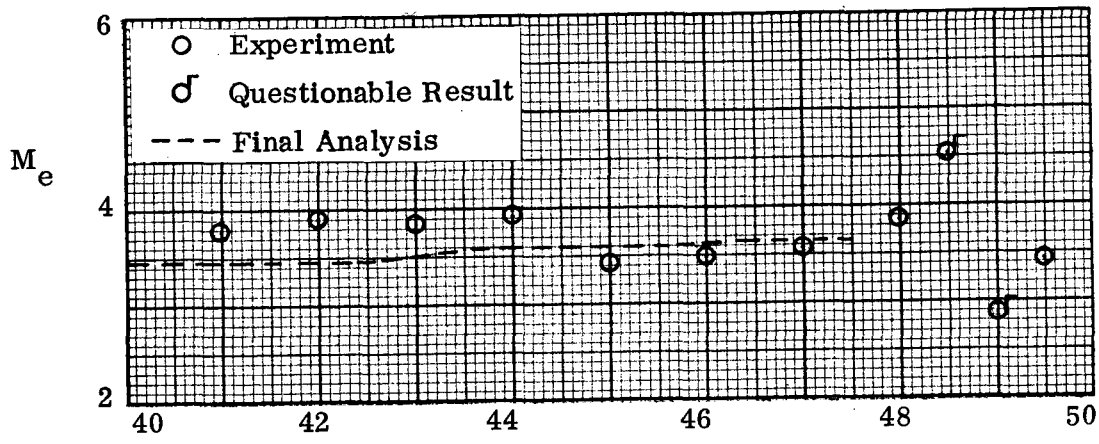

(d) Mach Number

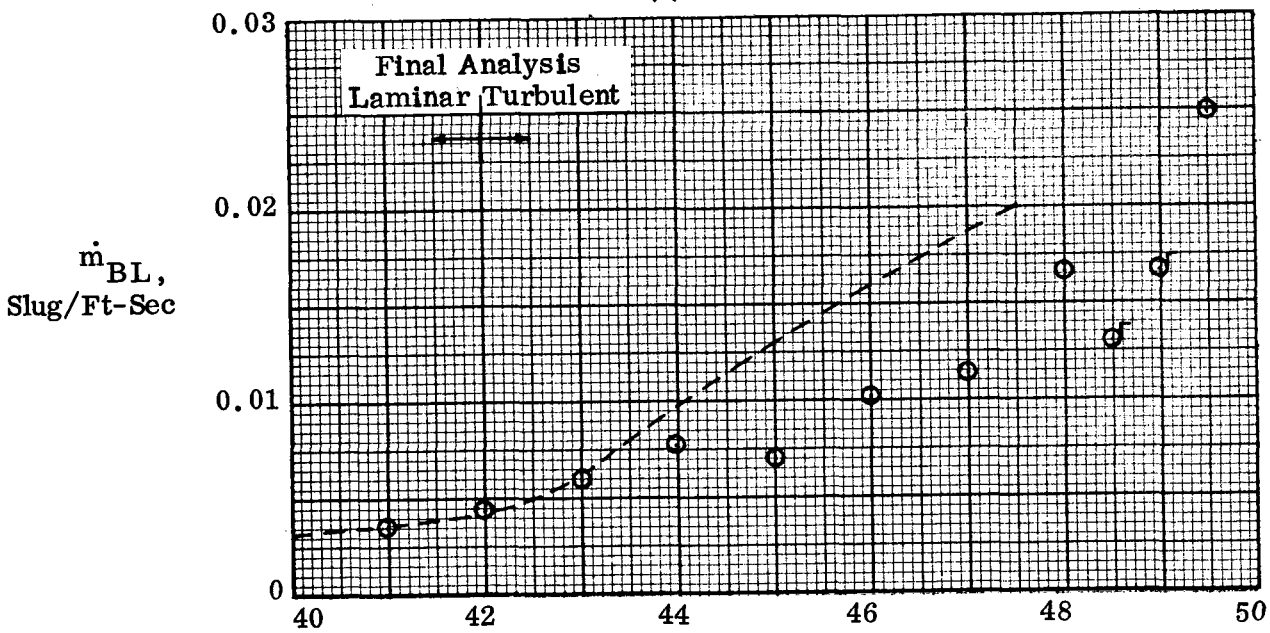

(e) Mass Flow

Figure 80. Concluded.

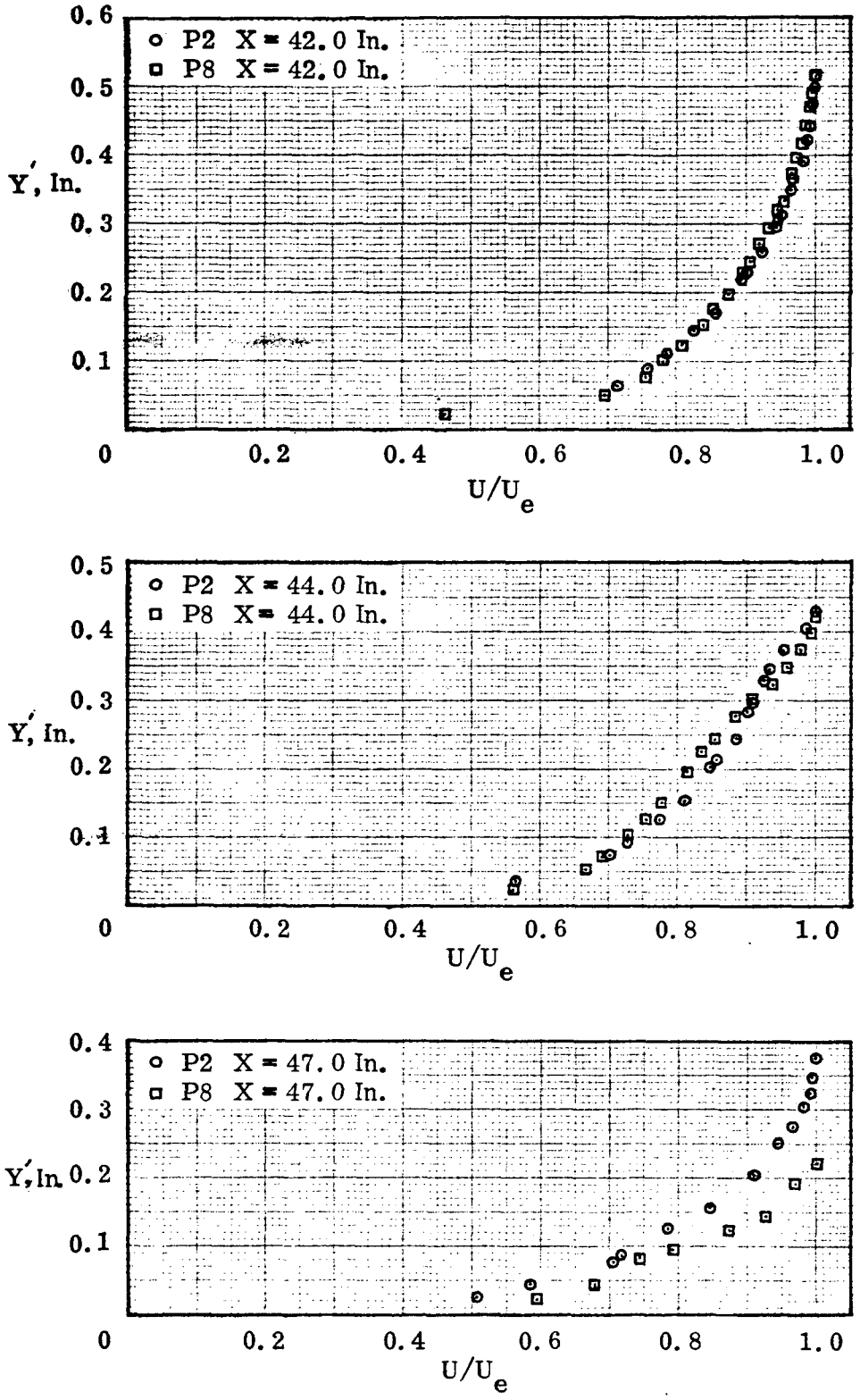

(a) Centerbody

Figure 81. Comparison of Boundary-Layer Velocity Distributions, P2 and P8 Inlet Models.

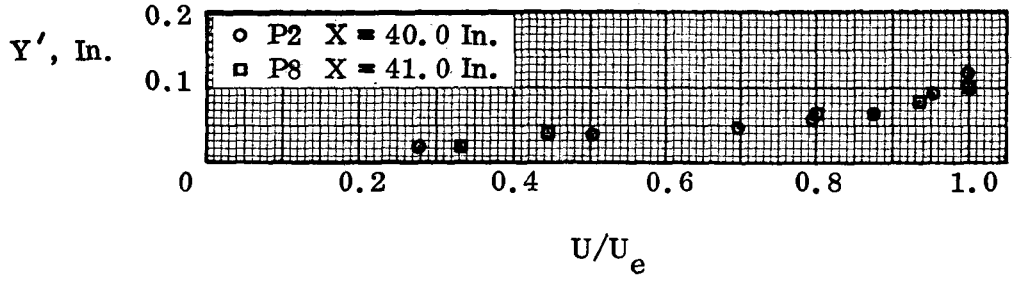

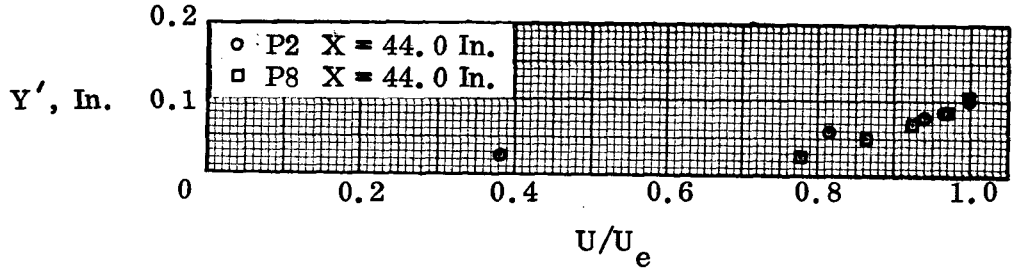

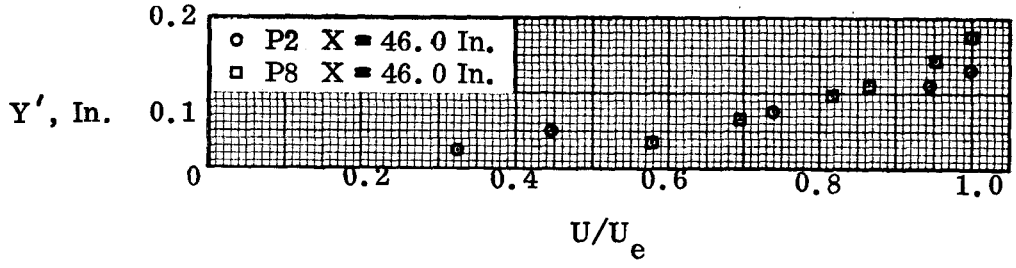

(b) Cowl

Figure 81. Concluded.

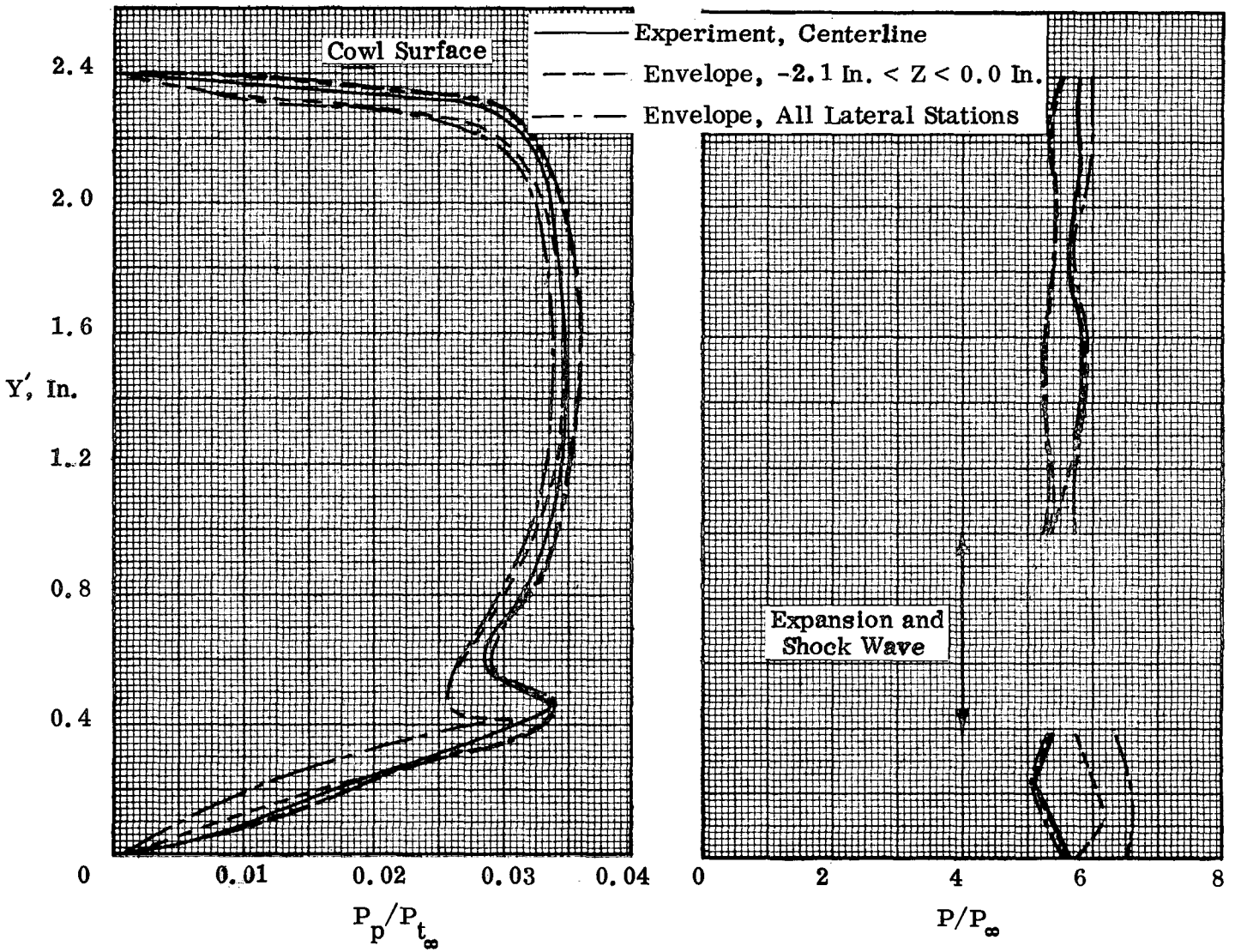

(a) Pitot Pressure

(b) Static Pressure

Figure 82. Flowfield Properties at Throat Station, P2 Inlet Model.

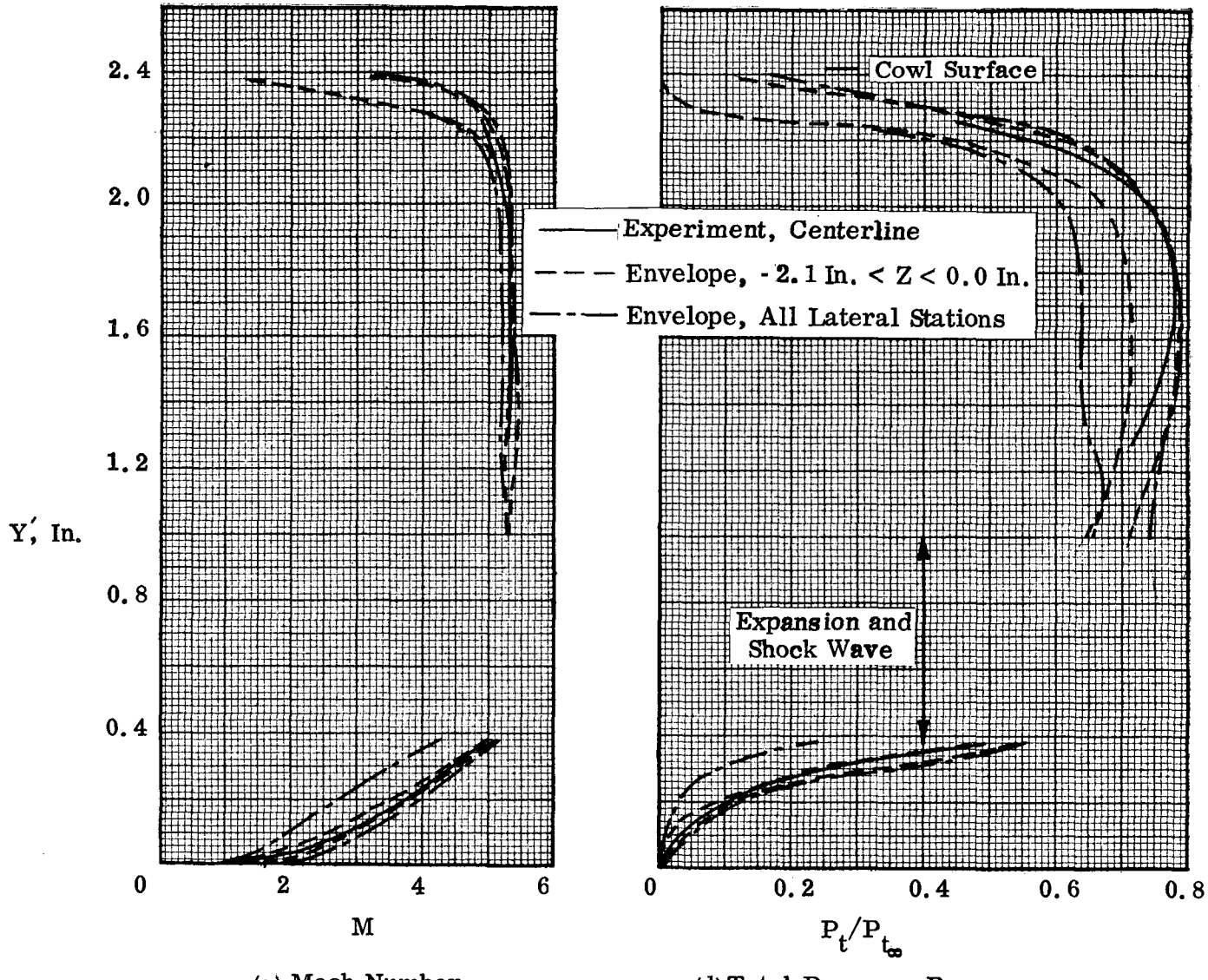

(c) Mach Number

(d) Total Pressure Recovery

Figure 82. Concluded.

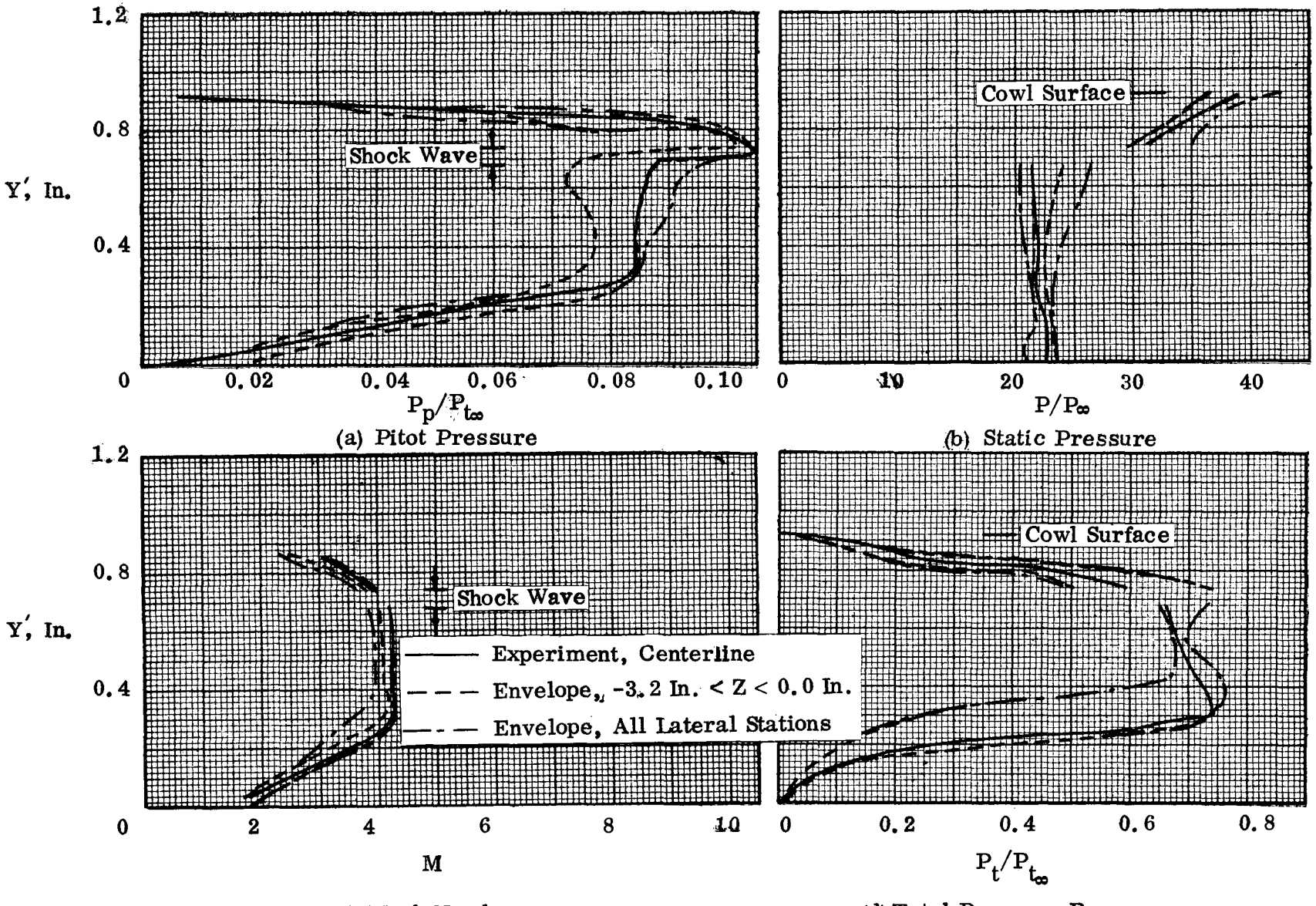

Figure 83. Flowfield Properties at Throat Station, P8 Inlet Model.

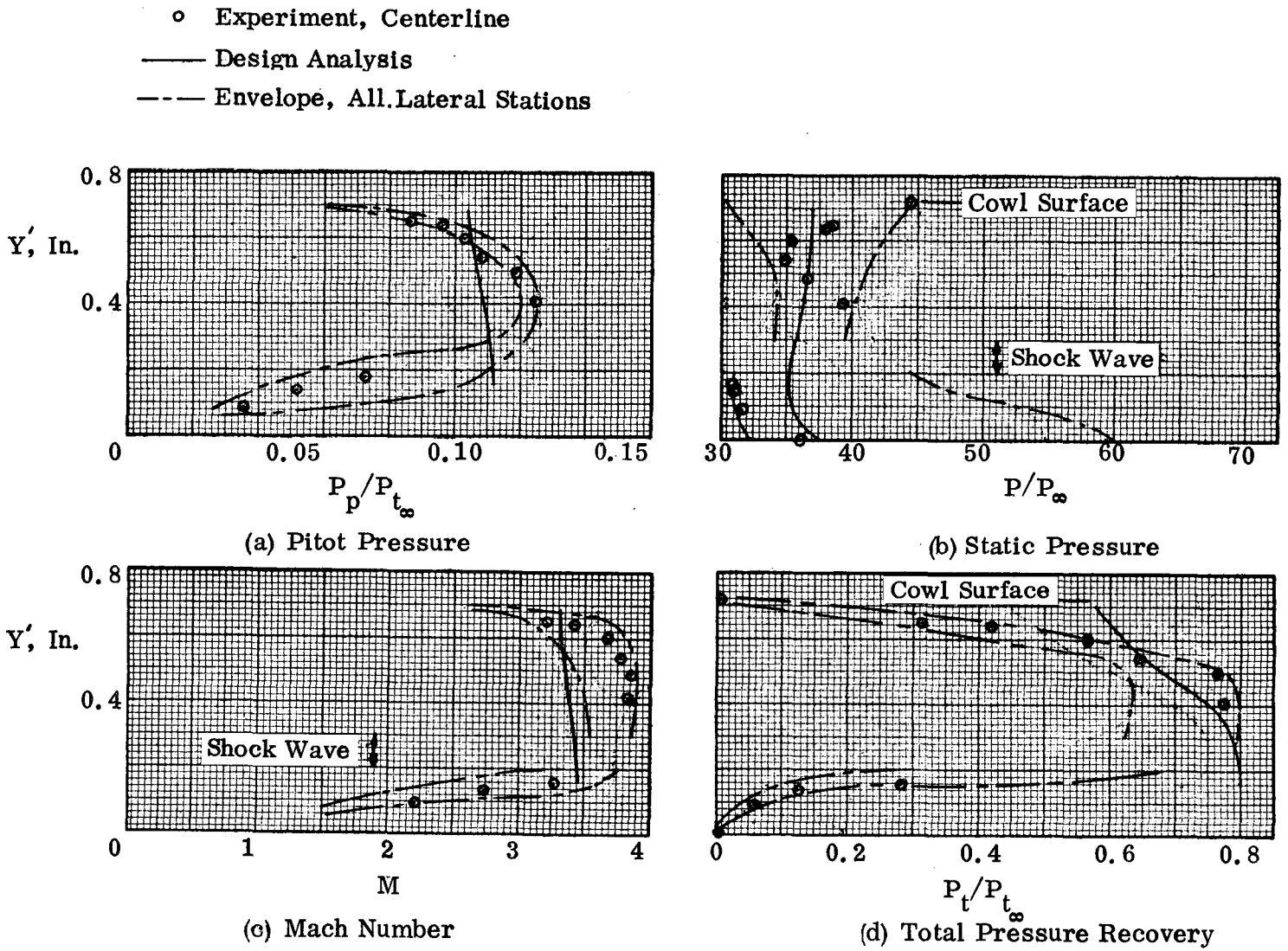

Figure 84. Flowfield Properties at Throat Station, P12 Inlet Model.

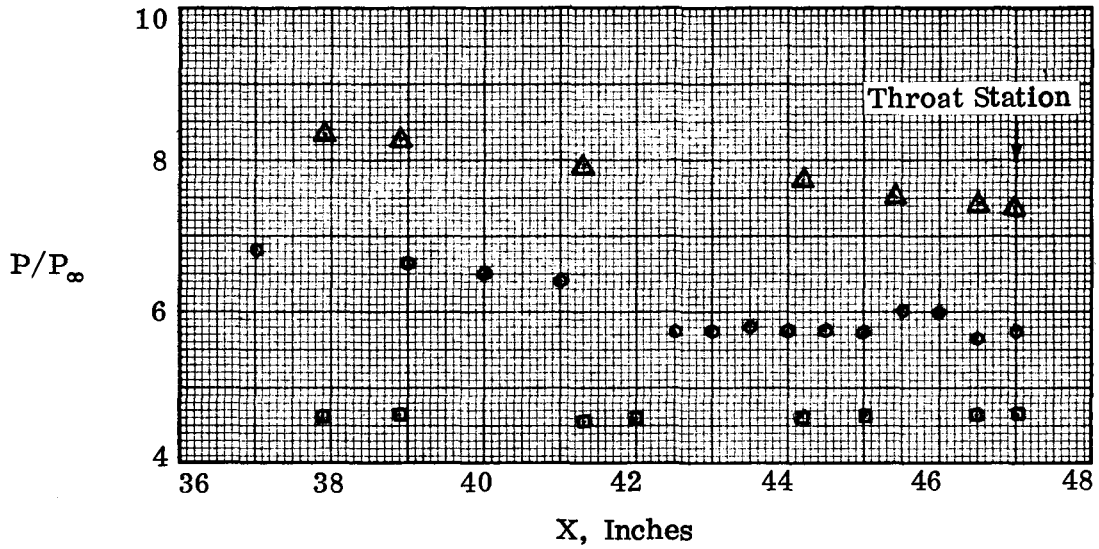

(a) Cowl Surface

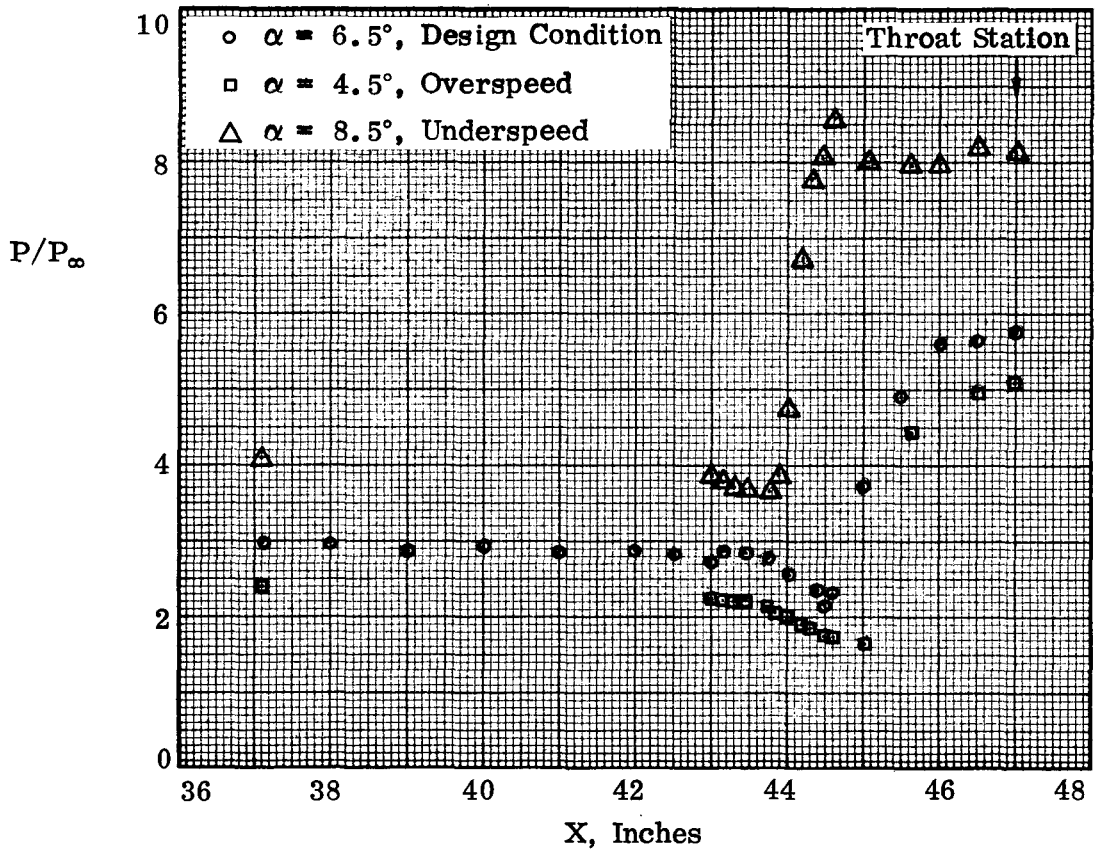

(b) Centerbody Surface

Figure 85. Effect of Off-Design Operation on Surface Static-Pressure Distributions, P2 Inlet Model.

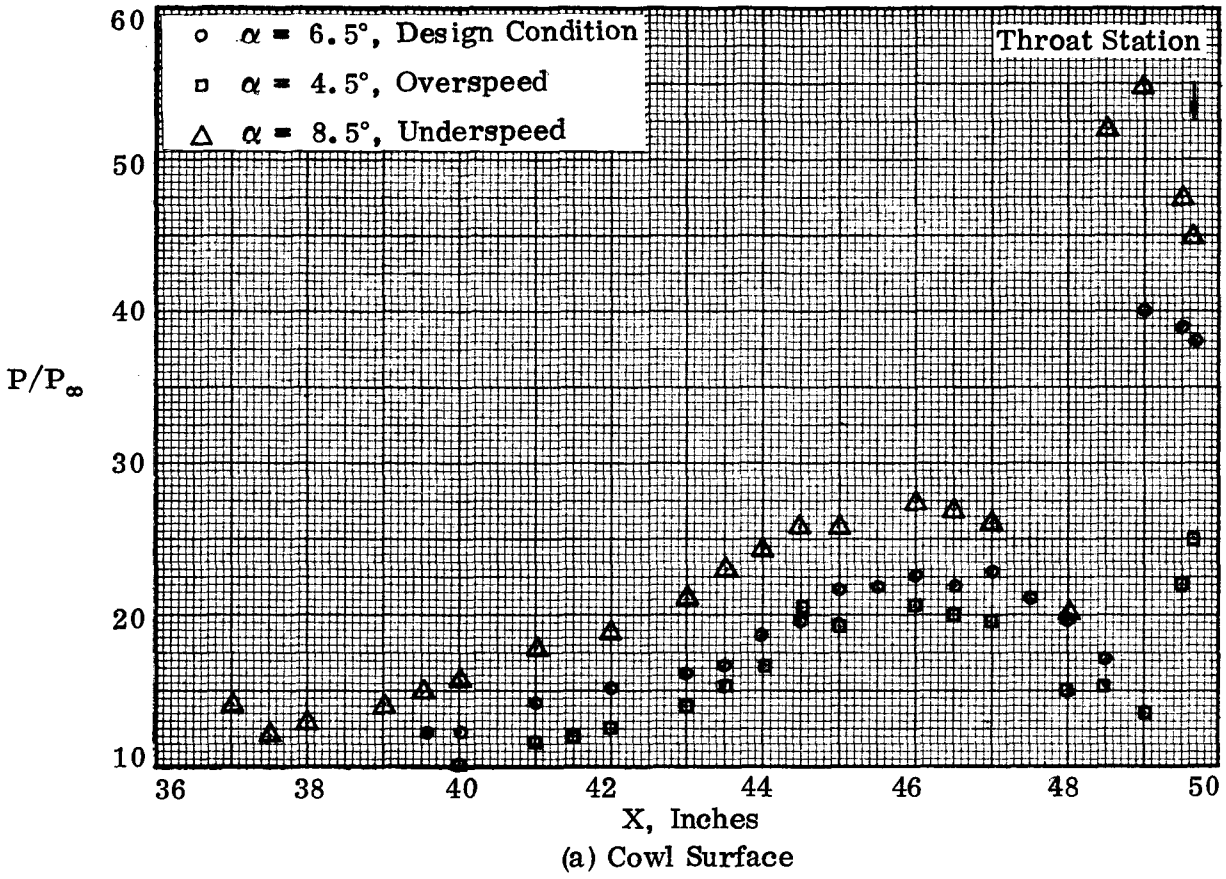

(a) Cowl Surface

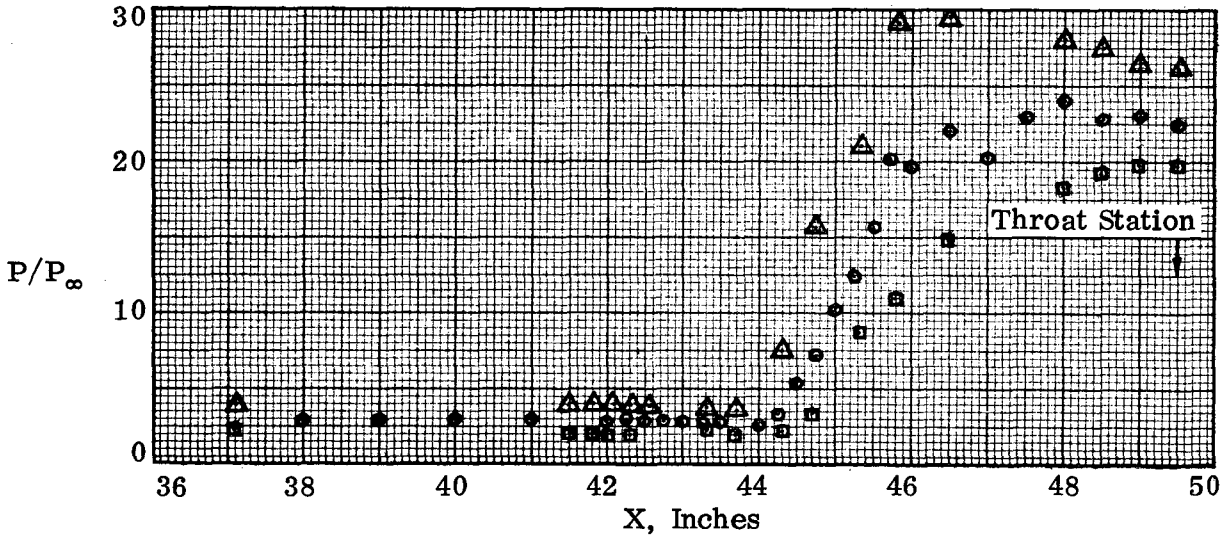

(b) Centerbody Surface

Figure 86. Effect of Off-Design Operation on Surface Static-Pressure Distributions, P8 Inlet Model.

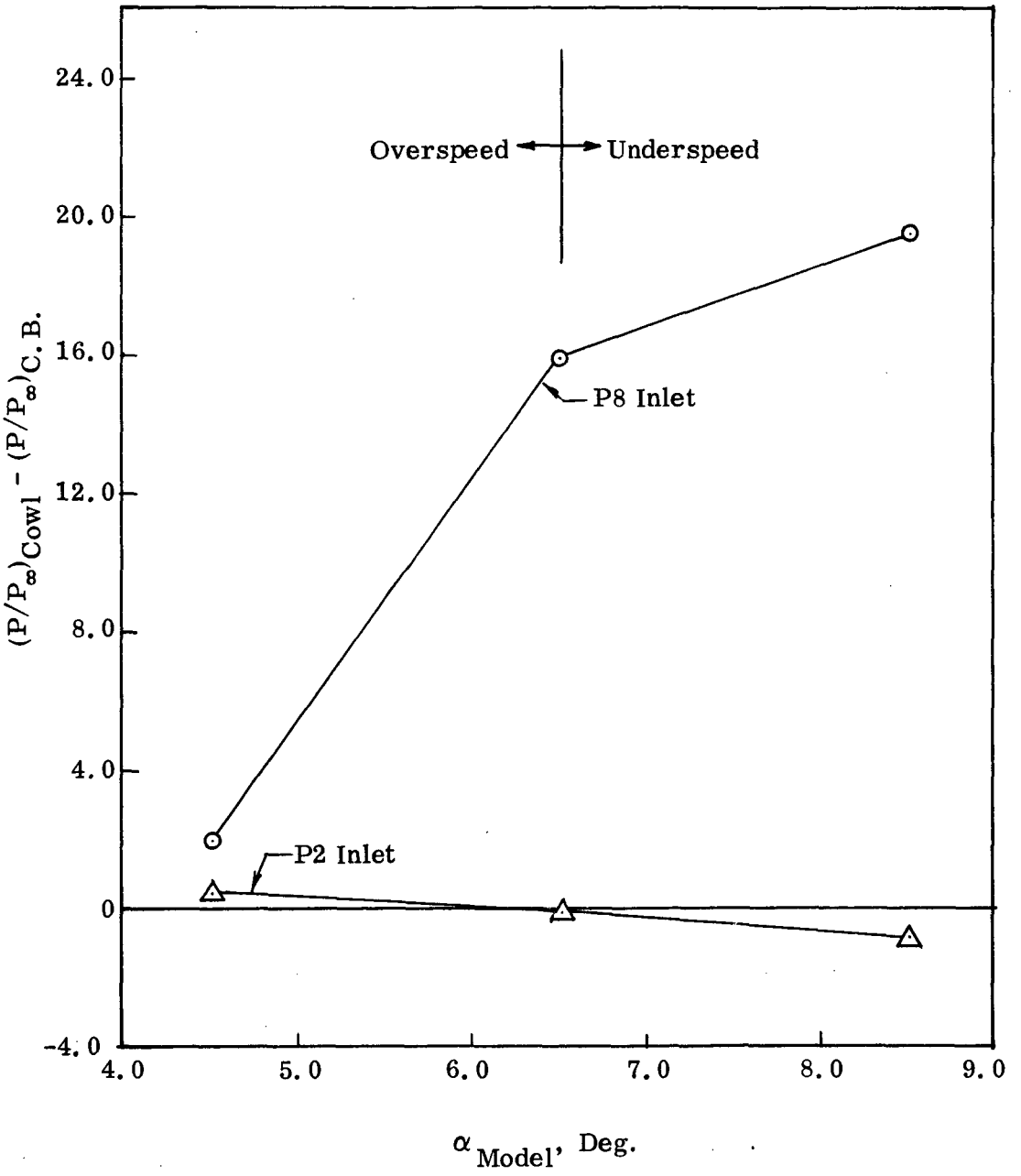

Figure 87. Effect of Off-Design Operation on Inlet Throat Pressure Differential.

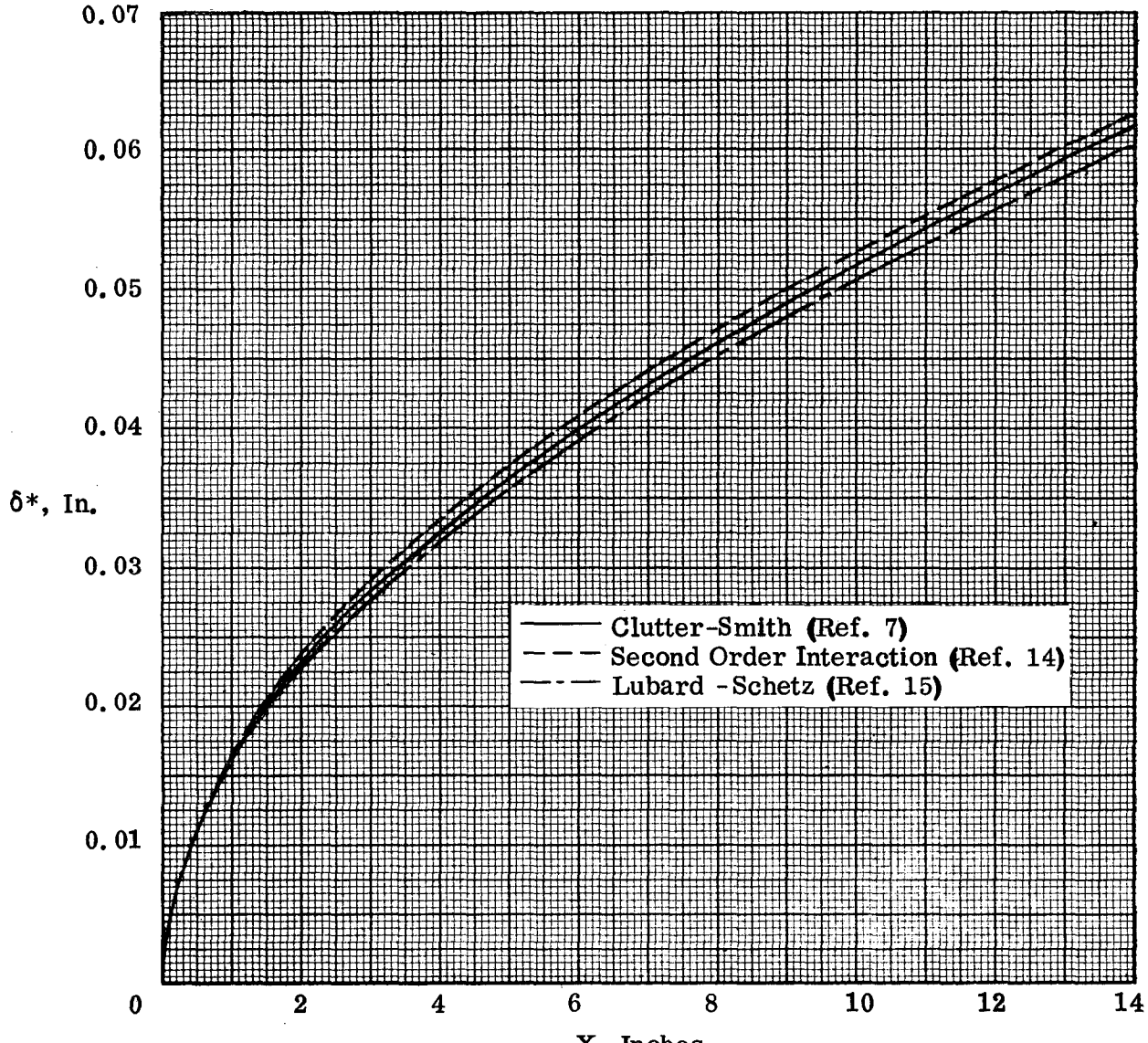

(a) Laminar Boundary Layer

Figure 88. Wedge-Forebody Boundary-Layer Development.

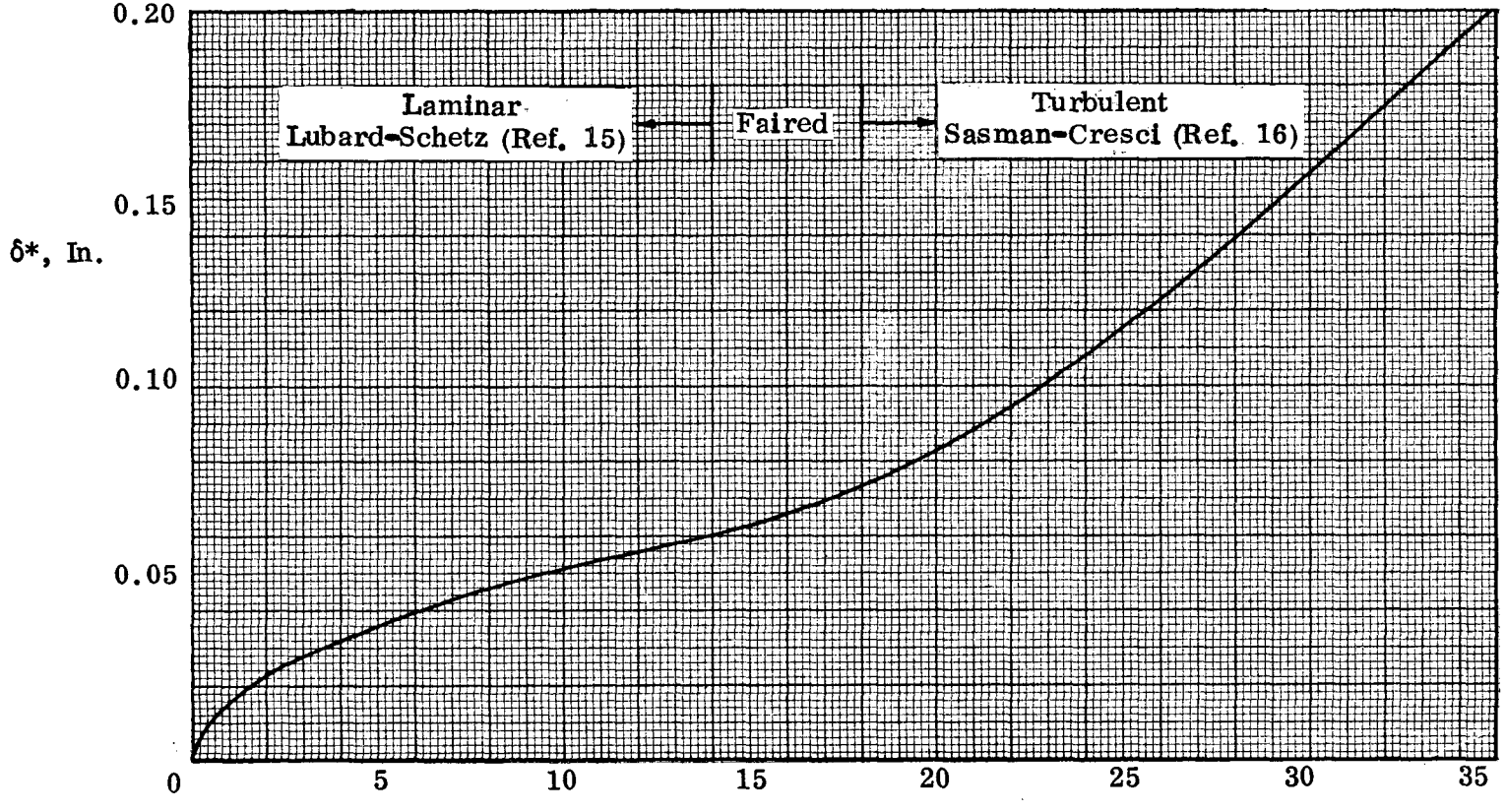

(b) Laminar and Turbulent Boundary Layers

Figure 88. Concluded.

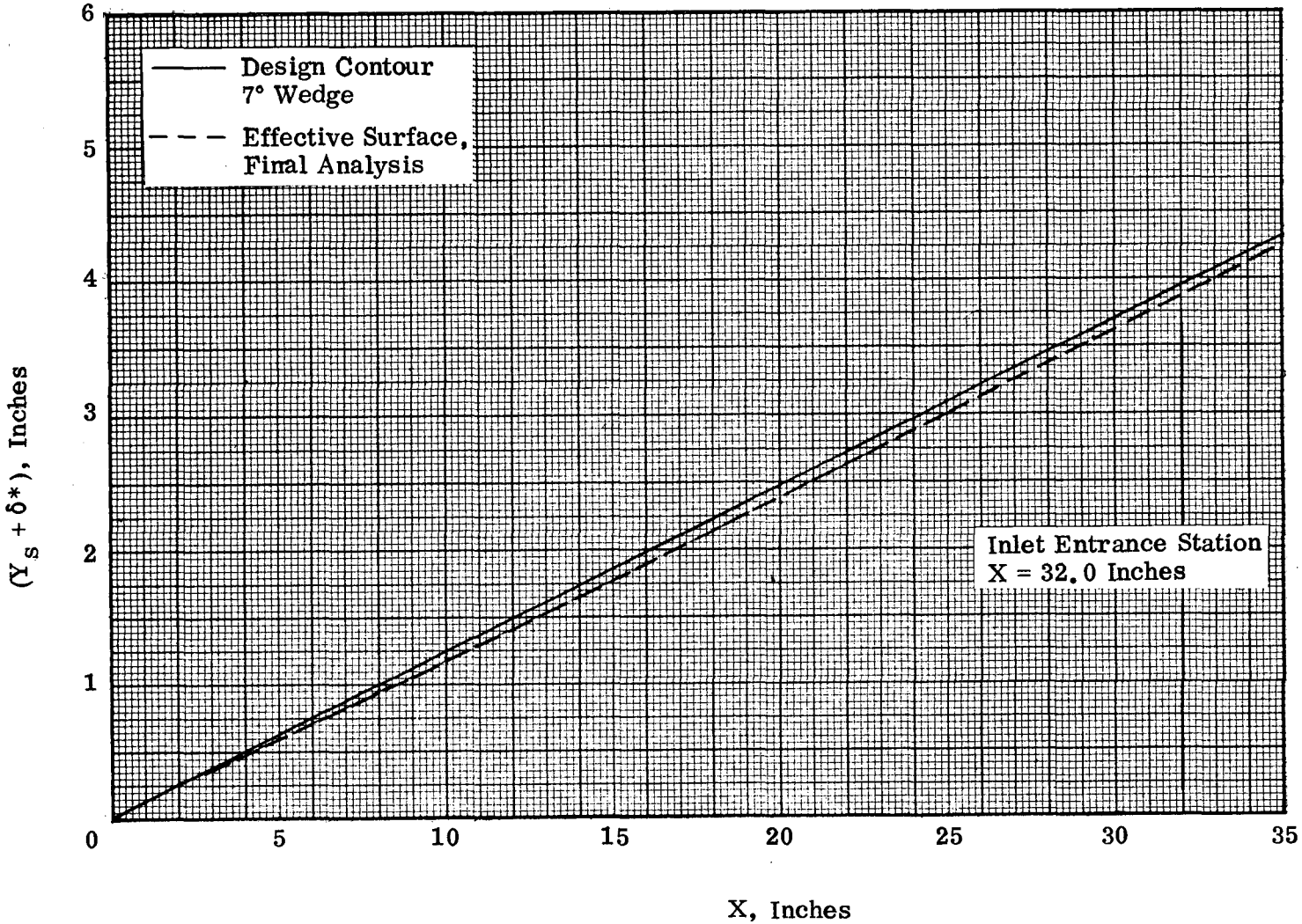

Figure 89. Wedge-Forebody Effective Surface Contour.

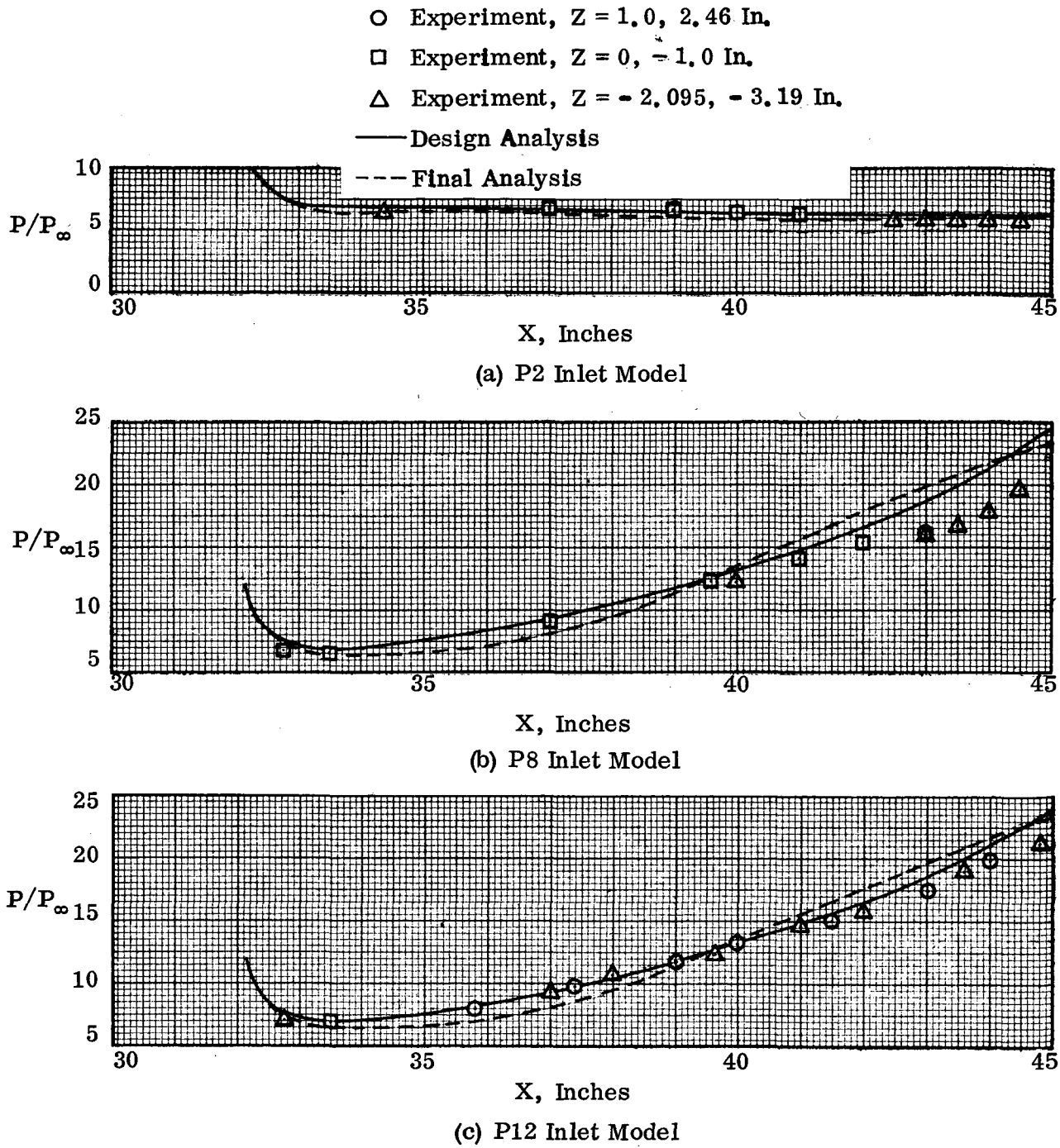

Figure 90. Cowl Surface Static-Pressure Distributions.